

The dynamics of the charged particles in a dual frequency capacitively coupled dielectric etch reactor.

Garrett Curley

▶ **To cite this version:**

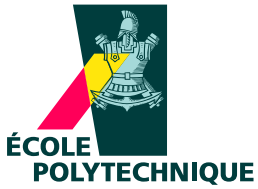
Garrett Curley. The dynamics of the charged particles in a dual frequency capacitively coupled dielectric etch reactor.. Fluid Dynamics [physics.flu-dyn]. Ecole Polytechnique X, 2008. English. NNT : . tel-00416652

HAL Id: tel-00416652
https://pastel.hal.science/tel-00416652

Submitted on 14 Sep 2009

HAL is a multi-disciplinary open access archive for the deposit and dissemination of scientific research documents, whether they are published or not. The documents may come from teaching and research institutions in France or abroad, or from public or private research centers.

L'archive ouverte pluridisciplinaire **HAL**, est destinée au dépôt et à la diffusion de documents scientifiques de niveau recherche, publiés ou non, émanant des établissements d'enseignement et de recherche français ou étrangers, des laboratoires publics ou privés.



Thèse présentée pour obtenir le grade de

DOCTEUR DE L'ÉCOLE POLYTECHNIQUE

Spécialité :

Physique des plasmas

Présentée par :

Garrett Anthony Curley

Dynamique des espèces chargées dans un réacteur de gravure diélectrique à couplage capacitif excité par deux fréquences

The dynamics of the charged particles in a dual frequency capacitively coupled dielectric etch reactor.

Thèse soutenue le 30 avril 2008

Devant le jury composé de Messieurs:
Nicholas St. J. BRAITHWAITE (rapporteur)
Gilles CUNGE (rapporteur)
Pere ROCA i CABARROCAS (président du jury)
Jean-Paul BOOTH (directeur de thèse)
Rémi DUSSART
David GRAVES

Résumé

Les plasmas à couplage capacitif excités par deux fréquences sont utilisés pour la gravure des diélectriques, étape importante dans la fabrication de composants de microélectronique. L'utilisation des deux sources RF, une à basse fréquence, l'autre à haute fréquence, est censée permettre le contrôle indépendant du flux ionique et de l'énergie ionique. Les gaz fluorocarbonés, tels que c-C_4F_8 et CF_4, jouent le rôle clé en fournissant les espèces nécessaires à la gravure des motifs nanométriques. Ces plasmas fluorocarbonés sont complexes, ils sont composés de plusieurs types de radicaux neutres, d'ions positifs et d'ions négatifs. Nous étudions un réacteur industriel modifié, avec des mélanges gazeux de type $Ar/O_2/c$-C_4F_8 et $Ar/O_2/CF_4$, à des pressions proches de 50 mTorr (6.6 Pa) et excité par des sources RF de 27 et 2 MHz, en mode simple fréquence et en mode double fréquence. La mesure des ions négatifs et leurs effets sur les propriétés électriques du plasma est le sujet d'étude principal de cette thèse.

Plusieurs techniques de diagnostics sont mises en oeuvre pour caractériser les densités et les flux des particules chargées. Une sonde de flux ionique à polarisation RF, capable de fonctionner avec une couche déposée sur sa surface est installée dans l'électrode du haut et utilisée pour mesurer le courant ionique arrivant sur la surface de cette électrode. La densité électronique est mesurée dans le centre de la décharge par une sonde de résonance micro-ondes à un quart de longueur d'onde, communément appelée sonde hairpin . Une version flottante de cette sonde est utilisée pour éviter les effets de polarisation RF et les gaines RF qui pourraient se former autour des fils de la sonde. Une technique de spectroscopie basée sur le déclin d'une cavité optique (CRDS) est appliquée à la mesure de la densité d'ions négatifs du fluor en détectant l'absorption large bande due au photodétachement de l'ion.

Les densités électroniques, les courants ioniques et les densités d'ions négatifs sont mesurés pour une variété de conditions plasma pour des excitations à simple fréquence et double fréquence. L'effet du changement de mélange gazeux et de la puissance RF sont particulièrement étudiés. La fraction d'ions négatifs, $\alpha = n_n/n_e$, est déduite des mesures de sondes en comparant le rapport du flux ionique sur la densité électronique, Γ_i/n_e, à la valeur théorique obtenue par un modèle fluide d'un plasma électronégatif. Des modèles fluides de la littérature ont étés modifiés pour prendre en compte la mobilité variable des ions positifs caractéristiques des pressions utilisées dans cette étude (environ 50 mTorr ou 6.6 Pa).

La fraction d'ions négatifs est élevée dans le plupart des mélanges plasma de type $Ar/O_2/c$-C_4F_8. Dans les mélanges $Ar/O_2/CF_4$, le plasma n'est électronégatif que pour de faibles débits de O_2. Il est proposé que l'oxygène détruit les précurseurs nécessaires à la formation d'ions négatifs. Le contrôle indépendant du flux ionique dans un plasma excité à deux fréquences n'a pas été mis en évidence. Rien ne permet de supporter la théorie selon laquelle les ions négatifs de fluor peuvent atteindre les parois du réacteur en présence de puissance RF à basse fréquence (2 MHz). Une découverte clé de cette étude est que la température des ions négatifs devrait être très élevée si une corrélation est à faire entre les résultats expérimentaux et théoriques.

Abstract

Dual frequency capacitively coupled plasmas (DF-CCP) are used for the etching of semiconductor based dielectrics as part of the microelectronics fabrication process. The use of two frequencies is intended to allow for the independent control of the ion flux and the ion energy. Fluorocarbon gases such as c-C_4F_8 and CF_4 play the key role in producing the precursor species that eventually etch the nano-scale patterns. These fluorocarbon-containing plasmas are complex in nature, forming many types of neutral radicals, positively charged ions and negatively charged ions. We study a customized industrial etch reactor, running in $Ar/O_2/c$-C_4F_8 and $Ar/O_2/CF_4$ gas mixtures at pressures in the region of 50 mTorr (6.6 Pa) and driven by 2 and 27 MHz RF power, either separately or simultaneously. The measurement of the negative ions and their effect on the plasma's electrical properties are the main focus of this thesis.

Several diagnostic techniques are implemented to characterise the densities and fluxes of the various charged species. A deposition tolerant, RF biased ion flux probe, installed co-planar with the upper electrode, is used to measure the ion current arriving at the electrode surface. The electron density in the centre of the plasma is measured using a quarter-wavelength microwave resonator probe, known commonly as a hairpin probe. A floating probe design is used to avoid the effects of RF biasing and subsequent RF sheath formation on the probe wires. Cavity ring-down spectroscopy (CRDS) is applied to the measurement of the negative fluorine ion density by the absorption in its broadband photodetachment continuum.

The electron densities, ion currents and negative ion densities are measured under various plasma conditions for both single and dual frequency excitation. The effect of various plasma gas mixtures and various applied RF powers are particularly studied. The negative ion fraction, $\alpha = n_n/n_e$, is deduced from the probe measurements by comparing the ratio of the ion flux to the electron density, Γ_i/n_e, to the theoretical ratios obtained by an electronegative plasma fluid model. Fluid models from the literature were modified to account for the variable ion mobility that is characteristic of the pressures used in this study (about 50 mTorr or 6.6 Pa).

Plasmas containing $Ar/O_2/c$-C_4F_8 mixtures were found to be strongly electronegative under most conditions when the c-C_4F_8 flow rate was greater than 6 sccm. $Ar/O_2/CF_4$ plasmas appeared strongly electronegative either in conditions of low CF_4 flow rates (Ar/O_2 dominated plasma) or when the the O_2 flow rate went to zero (an Ar/CF_4 plasma). A proposal that oxygen destroys the precursors to negative ion formation is put forward. The independent control of the ion flux in dual frequency mode was not observed in the conditions studied, neither was there evidence found to support the theory that the negative fluorine ions escape to the walls in the presence of the low-frequency (2 MHz) RF power. One of the key findings of this study is that the temperature of the negative ions must be very hot ($\gamma \sim 5$) if the experimental and theoretical results are to agree.

Acknowledgements

The results presented in this manuscript could not have been obtained without the support of the following people whom I wish to thank.

First and foremost, I wish to thank Dr. Jean-Paul Booth for having given me the opportunity to pursue both a Masters and a Ph. D. in France. His availability and regular advice allowed me to progress rapidly in my understanding of plasma physics. I wish to thank him also for giving me numerous occasions to present my work at international conferences, where I was able to forge links with the rest of the plasma physics community.

I particularly wish to thank Dr. Pascal Chabert, for being constantly present to discuss plasma physics, world politics, French history and the secrets to being a Parisian. I especially wish to thank him for his role as a co-supervisor in the final year of my Ph. D. and for organising the jury for my defence.

I would like to acknowledge my gratitude to Prof. Jean-Marcel Rax, director of the Laboratoire de Physique et Technologie des Plasmas (LPTP), for having welcomed me into the laboratory, and also for accepting me onto the Physics of Plasma Masters programme, which ultimately allowed me to continue as a Ph. D. student at the Ecole Polytechnique.

Dr. Cormac Corr, a fellow Irishman and a great friend and colleague from the get-go, who helped me settle into life in Paris and who was the corner stone of many an LPTP outing. In particular, for having worked long and hard on the UV-CRDS experiment that eventually led to some of the key results presented in this thesis.

A big thanks to Jean Guillon, CNRS research engineer at the LPTP, for his wealth of experience and patience in constructing and modifying the experimental equipment. Our discussions on the design of the hairpin probe are amongst my best memories of the last four years.

The secretarial and IT team who were always available and helpful in carrying out the wide variety of administrative and IT tasks: thank you Cathy, Isabelle, Philippe, Malika and Cherifa.

To the two extra pairs of hands who journeyed all the way from Slovakia and Serbia and who contributed immensely to the work of this thesis. Thank you Tomáš and Dragana.

A warm thank you to the entire staff of the LPTP. To the researchers: Dr. Jolly, Dr. Hennequin, Dr. Raimbault, Dr. Larour, Dr. Arantchouk. To the technical team: Jean-Paul, Christian and Bruno. Not forgetting of course, my fellow young researchers whom I had the pleasure of meeting over the last three years and who created a most enjoyable work atmosphere. In alphabetical order: Albert, Ane, Claudia, Cyprien, Elisée, Emilie, Gary, Joseph, Katia, Laurent, Lina, Nicolas B., Nicolas L., Nicolas P., Olivier, Paul, Pierre, Richard, Sébastien C., Sébastien "James" Dine, Sedina and Xavier.

The contribution of Lam Research to this project is much appreciated. I thank especially Dr. Doug Keil for having invited me to intern at Lam in Fremont, California for six months. My experience there was one of those 'fast learning curve' moments that helped open my eyes to the world of semiconductor manufacturing. Thanks also to Chris, Roberto, Mitch, Maryam, Luc & Ana and Neil at Lam for their

friendship during my stay there.

A special thanks to Dr. Bert Ellingboe of Dublin City University who introduced me to the field of plasma physics and who helped me initiate contact with Jean-Paul Booth and Pascal Chabert at the LPTP.

To all those who helped me settle into my new life in France, I wish to extend my deepest gratitude: my colleagues from the DEA (Masters) course; my friends who I met during my year at the Fleming residence (our "soirées du mercredi" will long be remembered); all those who I met during my three years at the Cité Internationale Universitaire de Paris (dinner time seemed like a UN meeting!); my Irish friends who never let me forget how we Irish have the best of craic!

I wish to thank Prof. Roca i Cabarrocas for presiding the jury of my defence. Prof. Braithwaite and Dr. Cunge for their time and diligence in reading and reporting my thesis. Also, Dr. Graves, Dr. Dussart and Jean-Paul for participating on my jury.

Finally, I wish to thank those closest to my heart. My parents, Tony and Geraldine, who supported and encouraged me throughout all my university years and made the trip over from Ireland to be present at my defence. Thank you to my big sis, Zita, and my li'l' bro, Conan, who also came over from Ireland for my defence. It really meant a lot for me to have you all close by on that big day.

And last, but by no means least, I would like to thank my *chérie*, Corinne, for her affection, her support and most importantly her patience throughout the years and in particular during the writing of this thesis.

Contents

Acknowledgements **v**

Symbols and Abbreviations **xi**

1 Introduction **1**

1.1 The context and objectives of this study 1
1.2 Low-pressure plasmas for surface processing 5
1.2.1 Basic plasma equations 8
1.2.2 Case of a bounded plasma 10
1.2.3 Edge-to-centre density ratio 12
1.2.4 Radio frequency plasma sources 13
1.3 Dual-frequency capacitively-coupled plasmas 18
1.3.1 History 20
1.3.2 Principle of operation of dual freqency capacitively coupled plasma sources 21
1.3.3 Triple and multiple frequency plasma excitation 23
1.4 Dielectric etching 24
1.4.1 Fluorocarbon containing plasmas 24
1.5 Electronegative Plasmas 28
1.5.1 Negative ions in fluorocarbon plasmas: production and loss 29
1.5.2 Plasma theory in the presence of negative ions 32
1.5.3 The role of negative ions in industrial plasmas 39
1.5.4 Measurement of negative ion densities 41

2 Experimental setup and diagnostic techniques **49**

2.1 The dual-frequency plasma chamber 49
2.1.1 The plasma chamber 50
2.1.2 The vacuum/pumping system 51
2.1.3 The rf power generators 53
2.1.4 The electrostatic clamping (chuck) unit 54

2.1.5 Cooling . . . 56
2.2 Electrical diagnostics . . . 56
2.2.1 The ion flux probe . . . 56
2.2.2 The microwave resonator probe - "*Hairpin probe*" . . . 67
2.2.3 Calculation of the hairpin sheath size . . . 77
2.2.4 The Floating Hairpin . . . 79
2.2.5 Design and construction of the hairpin probe . . . 80
2.2.6 Operation of the hairpin probe . . . 82
2.2.7 Comparison between two hairpin probe designs . . . 84
2.3 Cavity Ring-Down Spectroscopy . . . 87
2.3.1 Principle of absorption spectroscopy . . . 87
2.3.2 Absorption of the negative fluorine ion . . . 90
2.3.3 Cavity ring-down spectroscopy . . . 92

3 Results and analysis 101
3.1 Introduction . . . 102
3.2 Fluorine negative ion densities . . . 103
3.2.1 $Ar/O_2/c\text{-}C_4F_8$ . . . 103
3.2.2 $Ar/O_2/CF_4$ . . . 105
3.3 Determining the negative ion fraction . . . 107
3.3.1 Negative ion fractions from CRDS and the hairpin probe . . . 108
3.3.2 Two-probe technique: simple model . . . 109
3.3.3 Two-probe technique: fluid model . . . 115
3.3.4 Comparison of the various estimations of the negative ion fractions 118
3.3.5 Introducing variable mobility to the fluid model . . . 120
3.4 Charged particle dynamics - Effect of gas composition . . . 126
3.4.1 $Ar/O_2/c\text{-}C_4F_8$ – varying the $c\text{-}C_4F_8$ gas flow . . . 126
3.4.2 $Ar/O_2/c\text{-}C_4F_8$ – varying the O_2 and $c\text{-}C_4F_8$ gas flows . . . 130
3.4.3 $Ar/c\text{-}C_4F_8$ – varying the $c\text{-}C_4F_8$ gas flow . . . 133
3.4.4 $Ar/O_2/CF_4$ – varying the O_2 and CF_4 gas flows . . . 135
3.4.5 $Ar/O_2/CF_4$ – varying the O_2 gas flow . . . 136
3.4.6 $Ar/O_2/SF_6$ – varying the O_2 and SF_6 gas flows . . . 138
3.4.7 CF_4 plasma – effects due to SF_6 addition . . . 139
3.5 Charged particle dynamics – Effect of pressure . . . 140
3.5.1 $Ar/O_2/c\text{-}C_4F_8$ – varying the pressure: 25 – 100 mTorr . . . 141
3.5.2 Pressure effects on the ion flux probe I–V curves . . . 141
3.6 Charged particle dynamics – Effect of applied power . . . 143
3.6.1 $Ar/O_2/c\text{-}C_4F_8$: 160/8/16 sccm . . . 144

3.6.2 Ar/c-C_4F_8 : 160/24 sccm . . . 150
3.6.3 Ar/O_2 : 160/24 sccm . . . 151

4 Conclusions and perspectives **155**
4.1 Diagnostics in DF-CCP industrial chambers . . . 155
4.1.1 Ion flux probe . . . 155
4.1.2 Hairpin probe . . . 156
4.1.3 Cavity ring-down spectroscopy . . . 156
4.2 Validity of the two-probe technique for measuring α . . . 156
4.3 The relationship between n_e and Γ_i . . . 157
4.4 The role of dual frequency RF power coupling . . . 158
4.5 Processing plasmas and the role of electronegativity . . . 158
4.6 Perspectives . . . 159

Appendix A - Hairpin Sheath Correction **161**

Appendix B - Comparison of Stenzel's hairpin with Kim's hairpin **163**

Appendix C - Normalisation of ion fluid equations - variable mobility **165**

Bibliography **168**

Symbols and Abbreviations

Symbol	Description
a	radius of hairpin wires
α	$= n_n/n_e$, the negative ion fraction
α_0	$= n_{n0}/n_{e0}$, the negative ion fraction in the discharge centre
α_s	$= n_{ns}/n_{es}$, the negative ion fraction at the plasma-sheath boundary
amu	atomic mass unit = $1.66053886 \times 10^{-27}$ kg
b	radius of sheath around the hairpin wires, i.e. $b - a$ = sheath thickness
c	speed of light (electromagnetic waves) in vacuum, = $2.998{\times}10^8$ m.s^{-1}
d	inter-electrode distance or a diameter (example: of the ion flux probe)
e	elementary charge, = $1.60217646 \times 10^{-19}$ C
ϵ_0	permittivity of free space = $8.854{\times}10^{-12}$ F.m^{-1}
eV	electron-volt (1 eV = 1.602×10^{-19} J $\equiv$ 11604.5 K)
f	frequency (Hz)
γ	electron temperature to negative ion temperature ratio, T_e/T_n
γ_i	electron temperature to positive ion temperature ratio, T_e/T_i
h	half-distance seperating the two hairpin wires
h_l	positive ion edge-to-centre density ratio, $= n_{is}/n_{i0}$, along the axis
I_0	positive ion current density to the ion flux probe (usually in mA.cm^{-2})
k or k_B	Boltmann constant, = $1.3806503{\times}\ 10^{-23}$ m^2 kg s^{-2} K^{-1}
l	plasma bulk length along the axis (cylinder)
λ_i	positive ion mean free path
m_e	electron mass = $9.10938188{\times}\ 10^{-31}$ kg
m_i	ion mass = ion atomic mass $\times$ $1.66{\times}\ 10^{-27}$ kg
m_n	anion mass = anion atomic mass $\times$ $1.66{\times}\ 10^{-27}$ kg
n_e	electron density
n_i	positive ion density
n_g	neutral gas density
n_n	negative ion density
p	pressure
P	power
r	radius (of cylindrical plasma or the ion flux probe)
sccm	standard cubic centimetres per minute (unit of gas flow)
T_e	electron temperature
T_i	positive ion temperature
T_n	negative ion temperature
ω	angular frequency = $2\pi f$ (rad.s^{-1})

Chapter 1

Introduction

Contents

1.1 The context and objectives of this study 1
1.2 Low-pressure plasmas for surface processing 5
1.2.1 Basic plasma equations 8
1.2.2 Case of a bounded plasma 10
1.2.3 Edge-to-centre density ratio 12
1.2.4 Radio frequency plasma sources 13
1.3 Dual-frequency capacitively-coupled plasmas 18
1.3.1 History 20
1.3.2 Principle of operation of dual freqency capacitively coupled plasma sources . . 21
1.3.3 Triple and multiple frequency plasma excitation 23
1.4 Dielectric etching 24
1.4.1 Fluorocarbon containing plasmas 24
1.5 Electronegative Plasmas 28
1.5.1 Negative ions in fluorocarbon plasmas: production and loss 29
1.5.2 Plasma theory in the presence of negative ions 32
1.5.3 The role of negative ions in industrial plasmas 39
1.5.4 Measurement of negative ion densities 41

1.1 The context and objectives of this study

The end of the 20^{th} century and the beginning of the 21^{st} have seen the widespread introduction of many high-tech devices into the lives of everyday citizens in every corner of the developed world. Personal computers, mobile telephones, hand-held multimedia players, home entertainment systems, GPS navigation devices and high-speed internet access are but some of the many products that were confined to the realms of science fiction only 30 years ago. Their existence has been made possible by the astonishing progress being made in the semiconductor integrated circuit device manufacturing industry. This

progress has allowed for both the miniaturisation and greater computational power of each successive generation of microprocessor, as well as the ever increasing capacity and decreasing cost of solid state memory devices. It is estimated that roughly one third of all steps in integrated circuit manufacture are plasma based and as such the advent of plasma processing was, and still is, one of the fundamental pillars of this technological revolution.

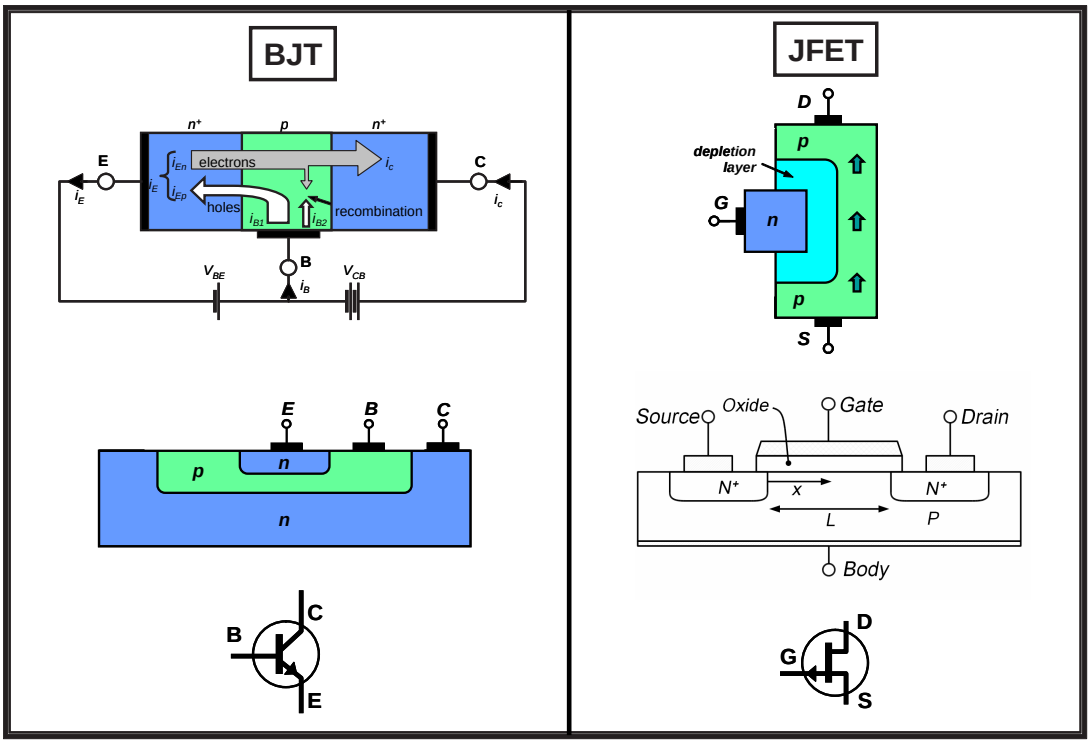


Figure 1.1: Bipolar junction transistor (BJT) and junction field effect transistor (JFET). Top: schematic current flow; Middle: planar construction; Bottom: circuit symbol.

The basic element of a microprocessor or a memory chip is the semiconductor transistor, a device allowing for the *almost* instantaneous amplification or switching of electrical signals. A transistor works by using a small current or voltage to control the flow of a much larger current. Semiconductor materials such as silicon or germanium, under normal conditions, have similar properties to insulators. Their electrical properties can, however, be modified by doping them with impurities (e.g. boron or phosphorus) so that they become either p-type material (positive charge carriers, or holes, dominate) or n-type material (electrons, or negative charge carriers, dominate), allowing the semiconductor to conduct nearly as well as a metal. The invention of the semiconductor transistor is largely attributed to Shockley and co-workers in Bell Labs in 1947. The modern day triode (three terminal) design was first proposed by Shockley's colleagues, Bardeen and Brattain in 1950 [Bardeen 50].

Two common basic transistor architectures are the bipolar junction transistor (BJT)

and the junction field effect transistor (JFET). Figure 1.1 shows representations of these two transistors. The BJT is basically two diodes end-to-end that share the same cathode (pnp configuration) or the same anode (npn configuration). One diode junction is biased positively, the other is biased negatively. The JFET operates by varying the voltage at the gate (n-type in the figure), which varies the size of a depletion layer extending into the p-type channel. The larger the depletion layer, the smaller the current and vice-versa. JFET's and their derivatives play a very large role in today's microchips. Moreover, making the gate element smaller makes the transistor faster and this has been one of the principal techniques used over the years to increase the speed of microchips. Indeed, recent generations of chip technologies have been named after their gate length (e.g. 0.13-μm technology). Today, transistors with gate lengths of less than 100 nm are being constructed, dimensions that are only possible to obtain with plasma processing and optical lithography.

Today's microprocessors contain over a billion transistors packed into a few square centimetres – the larger the number of transistors, the more powerful the device. The number of transistors per chip has increased at an exponential rate since 1965, closely following the prediction of Gordon Moore in that year when he suggested that the transistor to chip ratio would double every 18 months. The industry has worked hard to make this statement a reality, thus making it a self-fulfilling prophecy. To achieve this it has been necessary to reduce the average transistor size from one chip generation to the next. Reducing the size also speeds up the calculations as the reduced distance between components means faster communication between them can occur. Current industrial research and development is focused on the production of 45 nm long gates, which corresponds to less than 200 atoms. It is therefore evident that there is a physical limit to how small one can make a transistor. Moreover, it is also becoming more and more difficult to dissipate the heat generated as the switching frequencies get higher (microwave region) and the 'free' space between components is reduced. The theoretical gate length limit from simulations is about 4 nm or 16 atoms long[1]. However, new construction techniques such as 3-D stacking and the introduction of dual-gate and tri-gate transistor manufacturing techniques are allowing some of these limits to be pushed further.

Two areas of active R & D are the introduction of high-k gate dielectric material and the move towards more conductive interconnect wires. The gate dielectric separates the gate from a contact electrode so that the application of a voltage to the gate is by capacitive means only. For the past 40 years, silicon dioxide (SiO_2) has been the dielectric material of choice but as gate sizes have reduced so has the dielectric thickness (< 2 nm) creating less efficient transistors due to leakage current. By replacing the thin SiO_2 dielectric with a material of higher permittivity, or high-k, it will be possible to continue the shrinking

[1]Source: Presentation by Professor Michael A. Lieberman at ICPIG 2005, entitled: Plasma processing in the 21st century.

of transistor sizes. Future 45 nm Intel chips will soon be using hafnium dioxide (HfO_2) as the high-k material in the gate dielectric.

The manufacturing of microprocessors involves, amongst other steps, silicon substrates (wafers) containing regions of doped silicon being immersed into chemically reactive plasmas where the submicron device features (transistors, capacitors, etc.) are then etched onto the surface. Once the first layer of devices has been manufactured it is necessary to build up several back-end insulating (dielectric) layers where holes (vias) and trenches will be etched for placement of the conducting interconnectors. Up to seven or eight dielectric layers may need to be put down and subsequently etched, and so the majority of the plasma processing steps in manufacturing integrated circuits are the dielectric etch steps. Figure 1.2 shows a scanning electron microscope (SEM) image of the cross-section of a typical integrated circuit which has being built up using plasma processing.

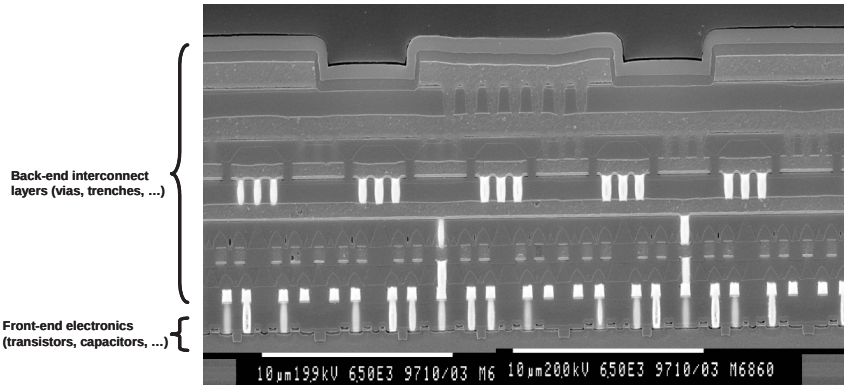


Figure 1.2: Superposition of layers of doped silicon, conductor (Al, W) and dielectric (SiO_2) all etched and deposited by plasma processing. This photo is of 0.25 μm CMOS architecture. Source: STM.

In the present work we are interested in plasmas tailored for etching SiO_2 dielectric layers. These plasmas involve the use of fluorocarbon gases such as *carbon tetrafluori*de (CF_4) and *octafluorocyclobutane* (c-C_4F_8), along with argon and oxygen (Ar + O_2) gases. Capacitive RF power coupling is the method of choice for striking and sustaining such plasmas because of the low dissociation rates obtained, which favours larger passivating molecules, and also the high ion energies at the surface. To obtain independent control of the ion energy and the ion flux to the silicon substrate, dual frequency capacitive discharges (DF-CCP) are widely used. However, despite this widespread use, little fundamental research over the last two decades has been dedicated to their study. The past seven years have, however, seen a marked increase in this research area. At the beginning of this Ph. D. project, however, the field was still highly deficient in experimental data. Moreover, many publications tended to study either the overall plasma chemistry in industrial systems or the physics fundamentals in ideal electropositive (e.g. pure argon) laboratory plasmas. The motivation for this research, however, was to study the physical properties of a DF-CCP source under complex industrial conditions. This ne-

cessitated the acquisition of an industrial chamber, which was donated to the LPTP by Lam Research Corporation[2]. This plasma chamber was previously installed and used by Nicolas Bulcourt who completed his thesis on "*The study of CF and CF_2 radicals in a dual frequency 27 + 2 MHz capacitively-coupled $Ar/O_2/C_4F_8$ discharge*" [Bulcourt 07].

Dielectric etch plasmas are known for their harsh environment towards common diagnostic techniques, due in large part to their restrictive geometry, large RF voltages and chemically reactive plasmas. This study was challenged with developing measurement techniques capable of being used in such industrial reactors with particular emphasis on the study of the electron density, n_e, and positive ion flux, Γ_i, in a mixture of argon, oxygen and octafluorocyclobutane ($Ar/O_2/c\text{-}C_4F_8$). CF_4, was sometimes substituted for $c\text{-}C_4F_8$.

Fluorocarbons, being halogen derived gases, can produce significant quantities of negative ions. The presence of negative ions can modify the plasma structure and results in a reduction of the positive ion flux leaving the plasma. If the negative ions are capable of reaching the walls then they may also participate in the etching process. Therefore, characterising the plasma electronegativity was also a desired goal and a combination of probe measurements and optical diagnostics were employed to estimate the negative ion fraction and density. The context of the results obtained with regard to the dual frequency case versus the single frequency case was constantly examined.

It was also a primary aim to compare the experimental results to existing models and then to develop new theories and models where applicable. For example, it is a common belief that negative ions are confined within the bulk plasma by the sheath potential. However, recent numerical simulations in a DF-CCP have shown evidence of negative ions escaping to the walls. We performed experiments to test this theory.

1.2 Low-pressure plasmas for surface processing

Plasmas may be used for a wide variety of industrial purposes and have replaced liquid chemicals for many applications. The terms dry processing and wet processing apply to both methods respectively. There are various applications of plasmas in the domain of surface processing, but generally speaking they can be divided into one of two categories: (i) etching and (ii) deposition. Plasma etching is defined as the removal of material from a surface either through chemical or physical means. In plasma deposition both chemical and physical processes also occur but the result is a net transfer of material from the plasma and/or gas to the surface. Many of the advantages associated with plasma etching are also applicable to plasma deposition. In fact, the full story when it comes to plasma surface processing is that both etching and deposition occur simultaneously, with the

[2]Lam Research Corporation, based in Fremont, California, USA, is the world leader in dielectric etch tools. For further information see: http://www.lamrc.com

most important process deciding the net outcome. Often, a particular gas mixture in a particular chamber can pass from etching to depositing, and vice versa, as the various parameters such as pressure and power are varied.

One can create a plasma using relatively stable feedstock gases and then obtain a wide variety of chemically reactive by-products due to the dissociation of the various molecules through electron-neutral collisions. The chemical aspect of etching involves the neutral gas molecules and their dissociated by-products reacting with the molecules of the surface to be etched and producing volatile molecules which can be pumped away. This process is, from an engineering viewpoint, not much more advantageous than using liquid chemicals, though it is a much cleaner process from an environmental perspective. The physical aspect of etching is a plasma only process. The positive ions are accelerated from the plasma and across a space-charge sheath separating the plasma from the walls, striking the surface with sometimes enough energy to remove material. This is known as ion bombardment or ion sputtering. Typical industrial plasmas, however, do not produce ions with enough energy to efficiently etch a surface by purely physical means. Nonetheless, Coburn and Winters (1979) showed that the combined actions of both neutral gas etching and ion bombardment produced a much faster etch rate than the simple algebraic addition of the two [Coburn 79]. This important result, reproduced in figure 1.3, is the basis of modern day industrial etching.

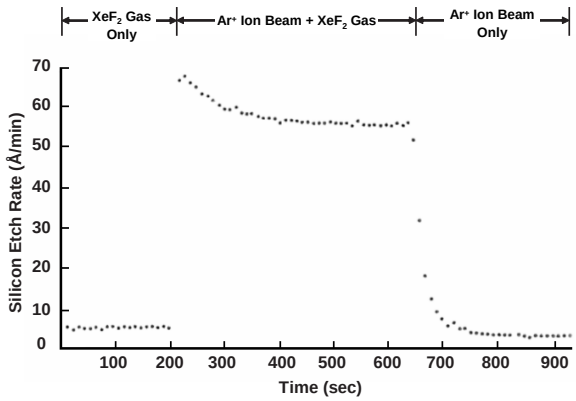


Figure 1.3: Ion-assisted gas-surface chemistry using Ar^+ and XeF_2 on silicon. (Coburn et al. 1979)

A crucial characteristic of plasma etching is the ability to etch *anisotropically*, that is, in a single direction. This is the result of the synergy between the ions and the surface chemistry. As the ions are accelerated by a uni-directional electric field across the sheath, their direction on impact is primarily perpendicular to the surface. If one covers the surface to be etched with a patterned mask, the unprotected areas will be etched in a mainly vertical direction as the synergetic etching will only occur in the area beneath the mask opening. At the same time, the low ion bombardment rate on the walls of the trench or via (hole) being etched may allow for the depositing of a protective layer

through a process known as polymerisation (or passivation). This layer further prohibits the etching of the side walls. By adjusting the plasma parameters so as to strike a desired balance between vertical ion assisted etching and side wall passivation, it may be possible to obtain very high aspect ratio etch profiles.

This thesis is concerned with the study of low-pressure plasmas used in the industrial application of surface etching. The term *low-pressure* defines a pressure regime whereby the positive ions undergo, on average, no more than one elastic collision before being lost to the walls. The characteristic length in-between collisions is called the *mean-free path*, λ_i, and so at low pressures:

$$\lambda_i = 1/n_g\sigma_{in} \geq l/2 \tag{1.1}$$

where n_g is the density of the neutral gas ($n_g \gg n_i$ in a weakly ionised plasma), σ_{in} is the ion-neutral collision cross section and l is the plasma length. The collision cross section is determined experimentally and is a function of the ion energy. Figure 1.4 shows the collisional cross sections for argon ions in a pure argon discharge. In an industrial plasma, the neutral argon atoms are in thermal equilibrium with the surrounding gas and so have a temperature close to room temperature, i.e. 300 K or about 0.026 eV. The positive ions, however, are accelerated by a small DC gradient in the plasma known as the presheath, giving them an energy at the edge of the plasma close to $T_e/2$ or about 2 eV in a typical industrial plasma. This corresponds to a cross sectional area of roughly 0.7×10^{-18} m^2. Assuming a plasma chamber length of 2 cm and that the plasma occupies the entire chamber volume, i.e. sheath size is much less than the plasma bulk dimensions, then the maximum gas density required to satisfy the condition in equation 1.1 is:

$$n_g \leq 2/l\sigma_{in} \approx 1.4 \times 10^{20} \text{ m}^{-3}$$

which at a temperature of 300 K would mean that the pressure should be less than or equal to 0.61 Pa or about 5 mTorr. The pressures in this study are generally in the 50 – 60 mTorr range (6.5 – 7.5 Pa), which means that the ions are not strictly in a low-pressure (collisionless) regime. Instead, they are in what is termed an *intermediate pressure* regime. This is particularly true for the bulk, quasineutral, plasma region. However, the gas temperature in our plasma conditions has been measured to be close to 500 or 600 K, extending the low-pressure regime to about 1.5 Pa or (10 mTorr). In the sheath, the positive ions gain energies of many tens of volts and the sheath dimensions are often small enough such that the ions may be considered to undergo no collisions as they traverse the sheath. This is commonly known as ion free fall. The importance of asserting that our bulk plasma region is characteristic of an intermediate pressure regime will be a decisive factor in the choice of fluid model equations presented later on.

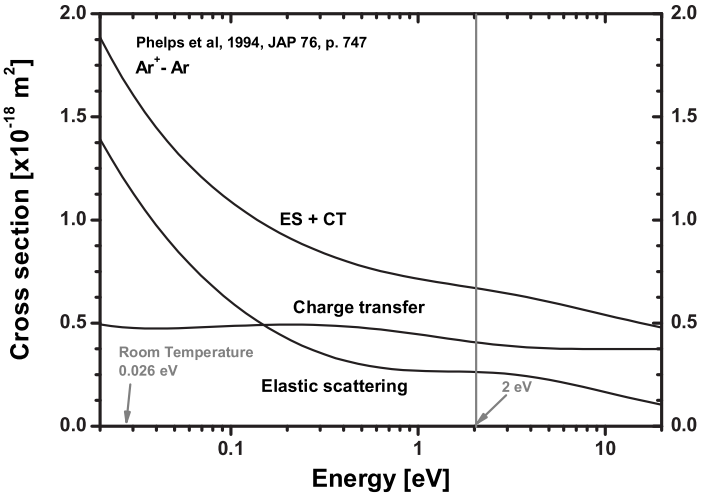


Figure 1.4: Values for elastic scattering, charge transfer and the sum of the two mechanisms (ES+CT) for argon ions in an argon plasma [Phelps 94].

1.2.1 Basic plasma equations

The word *plasma* is used to refer to those gases in which the constituent atoms and molecules have been partially or wholly ionised. However, not all partially ionised gases are plasmas. For an ionised gas to be considered a plasma, the long range coulombic interactions between the charged particles must exhibit collective behaviour. Such collective behaviour includes the property of electric field screening, where the charged particles constantly rearrange their position so as to eliminate the build up of an electric field within the gas. Strong electric fields only exist locally between a charged particle and its immediate neighbouring charged particles. To quantify this screening effect, a characteristic screening length known as the Debye length, λ_D, is used. This length defines a sphere (the Debye sphere) of radius λ_D around a charged particle. On the surface of this sphere the electric field of the particle has a magnitude $1/e$ times that of its magnitude at the centre of the sphere:

$$E(x) = E_0 e^{-x/\lambda_D} \tag{1.2}$$

In this study, the charged particles are not in thermal equilibrium: the electrons are 'hot', the positive ions are 'cold'. The majority of the screening process is therefore carried out by the fast electrons, reorganising themselves amongst the much slower positive ions. The Debye length can then be defined solely in terms of the electron temperature and density:

$$\lambda_D = \sqrt{\frac{\epsilon_0 k_B T_e}{n_e q_e^2}} \tag{1.3}$$

where n_e is the electron density, ϵ_0 is the permittivity of free space, k_B is Boltzmann's constant, T_e is the electron temperature (in Kelvin) and q_e is the charge of an electron.

The Debye length gives a scale length to non-neutrality such that in conditions whereby $\lambda_D \ll L$ the plasma is said to be quasi-neutral and the positive and negative charge densities can be considered equal throughout the plasma. Quasi-neutrality is described by the following general equation:

$$n_e + \sum_x n_{nx} = \sum_y q_{iy} n_{iy} \tag{1.4}$$

where n_{nx} indicates the densities of the negative ion species, n_{n1}, n_{n2}, n_{n3} etc. n_{iy} indicates the densities of the positive ion species, n_{i1}, n_{i2}, n_{i3} etc. and q_{iy} indicates the ionisation of the positive ion species, n_{iy}. In an electropositive plasma with only a single positive ion species, this equation reduces to the simple expression:

$$n_e = n_i \tag{1.5}$$

A second collective phenomenon is the *plasma oscillation* or *plasma frequency*. It describes the ability of a swarm of charged particles to respond to an electric field perturbation. In cold plasma physics (cold positive ions, hot electrons) it is synonymous with the response of the electrons, i.e. the electron frequency. If an electric field is created non locally within a plasma (i.e. over a distance greater than λ_D) the electrons will attempt to nullify it by rearranging their positions. However, the mass of the electrons will result in an *inertial* overshoot of the equilibrium position, and so the electrons begin a periodic oscillation. Accordingly, the amplitude of this frequency will depend on both the electron density and the electron mass, m_e:

$$\omega_p = 2\pi f_p = \sqrt{\frac{n_e e^2}{m_e \epsilon_0}} \tag{1.6}$$

where f_p is plasma frequency and ω_p is the angular plasma frequency. A similar frequency exists to describe the response of the positive ions to a perturbing electric field. This is known as the plasma ion frequency or simply, the ion frequency:

$$\omega_{pi} = 2\pi f_{pi} = \sqrt{\frac{n_i e^2}{m_i \epsilon_0}} \tag{1.7}$$

No plasma is infinite in size and so understanding the finite boundary of a plasma is as important as understanding the plasma itself. Indeed, a plasma does not simply fade away over large distances, even in the expanse of space. The presence of gradients in potential give rise to electric fields that accelerate the heavy, less mobile, positive ions while simultaneously slowing the electrons. The ions are accelerated until such time

that they gain enough energy to produce charge separation. For this to be possible, the ions must overcome the electrostatic forces attracting them back into the quasi-neutral equilibrium state, i.e, their velocity must be faster than the return speed to equilibrium. In other words, at the boundary the ions must have at least a speed, u_s, such that they break the screening effect (λ_D) in a time less than the period of oscillation (ω_{pi}):

$$u_s \geq \lambda_D \times \omega_{pi} = \sqrt{\frac{kT_e}{m_i}} \tag{1.8}$$

Once this velocity is reached and charge separation occurs, quasineutrality breaks down and the collection of charged particles ceases to be defined as a plasma. This velocity is also known as the Bohm velocity, u_B, which is a specific result of the Bohm criterion [Bohm 49]. This velocity is also equivalent to the ion acoustic speed or ion sound speed. This can be understood in a hand-waving fashion as follows: an electrostatic pressure wave (acoustic wave) propagating through a plasma can only go as fast as is allowed to preserve quasi-neutrality. The wave will therefore propagate at a frequency no more than the ion frequency, ω_{pi} and will perturb the plasma over distances no more than the screening length, λ_D. Hence it will travel at a speed, $c_s = \sqrt{kT_e/m_i}$.

As energy must be conserved at all times, the acceleration of the ions comes at the expense of an energy loss from the electrons: as the ions accelerate through the plasma, the total plasma density decreases and so the electron pressure decreases. Energy is therefore being transferred from the electrons to the ions. At the plasma boundary, where charge separation occurs, the electron density (pressure) goes to zero and so a maximum of energy is transferred to the ions as they break free from the 'grip' of the plasma – the plasma boundary can therefore also be seen as a form of resonance zone for energy transfer.

1.2.2 Case of a bounded plasma

In a laboratory, the plasma is confined within a container known as a chamber or reactor. This walled environment imposes a number of boundary conditions on the plasma. These boundary conditions are generally determined by particle loss and energy loss to the walls. Let us first take the case of quasineutrality and charge balance. Due to their higher mobility, the electrons will initially be lost to the *grounded* walls at a much faster rate than the heavier ions. This results in a small layer close to the walls dominated by positive ions, forming a positive space charge region known as a *sheath*. As the sheath is positive with respect to the wall, the electric field which forms is directed from the plasma to the walls, therefore repelling further electrons from reaching the walls while at the same time accelerating the ions to the walls. The equilibrium state occurs when the electron and ion fluxes to the walls are equal, i.e. zero net current to the walls.

As a consequence of sheath formation, the plasma is always at a positive potential with respect to ground. As the sheath is a layer of charge separation, the ions entering this space charge region must gain enough energy to break free from the quasineutral plasma. The energy required is that which gives the ions a speed equal to the Bohm velocity, as in equation 1.8.

The temperature of the electrons is such that their thermal velocity is much greater than their drift velocity and so their density distribution is determined from the equilibrium between their pressure and the electric field that builds up in the plasma and the sheath.

$$eE + \nabla P = 0 \tag{1.9}$$

This is known as a Boltzmann distribution and takes the form of an exponential decrease in density. As the electrons attempt to penetrate the sheath their density profile is given by:

$$n_e(x) = n_{es} \exp\left(-\frac{eV(x)}{kT_e}\right) \tag{1.10}$$

where x is the distance into the sheath, n_{es} is the electron density at the sheath entrance and $V(x)$ is the potential within the sheath such that $V(x = 0) = 0$.

Now take the case of particle balance. Due to the condition at the walls that $I_e = I_i$, the rate of electron loss to the walls can be expressed as:

$$\text{Electron loss} \equiv n_{is} u_B A$$

where n_{is} is the positive ion density at the plasma-sheath boundary and A is the area of plasma at the plasma-sheath boundary. We will define here the ratio of the ion density at the plasma-sheath boundary to the ion density at the plasma center as $h = n_{is}/n_{i0}$. The production of electrons and ions is through electron impact ionisation:

$$\begin{aligned} A + e^- &\rightarrow A^+ + e^- + e^- \\ AB + e^- &\rightarrow A + B^+ + e^- + e^- \end{aligned}$$

which depends on the electron density, the neutral species' densities and an ionisation coefficient. Taking the simple case of a plasma in a rare gas, say argon, the electron production can be expressed as

$$\text{Electron production} = n_e n_g K_{iz}(T_e)\mathcal{V}$$

where $K_{iz}(T_e)$ is the ionisation rate as a function of the electron temperature for the particular neutral species and $\mathcal{V}$ is the plasma volume. In a steady-state plasma, the

electron density remains constant:

$$\begin{aligned} \frac{dn_e}{dt} &= \text{Electron loss} + \text{Electron production} = 0 \\ &= -An_{is}u_B(T_e) + \mathcal{V}n_e n_g K_{iz}(T_e) \\ Ahn_e u_B(T_e) &= \mathcal{V}n_e n_g K_{iz}(T_e) \end{aligned} \tag{1.11}$$

where we have used quasineutrality ($n_e = n_i$) and the h-factor to substitute hn_e for n_{is}. For the purpose of this study we will assume that the plasma is confined within a cylindrical chamber and so $\mathcal{V} = \pi r^2 l$, where l is the plasma length. We will further assume that the plasma radius, r, is much larger than the plasma length, l – i.e. two parallel circular plates in close proximity to one another. We can therefore assume that the majority of the electron loss is to each end of the chamber and so $A \approx 2\pi r^2$. Equation 1.11 can therefore be rearranged to show that:

$$\frac{h_l u_B(T_e)}{K_{iz}(T_e)} = \frac{n_g l}{2} \tag{1.12}$$

where h has been redefined as h_l to emphasise that the density gradient considered is along the length of the plasma. The solution of this equation shows that the electron temperature is primarily a function of both the neutral gas density (and so pressure) and the plasma geometry. T_e, to a first approximation, does not depend on the electron density and therefore does not have a dependence on the power absorbed by the plasma.

1.2.3 Edge-to-centre density ratio

The electron and ion densities at the plasma-sheath boundary are lower than at the plasma bulk centre. This can be attributed to the gradient in potential in a region known as the plasma presheath. This potential drop is a prerequisite for the acceleration of the positive ions into the sheath region. Assuming little or no potential gradient in the plasma bulk region ($V = V_p$ from the centre to the plasma-presheath edge) and taking the plasma-sheath edge as our reference point, such that $V_s = 0$, the potential across the presheath is $V_p - V_s$ and is positive. The kinetic energy a positive ion gains as it travels through this potential drop is that which allows it to reach the Bohm velocity:

$$e(V_p - V_s) = \frac{1}{2} m_i u_B^2 \tag{1.13}$$

an so replacing for the Bohm velocity, $u_B = \sqrt{kT_e/m_i}$, we have:

$$(V_p - V_s) = \frac{T_e}{2} \tag{1.14}$$

where T_e is now expressed in electron volts. The electron density across this potential is determined from the Boltzmann relation and so substituting 1.14 into equation1.10 we

have:

$$\begin{aligned} n_{es} &= n_{e0} \exp\left(-\frac{1}{2}\right) \\ n_{es} = n_{is} &\approx 0.6 n_{e0} \end{aligned} \tag{1.15}$$

The edge-to-centre density ratio, referred to throughout this thesis as the h_l-factor, is about 0.6 in an electropositive, collisionless plasma. The idealised collisionless case does not often exist, however, and it is more consistent to include the creation of ions, through ionising collisions, at the various positions throughout the plasma. The newly created positive ions have an initial velocity of zero and so the *average velocity* of the ion fluid, as it moves from the plasma centre to the plasma edge, is reduced. For the positive ions to escape into the sheath region they must have an average velocity of at least u_B. This requires the voltage drop across the presheath to increase accordingly. It can be shown that, when ionisation is taken into account in the particle balance equation, the h_l-factor in an electropositive, low-pressure plasma is 0.425 and the potential drop across the plasma is $0.854T_e$ [Tonks 29, Lieberman 05]. When the problem is analysed through fluid equations, a value of 0.5 is found for h_l [Sheridan 99b].

1.2.4 Radio frequency plasma sources

This section gives an introduction to the use of radio frequency power sources in low-pressure industrial plasmas. The two principal methods of transferring radio frequency power to the plasma, capacitive and inductive coupling, are then discussed.

Industrial plasmas used in surface etching are powered by alternating voltage sources oscillating in the radio frequency range. The radio frequency spectrum, as defined by the ITU-R[3], is that part of the electromagnetic spectrum extending from 3 kHz to 300 GHz, or from wavelengths of 100 km to 1 mm. It includes part of the audible range and all of the ultra-sonics, radio broadcast, television broadcast and microwave bands. In practice, however, scientists and engineers tend to treat radiofrequency applications differently from microwave applications, due to their significantly different orders of magnitude and the different methods of power transfer. Here, radiofrequency will generally refer to the range 100 kHz $\leq f \leq$ 200 MHz.

Alternating voltage sources are used because they are capable of striking and sustaining a plasma at much lower voltages than DC sources. RF discharges do not rely solely on ion-induced secondary electrons, unlike in DC discharges, although such electrons can play an important role at high pressures. Instead, in low-pressure RF discharges, ohmic and/or stochastic heating provide the principal mechanisms for electron heating. Also, because of their AC nature, RF discharges may be powered across insulating layers covering the

[3] *ITU-R:* The radiocommunication sector of the International Telecommunications Union, based in Geneva, Switzerland. 191 countries take part in the activities of the ITU. For more information, see: www.itu.int

electrodes.

Typical industrial and laboratory plasmas work with RF frequencies in between the positive ion oscillation frequency, f_{pi} and the plasma frequency, f_{pe}. The values of these frequencies in a pure argon plasma, with a plasma density of 10^{16} m^{-3}, are shown in figure 1.5. This range corresponds to the high frequency (HF) and very high frequency (VHF)

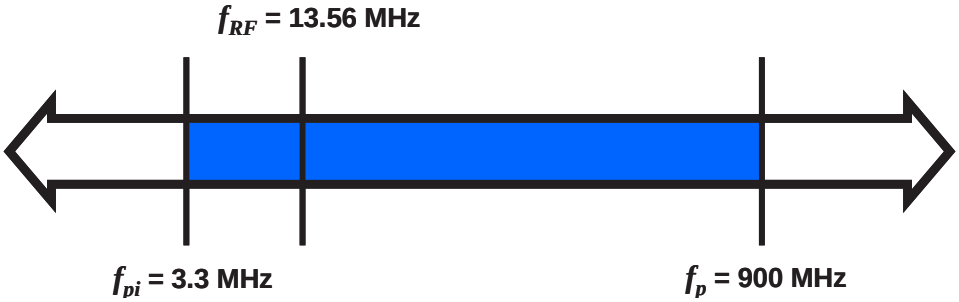


Figure 1.5: Ion and electron (plasma) frequencies in a pure argon discharge with a plasma density of 10^{16} m^{-3}. The ISM frequency of 13.56 MHz is indicated for reference.

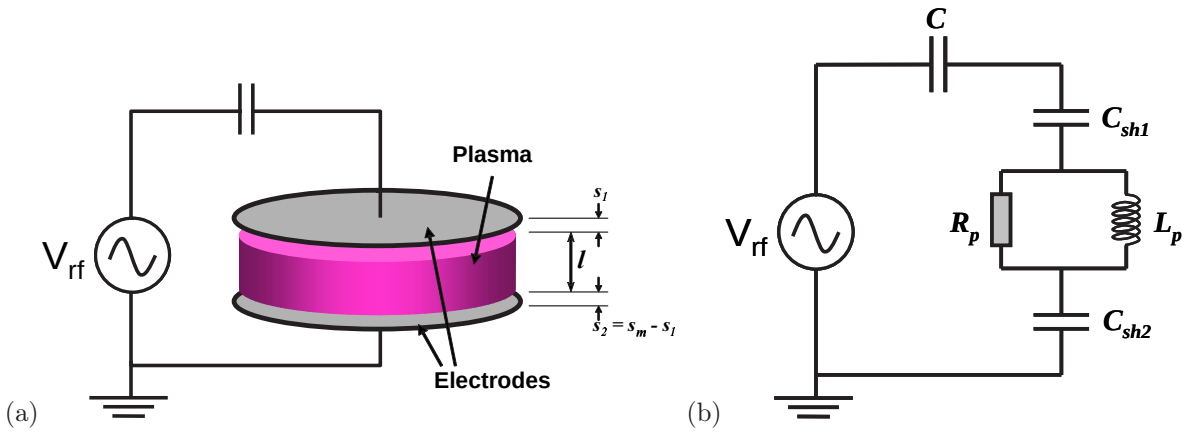
bands of the radio spectrum. These frequencies are low enough to allow the electrons to respond to the electric field and high enough to ensure low voltages for striking the plasma. Figure 1.5 also references 13.56 MHz. This is by far the most commonly used frequency in RF plasma devices. It is the centre frequency of the second ISM band[4].

The transfer of radio frequency power to a plasma is usually either by means of capacitive or inductive coupling, both of which are examined briefly in the following sections. Radio frequency power may also be transferred by the propagation of waves. These forms of power transfer are not examined here.

Capacitively coupled plasma sources

Possibly the simplest form of RF gas discharge is one excited by an electric field between two electrodes. When an oscillating voltage is applied between the electrodes, the discharge is referred to as a capacitive coupled plasma or CCP. The actual 'capacitance' is not between the electrodes directly, but rather between the electrodes and the plasma, i.e. across the sheaths. Figure 1.6 illustrates the basic principle of a capacitively coupled plasma and its equivalent electrical circuit. The sheaths are, to a good approximation, electron free and so act as capacitive barriers between the electrodes and the conducting plasma, allowing only displacement current to pass. The electron rich plasma allows conduction current to flow, but due to collisions between the electrons and the neutral gas molecules a resistive component, R_p is introduced to the plasma bulk's equivalent circuit. The electron inertia (c.f. plasma frequency) introduces a retarding phase shift into the RF current. This phase shift can be modelled as being equivalent to that created by the

[4]The industrial, scientific and medical (ISM) radio bands are defined by the ITU-R. The first four ISM bands are: 6.780 MHz ± 0.015 MHz, 13.560 MHz ± 0.007 MHz, 27.120 MHz ± 0.163 MHz and 40.68 MHz ± 0.02 MHz.



(a) (b)

Figure 1.6: (a) Schematic diagram of a capacitivly coupled plasma discharge; (b) Simplified equivalent circuit of a capacitive discharge.

reactance of an inductor, L_p, and so the bulk's equivalent circuit is that of a resistor and an inductor in parallel.

The impedance of the two capacitive sheaths is equal to the sum of their individual impedances:

$$(Z_{sh1} + Z_{sh2}) = Z_{sh} = \frac{1}{j\omega C_{sh}} \tag{1.16}$$

where ω is the RF source frequency and C_{sh} is the sum of the individual sheath capacitances, $C_1C_2/(C_1 + C_2)$.

In low pressure conditions, electron collisions with the neutral gas is rare and so the resistive component of the plasma bulk impedance is small compared to the inductive component:

$$j\omega L_p > R_p \tag{1.17}$$

where L_p and R_p are the inductance and resistance of the plasma bulk respectively. At the RF frequencies used in this study and with the plasma densities typically obtained we also have the following relationship between the sheath impedance and the bulk impedance:

$$Z_{sh} \gg Z_p \tag{1.18}$$

The quasi-neutrality of the plasma bulk implies that there is no electric field across the plasma. This is not strictly true as a small DC electric field exists to accelerate the ions into the sheath and some RF field must also exist if the electrons are to be heated. Nonetheless, as equation 1.18 implies, the majority of the voltage supplied by the rf source falls across the sheaths and so we have

$$V_1(t) + V_2(t) \approx V_{rf}(t) \tag{1.19}$$

where $V_1(t)$ is the sheath voltage at electrode 1 and $V_2(t)$ is the sheath voltage at electrode 2. The varying voltage between the electrodes and the plasma will push and pull the

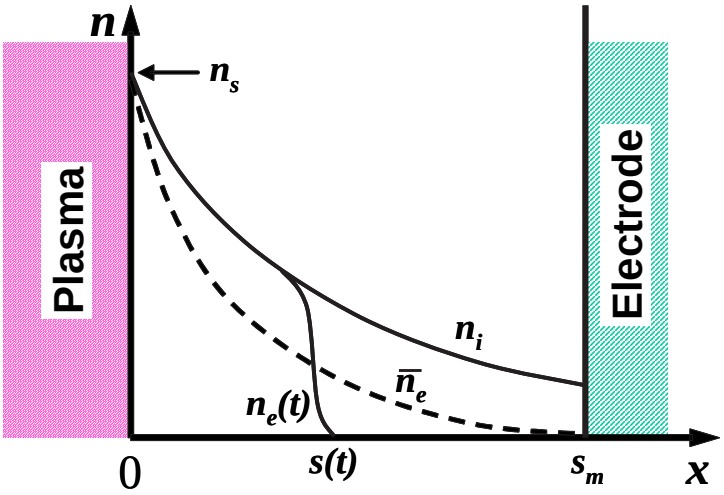


Figure 1.7: Schematic plot of the densities in a high-voltage, capacitive rf sheath.

boundaries of the latter back and forth. When the voltage drop is at a minimum at one electrode the sheath will collapse, while at the other electrode the voltage will be at a maximum, i.e. V_{rf}, and so the sheath size will be at a maximum. In effect, the plasma bulk will oscillate back and forth between the electrodes. As the ions respond only to the time-averaged electric field and not the instantaneous field oscillating at RF frequencies, this equates to the oscillation of an electron front moving back and forth to the walls. This is illustrated schematically in figure 1.7. This front separates a region of quasi-neutrality (plasma) from a region where $n_e = 0$ (sheath).

At a particular time, t, during the rf cycle the electron front is at a position $s(t)$ into the positive ion sheath. The plasma bulk maybe considered to be of a fixed size, l, such that at any given time:

$$d = s_1(t) + l + s_2(t) \tag{1.20}$$

where d is the distance between the electrodes, $s_1(t)$ is the sheath thickness at electrode 1 and $s_2(t)$ is the sheath thickness at electrode 2. The thickness of the sheaths are, to a first approximation, 180° out of phase such that $s_1(t) = s_m - s_2(t)$.

In a practical set-up, one of the electrodes is usually grounded whereas the powered electrode is electrically floating. In most cases, the chamber walls are also grounded, creating an asymmetric configuration. During a complete RF cycle, a greater flux of electrons arrives at the powered electrode and a negative DC voltage, known as *self-bias voltage*, builds up on the powered electrode to equalise the currents. When the asymmetry is significant, this bias depends solely on the the RF voltage amplitude and the electron temperature [Swift 70]:

$$V_{bias} = V_f - \frac{kT_e}{e} \ln \left[I_0 \left(\frac{eV_{rf}}{kT_e} \right) \right] \tag{1.21}$$

At high gas pressures the electron heating is dominated by collisions with the back-

ground gas, known as ohmic heating. However, at low gas pressures the only form of power absorption by the electrons in capacitive plasmas is collisionless stochastic heating [Lieberman 05]. The oscillating high voltage sheaths form a moving potential barrier that reflects the electrons. This is similar to that which occurs in an elastic collision of a ball with a moving wall

$$u_r = -u + 2u_{es} \tag{1.22}$$

where u and u_r are the incident and reflected electron velocities parallel to the time-varying electron sheath velocity u_{es}. If one assumes a constant n_e at the plasma-sheath boundary then the energy gained will average to zero. However, in reality, the electron velocity distribution is a time-varying function and so the integration over all velocities and times yields a net stochastic power absorption:

$$S_{stoc} = -2m_e \int_{u_{es}}^{\infty} u_{es}(u - u_{es})^2 f_{es}(u,t)du \tag{1.23}$$

The solution to this equation will not be discussed here as it is still an active area of research that is beyond the scope of this thesis. Self-consistent plasma and sheath models are required making the analysis difficult. However, several models used have been validated by PIC simulations and have shown that collisionless heating can be the principal heating mechanism in capacitive RF plasmas at low pressures[Gozadinos 01].

Inductive coupled plasma sources

As their name suggests, inductive coupled plasma (ICP) sources utilise the property of electromagnetic induction to transfer power to the plasma. The basic method of operation involves locating a non-resonant (at RF frequencies) coil close to the zone where a plasma is to be created. A dielectric barrier, or window, is often placed between the induction coil and the plasma. The schematic diagram of a particular ICP is shown in figure 1.8 (a). Assuming breakdown has occurred and a plasma has been ignited, the RF current circulating in the coil induces an oscillating axial magnetic field, which in turn induces an oscillating toroidal current in the plasma. This oscillating current in the plasma results in the heating of the electrons. Contrary to capacitive coupling, the inductive field penetrates the bulk plasma directly and so very little of the power is coupled to the sheaths. This allows ICPs to create high density plasmas using significantly lower powers than CCPs.

At low electron densities the power supplied by the induced current may not be sufficient to sustain the plasma. Instead, the plasma is primarily powered capacitively by the varying electric field between different segments of the coil. As the rf power is increased the induced current (or inductive power) becomes more and more dominant. The switch from a predominantly capacitively powered plasma (E-mode) to a predominantly induc-

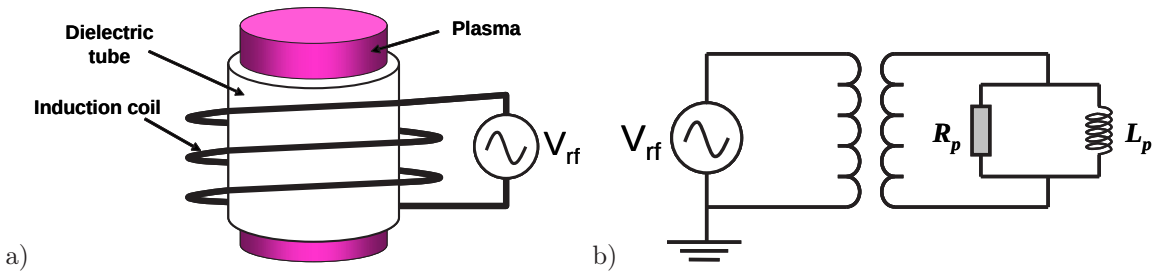


Figure 1.8: a) Schematic diagram of an inductively coupled plasma discharge; b) Simplified equivalent circuit of an inductive discharge.

tively powered plasma (H-mode) is not gradual but rather occurs as a sudden transition. This transition is observed as a sudden increase in the plasma density. This dependence on electron density leads to notable hysteresis effects as the power is reduced and the plasma switches from H-mode to E-mode [Turner 99]. This step like behaviour between the capacitive and inductive modes may, under certain conditions, play an important role in creating instabilities known as E-H (pronounced "E to H") instabilities [Chabert 01].

Impedance matching

The amount of power transferred to a load will depend on the impedance of both the load, Z_L, and the power source, Z_S. It can be shown that the maximum power dissipation in the load occurs when $Z_L = Z_S$. All RF power supplies must be impedance matched to the plasma reactor they are powering if maximum power efficiency is to be achieved. As most generators have a 50 Ω output impedance, the combined impedance of the reactor and the plasma must be made as close as possible to 50 Ω. The impedance of a typical plasma chamber is mostly capacitive and so this must first be counter balanced to produce a real, i.e. resistive, impedance. This is achieved by the addition of what is known as a matching network or matchbox after the generator output and before the reactor input. A typical matching network may consist of a large fixed inductor in series (for capacitive coupling) and one or two variable capacitors in parallel (to ground). The reactance of the circuit cancels that of the chamber and plasma and the variable capacitors are used for fine-tuning. The matchbox is designed such that the matching circuit and the chamber capacitance form a resonant LC circuit at the RF frequency and so power is efficiently transferred between the matchbox and the plasma chamber.

1.3 Dual-frequency capacitively-coupled plasmas

This section describes in detail the operation of dual RF frequency capacitively-coupled plasmas or DF-CCP's. First, an overview is presented of what led to the development of such sources, and then a brief history of DF-CCP sources is discussed. Next, the actual

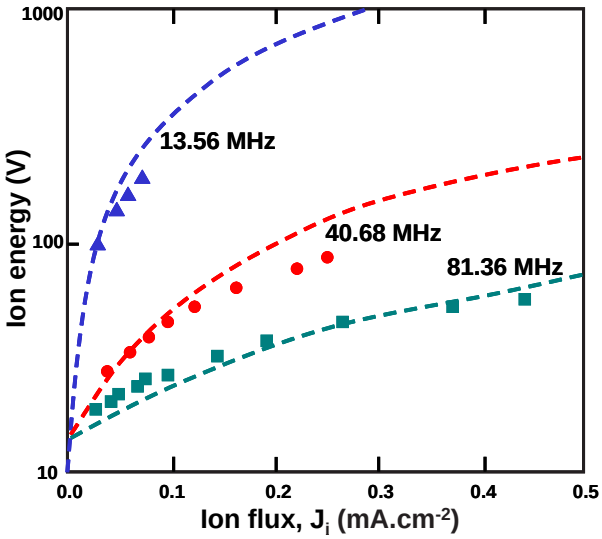


Figure 1.9: The dependent nature between ion energy and ion flux in various single frequency capacitive discharges. Dashed lines are from PIC simulations, data points are from experiments. (from Perret et al. 2005)

physics behind their operation is described and finally, a short commentary on the future tendencies in multi-frequency RF plasma sources is presented.

The ion-assisted chemical etching process requires ions of sufficient energy to weaken the chemical bonds at the surface and also requires sufficient fluxes of ions to make the process worthwhile. From a plasma physics viewpoint, this necessitates sufficient sheath voltages to accelerate the ions and sufficient plasma densities to produce the required ion flux. Capacitively coupled plasma sources have the natural advantage of producing high voltage sheaths and therefore high ion energies. However, to increase the plasma density (and ion flux) one must increase the power from the RF supply. This entails an increase in the RF supply voltage and so the sheath voltage also increases. In other words, one cannot control the plasma density (ion flux) and sheath voltage (ion energy) independently of one another. This creates problems for fragile surfaces which are damaged by highly energetic ions – a limit is placed on the ion flux, and therefore the etch rate, before surface damage occurs. The relationship between the ion energy and the ion flux in various single frequency capacitive discharges is shown in figure 1.9[Perret 05]. This graph also points out that it is possible to produce high density CCP plasmas with low ion energies by moving to higher frequencies, but then one loses the option of having a high energy ion source. Higher densities may also be produced by introducing fixed magnetic fields close to the surface to be etched (the substrate). The electrons are trapped along the magnetic field lines due to the *Larmor effect*[5]. This results in a reduced electron loss rate to the walls and therefore higher steady state densities can be achieved.

[5]Larmor effect: In the presence of a magnetic fields, charged particles will tend to follow the field lines in a circular motion. Named after Sir Joseph Larmor (1857 – 1942), a Northern Irish physicist

Inductive discharges, in principle, have the opposite problem to capacitive discharges. They are capable of producing high density plasmas, but are not capable, by themselves, of creating the necessary sheath voltages in front of the substrate. Most inductive sources, therefore, bias the substrate holder independently, either using a DC voltage or an RF voltage supply. The RF frequency used is commonly in the 100 kHz to 13.56 MHz range. Plasma etch chambers of this type were the forerunners to later dual frequency plasma sources. They originally satisfied the demands from industry for independent control of ion energy and ion flux. However, ICPs by their nature are high density, large volume plasma sources and therefore result in highly dissociated gases. The resultant deficiency in large molecular radicals causes a lack of passivation in the dielectric etch process and so ICP tools were incapable of achieving the high aspect ratio and high selectivity required by industry. On top of this, attempts to get higher ion energies by increasing the bias potential resulted in the sputtering of the dielectric windows, thus reducing the window lifetimes. These issues were amongst the principal reasons that the main industrial etch companies decided to develop dielectric etch tools capable of providing independent control of both the ion energy and flux – the dual frequency capacitively coupled plasma source.

1.3.1 History

The first known record of a dual frequency RF plasma source for plasma etching appears to be a US patent submitted by G. Gorin of the Tegal Corporation in 1984 (US patent 4,464,223). The first known record of a dual frequency, *but entirely capacitively coupled*, RF plasma source appears to be by H. Goto et al. in 1992 [Goto 92]. The first patent specifically for a dual frequency capacitively coupled plasma etch chamber was by Varian Associates Inc. in 1997 (US patent 5,656,123, filed in 1995).

Despite their prolonged use in the plasma etch industry, dual frequency plasmas – and in general, multi frequency plasmas – are still a relatively understudied plasma source. During the 1990's only a handful of papers were published regarding dual frequency sources [Goto 92, Myers 92, Myers 94a, Myers 94b, Jaiprakash 94, Tsai 96, Kitajima 99, Rauf 99], about half of which were model orientated, the other half experimental. One explanation put forward for this lack of published work is that the various companies using these sources were very reluctant to release trade secrets and so refrained from financing open academic research into this area. By 2000 it was generally acknowledged that all the major players in the industry had access to some form of dual frequency CCP source and as such the number of industry supported projects in academia began to rise. As of the end of 2007, no less than 40 articles on dual frequency plasma sources have been published. At least three quarters of these publications have been either analytical or numerical such as those by Robiche et al. (2003), Georgieva et al. (2003), Boyle et

al. (2004), Kim et al. (2004), Lee et al. (2004), and Salabas et al. (2005) [Robiche 03, Georgieva 03a, Boyle 04a, Kim 04a, Lee 04, Salabas 05]. It is only in the last three years that the trend has shifted towards experimental studies such as those by Gans et al. (2006), Booth et al. (2006), Karkari et al. (2006), Worsley et al. (2006) and Curley et al. (2007) [Gans 06, Booth 06, Karkari 06, Worsley 06, Curley 07]. These experimental results will play a vital role in validating the theoretical models.

1.3.2 Principle of operation of dual freqency capacitively coupled plasma sources

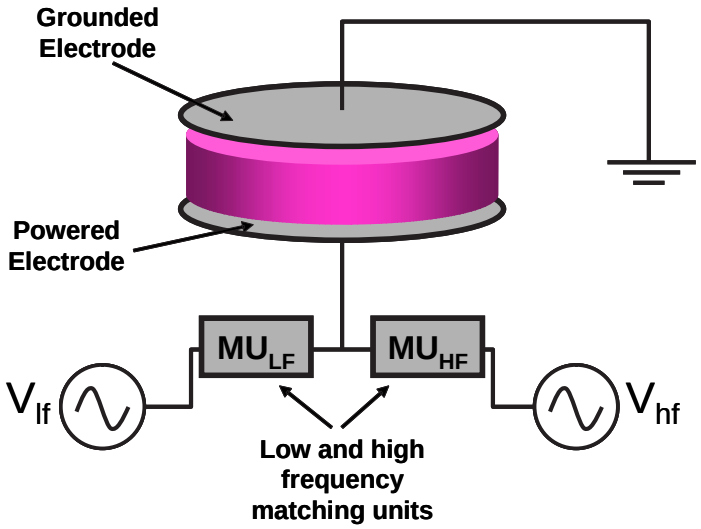


Figure 1.10: Schematic diagram a dual frequency capacitively couple plasma source.

The motivation for dual frequency sources is the independent control of the ion flux and the ion energy. To this end, a 'high' frequency RF source, V_{hf}, and a 'low' frequency RF source, V_{lf}, are used such that:

- the high frequency source controls the ion flux.
- the low frequency source controls the ion energy.

The ratio of the two frequencies is typically greater than 10. Using the equivalent circuit model of a CCP (c.f. figure 1.6 (b)) this independent control of the ion flux and ion energy can be explained as follows. The RF voltage supplied by both sources will fall mainly across the sheaths as $Z_{sh} \gg Z_p$. However, as $Z_{sh} \propto \omega^{-1}$ this will be much more the case for the lower of the two frequencies. Conversely, as $Z_p \propto \omega$, the high frequency source will have a greater proportion of its voltage fall across the plasma than the low frequency source.

To achieve greater control, certain conditions must be met. First let us take a look at the electron power balance. It can be shown that the plasma density, n, is proportional

to the power absorbed by the electrons, P_e, [Lieberman 05]. In RF discharges the power absorbed by the electrons is proportional to the applied voltage and the square of the excitation frequency, and so

$$\begin{aligned} P_e &\propto \omega^2 V_{rf} \\ \Rightarrow n &\propto \omega^2 V_{rf} \end{aligned} \tag{1.24}$$

This can be seen experimentally, as is inferred from figure 1.9 (Perret et al. 2005) and in work by Jolly et al. [Jolly 05]. If one now assures that the following condition is met:

$$\omega_{hf}^2 V_{hf} \gg \omega_{lf}^2 V_{lf} \tag{1.25}$$

then the high frequency source will control the plasma density and therefore the ion flux [Boyle 04a]. This is, of course, assuming that no complex heating results from any interaction between the two voltage sources.

The ion energy is equivalent to the total DC bias voltage across the sheath. As explained in section 1.2.4, the sheath voltage is almost entirely determined by the applied RF supply voltage, so in the case of a dual frequency source

$$E_i \sim |V_{hf} + V_{lf}| \tag{1.26}$$

From this, it follows that if the condition

$$V_{lf} \gg V_{hf} \tag{1.27}$$

is held then the low frequency source will control the ion energy. By combining the relations in equations 1.25 and 1.27 then we obtain the following condition for independent control of ion flux and energy [Lieberman 05]:

$$\frac{\omega_{hf}^2}{\omega_{lf}^2} \gg \frac{V_{lf}}{V_{hf}} \gg 1 \tag{1.28}$$

The above conditions are made based on the notion that a DF CCP is a simple superposition of two single frequency plasma sources. However, it may be more physically realistic to assume that there is some form of coupling between the high and low frequency components. This appears to be the case in one particularly important area – collisionless stochastic heating (see the end of section 1.2.4). It turns out that a synergetic stochastic heating effect occurs in a dual frequency sheath due to the presence of a high frequency sheath being carried back and forth across a low frequency sheath. Figure 1.11 (a) shows a schematic representation of a high voltage dual frequency sheath, illustrating the presence of a HF sheath motion and a LF sheath motion. On average, the electrons are reflected back into the plasma with a net gain in energy. However, as opposed to the single

frequency scenario, the stochastic heating process now takes place over a wider sample of the sheath region. The HF sheath is effectively carried over the LF sheath region. This results in a greater heating of the electrons than in single frequency plasmas. The moving hard wall model has been extended to the dual frequency case ([Kawamura 06]) producing the following analytical result:

$$S_{stoc} = \underbrace{\frac{1}{2} m \bar{v_e} \frac{J_{HF}^2}{e^2 n_s}}_{\text{High freq part}} \times \underbrace{\left(1 + \frac{\pi}{4} H_{LF}\right)\left(\frac{H_{LF}}{H_{LF} + 2.2}\right)}_{\text{Low freq part}} \tag{1.29}$$

where, J_{HF} is the high frequency current density, $H_{LF} = 0.55(V_{LF}/T_e)^{1/2}$ is the low frequency enhancement factor and $\bar{v_e} = \sqrt{8eT_e/\pi m_e}$ is the mean thermal electron speed. What this shows is that the stochastic heating in a DF-CCP is not simply the addition of the two single frequency processes, but rather is a product of both processes.

Fluid models by Turner & Chabert [Turner 06a, Turner 06b, Turner 07] have shown similar results. See figure 1.11 (b)[6].

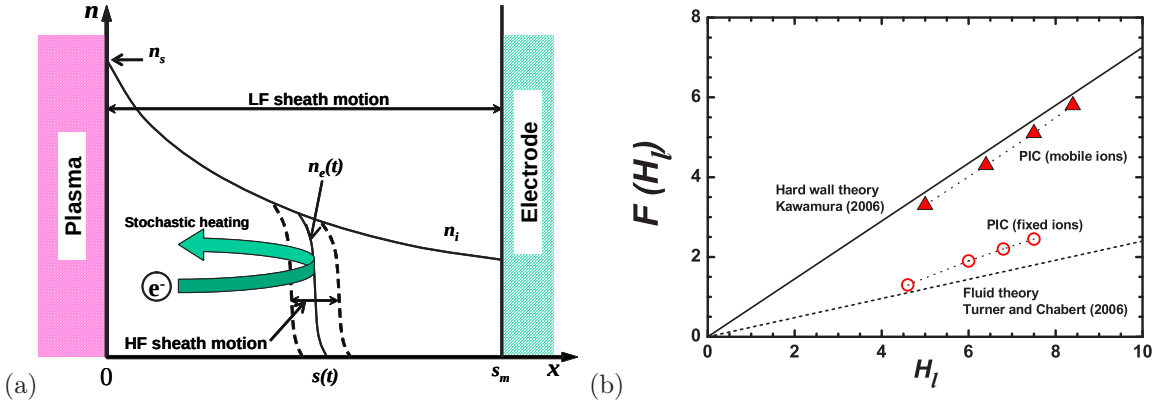


Figure 1.11: (a)Schematic representation of a dual frequency capacitive sheath; (b) Comparison of the analytical models (continuous and dashed lines) and PIC simulations (symbols) of the dual frequency stochastic heating mechanism.

1.3.3 Triple and multiple frequency plasma excitation

Currently, triple frequency excitation of plasmas for etch reactors is being examined by the major industrial players. The motivation is to augment the advantages of a dual frequency process by introducing a third, intermediate frequency. The purpose of this frequency is to control the ion energy distribution function.

[6]Part (b) of this figure is reproduced from a presentation given by M. A. Lieberman at the RF Plasma Workshop in Dublin, June2007.

1.4 Dielectric etching

Microelectronic devices such as micro-processors and solid state memory chips are fabricated by modifying the physical properties and structure of silicon. The silicon starts off in the form of a wafer, i.e. a circular slice of a long silicon column or ingot. Several standardised wafer diameters exist, notably 150 mm (6 in), 200 mm (8 in) and 300 mm (12 in). The larger the wafer, the greater the number of devices that can be fabricated thanks to a higher throughput. A specific wafer diameter, however, requires the entire production chain, from ingot growing to the dicing of the processed wafer into individual devices, to be compatible and so introducing a new standardised wafer diameter requires heavy investment and strict cooperation on the part of the entire semiconductor industry. There has already been much speculation as to whether or not the industry should move towards 450 mm diameter wafers sometime in the future[7].

The transformation of a wafer from silicon to chip involves a variety of processes such as polishing, cleaning, dopant implantation, photoresist development, plasma etching, metal deposition (back-end interconnects) and wafer dicing. An estimated one third of this transformation is entirely plasma based[Lieberman 05]. The first plasma steps involve doping areas of the silicon substrate to form the conducting gates. Close to 90 % of the plasma steps involve etching through insulating, or dielectric, layers on the wafer surface. An insulating layer may be formed on the wafer surface by exposing the wafer to oxygen, thus forming SiO_2. A mask outlining the circuit design to be etched is then imprinted onto this dielectric layer through a process of photoresist development. The wafer is then immersed in a chemically reactive plasma allowing the exposed areas of the mask to be etched. As indicated in section 1.2, the plasma will preferentially etch vertically, leading to anisotropic etching. This, however, is only in principle and in practice many, many parameters must be adjusted to achieve the desired etch profile.

1.4.1 Fluorocarbon containing plasmas

Fluorocarbon gases such as CF_4 and c-C_4F_8, are often used in the dielectric etch process for their anisotropic and selective etching capabilities. In the plasma environment they are readily dissociated into smaller molecular and atomic radicals. An overview of the principal dissociation paths and byproducts in CF_4 and c-C_4F_8 plasmas can be found in tables 1.1 and 1.2. These chemically reactive by-products are then capable of etching away the dielectric material, which is either SiO_2 or SiOCH for low-k devices.

The etching process involves the removal of silicon by the very chemically reactive fluorine atoms, forming a volatile gas phase product which is then pumped away. For

[7] A quick internet search with the expression "*450 mm wafer*" will bring up many relevant articles.

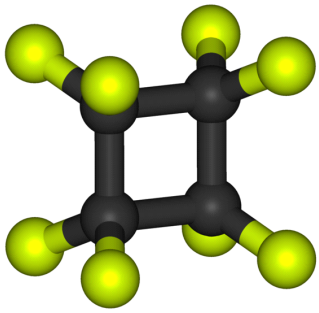


Figure 1.12: The c-C_4F_8 molecule: four carbon atoms (black) in a circular configuration, each in contact with two fluorine atoms (green). Source: Wikipedia.

example:

$$SiO_2 + CF_4 \longrightarrow SiF_4 + CO_2$$

where SiF_4 is volatile. The above process is not direct and so several intermediate dissociation and chemical bonding paths take place along the way. To ensure complete process control it is important that the parent gas does not react with the surface to be etched. The remaining carbon chemically bonds with the released oxygen to form a volatile product which is also pumped away. To ensure that all the carbon is removed, many process gas mixtures include additional oxygen.

Initially CF_4 was the most common fluorcarbon gas used in dielectric etch. Nowadays, a variety of C_xF_y type gases are used. c-C_4F_8 is valued for its high carbon to fluorine ratio which permits high aspect ratio contact hole etching, although c-C_4F_8 is more difficult to make than CF_4 and as such is much more expensive than CF_4 [8]. The DF-CCP in this study uses primarily a mixture of $Ar/O_2/c$-C_4F_8 with typical rations of 85%/5%/10%. One metric for illustrating the change in product gas mixtures over the years is the availability of electron impact cross-sections for both gases. Review data for CF_4 became widely available at the height of its use in 1994 [Bonham 94], while it was not until seven years later in 2001 that those for c-C_4F_8 were published by [Christophorou 01].

Tables 1.1 and 1.2 summarise the important electron–neutral collisional processes in CF_4 and c-C_4F_8 plasmas respectively. As these molecules are readily dissociated in the plasma, many other reactions involving the by-products also occur. The dissociation process is also one of the principal mechanisms for the formation of positive ions. Fig 1.13 shows the principal positive ions measured by mass spectrometry in a single frequency (40.68 MHz) CCP containing Ar, c-C_4F_8 and O_2 [Bulcourt 02]. The reactor used had an electrode diameter of 12 cm and an electrode spacing of 3 cm. The plasma was confined by a wire mesh configuration. Even though the argon gas accounted for over 85 % of the total gas mixture, it was the larger fluorocarbon positive ions which dominated. If

[8] Typical prices: CF_4 = 300 euros per cubic metre; c-C_4F_8 = 2100 euros per cubic metre

Dissociative ionisation	$CF_4 + e$	$\longrightarrow$	$CF_3^+ + F + 2e$
Neutral dissociation	$CF_4 + e$	$\longrightarrow$	$CF_3 + F + e$
	$CF_4 + e$	$\longrightarrow$	$CF_2 + 2F + e$
	$CF_4 + e$	$\longrightarrow$	$CF + 3F + e$
Electron attachment	$CF_4 + e$	$\longrightarrow$	$CF_3 + F^-$
	$CF_4 + e$	$\longrightarrow$	$CF_3^- + F$
Dissociation	$CF_4 + e$	$\longrightarrow$	$CF_3^+ + F^- + e$

Table 1.1: Important electron–neutral collisional processes in CF_4 plasmas.

Neutral dissociation	$C_4F_8 + e$	$\longrightarrow$	$C_2F_4 + C_2F_4 + e$
	$C_2F_4 + e$	$\longrightarrow$	$CF_2 + CF_2 + e$
	$CF_3 + e$	$\longrightarrow$	$CF_2 + F + e$
	$CF_2 + e$	$\longrightarrow$	$CF + F + e$
	$CF + e$	$\longrightarrow$	$C + F + e$
	$F_2 + e$	$\longrightarrow$	$F + F + e$
Ionisation	$C_4F_8 + e$	$\longrightarrow$	$CF_3^+ +$ products $+ 2e$
	$C_4F_8 + e$	$\longrightarrow$	$C_4F_7^+ + F + 2e$
	$C_4F_8 + e$	$\longrightarrow$	$C_2F_4^+ + C_2F_4 + 2e$
	$C_4F_8 + e$	$\longrightarrow$	$C_3F_5^+ +$ products $+ 2e$
	$C_2F_4 + e$	$\longrightarrow$	$C_2F_3^+ + F + 2e$
	$CF_3 + e$	$\longrightarrow$	$CF_3^+ + 2e$
Dissociative Attachment	$C_4F_8 + e$	$\longrightarrow$	F^-
	$CF_3 + e$	$\longrightarrow$	$CF_2 + F^-$
	$CF_2 + e$	$\longrightarrow$	$CF + F^-$
	$F_2 + e$	$\longrightarrow$	$F + F^-$

Table 1.2: Important electron–neutral collisional processes in c-C_4F_8 plasmas.

we take $C_3F_5^+$, $C_2F_4^+$ and CF_3^+ as the main ion species, then the average ion mass would be somewhere around 100 amu, as opposed to 40 amu if we assumed argon positive ions. It is therefore of quite significant importance to have an idea which ion mass to use for calculations such as that of the Bohm velocity. Where CF_4 is used, it is more likely that the majority ion species will be a mixture of CF_3^+, CF_2^+, CF^+ and Ar^+, and so the average ion mass will be closer to 50, making it possible to assume that argon ions dominate without incurring much error.

Other studies have also shown that heavy fluorocarbon ions are the major positive ion species in Ar/c-C_4F_8 plasma mixtures [Hirose 98]. In our reactor configuration, however, the small gap (2.5 cm) and high powers ($>$ 250 W) may mean that the presence of higher electron temperatures and densities will lead to greater fragmentation and therefore smaller positive ion species. Unfortunately, no ion mass spectrometry measurements are available in the literature for our experimental configuration. Vasenkov and Kushner have modelled a high power (1500 W) magnetically enhanced CCP in Ar/c-C_4F_8/O_2 discharges [Vasenkov 04]. Overall, they also found the large fluorocarbon ions to be dominant in the bulk plasma. However, the magnetic confinement near the substrate surface resulted in very high electron temperatures in this region ($T_e = 9$ eV), leading to Ar^+ ions dominating the ion flux to the surface.

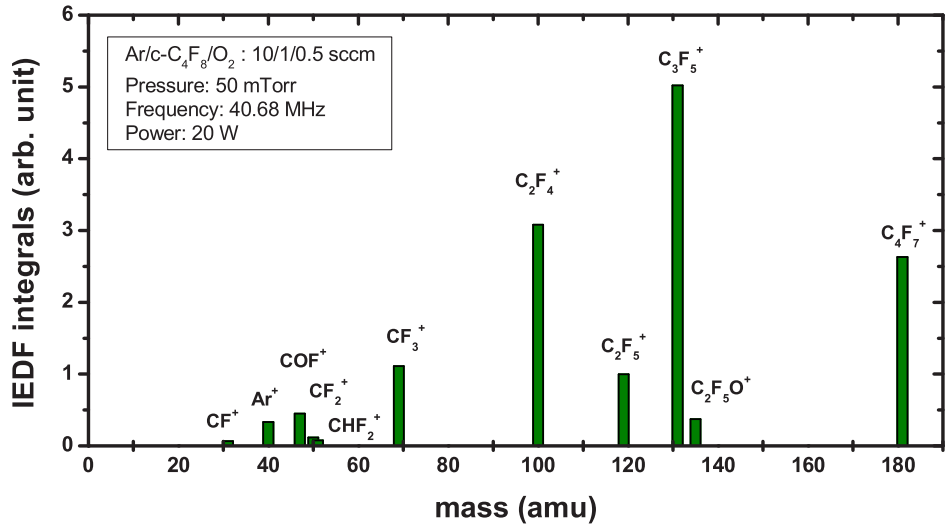


Figure 1.13: Principle positive ions measured by mass spectrometry in a single frequency (40.68 MHz) CCP containing Ar, c-C_4F_8 and O−2 [Bulcourt 02]. Pressure was 50 mTorr and applied power was 20 W. The proportion of each gas in the mixture is similar to that which is used in the experiments in this thesis.

1.5 Electronegative Plasmas

The study of electronegative plasmas is by no means a new area of research. As far back as 1935, John Spencer-Smith and co-workers were leading the way in negative ion diagnostic techniques [Spencer-Smith 35a, Spencer-Smith 35b]. Experiments were undertaken in DC glow discharges in iodine and diagnostics were limited to Langmuir probe measurements. However, the strong impact of negative ions on the probe characteristics (see figure 1.14) showed evidence for high electronegativity and resulted in the need for Spencer-Smith to make modifications to Langmuir probe theory. By adding iodine to helium it was also shown how quickly negative ions became the primary negative charge, with only trace amounts of iodine required. Spencer-Smith's supervisor, Prof. Emeléus continued working on electronegative discharges, such as in ref. [Emeleus 38], and in 1970, with the aide of Woolsey, put together a comprehensive selection of papers, produced from their work at Belfast, in the book *Discharges in Electronegative Gases* [Emeleus 70].

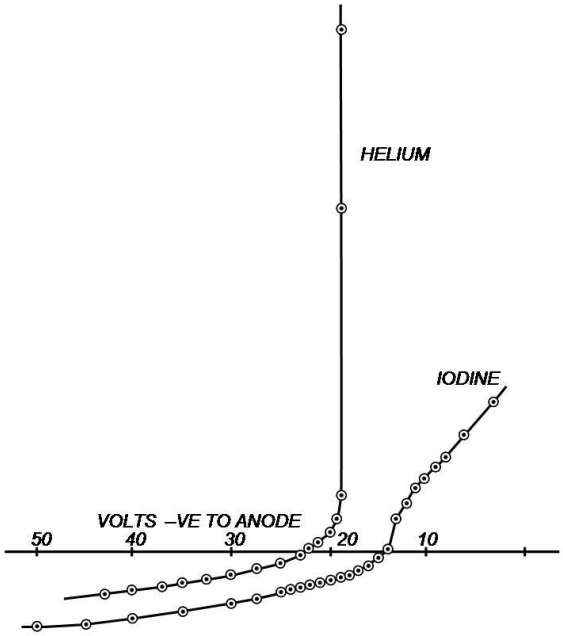


Figure 1.14: Probe characteristics in iodine and helium. Reproduced from Spencer-Smith, 1935 [Spencer-Smith 35a]

The study of electronegative discharges has been ongoing since those early years, with particular interest in the effect of negative ions on probe characteristics [Swift 70, Braithwaite 88]. The original motivations for studying negative ions were primarily for astrophysics. Today, interest in negative ions has also been fueled by (i) the requirement for high-energy and high-density ion beams in nuclear fusion and (ii) the presence of halogens in processing plasmas in the microelectronics industry. The last 15 years has seen a large number of papers dedicated to the measurement and understanding of such

plasmas, with Amemiya setting the stage nicely for this new found interest [Amemiya 90]. The reader is strongly encouraged to refer to this paper for an overview of negative ion studies. Because of the complexity involved in modelling electronegative plasmas, it has always been the case that electropositive theory takes precedence. Since electronegative plasmas are widely used in an industrial context, it is therefore timely and important to develop the understanding and quantitative theory of electronegative plasmas.

1.5.1 Negative ions in fluorocarbon plasmas: production and loss

The fluorocarbon gases used in this study are CF_4 and c-C_4F_8. This section examines in more detail the principal mechanisms of anion creation and destruction in these two gases. The consensus in the literature is that F^- and CF_3^- are the principal negative ion species formed in fluorcarbon plasmas. Jauberteau et al. was one of the first to make this assumption in experimental measurements of CF_4 [Jauberteau 89] . He based this assumption on a remark contained in a Ph. D. thesis by Bisschops where the CF_3^- density was estimated to be 5 % to 10 % that of the F^- density, though Bisschops appears not to back up this remark with any experimental or theoretical data [Bisschops 87]. Haverlag et al. [Haverlag 91] produced clear evidence that F^- was indeed the dominant negative ion in a low power CF_4 RF plasma, and backed up that claim by referring to mass spectrometry data in a pulsed RF CF_4 plasma taken by Overzet et al. [Overzet 89]. Haverlag also showed, however, that in C_2F_6 other negative ions may also be present in significant densities. As will be shown later, this may also be the case for c-C_4F_8. Haverlag's laser photodetachment results are reproduced in figure 1.15.

It is not all that surprising to discover that F^- is one of the major anion species in fluorcarbon plasmas. Fluorine produces the most stable anion of all the halogens, thanks in large part to its high electron affinity (3.401 eV)[Blondel 01]. The bigger issue is the identification of the other molecular negative ions that may be present and whether or not they are in significant numbers. Although CF_3^- has been suggested, there is little evidence to suggest that it plays a significant role in CF_4 plasmas, especially when the results of Haverlag [Haverlag 91] and Lin [Lin 93] are taken into account. However, to rule it out completely would be wrong, as it is more likely that the production and loss of CF_3^- is dependent on the plasma chemistry and input parameters (power, pressure). LeCoat et al. show clearly that CF_3^- is indeed a principal product of dissociative electron attachment to CF_4 [LeCoat 94]. It has been suggested that CF_3^- may become the dominant negative ion species under certain conditions in dual frequency capacitively coupled plasmas [Georgieva 03a, Georgieva 06a, Donkó 06]. In the presence of a silicon wafer, it has been shown that SiF_5^- can also reach significant densities[Lin 93]. To summarise, we can say that F^- is the majority anion in many cases, and may possibly be accompanied by large molecular anions.

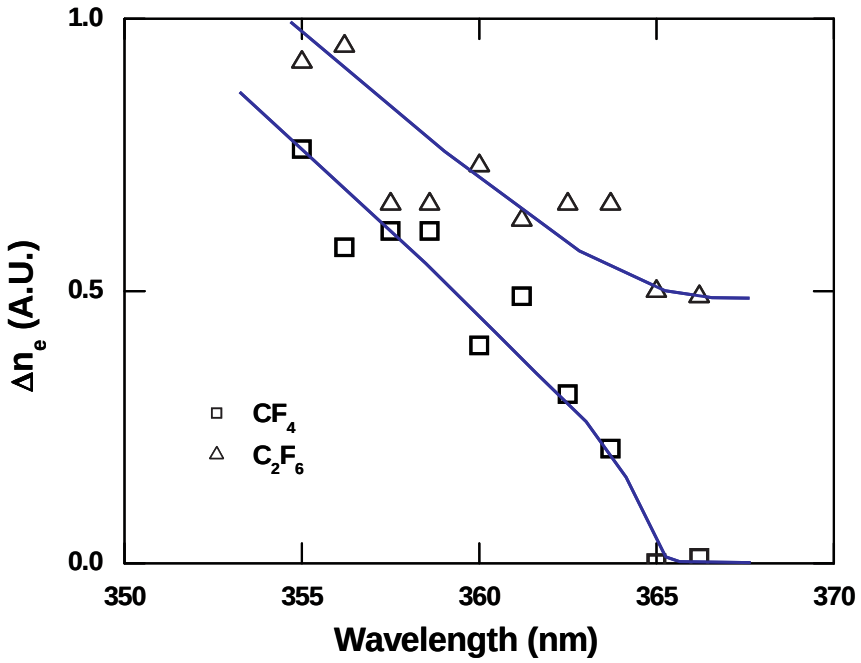


Figure 1.15: Figure reproduced from Haverlag et al (1991), ref. [Haverlag 91]. Intensity of the photodetachment signal in plasmas of CF_4 and C_2F_6 as a function of wavelength in the region of the F^- threshold, 364.5 nm. It shows that in CF_4 the F^- ion is the major negative ion whereas in C_2F_6 other negative ions may also be present in significant densities.

The principal mechanism for the formation of negative ions is dissociative electron attachment:

$$AB + e \rightarrow A^- + B$$

In the case of CF_4 (cf. table 1.1), this translates to the following reactions:

$$CF_4 + e \rightarrow CF_3 + F^- \tag{1.30}$$

$$CF_4 + e \rightarrow CF_3^- + F \tag{1.31}$$

In the case of c-C_4F_8 (cf. table 1.2) the following reaction is very probable [Sauers 79, Font 02]:

$$C_4F_8 + e \rightarrow F^- + products \tag{1.32}$$

The cross sections for the dissociative attachment of electrons to CF_4, C_2F_6 and C_3F_8 as a function of electron energy is shown in figure 1.16. Data is not readily available for c-C_4F_8 but one can see the trend showing that the cross-section increases and peaks at lower energies as the molecule size increases. c-C_4F_8 is expected to follow this trend. At lower energies ≤ 2 eV, attachment to the parent gas molecule is also possible [Sauers 79,

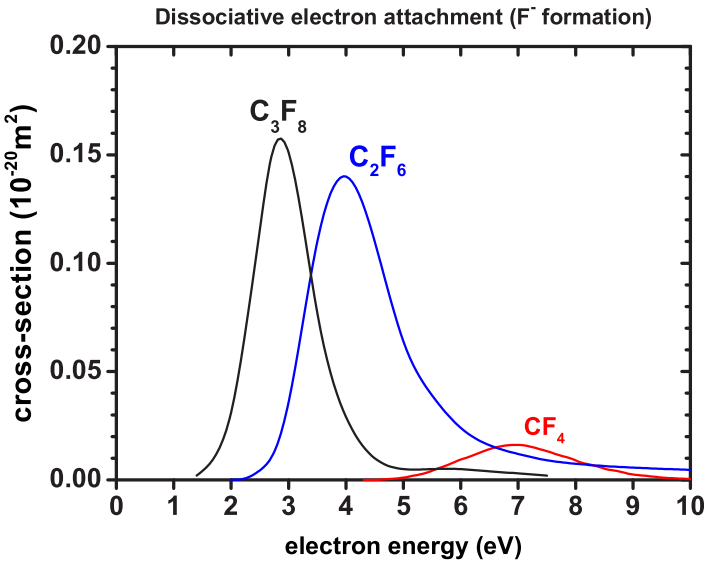


Figure 1.16: Cross sections for the dissociative electron attachment of C_3F_8, C_2F_6 and CF_4 forming fluorine negative ions

Font 02]:

$$C_4F_8 + e \rightarrow C_4F_8^- \tag{1.33}$$

In the plasma phase c-C_4F_8 readily dissociates into many subspecies such as C_2F_4, CF_2 and CF. This may create more pathways for the creation of negative ions. F^- may also be created by dissociative attachment to the fluorine molecule, F_2:

$$F_2 + e \rightarrow F^- + F \tag{1.34}$$

The loss mechanisms for negative ions are either ion-anion recombination:

$$A^+ + B^- \rightarrow AB$$

or some form of collision-induced detachment process:

$$A + B^- \rightarrow AB + e$$

$$A^* + B^- \rightarrow AB + e$$

$$e + B^- \rightarrow B + e + e$$

Some of the likely ion-anion recombination processes in CF_4 are:

$$CF_3^+ + F^- \rightarrow (CF_4) \rightarrow CF_3 + F \tag{1.35}$$

$$CF_3^- + CF_3^+ \rightarrow C_2F_6 \tag{1.36}$$

while in c-C_4F_8 there may be a greater variety of positive ions available for recombination,

notably CF_2^+, CF_3^+, $C_2F_4^+$ and $C_3F_5^+$.

A possible fast collision-induced detachment process in CF_4 and c-C_4F_8 could involve the molecular radical CF_2:

$$F^- + CF_2 \rightarrow CF_3 + e \tag{1.37}$$

The dominant loss process may be governed by a variety of parameters but the most influential are gas type and pressure. Generally, at low pressures the plasma is recombination dominated whereas at high pressures, for example in O_2 plasmas, detachment takes over [Edgley 75, Ferreira 88]. The differences in the two regimes influence the effect of the negative ion presence on the electron temperature. In recombination dominated plasmas the electron temperature has a lower limit if the plasma is to remain in a steady state. In detachment dominated plasmas, however, there is no limiting temperature since detachment provides another electron generation mechanism additional to ionisation [Franklin 02].

The production (attachment) and loss (recombination and detachment) mechanisms for the negative ions are summarised in the following equation:

$$\nabla \cdot (n_n v_n) = K_{att} n_e n_g - K_{rec} n_i n_n - K_{det} n_n n_x \tag{1.38}$$

where n_g is the neutral gas density, n_x is the density of the impacting species in the detachment process and K_{att}, K_{rec} and K_{det} are the attachment, recombination and detatchment rate coefficients respectively.

Another possible loss mechanism for the negative ions is loss to the walls. This has being suggested to be significant in DF-CC plasmas when the lower RF frequency is $\leq$ 2 MHz [Georgieva 03a, Georgieva 06a, Donkó 06]. They suggest that the negative fluorine ion, F^-, is mobile enough to follow the low-frequency source such that when V_{rf} is large enough the negative ions can be accelerated across the plasma sheath. The voltages used were 400 V and 800 V in Georgieva's and Donko's papers respectively. However, this has not been proven experimentally and one of the main aims of this study is to examine this theory.

1.5.2 Plasma theory in the presence of negative ions

The formation of negative ions in a low-temperature, low-pressure plasma leads to significant departure from the particle and energy equilibrium conditions found in an electropositive plasma. Whereas electropositive theory is founded on the large differences in mass and temperature between the negative charges (electrons) and positive charges (positive ions), these assumptions no longer hold when the negative ion density becomes significant. Two parameters specific to electronegative discharges are used in plasma theory to quantify the influence of the negative ions. The first is the ratio of the negative

ion density to the electron density and is known as the negative ion fraction:

$$\alpha = \frac{n_n}{n_e} \tag{1.39}$$

The second parameter is the ratio of the electron temperature to the negative ion temperature:

$$\gamma = \frac{T_e}{T_n} \tag{1.40}$$

which is a valid parameter only if we consider both species to be sufficiently thermalised. In many fluid models, this parameter is a metric for the difference in mass between both species. In fact, the precursive studies to electronegative plasma fluid modelling were those on plasmas containing two electron temperatures (e.g. [Wickens 79]). If we take the case where the negative ions are assumed to be in thermal equilibrium with the gas, then in a typical laboratory plasma ($T_g \sim 500$ K or 0.052 eV) with an electron temperature of 5 eV then we would have $\gamma \approx 96$. This effectively places an upper limit on the value of γ. The lower limit is $\gamma = 1$, which effectively equates to an electropositive plasma. We will examine later our estimations for the negative ion temperature.

We note here that the theory which follows is developed for the DC case only. The effect of RF fluctuations are ignored, unless otherwise stated.

Basic electronegative theory

The quasineutrality of the plasma is conserved in the presence of negative ions and so we have:

$$n_i(x) = n_e(x) + n_n(x) \tag{1.41}$$

where $x = 0$ is the plasma centre and $x = s$ is at the plasma-sheath boundary. If we assume that the positive ion losses are predominantly to the walls rather than via volume recombination, we can then consider the negative ions to be in thermal equilibrium with one another. The negative ions are, like the electrons, confined within the plasma bulk by the space charge sheath and as such we will assume a spatial distribution determined by the space potential:

$$n_e(x) = n_{es} \exp\left(\frac{V(x) - V_s}{T_e}\right) \tag{1.42}$$

$$n_n(x) = n_{ns} \exp\left(\frac{V(x) - V_s}{T_n}\right) \tag{1.43}$$

where $V_s = V(x = s)$ is the space potential at the plasma sheath boundary and $V(x = 0) = 0$. The positive ions, in the low pressure approximation, are in free fall in the

electrostatic potential. Applying conservation of energy we have:

$$n_i(x) = n_{is}\frac{u_s}{\sqrt{u_s^2 - u(x)^2}} = \frac{n_{is}u_s}{\sqrt{u_s^2 - 2(V - V_s)/m_i}} \tag{1.44}$$

If one assumes a continuous transition from the plasma to the sheath, then the following boundary condition may be applied to the plasma [Braithwaite 88]:

$$\frac{d\rho}{dV} = 0 \text{ at the sheath edge} \tag{1.45}$$

where ρ is the net space charge. This condition, when combined with equations 1.42 – 1.44, imposes that the positive ions must have a velocity, u_s, at the sheath edge [Wickens 79, Braithwaite 88]:

$$u_s = \sqrt{\frac{(n_{es} + n_{ns})T_eT_nk}{(n_{es}T_n + n_{ns}T_e)m_i}} \tag{1.46}$$

$$= u_B\sqrt{\frac{1+\alpha_s}{1+\alpha_s\gamma}} \tag{1.47}$$

where $u_B = \sqrt{kT_e/m_i}$ is the ion sound speed, or Bohm velocity, in an electropositive plasma and $\alpha_s = n_{ns}/n_{es}$ is the negative ion fraction at the plasma-sheath boundary. Note that when $\gamma = 1$ we find $u_s = u_B$. As $\gamma > 1$ in a typical electronegative discharge, the ion velocity, and therefore the ion flux is lower in an electronegative plasma for a given ion density. Figure 1.17 shows how the ion velocity is modified as a function of α_s and for various values of γ. It is important to be reminded, however, that it is the negative ion fraction *at the plasma-sheath boundary* which influences the velocity of the ions *entering the sheath*. As we will see later, there can be significant variations in α from the plasma centre to the plasma edge. In fact, plasmas containing negative ions often exhibit stratification, with a core electronegative plasma and an electropositive plasma-sheath boundary (see figure 1.19 in the next section). The flow of positive ions leaving the plasma will, of course, still depend on the ion density and velocity at the plasma-sheath boundary:

$$\Gamma_i = n_{is}u_s = n_{i0}h_lu_s \tag{1.48}$$

Subsituting for quasineutrality we get the following general equation describing the ion flux in an electronegative plasma:

$$\Gamma_i = h_lu_sn_{e0}(1 + \alpha_0) \tag{1.49}$$

where α_0 is the negative ion fraction at the plasma centre.

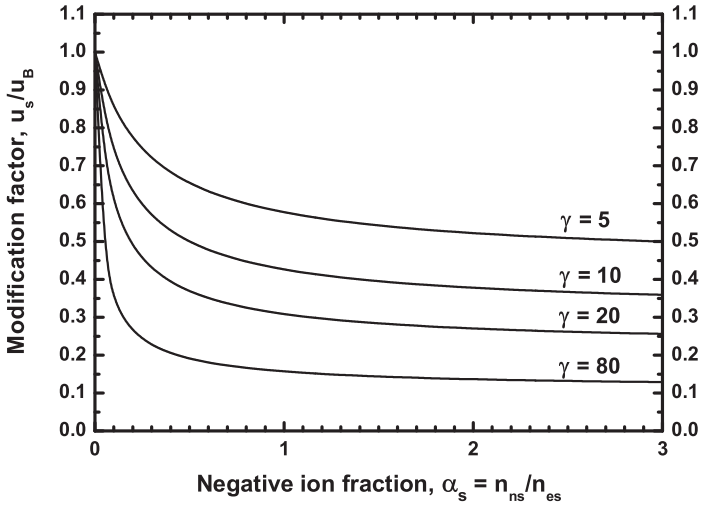


Figure 1.17: The ion velocity at the sheath edge in an electronegative plasma, normalised to the electropositive Bohm velocity, as a function of α_s and for various values of γ.

Electronegative discharge modelling

We can gain insight into the electrostatic structure of electronegative plasmas by applying fluid equations to simplified assumptions and boundary conditions. Ferriera et al. [Ferreira 88] were the first to show that this was possible in a self-consistent and simplified manner with no issues of numerical convergence. Their theory was largely based on the work of Edgley [Edgley 75] who showed that the negative ions were very much confined to the plasma bulk and that their flux was directed in towards the centre. The charged particles were subject to several boundary conditions, most notably that n_e and n_n are zero at the walls. They also took into consideration the production and loss mechanisms of the negative ions. The model gives a good insight into the spatial profile of an electronegative plasma. However, the model uses the quasineutrality assumption, i.e. no use of Poisson's equation, and does not use the ion sound speed as a boundary condition at the plasma edge. Furthermore, it is difficult to obtain quantitive information on the ion flux at the boundary, which is important for the analysis of probe characteristics.

Here we will discuss the model put forward by Sheridan et al. [Sheridan 99b, Sheridan 99a]. In particular, we will examine the model in what they termed a modestly collisional plasma. This model, unlike that of Ferreira and co-workers, is a fluid description of an expanding plasma with no final boundary condition. It is therefore an initial value problem with no eigenvalues, and therefore is computationally simpler. Quasineutrality is not assumed and so the Poisson equation is used. This allows for charge separation to occur and therefore the natural formation of a sheath. The model does not use the production and loss mechanisms for the negative ions as input parameters, but instead provides a general insight into the plasma's electrical structure for a fixed α_0 and γ. The

basic principles of the model will be outlined here so that the results can be interpreted.

At the centre of the plasma, $x = 0$, the following initial conditions are used:

- $n_e(x = 0) = n_{e0}$
- $n_n(x = 0) = n_{n0}$
- $\phi(x = 0) = 0$, the potential is zero.

The equations of continuity and motion for the cold, positive ion fluid are:

$$\frac{d(n_i v_i)}{dx} = \nu_{iz} n_{e0} \exp\left(\frac{e\phi}{kT_e}\right) \tag{1.50}$$

$$M_i n_i v_i \frac{dv_i}{dx} + M_i v_i \nu_{iz} n_{e0} \exp\left(\frac{e\phi}{kT_e}\right) = n_i eE - n_i F_c \tag{1.51}$$

where v_i is the ion velocity, ν_{iz} is the net ionisation frequency and F_c is the collisional drag force which is assumed to have the form $F_c = M_i v_i \nu_p$, where ν_p is the ion collision frequency for momentum transfer, i.e. constant mean-free-time collisions or *constant mobility* (CM). The decision by Sheridan to use constant mobility has important consequences for the model's results which will be examined when a comparison is made with the experimental results. Later in this thesis, we develop a variable mobility (VM) model which is more appropriate for the range of pressures used in our experimental studies.

During the normalisation process, the ionisation length is defined as

$$\Lambda = c_s/\nu_{iz} \tag{1.52}$$

where $c_s = \sqrt{kT_e/M_i}$ is the ion acoustic speed in the absence of negative ions. The model has four input parameters, namely:

1. The non-neutrality parameter: $q = \lambda_D/\Lambda$. When q is set to zero the model describes a quasi-neutral plasma with infinitely thin sheaths.
2. The negative ion fraction at the plasma centre: $\alpha_0 = n_{n0}/n_{e0}$
3. The ratio of the electron temperature to the negative ion temperature: $\gamma = T_e/T_n$
4. The ion collision parameter: $\beta_{cm} = \nu_p/\nu_{iz} = \Lambda/(c_s/\nu_p) = \Lambda/\lambda_{eff}$, where λ_{eff} is an effective mean free path. The subscript cm is a reference to the constant mobility origins of this parameter. Setting $\beta_{cm} = 0$ is equivalent to creating a collisionless model.

Several results from the model that are relevant to this study are presented in figures 1.18 and 1.20, which show the evolution of the normalised ion flux at the sheath edge as a function of the input parameters α, γ and β_{cm}. The normalised ion flux is defined as:

$$\frac{\Gamma_{is}}{n_{e0} c_s} \tag{1.53}$$

and in an electropositive plasma equates to the h_l-factor discussed in section 1.2. Figure 1.18 (a) examines the **collisionless case**, i.e. where $\beta_{cm} = 0$. The effect of the temperature ratio is quite evident with the ion flux having an increasingly large value as the ratio is reduced. What is striking is the 'knee' in the curves as α increases: for almost all values of γ the ion flux is only very weakly modified at low negative ion fractions. Then, at the knee, the normalised flux rises rapidly as the negative ion fraction is increased. The positive ion flux at a probe in a weakly electronegative plasma will be insensitive to α, especially for cold negative ions (high γ). The origin of this knee is the stratified nature of electronegative plasmas. The stratification occurs because the negative ions are more confined to the centre by the electric potential gradient. This means that the negative ion fraction at the sheath edge, α_s, is much less than that at the centre. This can be seen more clearly when equations 1.42 and 1.43 are combined to give α_s as a function of α_0 and the potential:

$$\alpha_s = \alpha_0 \exp\left[\frac{V_s(1-\gamma)}{T_e}\right] \tag{1.54}$$

where V_s is the potential at the plasma-sheath boundary. When equation 1.47 is then taken into account, it can be seen that the knee is where the negative ion fraction becomes important at the plasma-sheath interface and and a sudden variation of the ion flux occurs as was seen in figure 1.17.

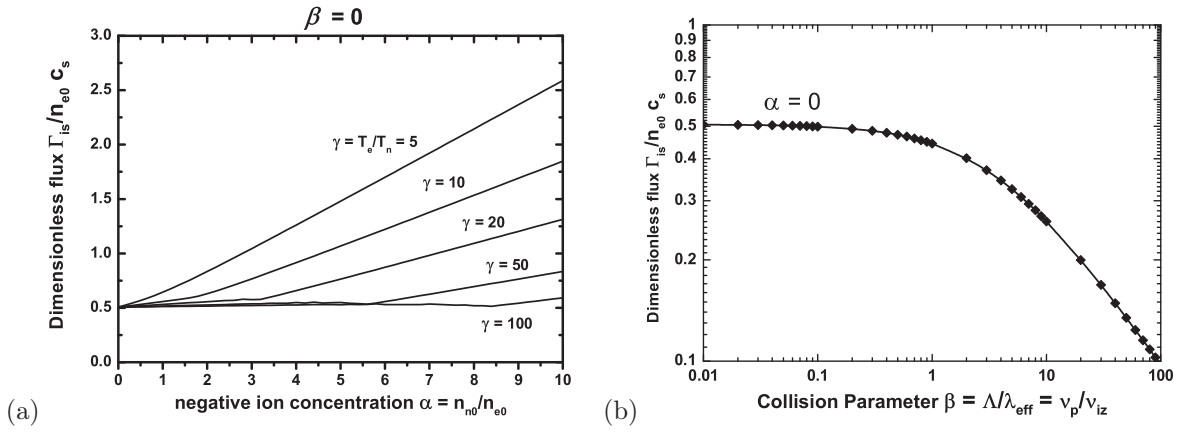


Figure 1.18: (a) The normalised ion flux as a function of alpha for various temperature ratios in a collisionless plasma; (b)The normalised ion flux as a function of the collisional parameter, β_{cm}, in an electropositive plasma ($\alpha = 0$).

Figure 1.19 displays the plasma electrical structure for various electronegativities in a collisionless plasma ($\gamma = 20$), using the fluid model. The densities are normalised to the positive ion density and the distance is normalised to the plasma length (in practice, to the point at which the ion flux saturates).

Figure 1.18 (b) examines the effect of collisions in the electropositive case, showing the normalised ion flux (the h_l-factor in this case) as a function of the collisional parameter,

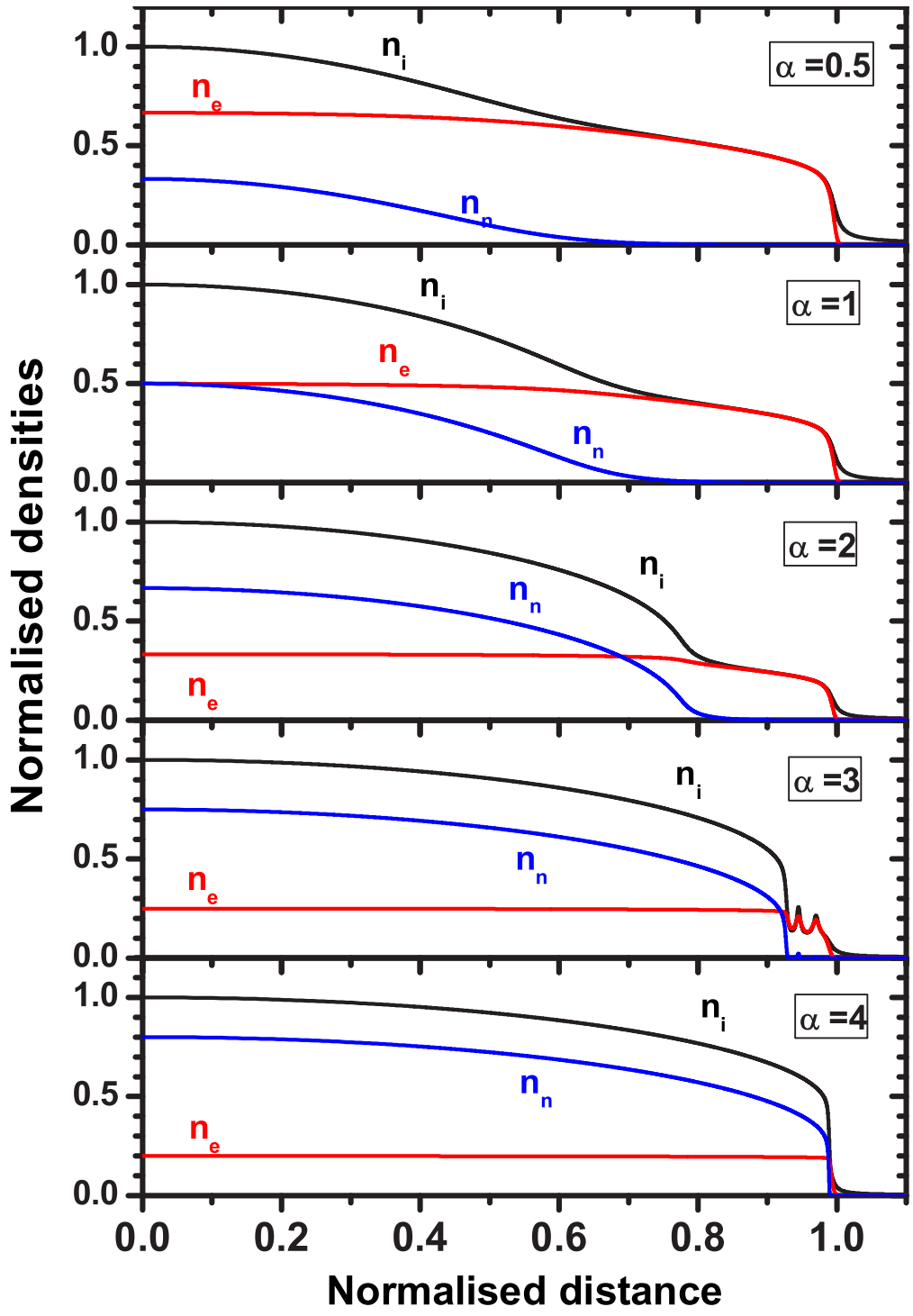


Figure 1.19: The effect of increasing electronegativity on the discharge structure. Profiles are for $\gamma = 20$ and $\beta_{cm} = 0$ (no collisions). The sheath is formed at $X = 1$. $\alpha_0 = 0.5$, 1 and 2 exhibits a stratified discharge. $\alpha_0 = 4$ exhibits electronegativity over the entire bulk region. $\alpha_0 = 3$ exhibits oscillations due to the formation of a double-layer-stratified discharge.

in effect as a function of the pressure. This graph is similar to the result by Lee & Lieberman of a heuristic solution describing h_l over various ion collisionalities[Lee 95]. At low collisionalities ($\beta_{cm} < 1$) the h_l-factor is close to the theoretical value of 0.5, whereas at higher values of β_{cm} the h_l-factor drops off rapidly, as predicted in the models of Godyak [Godyak 86]. The region between β_{cm} =1 and 100 is the region of interest for this thesis.

Figure 1.20 examines the ion flux as a function of the negative ion fraction for various temperature ratios and for four values of the collisional factor, 10, 20, 30 and 40. The reason for choosing these values will become clear in chapter 3. Note the difference in scale between these graphs and figure 1.18 (a). The more collisional the plasma, the less the normalised ion flux is modified for increasing α. Notice also that there is no 'knee' present in these curves. This means that when collisions are taken into account, the ion flux to a probe may be sensitive to changes in α even when the plasma is weakly electronegative. The temperature ratio again plays a very important role in determining whether or not the variation in the negative ion fraction will be visible to probe measurements.

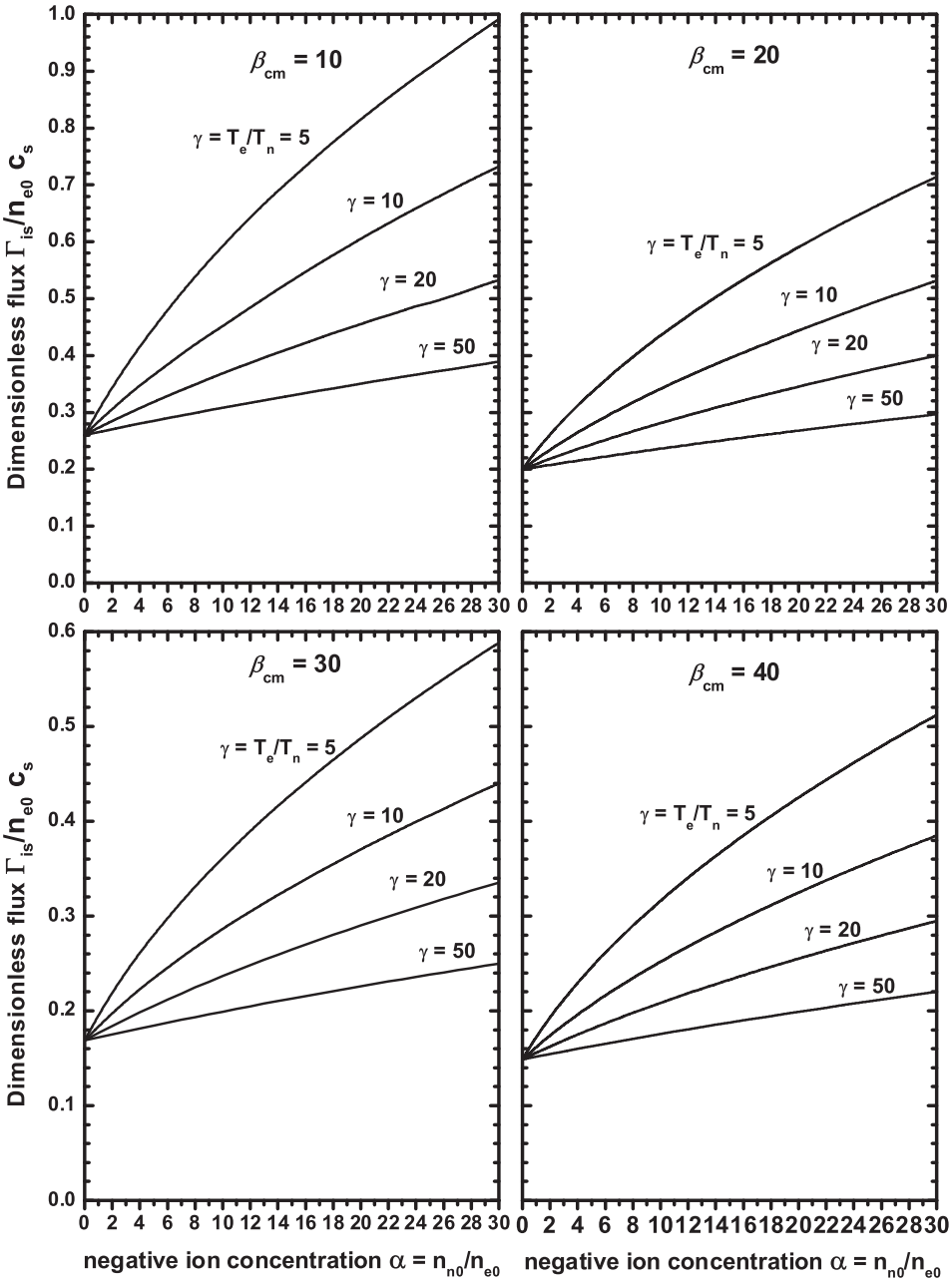
1.5.3 The role of negative ions in industrial plasmas

Firstly, it is important to note that the vast majority of industrial plasma process mixtures, or recipes as they are known, involve electronegative plasmas. When one examines figures 1.17 and 1.18 (a) it becomes clear that small changes to either α or γ can easily result in significant changes to the ion flux leaving the plasma. This in turn may lead to significant changes to the etch characteristics, bringing the process far from the original process window. A description of the plasma electronegativity over various parameter ranges could prove valuable in scenarios such as this.

Expected negative ion densities in CF_4 and c-C_4F_8

Several estimations and measurements of the maximum negative ion densities in CF_4 and c-C_4F_8 containing plasmas have been published. A summary of the most relevant publications with their results and study conditions are summarised in table 1.3. Our experimental conditions (50 mTorr–6.6 Pa, using c-C_4F_8, dual frequency, powers up to 1000 W) vary considerably from the majority of those in this table, which of course is one of the motivations for our study. Nevertheless, important conclusions may be made that can help guide us in our own work.

Although the table represents the maximum negative ion densities and fractions estimated/measured, the overall picture is that fluorocarbon containing plasmas are systematically electronegative, with CCP discharges producing the highest values of α. The study of an $Ar/CF_4/N_2$ (8:1:1)DF-CCP in a simulation by Georgieva et al. is the closest to our conditions and show that we can expect negative ion densities greater than



(a)

Figure 1.20: The normalised ion flux as a function of alpha for β_{cm} = 10, 20, 30 and 40.

Gases	Pwr/Volt	P (mTorr)	n_n	α	Study	Reference
CF_4	200 V	200	3.8×10^{10} cm^{-3}	~ 120	SF-CCP PIC/MC	[Georgieva 03b]
Ar/CF_4 (0.9/0.1)	200 V	200	2.1×10^{10} cm^{-3}	~ 10	SF-CCP PIC/MC	[Georgieva 03b]
Ar/CF_4 (0.5/0.5)	200 V	200	3.25×10^{10} cm^{-3}	~ 65	SF-CCP PIC/MC	[Georgieva 03b]
$Ar/CF_4/N_2$ (8/1/1)	700 V	30	1.7×10^{10} cm^{-3}	~ 11	SF-CCP PIC/MC	[Georgieva 03a]
$Ar/CF_4/N_2$ (8/1/1)	350+350 V	30	1.3×10^{10} cm^{-3}	~ 6.5	DF-CCP PIC/MC	[Georgieva 03a]
c-C_4F_8	200 W	25	2.1×10^{11} cm^{-3}	~ 3	ICP Exp	[Hebner 01]
CF_4	20 W	250	1.3×10^{10} cm^{-3}	~ 7	SF-CCP Exp	[Haverlag 91]
C_3F_8	20 W	115	3×10^{10} cm^{-3}	~ 32	SF-CCP Exp	[Haverlag 91]
Ar/c-C_4F_8 (0.9/0.1)	300 W	25	2.5×10^{11} cm^{-3}	~ 2	ICP Exp	[Kono 00a]
c-C_4F_8	10 W	100	2×10^{11} cm^{-3}	~ 100	SF-CCP Exp	[Kono 00b]
Ar/CF_4 (0.98/0.02)	250 mA	50	2×10^{9} cm^{-3}	3.6	SF-CCP Exp	[Kaga 01]
Ar/CF_4 (0.95/0.05)			1.9×10^{9} cm^{-3}	6.1	SF-CCP Exp	
Ar/CF_4 (0.93/0.07)			2×10^{9} cm^{-3}	6.8	SF-CCP Exp	
Ar/CF_4 (0.9/0.1)			2.2×10^{9} cm^{-3}	7.9	SF-CCP Exp	

Table 1.3: Calculated and measured maximum negative ion densities and fractions in various CF_4 and c-C_4F_8 containing plasmas.

1×10^{10} cm^{-3}. Figure 1.21 (a) is a reproduction of the results obtained by Kono and co-workers in a c-C_4F_8 CCP plasma. At 100 W and 100 mTorr they obtained negative ion densities of about 2×10^{11} cm^{-3}, amounting to 100 times that of the electron density. Figure 1.21 (b) is a summary of results obtained by Kono and co-workers in various electronegative ICP discharges. What this shows is that under similar conditions, c-C_4F_8 is capable of producing higher negative ion densities than other gas mixtures, in particular the very electronegative SF_6 gas. When the electron density is taken into account, however, SF_6 remains the most electronegative gas as can be seen in figure 1.22. This figure compares the electronegativities of various fluorine-containing plasmas as a function of the electron density to gas density ratio, n_e/n_g. The solid curves indicate the dependence of α on n_e/n_g expected for various values of K_{att}/K_{rec} and are obtained when assuming $K_{rec}n_in_n \gg K_{det}n_nn_x$. With this assumption, equation 1.38 reduces to the following simple expression at the steady state:

$$K_{att}n_en_g = K_{rec}n_in_n \tag{1.55}$$

such that when quasineutrality is substituted ($n_i = n_e + n_e$) we have the following relationship between the negative ion fraction and the other parameters [Kono 02]:

$$\frac{n_n}{n_e} = \left(\frac{K_{att}/K_{rec}}{n_e/n_g} + \frac{1}{4}\right)^{1/2} - \frac{1}{2} \tag{1.56}$$

1.5.4 Measurement of negative ion densities

This section briefly describes the different methods which have been developed to date for measuring negative ion densities, and to a lesser extent the negative ion temperature. It is useful to summarise the various techniques so that a comparison can be made with those

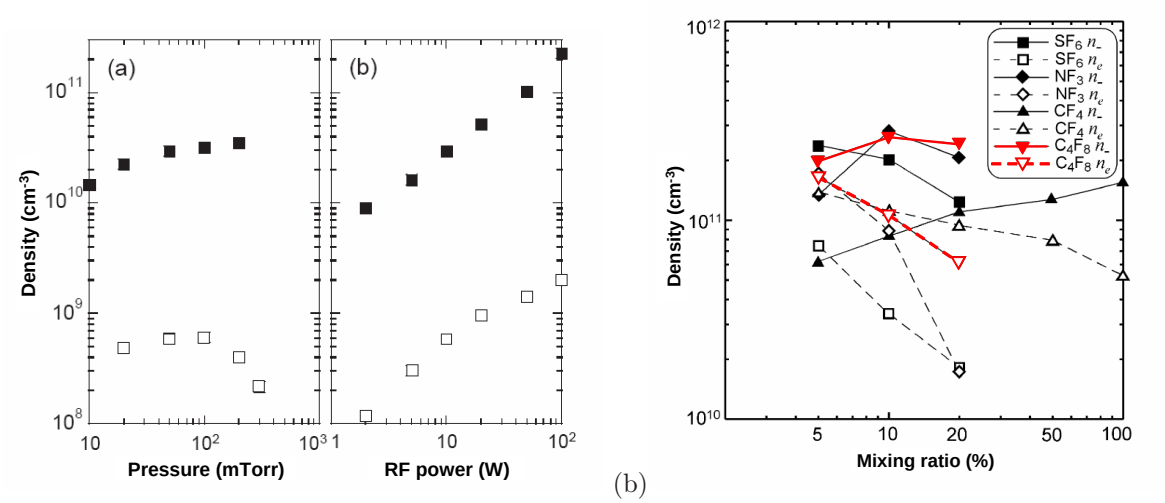


Figure 1.21: Negative ion and electron densities (a) in c-C_4F_8 CCP plasma as a function gas pressure and power [Kono 00b] (b) in various ICP gas mixtures with argon at a total pressure of 25 mTorr and 300 W power [Kono 02].

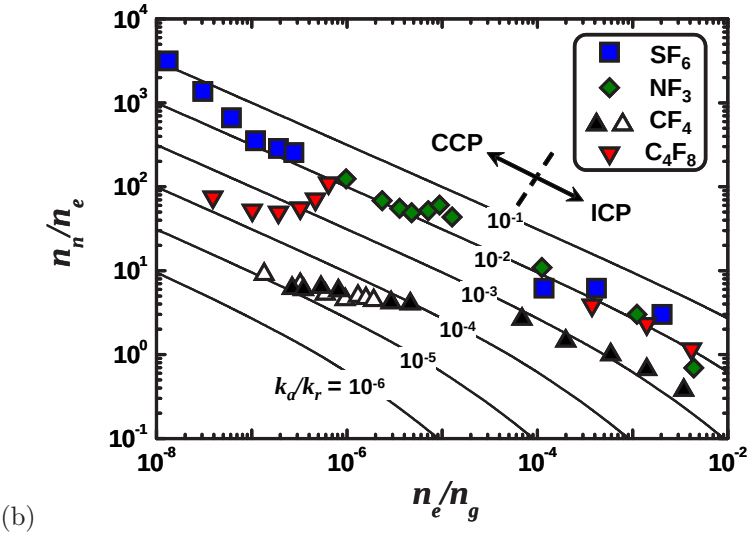


Figure 1.22: Negative ion fractions as a function of electron to molecular gas ratio for plasmas of various gases in ICP and CCP plasmas [Kono 02]. The solid lines are obtained from equation 1.56. Note that c-C_4F_8 does not strictly follow these lines in the CCP case, indicating that collision-induced detachment may not be negligible.

used in this study. Several important review articles were published at the beginning of the 1990's, the first by Hiroshi Amemiya [Amemiya 90] who reviewed probe measurements of negative ions, the second by Martha Bacal[Bacal 93] was a general review of plasma diagnostics in negative ion sources, and the third, again by Bacal[Bacal 00], reviewed the various photodetacment techniques. Much of what follows is explained in detail in those three papers.

Langmuir probes

(For more information on Langmuir probes see section 2.2.1)

Langmuir probes allow for localised current and density measurements with a relatively simple experimental setup. However, their sensitivity to fluctuations resulting from RF electric fields, particularly with respect to the plasma potential, requires a more complicated experimental approach and subsequent analysis. We decided against using Langmuir probes as the highly symmetric nature and large RF voltages, particularly with the 2 MHz source ($\sim>$ 200 V), in our experimental setup makes their use impractical. The aim of adapting Langmuir probe theory to electronegative plasmas is almost as old as Langmuir probe theory itself [Spencer-Smith 35a]. Some of the more recent work has been based on the analytical results of Braithwaite & Allen on the current characteristics to a spherical Langmuir probe[Braithwaite 88]. The basic principle of this theory is that the negative ion fraction, α, can be related to the ratio of the saturation current at the plasma potential,I_p, to the positive ion saturation current, I_i. Without going into the details, the analytical result showing this relationship is as follows:

$$\frac{I_p}{I_i} = \frac{\sqrt{\frac{M_i}{2\pi m_e}} + \alpha_0\sqrt{\frac{M_i}{2\pi\gamma M_n}} - \left(1 + \alpha_0\sqrt{\frac{1}{2\pi\gamma_i}}\right)}{\sqrt{2\eta_s}\left[\exp(-\eta_s) + \alpha_0\exp(-\alpha\eta_s)\right]} \tag{1.57}$$

where $\gamma_i = T_e/T_i$ and $\eta_s = \eta_s(\alpha_0, \gamma)$ is the normalised potential at plasma-sheath boundary. It is clear that to exploit this equation that we must know or estimate values for M_i, M_n and γ. In complex industrial gas mixtures this is not always possible as there are multiple positive ion species and negative ion species. The temperature ratio is all the more difficult to estimate as it is not possible to measure T_n directly. Nonetheless, several studies into the negative ion fraction using this method have been undertaken[Amemiya 90, Nikitin 96]. Nikitin et al. compared the results from the more reliable photodetachment technique to results obtained with the probe method[Nikitin 96]. This was undertaken in a hydrogen plasma and so to a good approximation the positive and negative ions were H_3^+ and H^-. By adjusting the value of γ to match the photodetachment results it was possible to estimate the negative ion temperature. They used values of 2 - 5 for γ. Overall they found good agreement between the probe technique and the photodetachment measurements.

Two probe technique

A variation of the Langmuir probe technique is the electrostatic two-probe method in conjuntion with electronegative plasma fluid models, first proposed by Chabert and co-workers[Chabert 99b, Chabert 99a]. A cylindrical Langmuir probe, to minimise the perturbations, is used to measure the electron current at the plasma potential. The authors assume that at this potential the contribution of the positive and negative ions is negligeable for $\alpha < 100$. A second, planar Langmuir probe with guard ring is used to measure the positive ion current and so sheath effects can be neglected. The ratio of the electron current to ion current can then be related to the normalised positive ion flux, $\Gamma_{is}/n_{e0}c_s$, which in turn can be related to a certain negative ion fraction via the results obtained from a fluid model[Sheridan 99b]. Up until recently this technique had only being employed in the collisionless regime. This two-probe technique is employed in this thesis and applied to the intermediate pressure (modestly collisional) regime [Curley 07]. The ion current is measured by means of an RF biased planar probe, whereas the electron density is measured directly using a microwave resonator probe.

Negative ion sensitive probe

An electrostatic probe designed specfically for obtaining negative ion density and temperature was developped by Amemiya [Amemiya 88, Amemiya 90]. The probe face consists of a flat surface with a small orifice, somewhat similar to that of an ion energy analyser. The probe surface is separated from a collector surface by a distance, d. A magnetic field is created parallel to the probe/collector surfaces and perpendicular to the orifice length. A positively biased retarding grid is placed somewhere in the system to repel the positive ions. Due to the large electron mass to negative ion mass ratio, m_e/M_n, the electrons are almost all deflected away by the magnetic field whereas the negative ions are collected. The negative ion density and temperature can be inferred from the current and voltage characteristics of the collector. A schematic representation of this probe is reproduced in figure 1.23. To my knowledge, no other use of this probe has been reported.

This probe, however, is not suitable for our experimental reactor. The positive bias required to repel the positive ions would need to be at least as large as the RF sheath at the electrode, possibly several 100's of volts. This perturbation, and also the small dimensions (2.5 cm gap) of our system, makes it undesirable to use such a probe.

Ion acoustic waves

Ion acoustic waves (IAW) travel in two modes in electronegative plasmas – a slow mode and a fast mode. The slow mode is heavily damped when negative ions become numerous, whereas the phase velocity of the fast mode is an increasing function of the negative ion

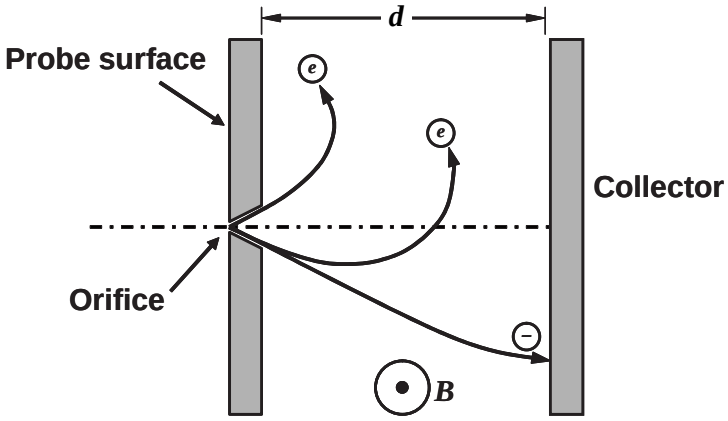


Figure 1.23: Schematic representation of the negative ion sensitive probe proposed by Amemiya [Amemiya 88].

fraction and is only weakly damped[D'Angelo 66]. St-Onge et al. used measurements of the ion acoustic phase velocity, v_ϕ, to estimate the negative ion fraction[St-Onge 00]. The relationship between v_ϕ and α is as follows:

$$v_\phi^{'} = v_\phi \pm v_{dr} \tag{1.58}$$

$$= c_s \sqrt{\frac{1}{1+k^2\lambda_D^2}\frac{1+\alpha M_n/M_i}{1-\alpha} + 3\gamma_i} \pm v_{dr} \tag{1.59}$$

where k is the wavenumber and v_{dr} is the ion drift velocity should any exist. The assumptions used to obtain this equation are that $\gamma_i \gg 1$ and that $M_n/M_i \sim 1$.

St-Onge and co-workers compared their results to those obtained using laser-induced photodetachment (LIPD) and found reasonable agreement between the two. The IAW results were systematically lower than those of the LIPD, particularly at pressures below 2 mTorr (total pressure range used: 0.25 – 5 mTorr). They attributed the discrepancies to possible errors in the estimation of the ionic masses. The technique had a spatial resolution of about 1 cm, corresponding roughly to the separation between the plane antennae used to excite and detect the acoustic waves.

This technique, however, only works for large electronegativities ($\alpha > 10$) and so would be unsuitable for our experiments where we would wish to examine transitions from electropositive mixtures to electronegative ones. The restrictive geometry of our DF-CCP chamber would also be a limiting factor.

Laser-induced photodetachment

Laser-induced photodetachment (LIPD) is by far the most widely used and trusted negative ion detection technique. As its name suggests, it involves photodetaching negative ions by a laser, i.e. photons of sufficient energy are used to excite the extra electron free

Anion	Threshold (eV)	Threshold (nm)
F	3.40	364.5
Cl	3.61	343.1
O	1.48	837.3
O_2	0.44	2817.8
O_3	2.10	590.4
C_4F_8	0.63	1968.8
H	0.76	1631.4
CF_3	2.01	616.8

Table 1.4: Electron affinities (photodetachment thresholds) for some common negative ion species.

from the ion, leaving behind a neutral atom or molecule:

$$X^- + h\nu \longrightarrow X + e$$

The resulting localised increase in the neutral and electron density can then be measured to estimate the negative ion density. Efforts have almost entirely concentrated on measuring the free electrons and apparently measurements of the neutrals have also been undertaken[Bacal 93, Bacal 00], but I have not studied that work. As the neutrals would be in their ground state, detecting them would require vacuum UV absorption or possible laser induced fluorescence (LIF). Various methods of detecting the increase in electron density have been proposed, namely, but not limited to:

1. variation of the saturation current of a positively biased Langmuir probe [Nikitin 96, St-Onge 00]
2. variation of the standing wave pattern in a microwave interferometer [Hebner 00, Kono 00a, Rauf 02]
3. variation of a microwave cavity resonance frequency [Haverlag 91, Hebner 01, Jauberteau 89, Kono 00b]
4. variation of the phase of the applied voltage (optogalvanic detection) [Gottscho 86]
5. variation of the discharge current [Belostotsky 05]

Some of the more commonly detected negative ions and their photodetachment thresholds are outlined in table 1.4.

The use of LIPD in our DF-CCP reactor would not be simple. As explained earlier, RF fluctuations make using Langmuir probes impractible. Microwave techniques are often geometry dependent and would not lend themselves easily to our small gap configuration. Other methods of detecting the photodetached electrons are only suitable to high values of α. It could be possible, however, to use the microwave cavity resonator (hairpin probe) which we use in this study for measuring the electron density. This has already been accomplished by others (see [Hebner 01]) and would be a possible candidate for use in our system.

Absorption

(For more information on absorption spectroscopy see section 2.3.1)
Instead of detecting the electrons or neutrals resulting from the photodetachment of a negative ion, one can also measure, through absorption spectroscopy, the loss of photons. This was first proposed by Quandt and co-workers on measurements of the negative hydrogen ion[Quandt 98a]. A He-Ne laser source was injected into a multipass Herriott cell used to lengthen the absorption path, allowing densities as low as 1×10^9 cm^{-3} to be measured. The results were compared to probe-based photodetachment experiments and were shown to be in good agreement. Negative ion detection by absorption has the advantage of being a non-perturbative direct measurement of the negative ion density. Very few assumptions, e.g. no sheath effects, are necessary to relate the absorption signal to n_n. The greatest sources of error are those caused by the uncertainty of the photodetachment cross section and the experimental noise (e.g. unstable light source). Unsucessful efforts were made to try to apply this techinque to UV broadband absorption spectroscopy of the negative fluorine ion[Curley 04a]. Absorption spectroscopy, however, does not allow space resolved measurements but only line integrated densities.

Quandt and co-workers extended the technique to the high sensitivity absorption technique known as *cavity ring-down spectroscopy* (CRDS)[Quandt 98b], again measuring the density of H^-. This was followed by the work of Grangeon et al. with measurements of H^- and O^- in a large area rf discharge[Grangeon 99]. This thesis shows the first application of CRDS to the measurement of the negative fluorine ion[Booth 06, Curley 07].

Mass Spectra

Mass spectroscopy can give important information on the negative ion species present in the plasma. This information is extremely valuable for numerical modelling and for interpreting experimental data. Mass spectra of negative ions in SF_6[Nagaseki 95, Sasaki 97], O_2[Lin 93, Stoffels 98] and CF_4[Lin 93, Stoffels 98, Ura 96] plasmas are some examples. As with the probe invented by Amemiya, the positive bias required to repel the positive ions and also the small dimensions (2.5 cm gap) of our system, would make the resulting perturbations undesirable in our plasma.

Negative ion temperature measurement

One of the most elusive plasma parameters is the negative ion temperature. To date, there is no consensus on how one should measure T_n and as such its magnitude in most plasmas remains an unknown. Some of the possible techniques have already been mentioned in this section and these will be summarised here along with other possble methods.

Matching experiments

The steps involved in this method involve measuring the negative ion densities with two experimental techniques where one is dependent and the other independent of T_n or γ. An example of dependent methods would be the Langmuir probe or two-probe technique. An example of an independent method would be a probe based photodetachment measurement. By adjusting T_n or γ in the dependent method so that the results match those of the independent method, one can obtain an estimation for the negative ion temperature. Of course, a reliable measurement of T_e is usually required. This technique is used in this thesis to estimate the negative ion temperature, where CRDS and hairpin probe measurements are compared with the two-probe technique.

Time-resolved photodetachment

Time-resolved photodetachment was first proposed as a negative ion temperature diagnostic by Bacal et al. [Bacal 91, Bacal 93]. This technique implies:

1. The creation of a controlled perturbation in the negative ion density, such as destruction by an initial photodetachment, followed by
2. the measurement of the recovery of the negative ion density towards its initial value and
3. fitting the measured results to a model of the density recovery process.

Negative ion sensitive probe

As mentioned in 1.5.4, the current and voltage characteristics of a negative ion sensitive probe can be used to obtain information on the negative ion temperature, in much the same way as Langmuir probes are used to measure T_e.

Chapter 2

Experimental setup and diagnostic techniques

Contents

2.1 The dual-frequency plasma chamber 49
2.1.1 The plasma chamber 50
2.1.2 The vacuum/pumping system 51
2.1.3 The rf power generators 53
2.1.4 The electrostatic clamping (chuck) unit 54
2.1.5 Cooling 56
2.2 Electrical diagnostics 56
2.2.1 The ion flux probe 56
2.2.2 The microwave resonator probe - "*Hairpin probe*" 67
2.2.3 Calculation of the hairpin sheath size 77
2.2.4 The Floating Hairpin 79
2.2.5 Design and construction of the hairpin probe 80
2.2.6 Operation of the hairpin probe 82
2.2.7 Comparison between two hairpin probe designs 84
2.3 Cavity Ring-Down Spectroscopy 87
2.3.1 Principle of absorption spectroscopy 87
2.3.2 Absorption of the negative fluorine ion 90
2.3.3 Cavity ring-down spectroscopy 92

2.1 The dual-frequency plasma chamber

The plama chamber under study is a modified dielectric etch tool donated to the LPTP by Lam Research Corporation[1]. It was a part of the *Lam Exelan* product range and designed for 130 nm (0.13 μm) gate etch in SiO_2 dielectric layers on 200 mm wafers. An

[1] http://www.lamrc.com

industrial plasma etch chamber, such as the Exelan, is never sold as an individual item but rather as part of an overall etch solution or package. Within this package, the main product is known simply as *the etch tool*. A tool comprises:

1. **Wafer loading station** where factory automated robots can place pods of 25 wafers, known as FOUPs.
2. **Wafer transfer station**: a series of robotic arms and air/vacuum chambers used for (i) taking the wafers from the FOUPs, (ii) aligning the wafers, (iii) transferring the wafers to the etch chambers.
3. A **cluster** of about four plasma etch chambers (e.g. an Exelan). Depending on the requirements of the customer, these chambers could be of the same type or a mix of several diffent types such as TCP, ICP and CCP. Each plasma chamber is run by its own computer and if needed (in troubleshooting cases for example) can be run independently of the tool.
4. **A user interface (UI)**, i.e. the main computer of the tool. Every element on the tool can be accessed and controlled by this interface. The UI's most important function is to allow for complete interaction between all elements on the tool, ensuring that the tool runs as smoothly and as efficiently as possible

The other components of the package sold to the customer usually include delivery and installation of the tool, customer staff training on the tool, maintenance (sometimes lifetime) of the tool. As one can imagine the cost of such a high-tech product is very high, often over a million dollars in value.

For our part, we only acquired the Exelan etch chamber, the RF power supply and the electrode cooling system. At a later stage we also acquired the electrostatic chuck mechanism.

2.1.1 The plasma chamber

The LPTP Exelan (see figure 2.1) is a capacitively-coupled, parallel plate chamber powered by two RF frequency power generators. The outer chamber structure is a square (37 cm side) anodised block of aluminium, hollowed out to form a 33 cm diameter cylindrical cavity. The entire upper surface is removable, forming a lid to access the chamber interior. A 250 mm silicon (Si) electrode is integrated into the upper grounded chamber lid. The process gases are supplied through this electrode by means of a shower head configuration. This electrode is surrounded by a 250 mm inner diameter, 300 mm outer diameter quartz insulating ring which forms part of the confinement structure described later. In an industrial context, this lid would only be opened for maintenance purposes as the wafers would normally be inserted through a small opening in the side wall. The

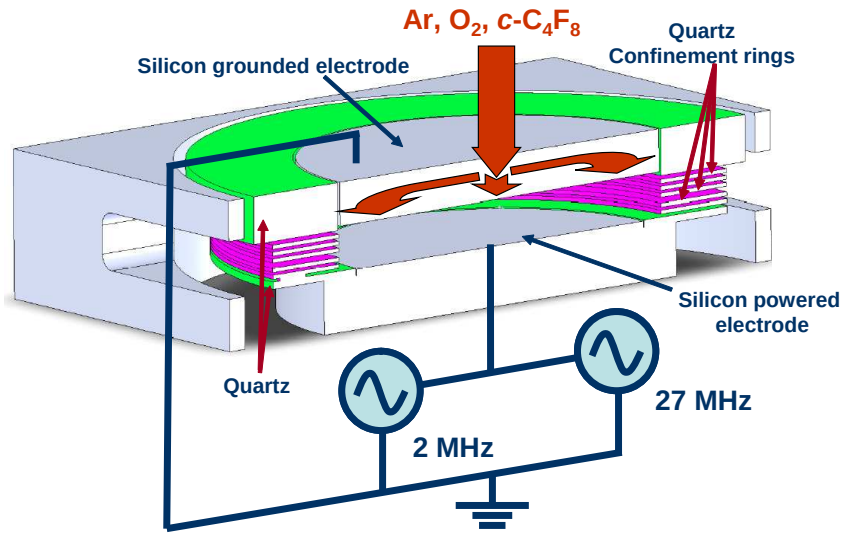


Figure 2.1: 3-D representation of the dual frequency dielectric etch chamber at the LPTP

aluminium chamber block is almost completely bottomless apart from a support structure for the lower electrode. Here, a 250 mm powered electrode is placed into position. The lower silicon electrode has a 25 mm wide step (1 mm down) on its outer edge where a silicon *edge ring* is positioned. The raised central area is where the 200 mm wafer is placed. A 25 mm gap separates both electrodes. Finally, the structure is made airtight underneath by a pumping chamber attached to a turbomolecular pump.

In the standard industrial design of this chamber, the plasma is confined by means of moveable (in a vertical direction) quartz rings. The rings create a physical barrier to the plasma, but also create a gradient in gas pressure that helps prevent a plasma from striking outside the rings. The movement of the rings is used to regulate the gas pressure with a fine precision. In our system, five fixed quartz rings, internal diameter 224 mm, outer diameter 315 mm, 2 mm thick and seperated by gaps of about 1.6 mm make up the plasma confinement structure. This form of plasma confinement is unique to our chamber and allows for improved optical access, while at the same time reducing the need for moving parts and accessories. However, as the rings are fixed they cannot be used for pressure control, as is the case in the industrial standard design.

2.1.2 The vacuum/pumping system

Figure 2.2 shows the vacuum/pumping scheme used. The primary pump, a BOC Edwards QDP40 dry pump, keeps the back end of the molecular pump at a pressure in the range to 1 – 10 mTorr (about 0.1 – 1 Pa, 10^{-6} – 10^{-5} atm). The molecular drag pump is an *Osaka Vaccum Ltd. TS443BW* helical grooved pump, operated by an Osaka TC440-C pump controller/PSU. The lowest pressures obtained in our chamber are $\approx 5 \times 10^{-7}$ Torr. The molecular drag pump is quite robust as it does not use fragile rotary blades as in

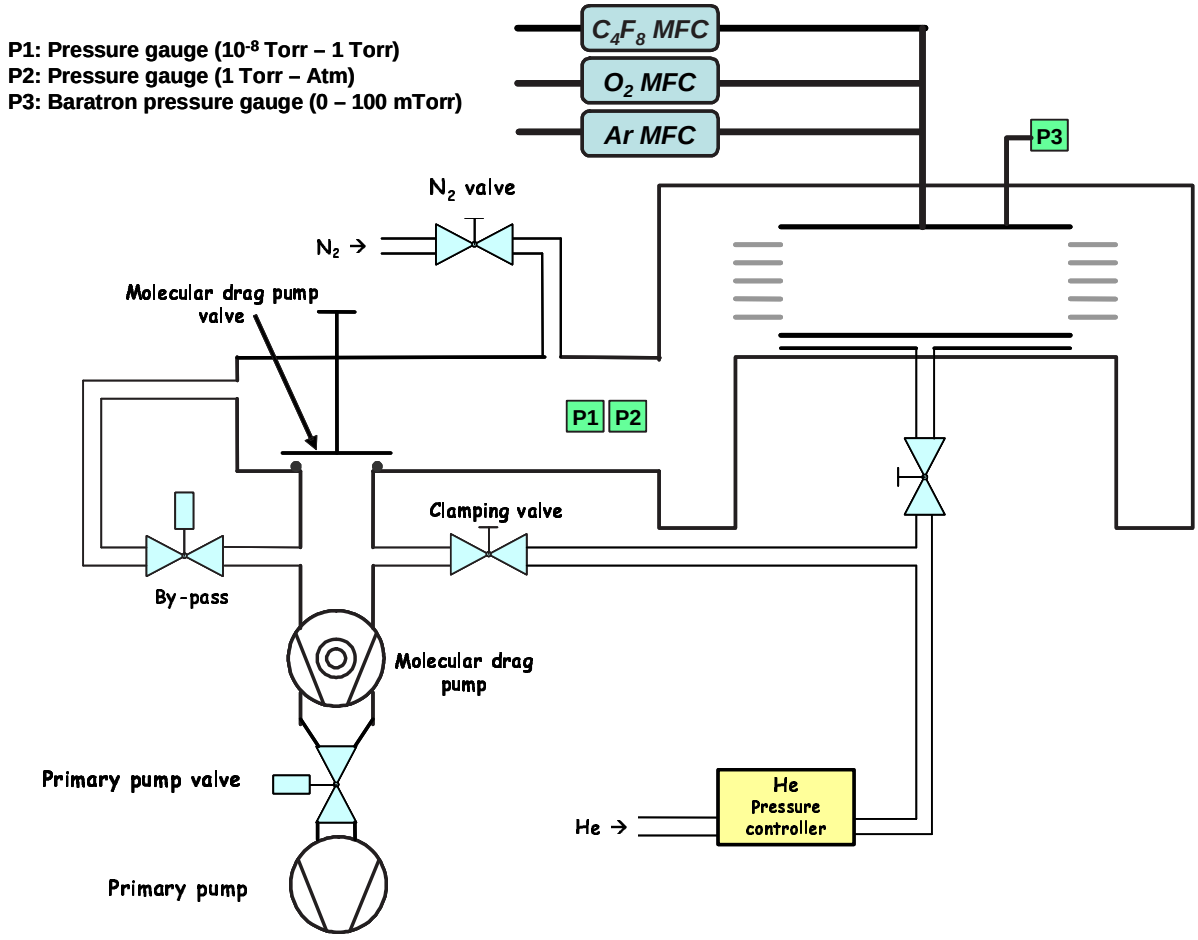


Figure 2.2: Pumping scheme of the LPTP dual-frequency capacitively coupled (Lam Exelan) chamber

turbomolecular pumps.

The chamber pressure is controlled manually by adjusting the total gas flow through the MFCs. There are two pressure gauges installed between the chamber and the molecular drag pump: one for high pressure (1 Torr – 1 atm) and one for low pressure (10^{-8} – 1 Torr. A 100 mTorr *Baratron* pressure gauge is used for the wafer area pressure (WAP), i.e. the pressure within the confinement rings.

A pressure gradient forms between the volumes inside and outside of the confinement rings. This pressure gradient is part of the confinement process as the plasma strikes more easily at high pressure than at at low pressure for a given voltage. The relationship between the breakdown voltage and the gas pressure, or more correctly the pressure-length product, *pd*, is commonly known as a *Paschen* curve. In the 1 – 100 mTorr region, for a 2.5 cm electrode separation, the breakdown voltage in argon varies by the about the same order of magnitude, i.e. 100. Empirically, it is preferable that the pressure ratio across the rings is greater than a factor of 10 to ensure that breakdown does not occur outside the confinement rings.

2.1.3 The rf power generators

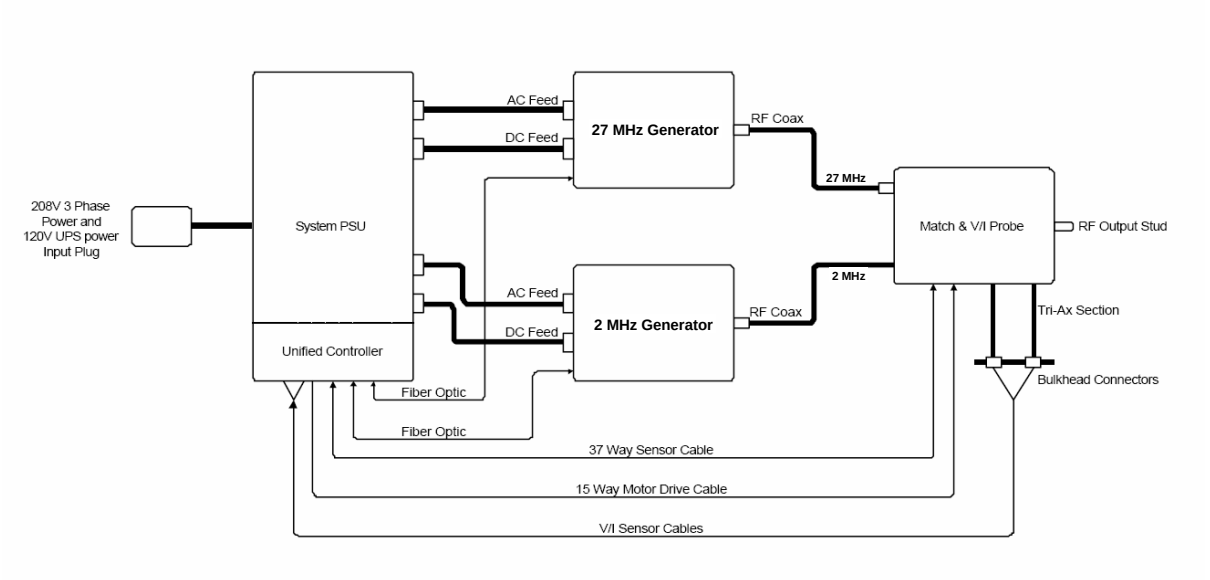


Figure 2.3: OneBox® block diagram

The two RF power generators (2 MHz and 27 MHz) are housed inside a Lam designed, MKS constructed, power delivery unit known as the *OneBox*®. An overall block diagram is shown in figure 2.3. The OneBox is comprised of the following components:

- Unified Controller: an onboard computer circuit board.
- Power supply unit (PSU): supplies DC power to certain Exelan chamber components,

e.g. the electrostatic chucking mechanism

- 27.12 MHz generator: 1.8 kW maximum power
- 2 MHz generator: 2.5 kW maximum power; frequency tunable from 1.8 MHz to 2.17 MHz.
- RF matching unit known as *Dual MATCHWORK*®: an air-cooled, automatic impedance matching network. It uses low-loss "L" configurations consisting of two vacuum-variable capacitors and a fixed inductor for the 27.12 MHz match, and RF relay-switched capacitors and a fixed inductor for the 2 MHz match. The unit is capable of handling 2500 W continuous RF power, simultaneous in each channel.
- Voltage and current probe, integrated into the matching network.

Each generator in the OneBox is cooled by water from the mains supply. The cooling is controlled automatically by means of thermostatically controlled solenoid water valves.

The OneBox is controlled by text (ASCII) commands sent from a PC, via an RS232 serial cable and fibre optic cable, to the Unified Controller. All commands are composed of three-letter words, followed by numbers, where applicable, and terminated by a carriage return. For example, to set generator 1 (2 MHz) to 500 W, the command used would be: `OEM1=500<cr>`, where `<cr>` indicates a carriage return. For the first two years of this project the software used to interface with the OneBox was a terminal program designed by the OneBox constructors, MKS, for debug purposes. As such, it was very restricting for use as an everyday tool. During the CRDS experiments, LabVIEW® was used to automate the acquisition process and some basic interaction with the OneBox was included. In the last year of this project, a more complete stand-alone LabVIEW interface to the OneBox was developped. A screenshot can be seen in figure 2.4.

2.1.4 The electrostatic clamping (chuck) unit

An electrostatic chuck (ESC) was added to the lower electrode assembly. The major system components include an ESC power supply, an RF filter board, a ceramic ESC and a helium pressure controller together with a computer acquisition (DAQ) card for the PC interface. The clamping force employed by this system is purely bipolar, as indicated schematically in figure 2.5. The ESC is capable of supplying between 0 V and 2000 V for chucking purposes. Helium gas is supplied through the ESC to the back of the wafer to ensure good thermal conduct between both. Typical chucking voltages are of the order of 800 V, whereas helium back pressures are about 7 torr supplied by around 1 or 2 sccm of flow.

The advantage of installing an ESC is the better control achieved over the substrate's temperature. This allows for greater repeatability of experimental results, as well as reducing temperature gradients within the plasma environment.

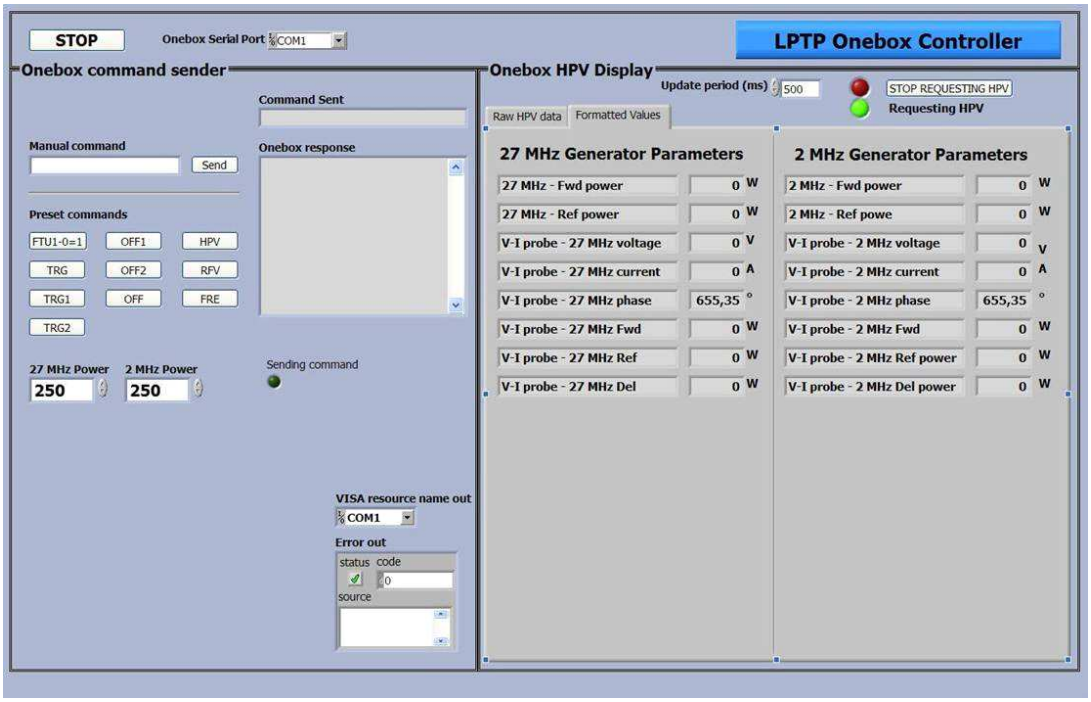


Figure 2.4: Screenshot of OneBox controller software at the LPTP.

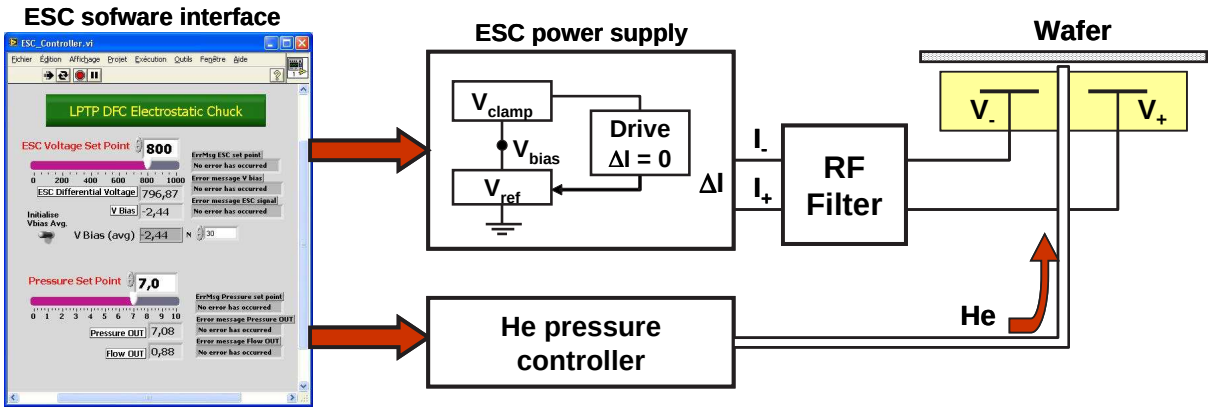


Figure 2.5: Schematic representation of the electrostatic chuck setup on the LPTP Exelan, showing a screenshot of the PC interface developed in-house.

2.1.5 Cooling

The lower powered electrode and ES chuck are kept at a constant temperature by means of a BOC Edwards TCU 40/80 temperature control unit. This unit supplies a perfluorinert cooling fluid in a closed loop. It works in a temperature range of -40 °C to +80 °C in 0.1 °C increments. The coolant temperature can be controlled to within ±1.0 °C of the set point. For all our experiments we set the TCU to operate at +20 °C. It is however, very noisy and not very pleasant to have beside the experiment.

In our set-up, the upper grounded electrode is cooled by water from the mains supply, and so its temperature may vary depending on the season. It is estimated to be between 5 °C in the winter and 15 °C in the summer.

2.2 Electrical diagnostics

Two forms of electrical diagnostics were implemented to characterise the properties of the plasma: A probe coplanar with the upper grounded electrode for measurements of ion currents to same electrode; a probe inserted into the plasma and designed to resonate at microwave frequencies to deduce the plasma density.

2.2.1 The ion flux probe

The ion flux probe is a deposition tolerant device allowing for a direct measurement of the ion current to a planar surface immersed in a plasma. Before explaining the operation of the ion flux probe, a brief introduction to the operation of *Langmuir probes* is required. A Langmuir probe can be defined as any conducting probe inserted into a plasma discharge and biased for the purpose of drawing either electron or ion current. It was first introduced by Irving Langmuir and analysed extensively by both Mott-Smith and Langmuir [[Mott-Smith 26]]. The cylindrical Langmuir probe is by far the most commonly used and in its basic form consists of a short length (≈ 1 cm) of a small diameter (≈ 0.01 cm) wire inserted into the plasma and then biased over a range of voltages, e.g. −30 V to +30 V with respect to the probe floating potential. A measurement of the total net current flowing from the plasma to the probe is put in place and a current against voltage graph is then traced. An example of what such a curve might look like is shown in figure 2.6. The figure is a schematic representation only with the ion saturation current exaggerated so that it is more visible.

The convention is such that, when tracing Langmuir probe I–V curves, current flowing into the plasma is taken as being positive and so positive current implies net electron current being drawn from the plasma. The origin, O, corresponds to $V = 0$ and $I = 0$. The floating potential, V_f, is defined as the potential where $I_e = I_i$ and corresponds

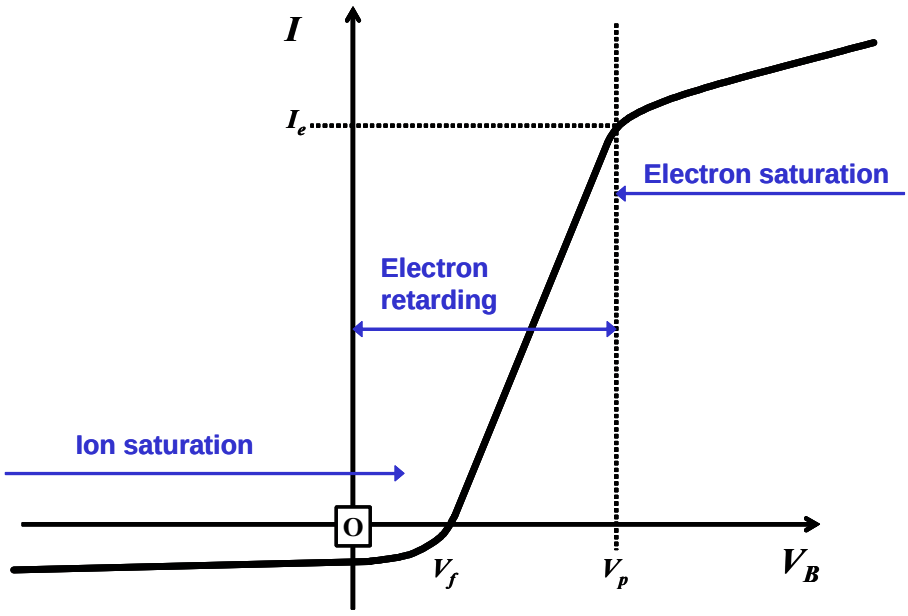


Figure 2.6: Example of a characteristic I – V curve obtained from a Langmuir probe

to $I = 0$ on the I–V curve. It is equivalent to the potential of an isolated (floating) surface immersed within the plasma. V_p designates the plasma potential, such that when $V = V_p$ no sheath is present around the probe and so the electron and ion currents are purely thermal. The probe current at V_p is considered to be electron dominated since the electron thermal velocity is much greater than the ion thermal velocity:

$$I\left(V_p\right) \cong I_e\left(V_p\right) = I_e\left(sat\right) \tag{2.1}$$

The term $I_e\left(sat\right)$ is used to denote the beginning of the electron current saturation region. Beyond V_p the increase in current is primarily due to the increase in the current collection area as an electron sheath forms.

For bias voltages less than V_p the positive ion sheath repels electrons of an energy less than $kT_e/e - (V_p - V)$ and so the probe current becomes progessively dominated by positive ions as the bias voltage becomes more negative with respect to the plasma potential. The ion current saturation, as with the electron current saturation, is not flat and increases as the positive ion sheath expands, creating a larger collection area.

To summarise, a Langmuir I–V curve can be roughly separated into three regions:

$$V < V_f \quad \Rightarrow \quad I_e < I_i \Rightarrow \lim_{V \to -\infty} I_e = 0 \tag{2.2}$$

$$V_f \leq V \leq V_p \quad \Rightarrow \quad I_i \leq I_e \leq I_e(sat) \tag{2.3}$$

$$V > V_p \quad \Rightarrow \quad I_e > I_e(sat) \gg I_i \tag{2.4}$$

Another form of Langmuir probe is a planar probe. This involves biasing a flat, often circular, conductor in contact with the plasma. Common diameters for such probes

range from 5 to 15 mm. The principal advantage of using a planar probe is that one can assume the sheath area, A_s, and therefore the collection area, to be equal to the probe area, regardless of bias voltage. To eliminate eventual edge effects, planar probes are often surrounded by a *guard-ring* biased to the same potential as the central probe. However, planar probes are only used in the region $V < V_f$ as their large collection area makes them unworkable in the electron current region due to the excessive current they would draw, which may be difficult for a measurement circuit to sustain (heat-loading), as well as creating large perturbations of the plasma.

The *ion flux probe* was originally developed and patented by Braithwaite and Booth [Braithwaite 96] (US patent: 5,936,413) as a deposition tolerant technique for measuring the ion current in a plasma. It is a planar probe placed in contact with the plasma, the basic circuit of which is shown in figure 2.7. The probe is not biased by a DC source, but rather works in a self-biasing mode. This is accomplished by applying a series of RF bursts to the probe across a series capacitor, C_p . The RF frequency chosen is not particularly important, but the on-time and off-time of the RF burst may need to be adjusted for various plasma conditions. At any given moment, the potential, V, of the probe surface can be described by:

$$C\frac{dV}{dt} = (\Gamma_i + \Gamma_e)\, eA \tag{2.5}$$

Assuming that electrons are in thermal equilibrium with the potential, a Boltzmann factor can be used to describe the electron flux to the probe as follows:

$$\Gamma_e = \frac{1}{4} n_{e0} \bar{v}_e e^{(V-V_p)/T_e} \tag{2.6}$$

where V_p is the plasma potential and $\bar{v}_e$ is the average electron thermal velocity which is equal to $(8kT_e/\pi m_e)^{1/2}$. The positive ion flux to the probe is determined by a simple relation with the Bohm velocity, u_B:

$$\Gamma_i = n_{i0} h_l u_B \tag{2.7}$$

During the initial stages of the RF on-time the probe draws net electron current ($m_e \gg m_i$), which charges the capacitor C_p, and begins to bias to a negative potential. Assuming the RF burst is long enough, the probe saturates at a bias potential large enough to repel electrons such that $I_e = I_i$. Averaged over one or more RF cycles, this steady state bias potential, V_{bias}, is given by [Swift 70]

$$V_{bias} = V_f - \frac{kT_e}{e} \ln\left[J_0\left(\frac{eV_{rf}}{kT_e}\right)\right] \tag{2.8}$$

where V_f is the pre-rf burst floating potential, I_0 is the modified bessel function of zero

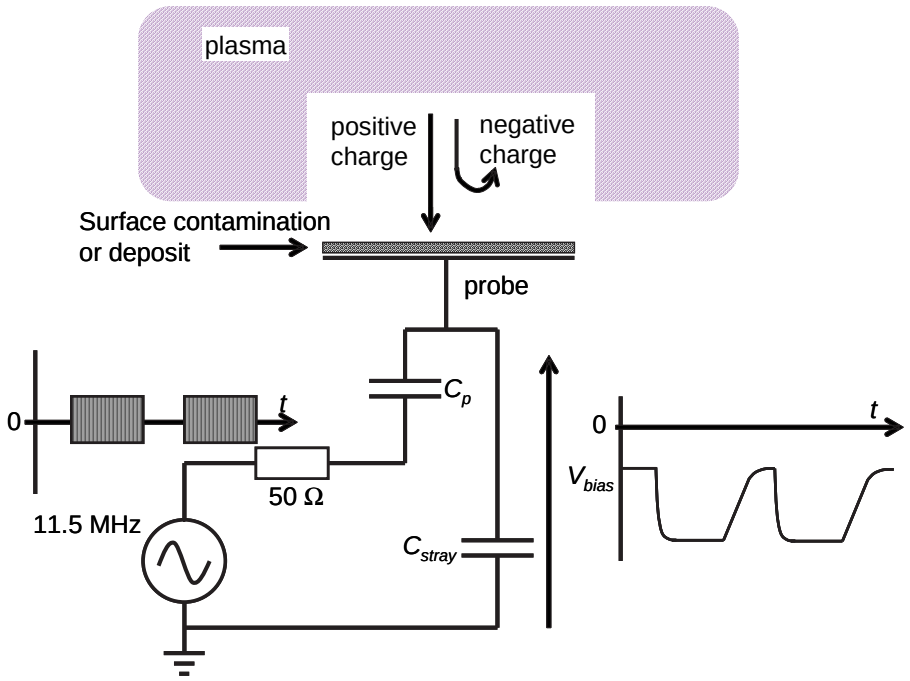


Figure 2.7: Basic experimental schematic of the ion flux probe (reproduction of figure 2 in ref [Braithwaite 96]).

order and V_{rf} is the amplitude of the rf voltage applied to the probe.

When the rf burst ends, the probe returns back to its pre-rf burst potential. Equation 2.5 is still valid for this return phase, but as $|V_{bias}| \gg T_e$ the flux of electrons is negligible and so equation 2.5 can be reduced to:

$$C \left.\frac{dV}{dt}\right|_{initial} = \Gamma_i e A \tag{2.9}$$

Therefore, the initial discharge rate of the probe is linear and is (i) proportional to the positive ion flux and (ii) is inversely proportional to the series capacitance. As the probe surface approaches the pre-rf burst potential, V_f, the electron flux gradually builds up until both the positive and negative flux are equal.

$$\Gamma_0 = n_{i0} h_l u_B = \frac{1}{4} n_{e0} \bar{v}_e e^{(V_f - V_p)/T_e} \tag{2.10}$$

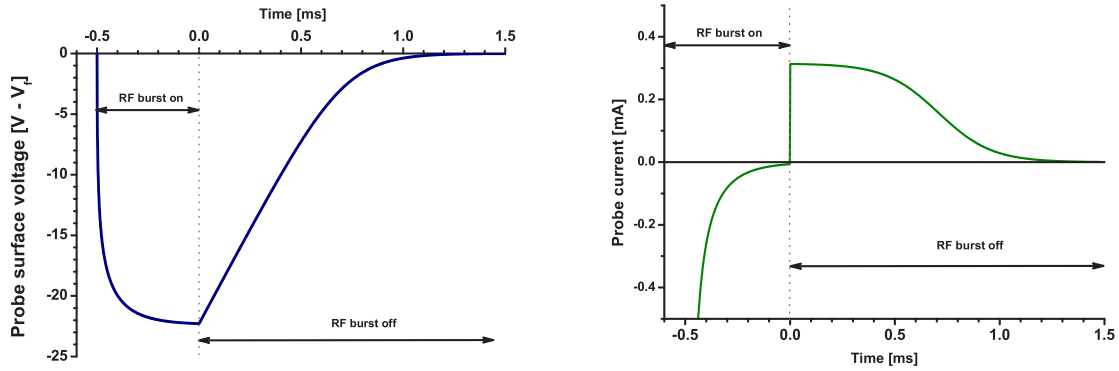
and the net current to the probe is:

$$I(V_f) = n_{i0} h_l u_B e A - \frac{1}{4} n_{e0} \bar{v}_e e A e^{(V_f - V_p)/T_e} = 0 \tag{2.11}$$

and therefore:

$$n_{i0} h_l u_B e A = \frac{1}{4} n_{e0} \bar{v}_e e A e^{(V_f - V_p)/T_e} = I_0 \tag{2.12}$$

where I_0 is defined as the value of the ion current and the electron current when $V = V_f$, which is also the value of the ion current for all values of V. We can now



a) b)

Figure 2.8: Calculations of a) the surface potential and b) the probe current during a burst of RF applied to 5 mm diameter probe using the analytical solutions found in [Braithwaite 03]. The burst begins at t = -0.5 ms and stops at $t = 0$. The following parameters were used: $C_p = 10$ nF, $T_e = 4$ eV, $\Gamma_i = 10^{16}$ ions cm^{-2} s^{-1}, $V_{RF} = 30$ V.

substitute I_0 into the equation for the net probe current for all values of V as follows:

$$\begin{aligned} I(V) &= n_0 h_l u_B e A - \frac{1}{4} n_0 \bar{v}_e e A e^{(V-V_p)/T_e} \\ &= n_0 h_l u_B e A - \frac{1}{4} n_0 \bar{v}_e e A e^{(V_f-V_p)/T_e} e^{(V-V_f)/T_e} \\ &= I_0 - I_0 e^{(V-V_f)/T_e} \\ &= I_0 \left(1 - e^{(V-V_f)/T_e}\right) \end{aligned} \tag{2.13}$$

Equation (2.13) will be used to describe the transient current, as a function of bias potential, through the series capacitor, C_p, as the probe returns to its pre-rf burst potential, V_f.

Figure 2.8 presents calculated $V(t)$ and $I(t)$ under ideal circumstances. The probe current is obtained by differentiating the voltage and multiplying by the value of the capacitance, C_p as shown in eq. (2.5). These calculations are possible based on the analytical results of Braithwaite *et al* [Braithwaite 03], where a detailed analysis of the transient RF self-bias of a planar electrode can be found. We are interested in the region just after the RF burst. $I(t)$ is plotted as a function of $V(t)$ so that we have a time independent I–V curve, equivalent to that which one would obtain using a Langmuir probe in the region described by equation (2.2). Figure 2.9 shows the I–V curve obtained using the data in figure 2.8. Note that the convention with ion flux probes is to represent the ion current as being positive.

The construction of the ion flux probe employed at the LPTP is shown in figure 2.10. It is a planar electrode 5 mm in diameter surrounded by a planar, 15 mm diameter, guard ring. Both the probe and guard ring are made from stainless steel. A 0.1 mm air/vacuum

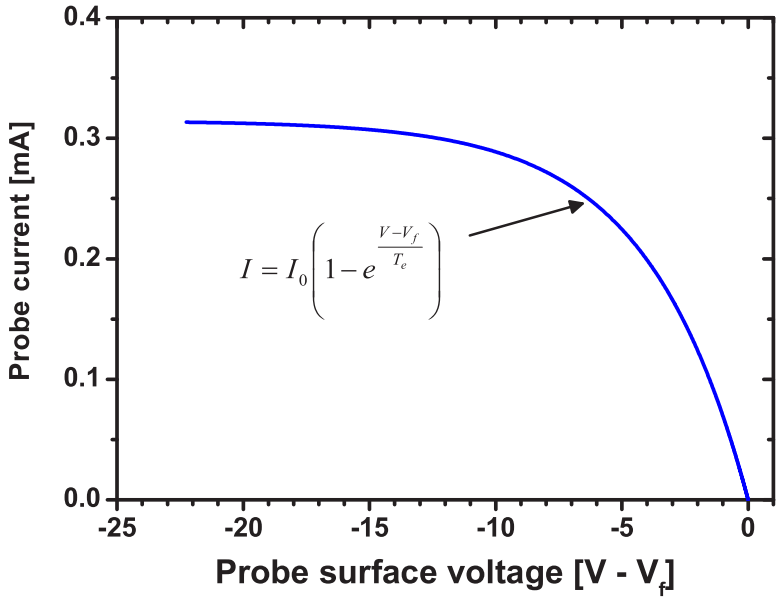
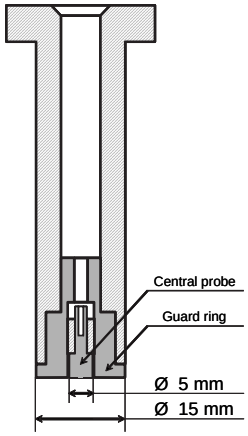


Figure 2.9: I–V curve of the simulated $V(t)$ and $I(t)$ data in figure 2.8. By definition, this curve can be fitted exactly using equation (2.13) as it is a simulation.

gap separates the two. The probe assembly is inserted through the top electrode and both the probe and guard ring surfaces are co-planar with one another and the upper, grounded electrode in the Exelan chamber. A 0.1 mm gap separates the guard ring from the upper electrode. The probe and guard ring are driven by a parallel output 11.5 MHz RF pulse modulated generator supplied by the Open University, which can supply 200 V peak-to-peak. A voltage and current measurement circuit was built in-house for use with the ion flux probe, the schematic of which is shown in figure 2.11. The principal components are a step-up transformer (doubles the RF voltage), the series capacitor to the probe (10 nF), a voltage measurement stage (x10 voltage divider) and a current measurement stage (voltage measurement across a 1 kΩ resistor). The current measurement is possible thanks to the transformer coupling, which allows for RF power transfer to the probe, while also allowing for discharging of the probe with current passing from ground and through the current measurement resistor. The measurement circuit incorporates low-pass RF filters as we are only interested in the "slow" transient phase after the RF-burst. Although the current could be obtained by differentiating the voltage data, a direct measurement is useful as it allows for real-time measurement of the current and simplifies the post analysis. Another advantage is the better S/N ratio obtained.

The guard ring is coupled to the RF generator by means of a variable capacitor such that for a given ion current the discharge rate of both the probe and guard ring are

identical. As the guard ring has a surface area 8 times that of the probe, its capacitor is about 8 times the value of the probe's. The guard ring is supplied by a second, parallel output, from the RF generator. Unlike the main probe, however, there is no step up (2x) transformer for the guard ring voltage. This has an effect on the bias voltage that can be obtained, but as will be seen later (see page 67 and figure 2.15) the external circuit parameters also play an important role.

a) 

b) 

Figure 2.10: a) Detail of the construction of the LPTP guarded ion flux probe; b) photo of the ion flux probe before installation in plasma chamber.

The voltage and current outputs are measured using a HP 54510A 2 channel digitizing oscilloscope and this data is then transferred across a GPIB interface to a PC. Here it is either converted to ASCII format and saved for post-processing or processed in near real-time using a LabVIEW interface. The former was used in the majority of cases while the latter was used only in the last year. The LabVIEW interface was not true real-time as there was a significant delay (1 – 2 seconds) in acquiring the data using the oscilloscope and then transferring the data across the GPIB connection to the PC.

Examples of measured I–V curves taken with the ion flux probe are shown in figure 2.12. Here, current and voltage measurements are taken for various guard ring configurations: (i) the guard ring is driven using the 11.5 MHz rf generator and its bias voltage and discharge rate is matched to that of the central probe; (ii) the guard ring is grounded; (iii) the guard ring is floating. Differences are seen between the slopes in the ion current saturation region and small variations are observed in the floating potential. The variations in V_f can be explained by the fact that the probe and guard ring are part of a larger surface (the grounded electrode) absorbing current from the plasma. Although the net current to this surface must be zero, localised zones may have a non-zero net current. In the cases where the guard ring is not driven, the large slopes are mainly due to edge effects on the probe. The slope in the case of the driven guard ring can be partially attributed to a leakage current from the measurement device. The measurement circuit has a high impedance, $\approx 10M\Omega$, but when these measurements were taken a 1 MΩ voltage probe

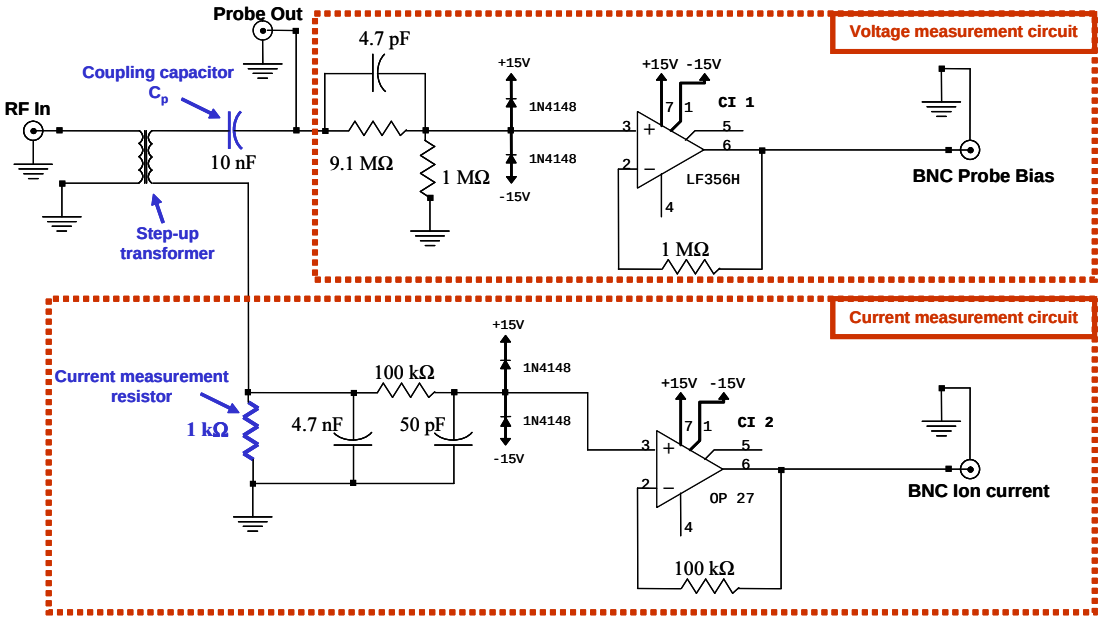


Figure 2.11: LPTP ion flux probe measurement circuit

was used for testing purposes. The measured current is corrected to find the true current to the probe:

$$\begin{aligned} I(t) &= I_{measured}(t) + I_{leak}(t) \\ &= I_{measured}(t) + V(t)R_{leak} \end{aligned} \tag{2.14}$$

In this case the result is a perfectly flat ion current saturation region. When using the measurement circuit (high 10 MΩ impedance) the effect of correcting for the leakage current was minimal. However, a slope may persist in this region even with the leakage current is corrected for. When fitting the I–V curves it was therefore necessary to take this slope into account as follows:

$$I = I_0 \left[1 - m(V - V_f) - \exp\left(\frac{V - V_f}{T_e} \right) \right] \tag{2.15}$$

where m is the slope in the saturation region. Table 2.1 compares the results of fitting the I–V curves in figure 2.12 using the slope as a parameter. It is interesting to note that despite the differences in the curves, the discrepencies found in the value of the ion current never exceed 3%. This shows the robustness of the fitting equation and allowed the continued use of the probe with confidence when the guard ring could not be used for various reasons.

To make matters more complicated, equation 2.15 does not always fit the data as one would hope. Figure 2.13 (a) shows two experimental I–V curves taken in similar conditions, but with one in a 27 MHz only plasma and the other in a 2 and 27 MHz

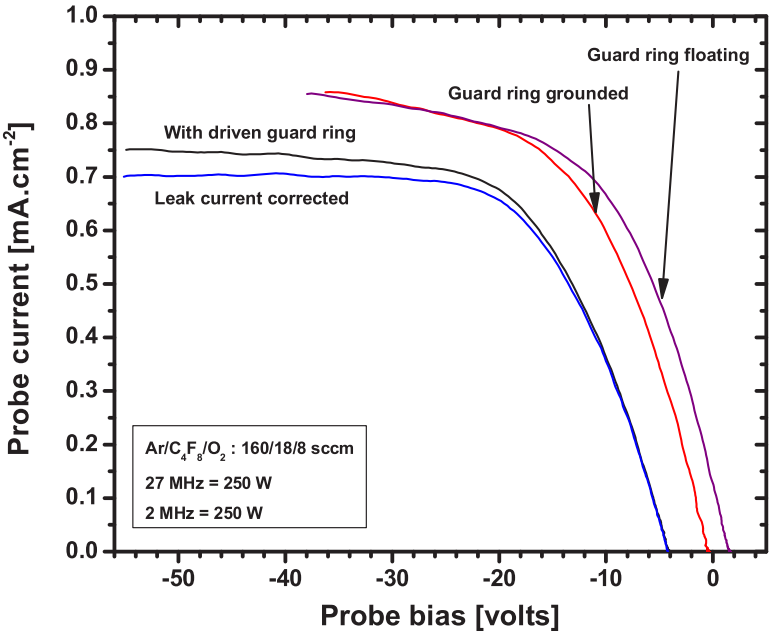


Figure 2.12: I–V curves taken using the ion flux probe under various guard ring configurations.

	Fitted ion current	Fitted slope parameter
With driven guard ring	0.71276	0.00107
With driven guard ring and leak current corrected:	0.71003	0.00024
Guard ring grounded:	0.73287	0.0049
Guard ring floating:	0.72074	0.0049

Table 2.1: Comparison of different probe and guard ring setups

plasma. Both curves were fitted using equation 2.15. In the single frequency case an almost perfect fit was obtained and it is difficult to distinguish the experimental data from the fitted curve. However, in the dual frequency case the fitted curve (continuous, red line) deviates noticeably from the experimental data (square dots).

To understand what we believe is causing the discrepancy, it is useful to examine the electron current separately. This is possible by fitting the ion saturation current region with a straight line and then using the result to subtract the ion current from the I–V curve as follows:

$$I_e(V) = I(V) - I_0[1 - m(V - V_f)] \tag{2.16}$$

The result obtained is shown in figure 2.14, but note that the electron current is plotted as being positive for ease of comparison to conventional Langmuir I–V curves. Maxwellian electrons should have a linear response to the bias voltage, in the region shown here, when plotted on a semi-log scale. This can seen to be the case for the single frequency data, but the dual frequency electron current is non linear at large negative bias, appearing truncated. This implies a reduction in high energy electrons and the shape of this curve resembles that of a *Druyvesteyn EEDF* [Druyvesteyn 40]. The characteristic of Druyvesteyn distributions is that the electron energy, $f(\epsilon) \propto \exp(\epsilon^2)$ as opposed to $\exp(\epsilon)$ in the case of a Maxwellian distribution. We modified equation 2.15 to take this square dependence into account as follows:

$$I = I_0 \left[1 - m(V - V_f) - \exp\left(\frac{(V - V_f) - k(V - V_f)^2}{T_e}\right)\right] \tag{2.17}$$

where k describes the degree of Druyvesteyn character. Figure 2.13 (b) shows this fit function being used on the same two I–V curves as in (a). Table 2.2 summarises the values of the parameters used in both (a) and (b).

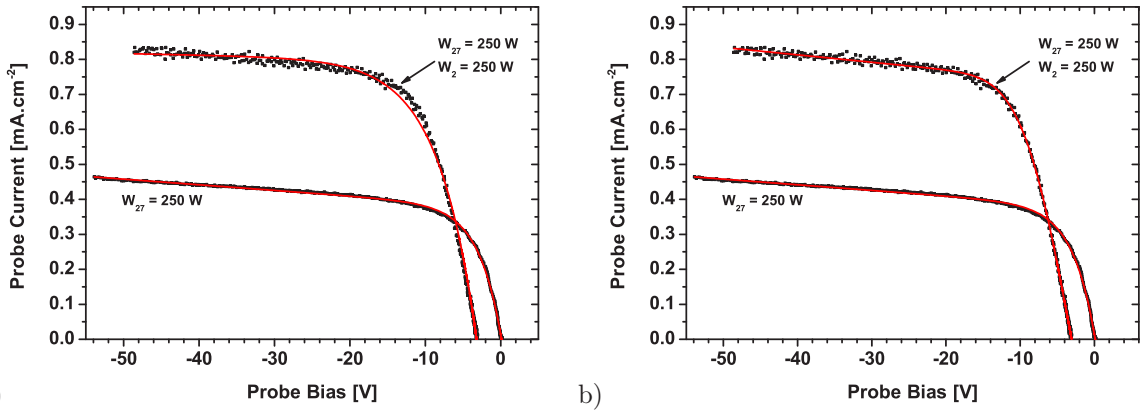


Figure 2.13: a) Fitting I–V curves using equation equation 2.15; b) Fitting I–V curves using equation 2.17.

Another issue that figure 2.12 brings forward is the change in the maximum bias voltage, V_{bias} obtained with and without the guard ring. Indeed, obtaining identical V_{bias}

	I_0	m	V_f	T_e	k
Maxwellian fit					
27 MHz	0.3768	0.00429	0.11	3.0	–
27 + 2 MHz	0.7972	5.2E-4	-3.2	5.1	–
Druyvesteyn fit					
27 MHz	0.3768	0.00429	0.11	3.0	0
27 + 2 MHz	0.7346	0.00289	-3.1	6.7	0.08969

Table 2.2: Fit parameters for the I–V curves shown in figure 2.13

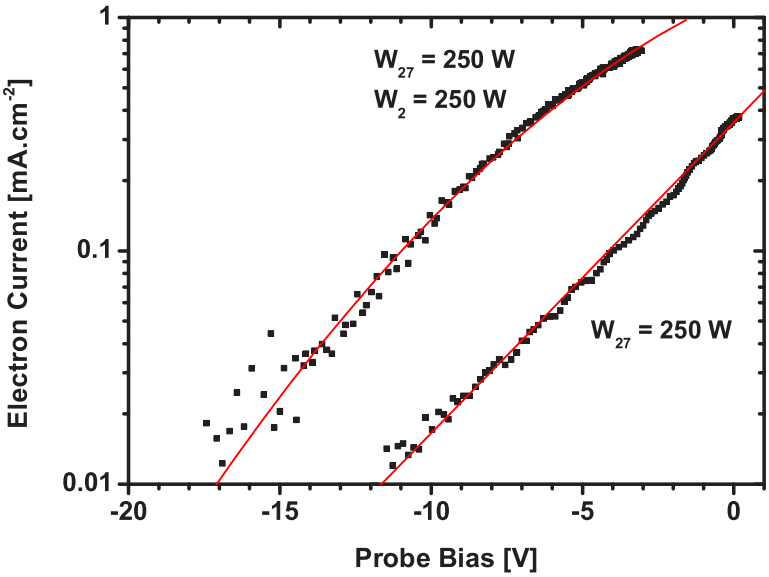


Figure 2.14: The electron current as a function of probe bias voltage, obtained by subtracting the ion current (with slope) from the data shown in figure 2.13. The experimental data (black dots) is fitted with a straight (red) line in the single frequency case, and a 2^{nd} order polynomial (red) line in the dual frequency case.

on both is not as simple as applying equal rf voltage to both, even though equation 2.8 would suggest that this should be so. Due to coupling between the driven central probe and the outer guard ring, the rf voltage on each surface is not only related to the voltage supplied by the pulsed rf generator but also the external circuits connecting the generator to each surface. A parameter which was found to influence significantly V_{bias} is the parasitic capacitance to ground, such as C_{stray} in figure 2.7. To examine the effect of modifying the stray capacitance, a variable capacitor to ground was inserted into the guard ring branch of the circuit. The results are shown in figure 2.15. The probe bias and the guard ring bias are clearly strongly coupled, with a resonance-like effect occuring as a function of the parallel capacitance to ground. The probe and guard ring have equal bias at two points, namely 290 pF and 660 pF. However, these positions may change significantly for various plasma conditions. When the variable capacitor to ground was inserted into the probe branch of the circuit, the effect was much less noticeable. For the purpose of operating both the probe and guard ring in ideal conditions it was therefore necessary to include a variable capacitor to ground in the guard-ring circuit. Following from the results in figure 2.15, the preferred value of this capacitor varies in the region close to 300 pF. The equal bias at 660 pF is due more to the loss of RF power to ground than any resonance effect.

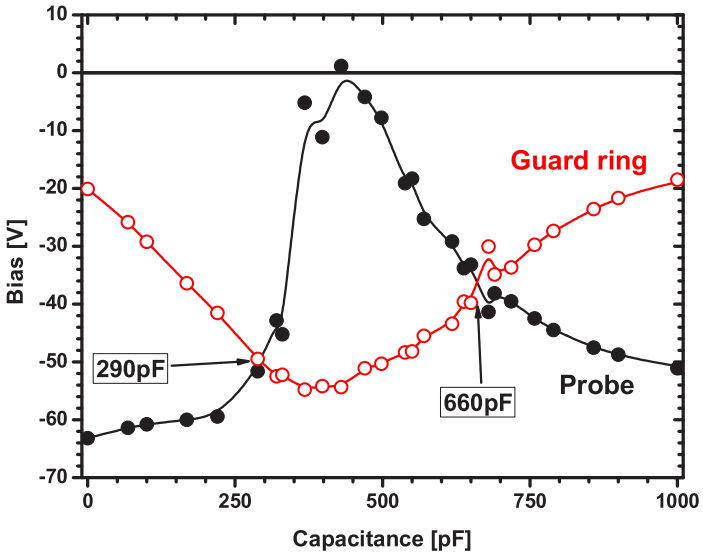


Figure 2.15: Maximum bias obtained on the probe and guard ring as a function of an applied parasitic capacitance from the guard ring to ground.

The complete experimental setup of the ion flux probe is shown in figure 2.16

2.2.2 The microwave resonator probe - "*Hairpin probe*"

Microwave-based electron density measurements were first developed in the 1930s for sounding the ionosphere and in the 1940s for laboratory based plasmas [Heald 65]. The

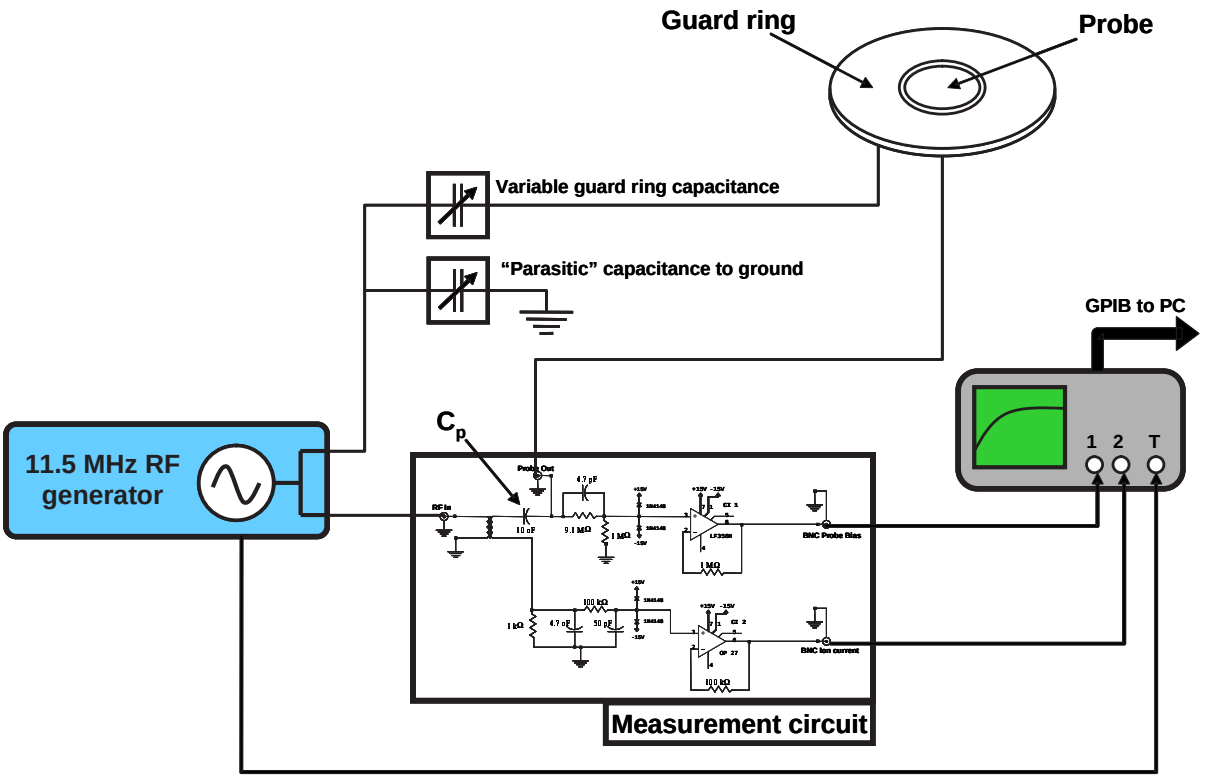


Figure 2.16: Complete experimental setup of the ion flux probe, with guard ring, at the LPTP.

majority of these microwave techniques involve the use of either microwave cavity resonance, such as in [Jauberteau 89, Haverlag 91, Kono 91], and microwave interferometry, as in [Jaiprakash 94, Kitajima 99, Sasaki 99]. The use of microwaves is based on the principle that many laboratory plasmas have densities such that the plasma frequency is in the microwave region. For example, plasmas in the density range 10^9 – 10^{12} cm^{-3} would have corresponding plasma frequencies, $f_{pe} = \omega_{pe}/2\pi$, in the 0.3 – 9 GHz range. The permittivity (or dielectric function) of a plasma, ϵ_p, is related to the plasma frequency, the propagating wave frequency, ω, and the electron collision frequency, ν_m [Lieberman 05]:

$$\epsilon_p = \epsilon_0 \left(1 - \frac{\omega_{pe}^2}{\omega(\omega - j\nu_m)}\right) \tag{2.18}$$

When a wave propagating in a plasma has a frequency such that $\omega \sim \omega_{pe}$, changes in the wave's propagating properties will be noticeable. As ω_{pe} is in the microwave region we will also have $\omega \gg \nu_m$. Therefore, normalising with respect to ϵ_0, equation 2.18 reduces to:

$$\epsilon_r = 1 - \frac{\omega_{pe}^2}{\omega^2} \tag{2.19}$$

where $\epsilon_r = \epsilon_p/\epsilon_0$ is the relative permittivity of the plasma.

Microwave cavity resonance and interferometry techniques do not usually require knowledge of the sheath characteristics, as is the case with electrostatic probes such

as the Langmuir probe. Measurements obtained with them are often considered more reliable and easier to interpret than those using Langmuir probes. Because frequency is easy to measure accurately, they are particularly powerful in determining small changes in n_e, being able to resolve changes many orders of magnitude less than the absolute plasma density. However, the disadvantages of microwave techniques are quite numerous. The most practical disadvantage is cost. Whereas a Langmuir probe requires relatively simple apparatus (dc supply, ammeter, wire and cables), expensive microwave sweep generators are usually required for cavity resonance and interferometry. Noise also presents a major problem, usually from the parasitic resonances originating from the reactor geometry. Probably the biggest disadvantage is the lack of spatial resolution, as the wavelengths of microwaves are often comparable to the reactor dimensions, except for very high ($> 10^{12}$ cm^{-3}) densities. Indeed, many microwave techniques provide little or no spatial resolution, unlike Langmuir probes which can access most regions of a plasma chamber. Also, cavity resonance and interferometry often require specific chamber geometries with easy access, and so are not very suitable for use in many of the chambers designed for industrial use, such as a small gap (1.5 cm) capacitive discharge.

More recent measurements using microwave probes have addressed the problem of spatial resolution. Some have proposed using the wave cut-off method, which uses the property that electromagnetic waves will not propagate in a plasma if their frequency is less than the plasma frequency [Kim 04b]. Blackwell et al. used the change in the impedance of a spherical probe immersed in the plasma to deduce the electron density [Blackwell 05]. There are now several techniques which utilise electromagnetic waves below the plasma frequency. These waves are present in the plasma as evanescent surface waves following the plasma-sheath boundary [Kokura 99, Dine 05]. Two versions of these probes exist, the plasma absorption probe (PAP)[Kokura 99] which requires knowledge of the sheath geometry and the plasma transmission probe (PTP)[Dine 05] which does not require knowledge of the sheath dimensions but is more complicated to construct.

Another electron density measurement device utilising microwaves is the *hairpin probe*, It is the probe described and used in this thesis. Since this probe has only recently gained popularity, a short account of its history is deemed appropriate. The hairpin probe was first introduced by R. L. Stenzel in 1976 [Stenzel 76] who called it the *microwave resonator probe*. Stenzel referred to it as *"A simple diagnostic tool for performing spatially resolved density measurements"*, invloving a parallel-wire quater-wavelength resonator immersed into the plasma. He also described it as being *"largely independent of sheath and thermal effects"*. Despite the advantages presented by Stenzel, no further work involving the hairpin was published until 1995. In that year, an article published by Jongdae Kim and K.C. Junglin purported to have invented what they termed a *"novel diagnostic technique employing a microwave resonator probe"* [Kim 95].

The next known use of the hairpin probe was by Hebner et al. in 2001 [Hebner 01]. They used a modified version of Stenzel's design which will be discussed briefly later on. The authors showed a very successful application of the hairpin probe, using it to detect the fluctuations in n_e from a photodetachment experiment. Despite the fact that the authors were well known amongst the cold plasma community, their article still failed to inspire others to use the hairpin probe. What is interesting, however, is that two papers were then published specifically on the hairpin probe, first in 2002 by Kondrat'ev et al. [Kondrat'ev 02] and then in 2004 by Piejak et al. [Piejak 04], where the authors of both papers were unaware of the work by Hebner in 2001, and the authors of the latter (Piejak et al.) were unaware of the paper by the former (Kondrat'ev et al.).

The paper by Piejak et al., however, brought the hairpin probe to a much wider audience thanks to (i) the high impact factor of the journal they published in (Journal of Applied Physics) and (ii) the eye-catching title they used for their paper, namely *"The hairpin resonator: A plasma density measuring technique revisited"*. It was this paper which coined the term *"hairpin probe"* and brought our attention to it. Several experimental papers have since been published with the hairpin as one of the principal diagnostic tools [Piejak 05, Haas 05, Dine 05, Karkari 06, Curley 07].

The hairpin probe presented in this thesis is based principally on the work of Piejak et al. in their 2004 paper, although on the advice of Prof. Braithwaite at the Open University we used a *floating hairpin* design. The following pages will explain the basic theory behind the hairpin probe, the construction of the hairpin probes at the LPTP, the correction for the presence of a sheath and some experimental results. It must be pointed out that most of what follows can be found in Piejak's two papers on the hairpin probe (see references [Piejak 04, Piejak 05]), though every effort has been made to give a description using my own words and understanding of the subject.

Hairpin probe theory

This section attempts to provide a description of the operation of the hairpin resonator in an intuitive manner. There are two models which can be used to describe the principle of operation of a hairpin resonator. The first uses the example of a resonating LC circuit , the second is based on transmission line theory. Both explain the same phenomenon from different angles, the former uses the basic principles of DC and AC transmission, the latter uses wave theory. Although the use of wave theory and transmission line theory is considered by some to be a more complete description, the concept remains abstract for many. I will start therefore with the more intuitive LC resonant circuit.

Imagine a basic LC circuit as shown in figure 2.17 (a) and that the capacitor, C, has a voltage V across it. When the switch is closed, current will flow through the

circuit to reduce the potential difference. Without the inductor, the capacitor would discharge instantaneously (a short-circuit). However, in the presence of the inductor, the changing current flowing through the inductor, L, induces a changing magnetic field that induces another current opposing the capacitor discharge current. This creates a potential difference known as the electromotive force,

$$V_{emf} = -L\frac{dI}{dt}$$

that opposes the voltage drop across both the inductor and the capacitor until V goes to zero. However, magnetic energy built up in the inductor continues to drive the current through it, charging the capacitor in the opposite direction until the magnetic energy is spent. The cycle then repeats itself with the capacitor discharging and the inductor building up magnetic energy. An ideal LC circuit resonates at a constant frequency, $\omega_r = 2\pi f_r$, with energy being transformed continuously from electrical to magnetic energy. ω_r is defined by the magnitude of the inductance and capacitance of the components:

$$\omega_r = \frac{1}{\sqrt{LC}} \tag{2.20}$$

In much the same way as pushing a swing at the right moment and at the right frequency can cause the height of the swing to increase, an LC circuit driven by an external AC source of frequency ω_r will absorb all incoming power. The circuit is therefore said to be in resonance and has an impedance of zero at its resonant frequency. At other frequencies the coupling of power will be less effective as the waveforms will destructively interfere. The general expression for the impedance of a series LC circuit is:

$$Z = j\omega L + \frac{1}{j\omega C} \tag{2.21}$$

$$= \frac{(\omega^2 LC - 1)j}{\omega C} \tag{2.22}$$

so that when $\omega = 1/\sqrt{LC}$ the total impedance will be zero and otherwise non-zero. Parts (b) of 2.17 show how (a) can be rearranged when the switch is closed. Part (c) is a schematic of a distributed LC circuit and closely resembles a U-shaped hairpin. The wires of a hairpin may be considered as inductors in series, while the separation between the wires forms a capacitor. This notion of capacitance between the wires will be used later for the sheath correction. Part (c) will also remind many of an LC ladder configuration used in describing a transmission line. This distributed LC circuit will also have a resonant frequency associated with the values of the inductors and capacitors along it.

Transmission line theory is used for the transmission of electric wave signals along two parallel conductors of infinite length. The most common example of everyday transmission lines are power cables from power stations and the twisted copper wires used in

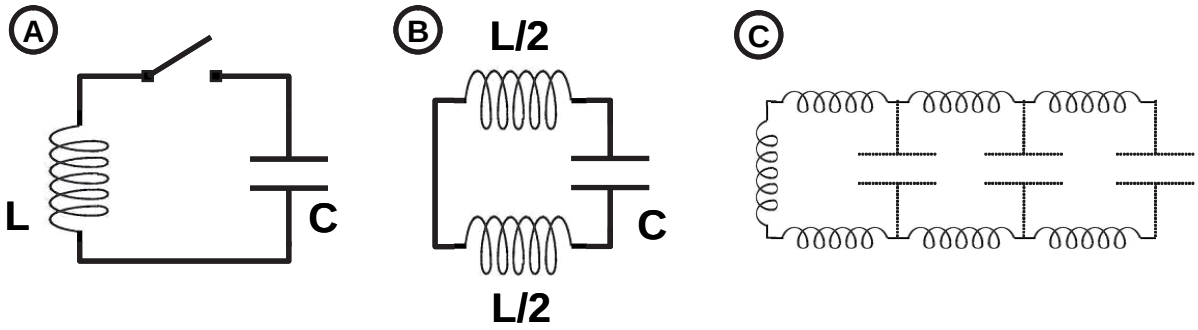


Figure 2.17: (a) Simple open LC circuit; (b) Simple closed LC circuit (c) A distributed LC circuit

telephone networks. The hairpin may be considered as a transmission line since the hairpin width is much smaller than the hairpin length. Connections between transmission lines and waveguides is must be impedance matched if maximum power transfer is to occur. For example, a 50 Ω coaxial cable or a glass optical fibre should ideally terminate at a 50 Ω or glass optical input (of identical refractive index) respectively, otherwise reflections of the incident signal/wave will occur. These reflected waves will interfere with the incident waves, resulting in a standing wave along the length of the cable/waveguide. The formation of a standing wave is the basis for the operation of a hairpin resonator.

Imagine a voltage waveform launched along a long, but finite, transmission line as in figure 2.18.

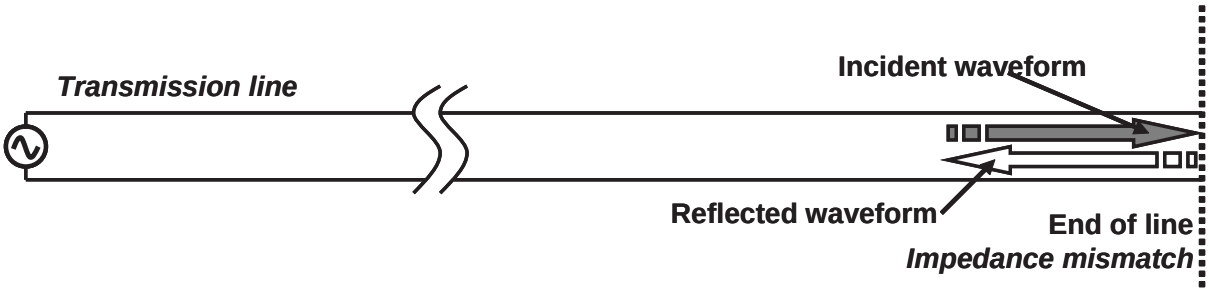


Figure 2.18: Transmission line

When the end of the line is reached an open circuit is encountered, the equivalent of an infinite impedance, and so the waveform is (ideally) completely reflected. For some frequencies, these reflections will destructively interfere with the incident waveform resulting in no power being transmitted down the line, which would seem normal from an AC point of view as the line forms an open circuit. However, if the line has a length equal to a multiple of a half wavelength, $L = \lambda/2$ then constructive interference will occur at all points resulting in a standing wave. The reason that a half wavelength is required is due to the *boundary conditions* imposed by the transmission line. At the end of the line the current must be zero for physical reasons (open-circuit). The start of the line is the voltage source, which in the case of a standing wave will become a current node

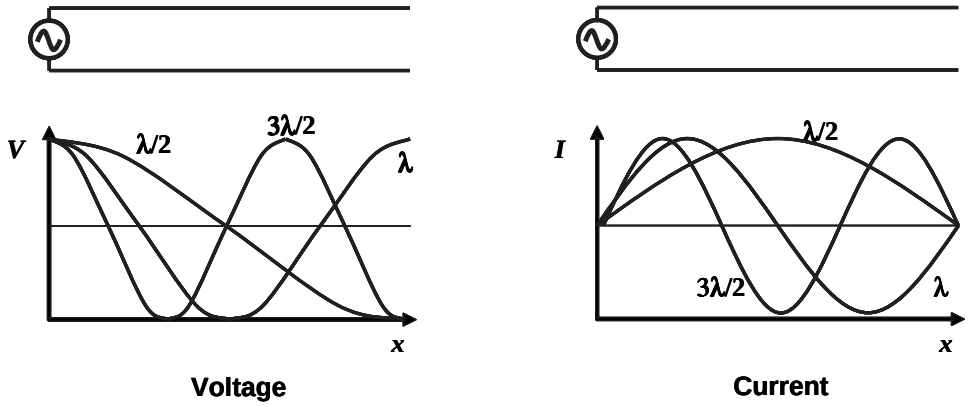


Figure 2.19: Allowed standing waves on a non-terminated (open circuited) transmission line.

(zero current because of infinite impedance of voltage supply) and a voltage antinode. Figure 2.19 shows how multiples of a half wavelength are able to satisfy these boundary conditions. Note the resemblance of the transmission line in this figure to the hairpin structure later on.

Once a standing wave forms, power from the voltage generator is completely absorbed into the wave formation in much the same way as an AC voltage supply of frequency ω will be absorbed by a resonant LC circuit when $\omega = 1/\sqrt{LC}$. In other words, a standing wave effect produces identical results to resonance. To bridge the gap between both theories one only needs to look at the phase difference between the voltage and the current, i.e. a quarter wavelength, or $\pi/2$. At a voltage antinode position corresponds to a current node position, so the energy stored between both wires at a position x is purely capacitive (electrical). In contrast, a voltage node position corresponds to a current antinode position and so the energy stored between both wires is now inductive (magnetic). There is also a $\pi/2$ phase difference in time. Hence, as with the LC circuit, energy is constantly being converted from electrical to magnetic energy.

We now know that a hairpin like structure can absorb power at a particular frequency either through resonance or the standing wave effect, both describing the same phenomenon from a different angle. The actual hairpin resonator differs slightly from fig. 2.19 in that we do not supply a voltage but rather a current. The basic structure is shown in figure 2.20 is a transmission line shorted at one end and open on the other. A high frequency (microwave) voltage signal is transmitted by a loop placed in close proximity to the shorted end, thus inducing a current in said end. The standing waves permitted on the hairpin differ from those in figure 2.19. At the shorted end the voltage must always be zero (voltage node), whereas the induced current forms a current antinode for all standing waves. The standing waves which satisfy the boundary conditions are those

where the hairpin length is equal to odd multiples of a quarter wavelength:

$$L = (2n + 1)\lambda/4 \tag{2.23}$$

The first three standing wave modes are shown in figure 2.21. In practice, the hairpin resonator probe uses only the first standing wave mode:

$$L = \lambda/4 \tag{2.24}$$

By using the relation $c = f\lambda$, where c is the speed of light in vacuum, equation 2.24 can

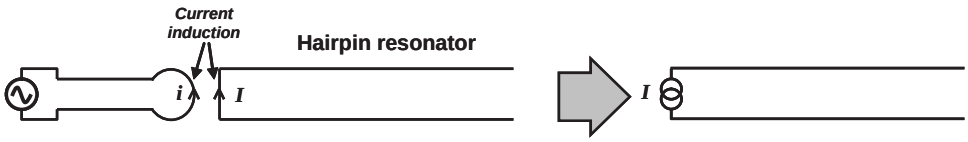


Figure 2.20: On the left, the basic operation of the hairpin resonator: a U-shaped wire forms a transmission line shorted at one end and open at the other. A current is induced at the shorted end. On the right, an equivalent circuit for the hairpin resonator, with the induced current replaced by an alternating current source.

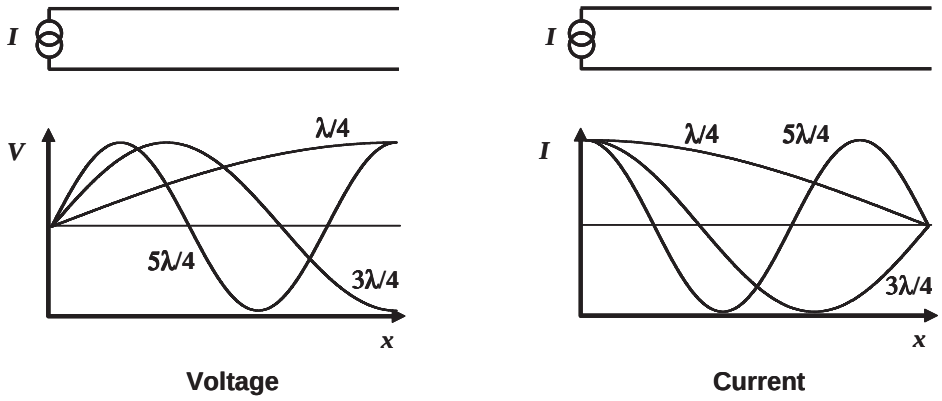


Figure 2.21: Equivalent ciruit of the hairpin resonator showing the first three modes of standing waves permitted.

be rearranged to give the first fundamental frequency at which the hairpin will resonate:

$$f = \frac{c}{4L} \tag{2.25}$$

The speed of an electromagnetic wave, however, will depend on the medium through which it travels. In optics, this gives rise to the index of refraction. In a plasma, the index of refraction is equivalent to the square root of the dielectric permittivity, ϵ, as the presence of electrons slows the phase velocity of the wave guided along the hairpin. The speed of the wave is modified such that $v = c/\sqrt{\epsilon}$ and so equation 2.25 becomes:

$$f = \frac{c}{4L\sqrt{\epsilon}} \tag{2.26}$$

where ϵ is the relative dielectric permittivity such that in vacuum $\epsilon = 1$. We define f_0 as the resonant frequency in vacuum and f_r as the resonant frequency for a given value of ϵ so that we have the relation:

$$f_r = \frac{f_0}{\sqrt{\epsilon}} \tag{2.27}$$

Using equation 2.19, this relation becomes:

$$f_r = \frac{f_0}{\sqrt{1 - f_{pe}^2/f_r^2}} \tag{2.28}$$

which finally rearranges to the following equation describing the shift in the hairpin resonant frequency when immersed in a plasma:

$$f_r^2 = f_0^2 + f_{pe}^2 \tag{2.29}$$

The resonant frequency of a hairpin in a plasma is easily related to the plasma frequency and therefore the electron density, since $f_{pe}^2 = ne^2/\epsilon_0 m_e$. The electron density can be simply related to the shift in resonant frequency, as summarized in the following equation:

$$\frac{n_e}{10^{16}\mathrm{m}^{-3}} = \frac{(f_r/\mathrm{GHz})^2 - (f_0/\mathrm{GHz})^2}{0.81} \tag{2.30}$$

Effect of a sheath on the hairpin probe

If an electron-depleted sheath forms around the wires of the hairpin then the resonance will be shifted towards f_0 and the electron density will be underestimated. Piejak et al. (2004) presented a method for correcting for the presence of a sheath and this will be briefly presented here. The theory involves relating the shift in effective capacitance formed by the wires of the hairpin in the presence of a sheath with the shift in the resonant frequency. Assuming one knows the thickness of the sheath, one can determine the correction that needs to be made.

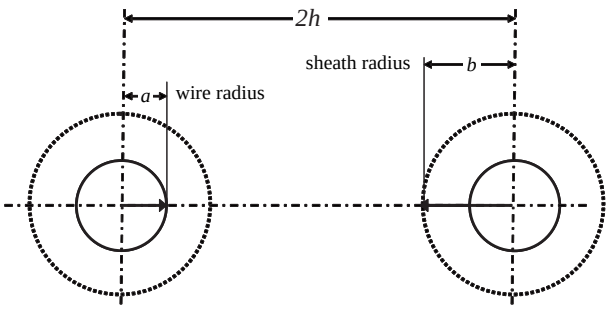


Figure 2.22: Schematic representation of the hairpin wires of radius a and separation $2h$, each surrounded by a sheath of radius b.

The observed capacitance across the hairpin wires is that of two parallel cylindrical conductors of radius a separated by a distance $2h$. This is given by (from *Engineering*

Tables and Data, 2nd Edition by A. M. Howatson *et al*):

$$C_{eff} = \frac{\epsilon_{eff}}{\text{arcosh}(\frac{h}{a})} \tag{2.31}$$

Where $\epsilon_{eff} = \left(\frac{f_0}{f_r}\right)^2$. From the *Handbook of Mathematical Functions* we have the following limiting condition:

$$x \geq 1 \Longrightarrow \text{arcosh}(x) = \ln\left[x + (x^2 - 1)^{\frac{1}{2}}\right] \tag{2.32}$$

In our case we have $x > 1$ ($h/a \approx 1.5\text{mm}/0.125\text{mm} = 12$) and so $x^2 \gg 1$. This means that:

$$\text{arcosh}(x) \cong \ln 2x \tag{2.33}$$

an so finally Eq. 2.31 takes the following form:

$$C_{eff} = \frac{\epsilon_{eff}}{\ln(\frac{2h}{a})} \tag{2.34}$$

This capacitance can be considered the result of two capacitors in series, i.e. (i) the capacitance across the sheath and (ii) the capacitance across the plasma. The capacitance across the sheath is the capacitance between an internal conductor of radius a and an external conductor of radius b = sheath radius, i.e. a coaxial capacitance. This coaxial capacitance per unit length (from *Engineering Tables and Data*, 2nd Edition) is given by:

$$C_{sheath} = \frac{2\epsilon_{sh}}{\ln(\frac{b}{a})} \tag{2.35}$$

If we take the capacitance across the plasma to be that of the capacitance between two parallel wires of radius b we have (from Eq. 2.34)

$$C_{plasma} = \frac{\epsilon_p}{\ln(\frac{2h}{b})} \tag{2.36}$$

This then gives us (remembering that there are two sheaths!):

$$\frac{1}{C_{total}} = \frac{1}{C_{sh}} + \frac{1}{C_p} + \frac{1}{C_{sh}} \tag{2.37}$$

$$= 2\left(\frac{\ln(\frac{b}{a})}{2\epsilon_{sh}}\right) + \frac{\ln(\frac{2h}{b})}{\epsilon_p} \tag{2.38}$$

$$= \frac{\epsilon_p \ln(\frac{b}{a}) + \epsilon_{sh} \ln(\frac{2h}{b})}{\epsilon_{sh}\epsilon_p} \tag{2.39}$$

Approximating $\epsilon_{sh} = 1$ (no electrons in sheath) we have the following expression for the hairpin capacitance:

$$C_{total} = \frac{\epsilon_p}{\ln(\frac{2h}{b}) + \epsilon_p \ln(\frac{b}{a})} \tag{2.40}$$

If we now equate equations 2.34 and 2.40, we can solve for ϵ_p and subsequently f_p^2 can be deduced. The complete calculation, step by step, can be found in Appendix 4.6, where it is shown that the presence of a sheath may be accounted for by using the following formula:

$$f_p^2 = \frac{f_r^2 - f_0^2}{1 - \frac{f_0^2}{f_r^2} \cdot \Lambda} \tag{2.41}$$

where $\Lambda = \ln(\frac{b}{a}) / \ln(\frac{2h}{a})$. The denominator in equation 2.41 is always less than 1, so the effect of the sheath correction is to increase the value of the measured plasma frequency. The correction is correlated to the hairpin geometry and, therefore, must be tailored to each new hairpin construction.

2.2.3 Calculation of the hairpin sheath size

Should we wish to correct for the presence of a sheath, we will need to know the value of b, the sheath radius around the probe. Piejak et al. (2004) describe a *step-front sheath model* (SFSM): a set of fluid equations are considered for ions moving without collision in a cylindrical electron-free sheath around a wire of radius a. The model is commonly used to describe the ion sheath around a Langmuir probe and will not be described here, but the results are shown in figure 2.23 (a). The curve in this figure can be fitted using the following:

$$\frac{b}{a} = 1 + 1.757 \left(\frac{a}{\lambda_D} \right)^{-0.63} \tag{2.42}$$

which can then be used in automated sheath correction. The results are presented in such a way that, if one knows the hairpin wire radius and can estimate the Debye length, then one can find the ratio b/a which is needed in the calulation of Λ. Of course, a chicken and egg situation arises because one must know the electron density, n_e, to estimate λ_D, but n_e is the quantity we are looking for. In practice, an estimate of n_e is made using the uncorrected sheath results, and then several iterations may be made until the difference between the uncorrected and corrected values of n_e is acceptably small. A spreadsheet program was sufficient to carry out this task.

The use of this step-front sheath model in estimating the sheath thickness around the hairpin wires requires the assumption that no RF fluctuations are present in the sheath. That is, the probe is assumed to be perfectly floating and has no capacitance to ground. The microwave signal to the hairpin, however, is coupled by a coax and loop set-up that is electrically grounded, so it is possible that with this model we are still underestimating the effect of the sheath.

2.23 part (b) shows a more direct application of the results in part (a). The correction factor is defined as the ratio between the electron density after sheath correction and the

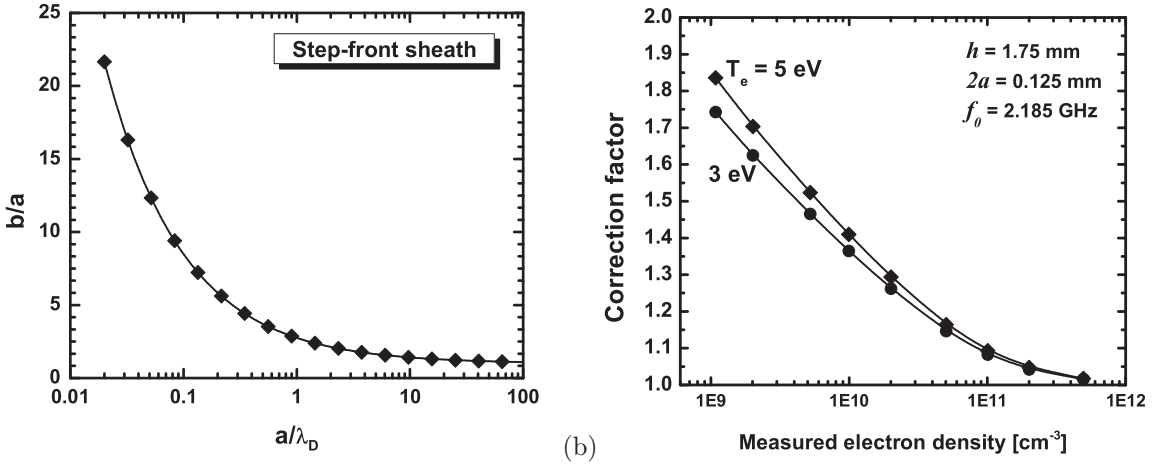


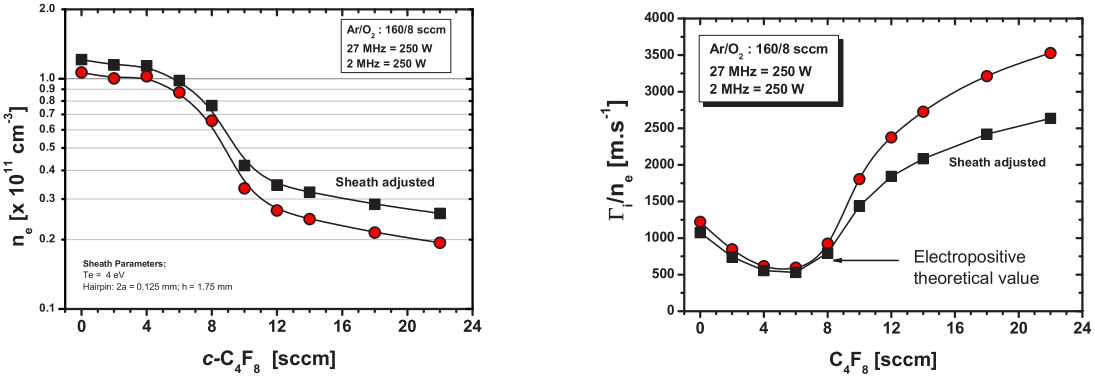
Figure 2.23: a) Ratio of sheath/probe radii versus probe radius normalised to the Debye length (from Piejak et al. (2004) [Piejak 04]); b) Correction factor, assuming floating sheath, as a function of the measured electron density, for two electron temperatures and for the hairpin dimensions used in this study.

electron density before sheath correction, or in other words:

$$n_e(\text{corrected}) = n_e(\text{uncorrected}) \times \text{Correction Factor} \tag{2.43}$$

The correction factor is shown for two different values of T_e (as $\lambda_D \propto \sqrt{T_e}$), namely 3 eV and 5 eV, and for a specific probe geometry, namely that of the hairpin most often used in this thesis. For high electron densities, $\geq 10^{11}$ cm^{-3}, the effect of a sheath is very small, introducing disparities of less than 10 %. On the other hand, for low densities, $\leq 10^{10}$ cm^{-3} the effect of a sheath can result in an underestimation of the electron density by more than 30 %. At around 10^9 cm^{-3} the electron density is underestimated by a factor of nearly 2. The majority of conditions in the experiments presented in this manuscript are in the middle ground, i.e. greater than 10^{10} cm^{-3} but usually not much more than 10^{11} cm^{-3}. Sheath corrections are therefore necessary for a rigorous analysis of the data, though the uncorrected density measurements should be acceptable for analysis of the trends in electron density.

Figure 2.24 (a) presents the electron density before and after a sheath correction. A $\log_{10}$ scale is used to emphasise the fact that the greater *relative* change is at the lower densities. Part (b) plots the ratio Γ_{is}/n_{e0} as a function of c-C_4F_8 flow, both before and after the sheath correction. This ratio will be used later in our analysis of the negative ion fraction. One can clearly see the large effect the correction has on this ratio at the higher c-C_4F_8 flow rates.



a) b)

Figure 2.24: a) Electron density in an Ar/O_2 plasma with various quantities of c-$C_4F_8$with and without the hairpin probe sheath correction; b) The ion flux to electron density ratio

2.2.4 The Floating Hairpin

The hairpin probe designed by Piejak et al. (2004) was such that the hairpin resonator was in fact DC grounded. In Piejak's large volume, highly asymmetric chamber this was fine since the plasma potential remained practically constant throughout the RF cycle. However, the symmetric geometry of the dual frequency capacitive chamber leads to strong oscillations in the plasma potential, several hundreds of volts in amplitude. If Piejak's grounded hairpin design were to be used in this environment, then a large RF sheath would form around the hairpin wires. The step-front sheath calculation presented in the previous section is that of a floating DC sheath and so could no longer be used in the presence of a RF sheath. Instead, one would need to use a Child-Langmuir sheath model, but one would need to know the magnitude of the voltage across the RF sheath. Assuming this value was known, it may be possible to correct for the effects of an RF sheath. However, the sheath correction (equation 2.41) is not valid in cases where the sheath radius, b, is of the same order of magnitude as the wire separation, $2h$. Thus, every effort must be made to keep the sheath as small as possible.

On the advice of Prof. Braithwaite at the Open University in the U.K., we decided to start out with a floating hairpin probe. Hebner et al. had previously used a floating version of the hairpin probe, but to my knowledge this was purely for engineering purposes and not to avoid RF sheath formation [Hebner 01]. The principle behind the floating hairpin probe is that the surface potential of the hairpin resonator will closely follow that of the oscillating plasma potential, with only a floating DC sheath potential between the two. Piejak later worked with Braithwaite and co-workers on the issue of using hairpin probes in oscillating RF plasma potentials, producing a paper on the subject [Piejak 05].

2.2.5 Design and construction of the hairpin probe

The actual construction of the hairpin probe required several design considerations to be accounted for:

- The plasma environment has a relatively high gas temperature (> 500 K). Certain materials, such as normal solder and the Teflon insulation in coax cables are not suited to these temperatures - this created the need to use high temperature materials.
- Damage to the probe by plasma etching is possible. This may also result in pollution of the plasma and/or deposition or metal on reactor walls and confinement rings.
- Secondary heating effects: RF capacitive coupling between the hairpin wires and the grounded coax appeared to be the source of heating in early designs, with evidence of the formation of "mini plasmas". The hairpin-to-coax distance needs to be close enough for the microwave signal coupling, but far enough away to avoid problems due to RF.
- Correction for the sheath effects in obtaining the electron density measurements necessitates the precise determination of hairpin geometric parameters. Moreover, all hairpin related theories are ideal models, to be used with as near perfect hairpins as possible, e.g. parallel wires.
- Acquiring good resonance (high Q-factor) was dependent on several parameters: wire separation , straight and parallel wires, coupling loop, distance between coupling loop and hairpin, good coax construction, good SMA adaptor connection. These were determined empirically for each hairpin probe.
- Hairpin length is application specific: short hairpin wires have a higher spatial resolution but require higher microwave frequencies to operate and have too low resolution for determining low electron densities; long hairpins are sensitive to low electron densities but have lower spatial resolution and greater plasma perturbation.
- Parasitic resonances and losses from the high frequency coax cables, the probe coax, poor connections and the high pass filter (need a large pass-band, e.g. Wainwright filter: 1-7 GHz) all contribute to difficulties in getting a good resonance signal.

Stentzel used two conduction loops at the end of two coaxes: one to send the signal, the other to receive the resonance. Piejak simply used one induction loop and one coax cable send the signal and then observed the resonance by measuring the reflected power. Our hairpin probe is based on Piejak's model, modified to a floating hairpin design on the advice of Prof. Braithwaite.

The first, and simplest, element to make is the hairpin itself. We used a 0.125 mm diameter tungsten wire which was then bent into a squared U-shape approximately 3 – 4

mm wide and about 3 cm long. It was always best to start out with a long hairpin and then shorten it when necessary.

The coupling of the microwave signal to the hairpin is by means of a coupling antenna at the end of a coax cable. Small diameter coax cables (1 – 2 mm) are rare and they almost all contain Teflon as a dielectric. Teflon begins flowing at temperatures above 200 – 250 °C, and in our plasma the gas temperature can easily exceed this. One needs to construct a coax which is capable of supporting up to (and maybe above) 400 °C. Inspired by Piejak we have made rigid coax cables using glass as the dielectric. Our coax dimensions are as follows:

- Internal copper conductor: 0.25 mm
- Pyrex capillary tube (dielectric): Int. 0.3 mm; Ext. 0.7mm
- External conductor: Int: 0.8 mm; Ext: 1.78 mm

The coupling antenna is fabricated by making a loop at the end of the coax cable using the centre conductor wire. The loop usually has a diameter of $\sim$ 2 mm. This needs to be done without damaging the fragile glass capillary tube. Connecting the loop to the outer conductor can be done using either normal solder (but risk of melting in plasma), spot welding (very difficult to spot weld copper to copper) or by using silver solder (very high temperature process with a high chance of weakening or even destroying the loop). In the end we chose the latter. The final design is similar to that in Figure 2.25 (a). The constructed coax then needs to be attached to a SMA plug. The majority of SMA plugs require the central coax conductor to be soldered directly to the plug pin. The problem with this is that when the SMA is tightened to a socket, friction can cause the pin to turn, which twists the central coax conductor and the coupling loop. It was not possible to find a straight SMA plug with a fixed pin connection. We therefore modified a right-angle SMA plug (with fixed pin) to obtain a straight plug with a fixed pin.

The coax then needs to be positioned so that it can couple power to the hairpin. We use a set-up whereby the hairpin is electrically floating, i.e. is not connected to the coax. We have found that trying to position the hairpin close to the coupling loop, while at the same time keeping the coax and loop isolated from the plasma, has been our main obstacle to making a hairpin probe. Our aim was to contain the coax and loop within a protective glass tube, in our case made of Pyrex and later of quartz. We have tried three methods of placing the hairpin. The first method, type A, involved using a standard glass tube to protect most of the copper coax cable except the loop at the end, and then creating a glass "sleeve" structure with an embedded hairpin. A schematic of this design can be seen in figure 2.25 (b) and a photo on the top right of figure 2.26. The second method, type B, involved using a standard glass tube, closed at one end, to cover the both the coax and loop. The hairpin was then glass welded into position, as can be seen schematically in figure 2.25 (c) and in the photo on the top left of figure 2.26. Although

these first two methods were satisfactory, they had the disadvantage of requiring support from a local glass blower whenever we wished to make a new design, or when the hairpin broke. A third design, type C, was therefore created to allow us to interchange hairpin wires more freely. It consisted of using a glass "collar" to hold the hairpin wires in place on the glass tube. A photo of this design can be seen in he photo on the bottom left of figure 2.26. This design also had the advantage of allowing the use of quartz for both the collar and the tube, which was not possible for the previous designs due to the difficulties in working with quartz.

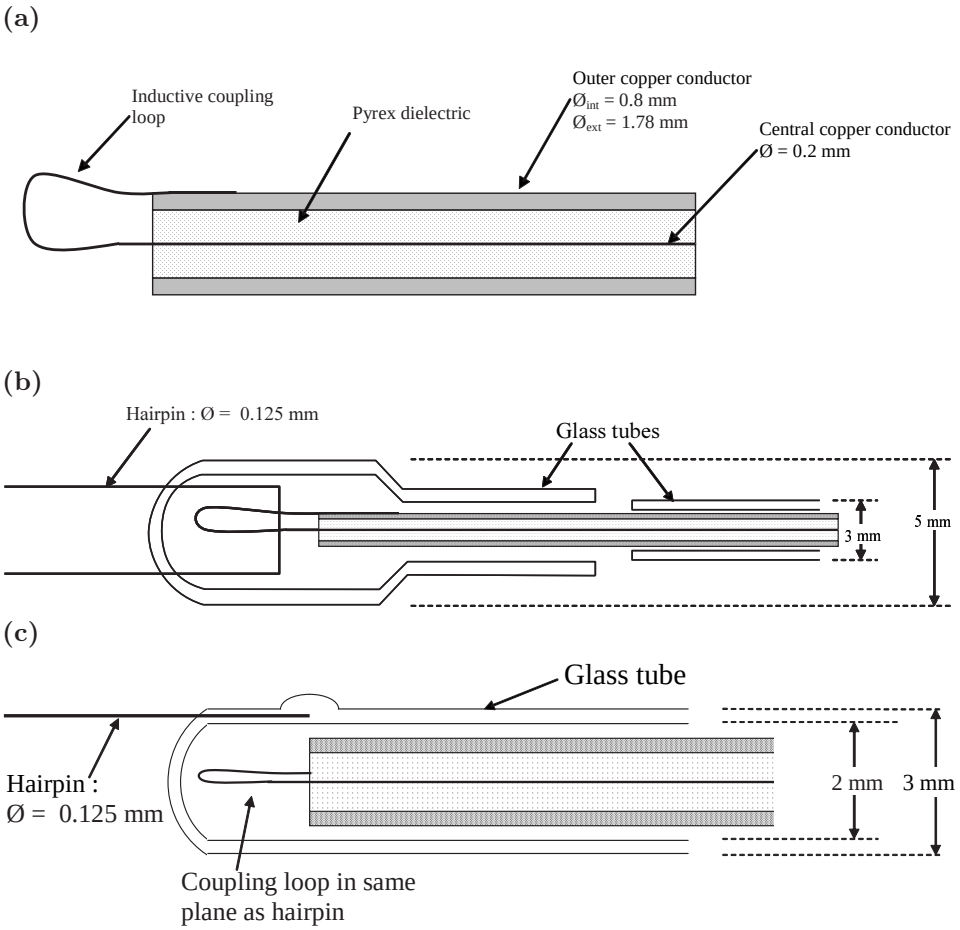


Figure 2.25: a) coax construction; b) first glass housing construction; c) second glass housing construction

2.2.6 Operation of the hairpin probe

The experimental setup can be seen in figure 2.27. A HP 8572 C network analyser was used to operate the hairpin probe. The frequency range of this device was from 300 Hz to 6 GHz with a maximum resolution of 10 Hz. The output (reflection) port was connected via a high frequency SMA coax cable to a high pass filter ($>$ 1 GHz) in series with the SMA connection to the probe. A SMA female-female vacuum feedthrough was used across

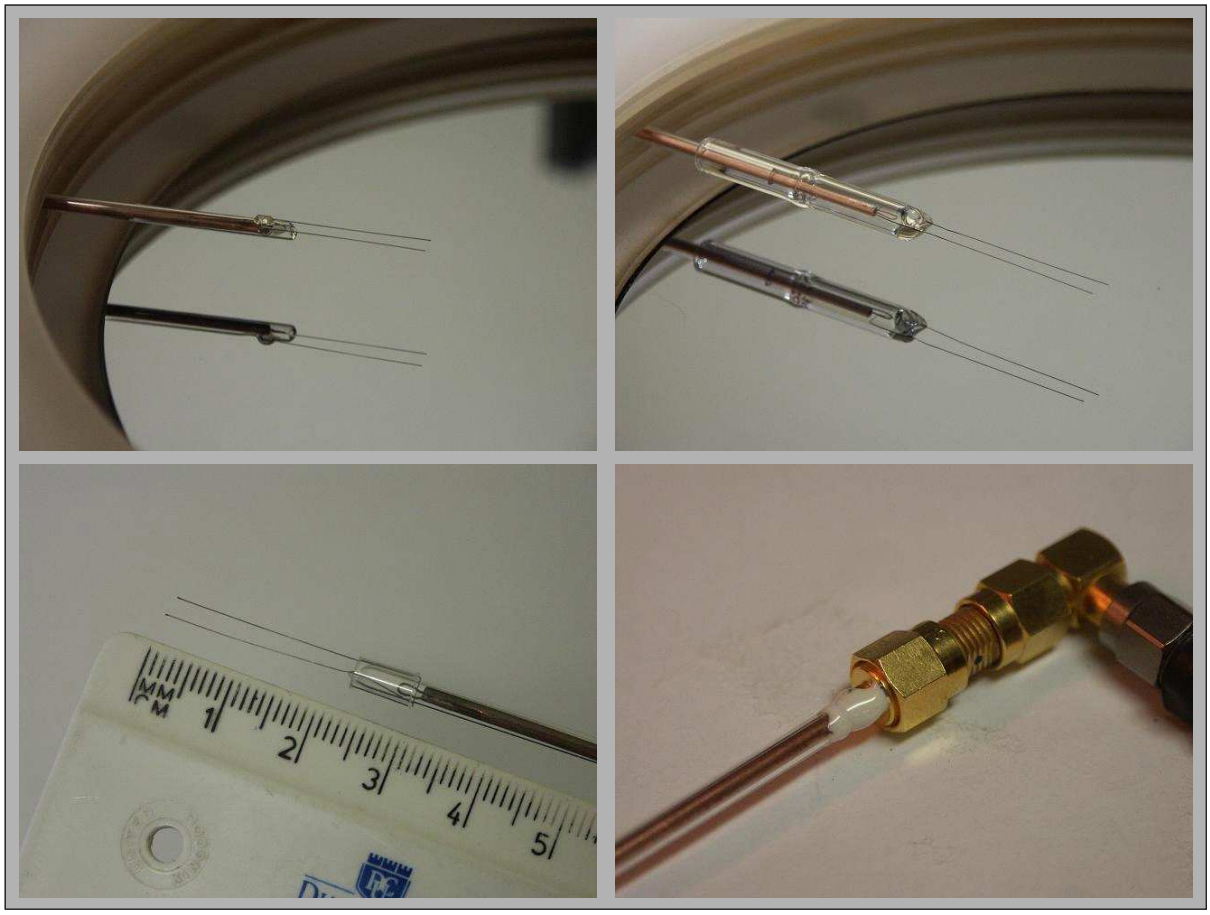


Figure 2.26: Top left: Hairpin probe design type A, with wire glass welded on top of Pyrex casing; Top right: Hairpin probe type B, with wires embedded in glass sleeve structure; Bottom left: Hairpin probe type C, with wire held in place by quartz collar; Bottom right: example of SMA connection

the chamber port flange. The high pass filter (model: Wainwright Instruments WHKS 1000-5SS) was limited to operating below 8 GHz, which was more than adequate for our experiments.

The network analyser was operated in reflection mode, so the power output level was not relevant. The frequency scale was adjusted (from previous experience) to the region we were interested in. This also allowed for high resolution data. Although the vacuum resonance peak was easily visible, the same cannot be said for the resonance peak in the plasma, which was largely broadened and attenuated. Parasitic resonance peaks also made things difficult so a background signal was usually taken and subtracted from the measurement signal. In practice, it was found that better S/N was obtained if we used the plasma signal as the background and subtracted this from the vacuum signal. In figure 2.28 this is the reason that the plasma resonance peak is positive whereas the vacuum resonance is negative. A raw signal (i.e. no background subtraction) always has a negative resonance peak. Taking the vacuum resonance just after measurement also allows for changes in f_0 due to heat effects.

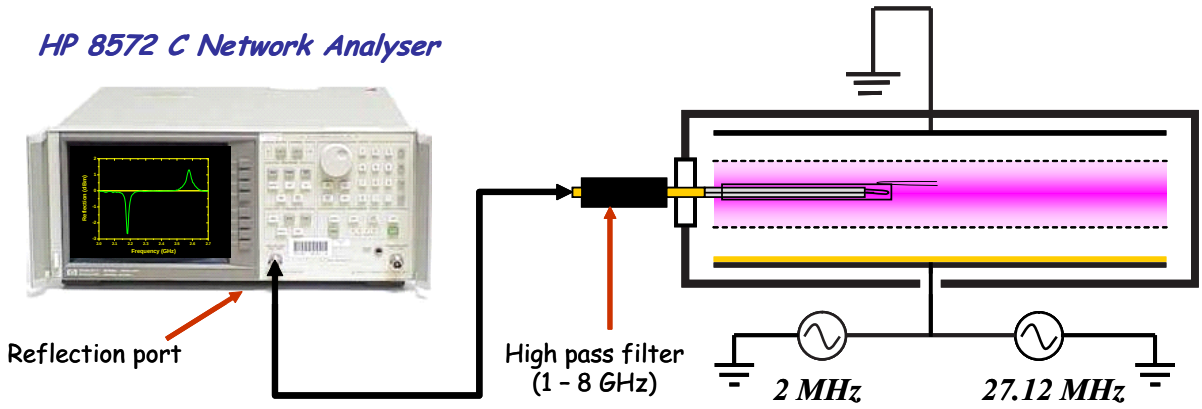


Figure 2.27: Experimental setup of the hairpin probe on the LPTP Exelan dual frequency reactor.

2.2.7 Comparison between two hairpin probe designs

As outlined in the previous section, during the course of this project, several hairpin probe designs were used. To quantify the difference in the electron density measurements between two different designs, two probes were inserted into the plasma chamber at the same time. Measurements were then taken with both probes in identical plasma conditions. However, it was not possible to use both probe simultaneously, so a short amount of time was necessary in between probe measurements to swap the appropriate cables. The aims of the experiment can be summarised as follows:

1. Compare consistency of results when hairpin geometry (length and width) is varied
2. Examine sheath effects.

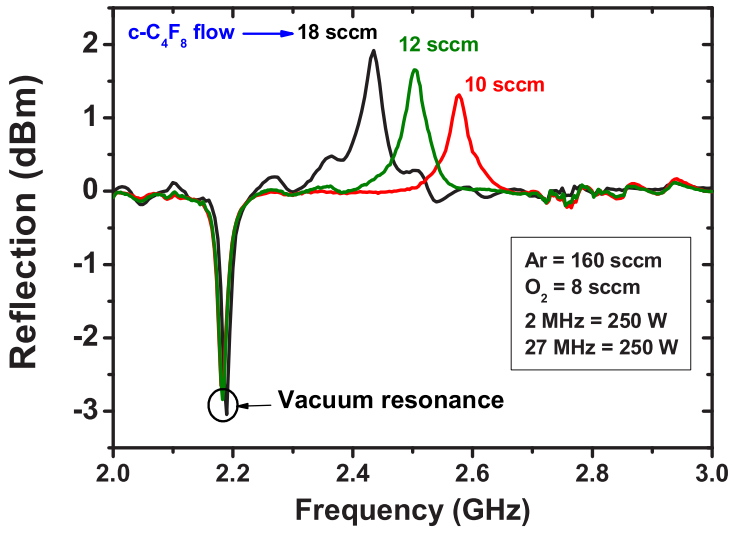


Figure 2.28: An example of the hairpin resonance as measured by the network analyser in a dual frequency $Ar/O_2/c\text{-}C_4F_8$ plasma. Note the presence of both the vacuum and plasma peaks due to the use of baseline subtraction.

The characteristics of the two hairpin designs are outlined in table 2.3 and a photo of both inside the chamber is seen in figure 2.29. Hairpin 1 is based on the design in figure 2.25 (b), whereas Hairpin 2 is based on the design in figure 2.25 (c). Hairpin 1 is noteable in that a non negligeable proportion of it is within the glass tube and is therefore never in contact with the plasma.

	Hairpin 1	Hairpin 2
Length, L	3 cm	3.5 cm
Width, $2h$	4 mm	2 – 2.5 mm
f_0	2.44 GHz	2.01 GHz
Description	Hairpin inserted into glass tube	Hairpin attached to top of glass tube

Table 2.3: Hairpin design characteristics used in the two hairpin experiment

Two identical experiments were performed, one for each probe. The results of both are shown in figure 2.30. When the results of the first experiment were analysed it was found that the electron density measured by hairpin 2 was on average less than that measured by hairpin 1. Two explanations were put forward: (i) the differences in the probe designs caused the discrepancy; (ii) the probes were not in the same position. It was important to rule out the latter, so the positions of both probes were examined. It was found that, due to their designs, the actual hairpin resonator on each probe was not in the same axial position as the other. Due to the small gap between the electrodes, a large density gradient occurs so it is important to have both hairpin resonators at the same axial location. This was achieved by rotating hairpin 2. The second experiment

was then a repeat of the first but now with both resonators in the same axial position. The result was surprising, but was also very good news. Despite the differences in probe design, both probes produced the same result exactly.

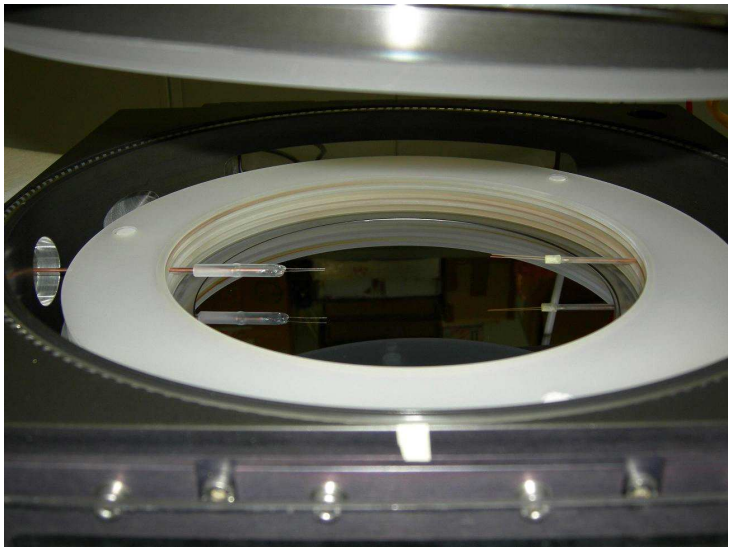


Figure 2.29: Two hairpin probes of different construction design inserted into the dual frequency plasma chamber.

The conclusion was, therefore, that the hairpin resonator is robust in terms of probe design and geometry. It was also concluded that the sheath correction was effective as it worked for two different spacings. However, it was still very surprising to see how close the measurements were, especially considering the design of hairpin 1. To explain this surprise, it was proposed that **the majority of the plasma dielectric permitivitty measurement by the probes occurs near the hairpin tip, i.e. where the electric field of the standing wave is at a maximum**. A simple experiment to prove this was carried out. It involved measuring the dielectric permittivity of a liquid by the hairpin probe, but with the hairpin probe immersed at various depths into the liquid. The liquid chosen was heptane, C_7H_{16}, a form of colourless petrol. The relative dielectric permittivity of heptane is 1.924 [Folgerø 96]. The results of the hairpin resonance in heptane can be seen in figure 2.31. The resonance is shown to shift to lower frequencies as the probe is lowered into the liquid. This is the opposite of what happens in a plasma. The curve is asymptotic in nature, reaching a value of 1.475 GHz as the hairpin becomes fully immersed in the heptane, the result being that the majority of the resonance shift occurs during the immersion of the first half of the hairpin resonator. This confirms the theory that the majority of the dielectric measurement occurs where the electric field is a maximum.

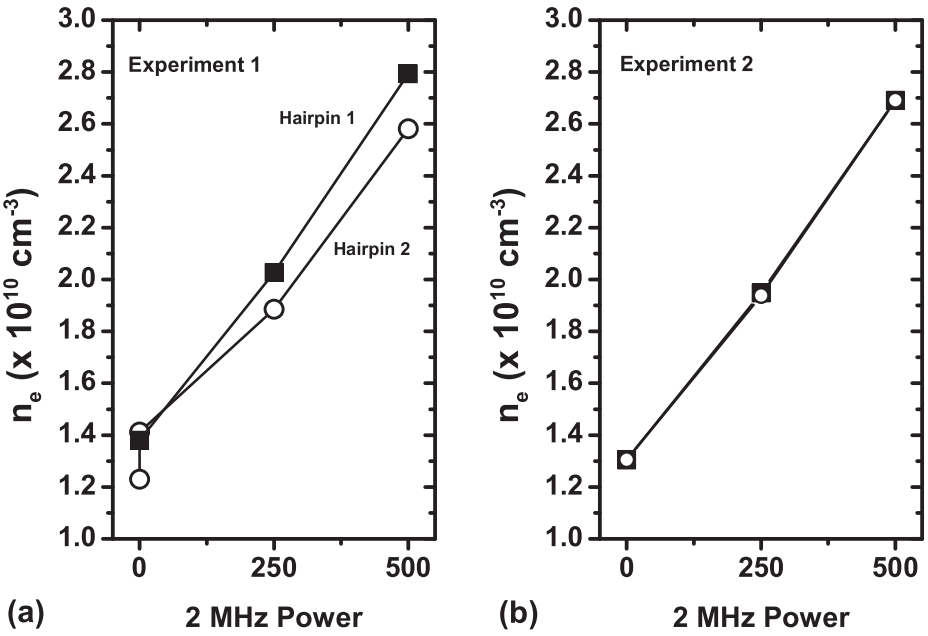


Figure 2.30: Electron density measurements as a function of 2 MHz power with two different hairpins in an $Ar/O_2/c\text{-}C_4F_8$plasma, 52 mTorr at a constant 27 MHz power of 250 W. (a) both probes were not identically aligned axially; (b) both probes in same axial position.

We can also estimate the value of the dielectric permittivity using the relation:

$$\epsilon = \frac{f_0^2}{f_r^2}$$

which gives 2.017 as the dielectric permittivity of heptane (about 3 % higher than the value given in [Folgerø 96]).

2.3 Cavity Ring-Down Spectroscopy

Absorption spectroscopy is a direct way to measure absolute species densities. We initially tried broadband absorption spectroscopy (BBAS) for the measurement of the negative fluorine ion, F^- [Curley 04b, Curley 04a]. As it was not sensitive enough, we turned to cavity ring-down absorption spectroscopy (CRDS).

2.3.1 Principle of absorption spectroscopy

An electromagnetic wave, of frequency ν, travelling through a medium may be absorbed by the atoms or molecules composing that medium. The absorption of the wave leads to the excitation of either an electronic, vibrational or rotational state of the atom or molecule. As these states are discrete (i.e. non continuous) in nature and as an electromagnetic wave exhibits a corpuscular nature (photons), the absorption occurs on a

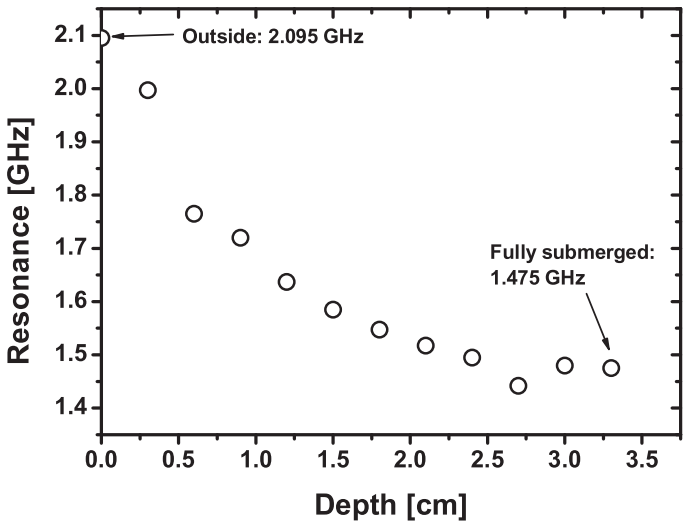


Figure 2.31: Variation of the hairpin resonance as it is immersed into various depths of heptane.

photon by photon basis where each photon has an energy:

$$E_{photon} = h\nu = hc/\lambda \tag{2.44}$$

where h is Planck's constant and is equal to 6.626068 $\times 10^{-34}$ m^2 kg s^{-1} or J.s. By taking the ratio of the light transmitted, I, to that of the incident light, I_0, for various frequencies or wavelengths, a transmission spectrum is obtained.

$$T(\lambda) = \frac{I(\lambda)}{I_0(\lambda)} \tag{2.45}$$

The corresponding absorption spectrum is therefore:

$$A(\lambda) = 1 - T(\lambda) \tag{2.46}$$

When the medium being studied is a plasma, the light emission from the plasma needs to be taken into account. In a typical absorption experiment, spectra are acquired in the following four modes:

1. Plasma on, light source on: $I_{source+plasma}$
2. Plasma off, light source on: I_{source}
3. Plasma on, light source off: I_{plasma}
4. Plasma off, light source off: $I_{background}$

From equation 2.45, the transmittance is defined and calculated as:

$$T = \frac{I_{source+plasma} - I_{plasma}}{I_{source} - I_{background}} \tag{2.47}$$

The absorption spectrum thus obtained can then be used to calculate the density of the absorbing species using the *Beer–Lambert law*[2]. The Lambert part of the law states that the proportion of light absorbed by a transparent medium is independent of the intensity of the incident light and that each successive layer of the medium absorbs an equal fraction of the incident light. This results in an exponential decay of the light intensity as it passes through the medium. Beer's part of the law introduces the dependence on density. A photon can be absorbed only if it encounters an atom or molecule. The probability of such an interaction occurring is directly proportional to the number of absorbing molecules encountered by the light beam. Accordingly, Beer's law states that the amount of light absorbed is proportional to the number density of the absorbing molecules through which the light passes. This is incorporated into the Lambert law to give the expression :

$$I = I_0 \times e^{-n\sigma(\lambda)L} \tag{2.48}$$

where n is the density, $\sigma(\lambda)$ is the molecule's absorption cross section and L is the length (or thickness) of the absorbing material.

In the limit where $n\sigma(\lambda)L \ll 1$, this expression may be written as:

$$\frac{I}{I_0} = 1 - n\sigma(\lambda)L \tag{2.49}$$

$$n\sigma(\lambda)L = 1 - \frac{I}{I_0}$$

$$n\sigma(\lambda)L = 1 - T \tag{2.50}$$

such that together with the relation given in equation 2.46 gives us the following relationship between the absorption and the material properties:

$$A(\lambda) = n\sigma(\lambda)L \tag{2.51}$$

The density of the absorbing molecule/atom is therefore given by:

$$n = \frac{A(\lambda)}{\sigma(\lambda)L} \tag{2.52}$$

The absorption cross section, $\sigma(\lambda)$, is a fundamental property of the absorbing medium and cannot be modified. The absorption path length, L, and the density, n, may be controlled to vary the magnitude of $A(\lambda$, though here n is the quantity to be determined. For proof of principle measurements and to improve the signal to noise (S/N) ratio, we can sometimes adjust the plasma parameters to give the largest possible value of n, and

[2]The law was in fact first discovered by Pierre Bouguer before 1729. It is mis-attributed to Johann Heinrich Lambert, who cited Bouguer's "Essai d'Optique sur la Gradation de la Lumière" (Claude Jombert, Paris, 1729) – and even quoted from it – in his "Photometria" in 1760. Much later, August Beer extended the exponential absorption law in 1852 to include the concentration of solutions in the absorption coefficient.

when possible we try to choose a wavelength such that σ is at a maximum.

Various absorption spectroscopy techniques exist and are chosen depending on the property and the quantity of the species one wishes to measure. The simplest method is broadband absorption spectroscopy (BBAS) and uses a broadband light source, such as a tungsten filament or a plasma arc [Booth 98, Bulcourt 04, Curley 04a]. After passing through the sample to be measured, the light is spectrally resolved using a spectrograph and is then recorded usually by a photodiode array (PDA) or a charged-coupled device (CCD) camera. BBAS has the advantage that the whole absorption band is measured simultaneously. This eliminates the drift problems associated with laser scans. It intrinsically allows for time-resolved measurements over the entire absorption band in a simple manner. However, the light sources used typically drift in light intensity during the measurement, introducing drift into the baseline. Even more problems are caused by the light intensity drifting unevenly across the spectral range, and so the baseline drift has a wavelength dependence. In the case of a Xenon arc lamp used for UV-BBAS, for example, the wavelength dependent baseline drift is often in the 10^{-4} – 10^{-3} range. Single atomic line transitions are often best measured by a scanning tunable laser, as long as the spectral width of the laser is small compared to the line being measured. The transmitted light intensity is measured over time by a photodiode as the laser wavelength is scanned. Tunable lasers have the advantage of high spectral resolution and high stability and so small spectral features can be measured with high S/N ratios. Their highly collimated beams also allow for very good space-resolved, line integrated measurements. These lasers are, however, often very expensive and encombersome, although some of these issues have recently been offset by the advent of cheaper diode lasers. Laser absorption measurements may also suffer from drift effects due to the combination of the time delay as the laser is scanned in wavelength and drift phenomena in the plasma (e.g. temperature changes). In such circumstances vibrational and rotational temperatures may be difficult to determine. Also, laser wavelengths are often spectrally limited and so large spectral features cannot always be measured.

2.3.2 Absorption of the negative fluorine ion

Negative ions can be detected by measuring the weak absorption due to photodetachment. Experimental measurements of the photodetachment cross section of the negative fluorine ion cross section have being made by Mandl et al. and Vacquié et al. [Mandl 71, Vacquie 87], as well as theoretical calculations using the many-body perturbation theory [Ishihara 74]. The results from these works are all within 20% of one another. For the purpose of this study we will use the more recent experimental results from Vacquié and co-workers. Figure 2.32 (a) depicts the photodetachment cross section of the negative fluorine ion over the wavelength range 300 – 380 nm. The threshold for

photodetachment is 364.5 nm or 3.402 eV. More recent measurements of the electron affinity of fluorine using electron spectrometry have put the exact value at 3.4011895 eV [Blondel 01].

Figure 2.32 (b) simulates the absorption spectra that would be obtained for various F^- densities in a single pass of our chamber (plasma diameter = 20 cm). Even when assuming large densities, say 3×10^{11} cm^{-3}, the maximum absorption obtained is only about 4×10^{-5}, which is well below the noise limit of typical UV-BBAS experiments. By using a multipass set-up (three passes) we hoped that this would increase the sensitivity of UV-BBAS to detect F^-. Our experimental set-up for UV-BBAS is shown in figure 2.33. The effective absorption length was increased from 20 cm to about 60 cm. This would bring the absorption due to high negative ion densities up to about 10^{-4}. Although it was possible to reduce the shot noise to 10^{-5}, fluctuations in the Xe arc lamp's spectral profile meant that attempts to reduce fluctuations in the baseline to less than 10^{-4} proved unsuccessful and we were unable to detect negative fluorine ions using UV-BBAS. However, this allowed us to put an upper limit on the F^- of about 2×10^{11} cm^{-3} [Curley 04b, Curley 04a].

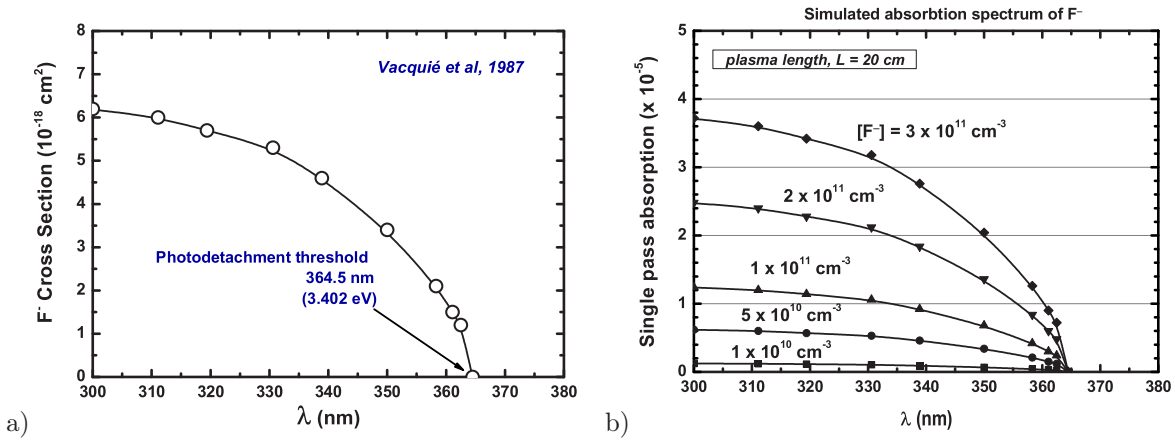


Figure 2.32: (a) Fluorine photodetachment cross sections from Vacquié et al. [Vacquie 87]; (b) Simulated absorption continuums of various densites of the negative fluorine ion using the cross sections in (a).

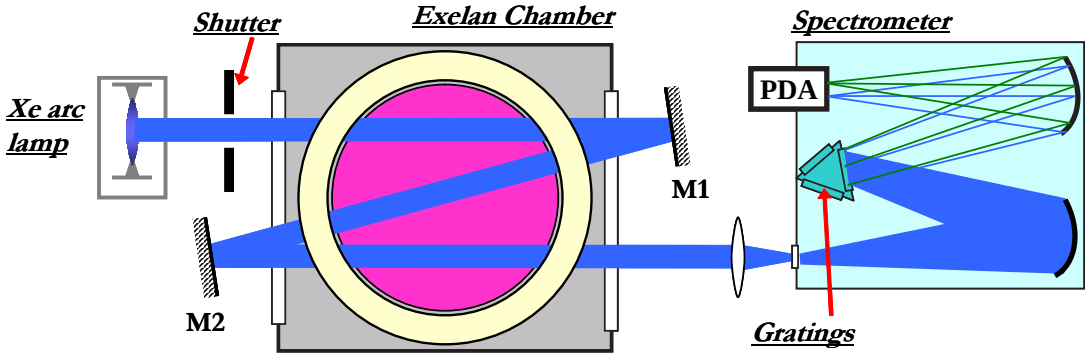


Figure 2.33: Experimental setup of the triple pass UV broadband absorption spectroscopy

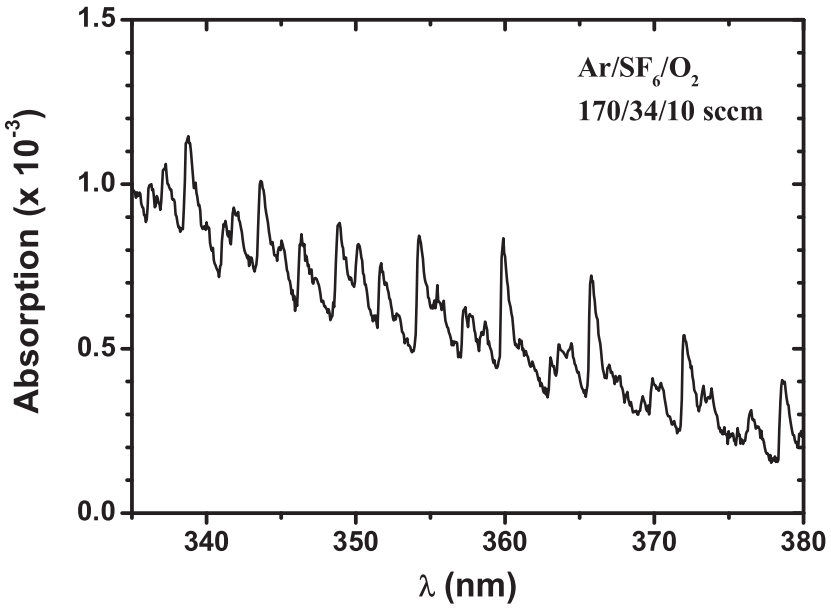


Figure 2.34: UV broadband absorption spectrum of an $Ar/SF_6/O_2$ plasma over the335 nm – 380 nm range. The relatively strong absorption bands of S_2 in this region make F^- dectection impossible.

2.3.3 Cavity ring-down spectroscopy

To measure the weak absorption signal of the negative fluorine ion, F^-, we decided to use a high sensitivity absorption technique known as *cavity ring-down spectroscopy* or *CRDS*. Measurements of the negative ions of hydrogen and oxygen had previously being undertaken by Quandt (1998) [Quandt 98b] and Grangeon (1999) [Grangeon 99] respectively. The negative fluorine ion had not previously being measured using this technique.

CRD spectroscopy is considered to be a mature diagnostic technique among the plasma community and also a wide variety of other communities. As such, the finer details will not be covered here but references to the most noteable publications will be made. The first known use of CRDS was by O'Keefe et al. in 1988 [O'Keefe 88]. It was considered a standard spectroscopic tool by the year 2000, as pointed out by Berden et al. in the review paper *Cavity ring-down spectroscopy: Experimental schemes and applications* [Berden 00]. During the compilation of that review paper, Berden and co-workers had catalogued over 190 papers on CRDS. They also note that "more and more papers appear with titles *without* the words *'cavity ring-down'*".

The year 2000 also saw the beginning of a series of successful short annual meetings known as the *Cavity Ring-Down User Meeting*. These meetings were also a measure of the evolution of CRDS. Whereas the first few meetings had a large component dedicated to the CRDS technique itself, the meeting in 2005 had evolved to a point whereby a large range of applications of CRDS were presented, but little on the fundamentals of the

technique. This again reflects the maturation of CRDS as a diagnostic technique.

Principle of the CRDS technique

There are several methods and variations of employing the CRDS technique. This section describes the CRDS technique as used in this study.

Unlike conventional absorption techniques which measure the magnitude of absorption, CRDS relies on the measurement of the *rate of absorption*. A pulsed laser beam is directed into an optical cavity formed by two highly reflecting ($> 99\%$) concave mirrors seperated by a distance, L. The packet of photons undergo multiple reflections within the cavity, but as the mirrors' reflectivities are not 100%, a small number are lost from the cavity at each reflection. If the loss through the mirrors follows Beer's law, the result is an exponential decay of photons in time within the cavity after the end of a light pulse. This is sometimes referred to as the ringing down of the cavity. If the photons exiting at one mirror are measured with infinite time resolution, one will observe a series of photon packets, the magnitude of each peak decaying exponentially over time, as shown in figure 2.35 (a). In practice, both the very short pulse lengths ($t_p \sim 10$ ns) and the pulse overlapping with itself ($L/c \leq t_p$) leads to detectors seeing only a continuous exponentially decaying continuum. Generally, the intensity of the light exiting the cavity is given by:

$$I(t) \propto \int_0^\infty I(\lambda) \exp\left[-\frac{t}{\tau(\lambda)}\right] .d\lambda \tag{2.53}$$

where $1/\tau(\lambda)$ is the decay rate, and $\tau(\lambda)$ is known as the ring-down time. In an empty cavity, the decay rate is solely determined by the reflectivity, $R(\lambda)$, of the mirrors and the optical path length, L, between the mirrors. If an absorbing species is present within the cavity, then this will add additional loss to the light pulse, therefore increasing the decay rate, or conversely, reducing the ring-down time. The ring-down time is given by:

$$\tau(\lambda) = \frac{L}{c\left[|\ln R(\lambda)| + \sum_j n_j \sigma_j(\lambda) d\right]} \tag{2.54}$$

where c is the speed of light, n_j is the density of the absorbing species, j, $\sigma_j(\lambda)$ is the wavelength-dependent cross section and d is the absorption path, which in our case will be the plasma diameter. The assumption is made that the absorbing species' density is independent of position. As $R(\lambda) \approx 1$, one can write $|\ln R(\lambda)| \approx 1 - R(\lambda)$.

If we are looking for a particular species in a spectral range where only that particular species absorbs, then the common form of equation 2.54 which is often used is:

$$\tau(\lambda) = \frac{L}{c\left[1 - R(\lambda) + [F^-]\sigma(\lambda) d\right]} \tag{2.55}$$

where we have specifically mentioned the negative fluorine ion as the absorption species

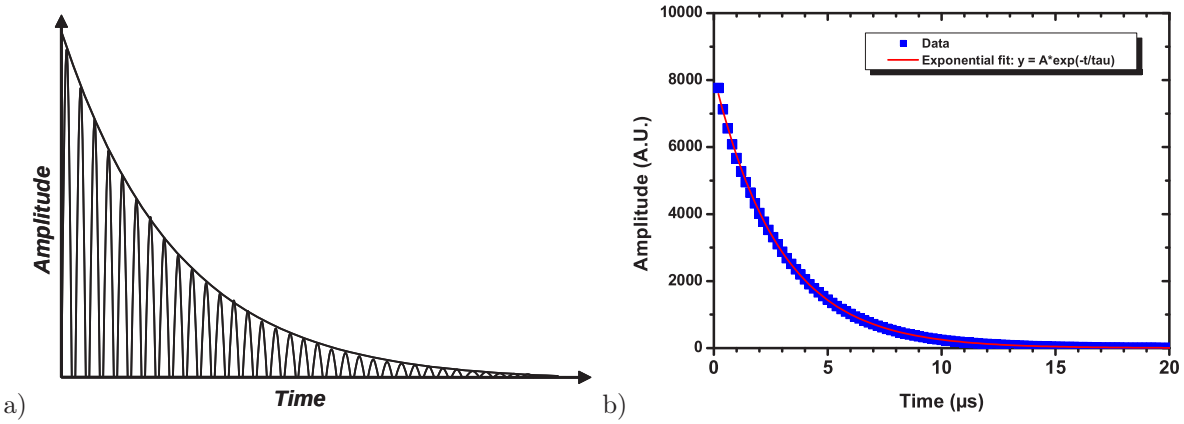


Figure 2.35: a) Exagerated schematic representation of individual pulses exiting a CRDS optical cavity; b) Experimental data showing ring-down of the light exiting the cavity, with accompanying exponential decay fit.

and where its density is denoted by $[F^-]$. The ring-down time depends only on the properties of the cavity and the absorbing species present in the cavity and is independent of the amplitude of the light inside the cavity. By measuring the ring-down time with both the plasma off, τ_1, and the plasma on, τ_2, we can calculate the absorption, $A = n\sigma d$.

$$\begin{aligned} \tau_1(\lambda) &= \frac{L}{c\,[1 - R(\lambda)]} \\ \tau_2(\lambda) &= \frac{L}{c\,[1 - R(\lambda) + A(\lambda)]} \\ A(\lambda) &= \frac{L}{c}\left(\frac{1}{\tau_2(\lambda)} - \frac{1}{\tau_1(\lambda)}\right) \end{aligned} \tag{2.56}$$

Experimental setup

The experimental set-up is shown in figure 2.36. The optical cavity consisted of two high reflectivity mirrors (Layertec or Los Gatos) of 1 m radius of curvature mounted 1.6 m apart on flexible bellows at the end of extension tubes. An argon gas purge was injected close to the mirrors, and 5 mm diameter apertures were installed between the extension tubes and the chamber in order to prevent reactive species from the plasma from reaching the mirror surfaces. The laser beam was produced by a frequency-doubled Nd-YAG (yttrium aluminium garnet) (532 nm at 10 Hz) pumped dye laser (Sirah, using either Styryl 8 or Pyridine 2 dyes) with frequency doubling. Typical laser energies were several tenths of a millijoule in the range of 340–380 nm, with a pulse duration of 9 ns. The laser beam was directed into the optical cavity and through the reactor at midheight. The laser beam quality was improved by a spatial filter consisting of a 50 mm focal length lens (L1) and a 50 μm pinhole (PH), and then injected into the cavity with a 60 mm focal length lens (L2). This improved the spectrum reproducibility and base line stability.

The light exiting the opposite end of the cavity was detected by a photomultiplier tube (Hamamatsu R3896) fitted with an UV bandpass filter (Schott DUG 11X) to exclude visible light.

The ring-down signal was passed through a 500 ns RC filter and digitized on a personal computer using a 14-bit vertical resolution fast data acquisition card (Gage Compuscope 14200), using a 200 ns sampling interval with 160 points per laser shot (i.e., 32 μs overall sample length). A LabVIEW^{TM} routine was developed to control the data acquisition sequence and determine the ring-down time for each laser shot in real time (see screenshot in figure 2.37). The ring-down time was calculated by fitting an exponential decay (with base line offset) using a weighted least-squares fitting algorithm. Depending on the laser wavelength, typical ring-down times between 2 and 4 μs were obtained. The plasma was switched on for 5 s and switched off for 5 s and the ring-down times for both "plasma on" and "plasma off" were calculated for 30 on/off cycles. In this way the noise could be reduced to the equivalent of 10^{-6} per single pass.

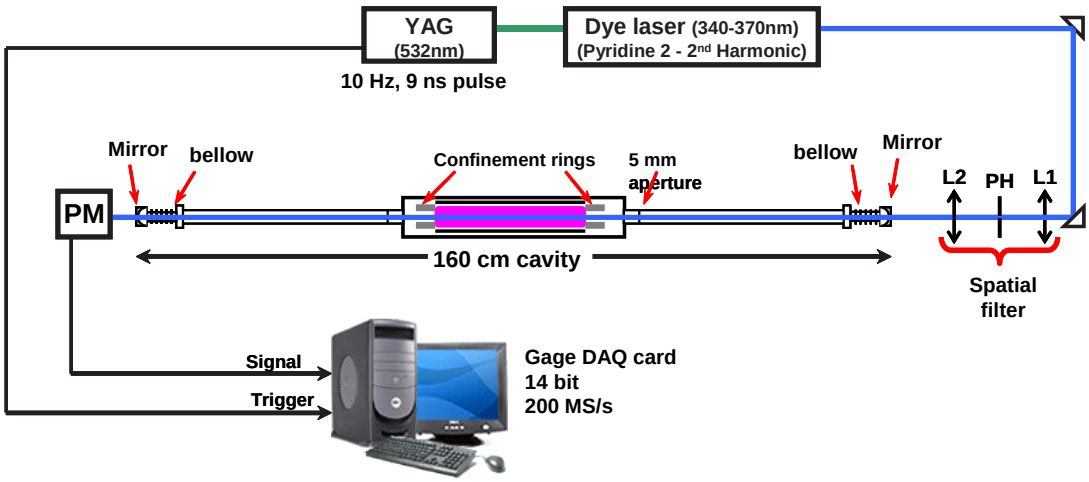


Figure 2.36: Schematic of the UV-CRDS experimental setup

Development of the CRDS experiment

Due to electromagnetic noise issues arising from the firing of the flash lamp in the YAG laser, a background signal was taken before each series of experiments. The analysis routine algorithm is outlined in figure 2.38 and should be fairly self-explanatory. A baseline was systematically subtracted for each laser shot before the data was fit. This was faster than adding a baseline parameter to the fit function, thereby leaving us with a simple exponential fit function:

$$A \exp -t/\tau \tag{2.57}$$

where A was the maximum amplitude at beginning of the pulse and τ was the ring-down time. The exponential fit function in LabVIEW was actually a linear fit of the natural

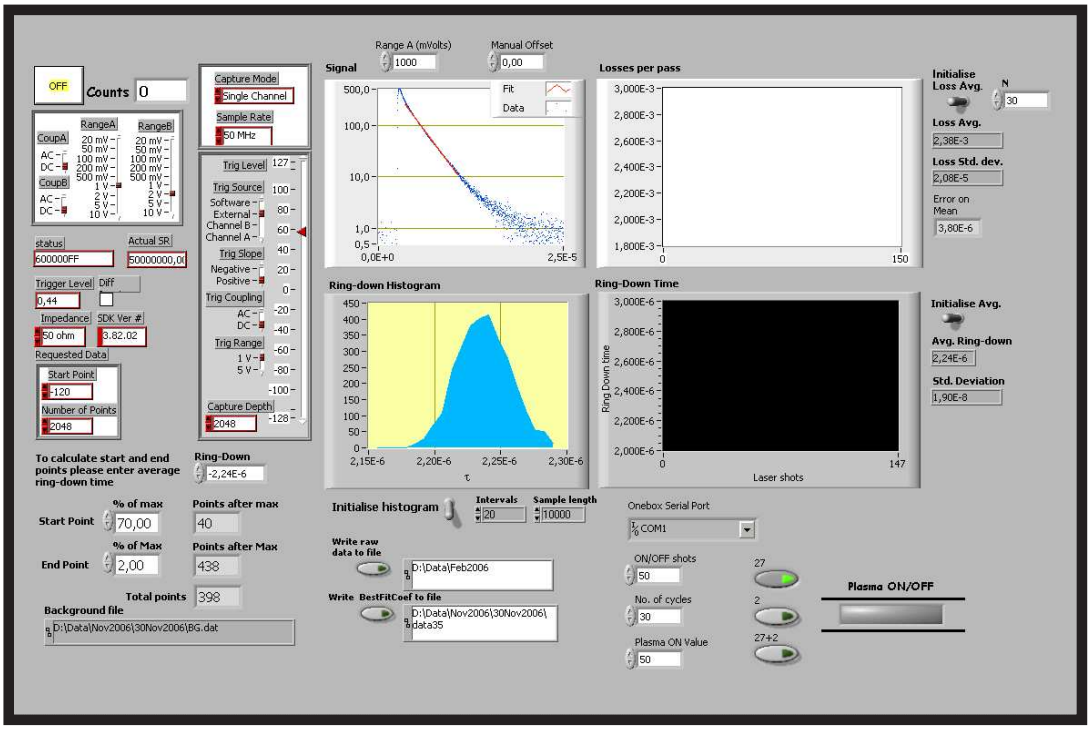


Figure 2.37: Screenshot of the LabVIEW routine used at the LPTP during the CRDS anaysis.

logarithm of the signal. Removing the baseline was therefore also necessary to avoid errors in the event of a negative baseline. The baseline was calculated by pre-triggering the acquisition card to about 1 μs before the laser shot and averaging most of those initial data points.

The mirror reflectivities were calculated for the various wavelengths under study. Mirrors from Layertec were initially used but underwent quite serious degradation in the first few months. A dramatic example of such degradation can be seen in figure 2.39. This was in one of our very first experiments with the use of plasma, but where only very short extension tubes were used. The mirrors were therefore not protected well enough from the plasma, even with the presence of argon gas flowing over their surfaces. This was the reason we moved to using very long extension tubes and it also led to us incorporating the small diameter (5 mm) apertures into those tubes. The addition of the longer tubes was sufficient to stop (or at least slow down significantly) the degradation due to plasma effects. However, when the mirrors were exposed to air they also suffered degradation. This may have been due to the deposition of water on their surfaces, possibly forming hydrofluoric acid due to the presence of trace amounts of fluorine from the plasma. Cleaning the mirror surfaces with acetone and optical lens tissue proved to be a very effective method in recovering from some of the degradation.

As a result of the damage sustained by the Layertec mirrors, but also due to a lower reflectivity than expected, they were replaced by mirrors fabricated by Los Gatos. A

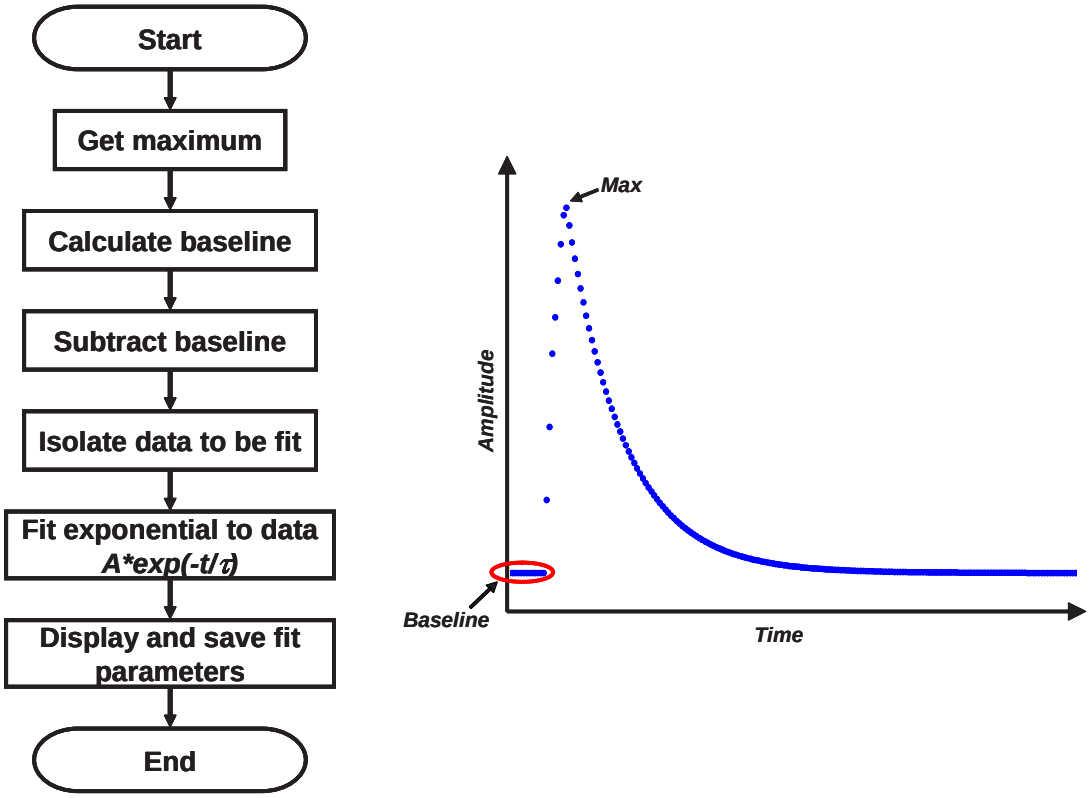


Figure 2.38: Flowchart of CRDS signal fitting algorithm.

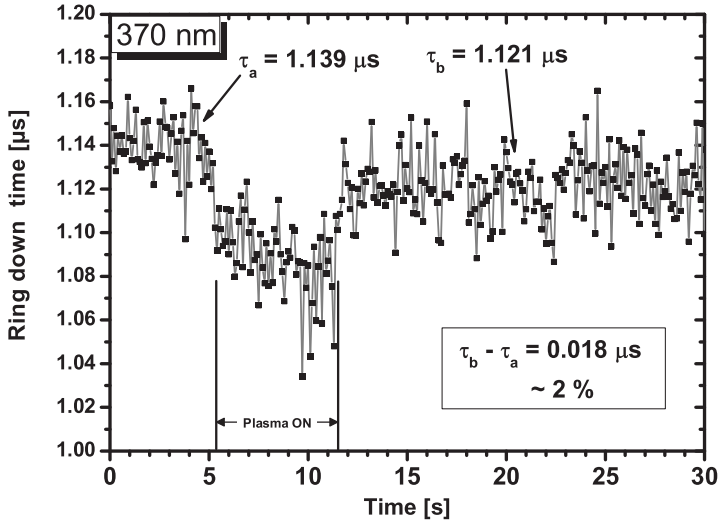


Figure 2.39: Ring-down times attained from single laser shots. The graph shows the average ring-down time before the plasma cycle ($\tau_a = 1.139\mu$s) and the average ring-down time after the plasma cycle ($\tau_b = 1.121\mu$s), a degradation of about 2% in just 6 seconds! The mirrors used were those by Layertec.

comparison of the reflectivities of both mirrors can be seen in figure 2.40. Note that the Layertec mirrors had already undergone some degradation when the reflectivities were measured, whereas those by Los Gatos were new and had not yet been exposed to plasma. With the new mirrors installed, reflectivities of about 99.9% were possible for a while. Over time, however, these mirrors also degraded slightly. While not being used, the mirrors are stored in a vacuum pumped desiccator to prevent them from degrading further.

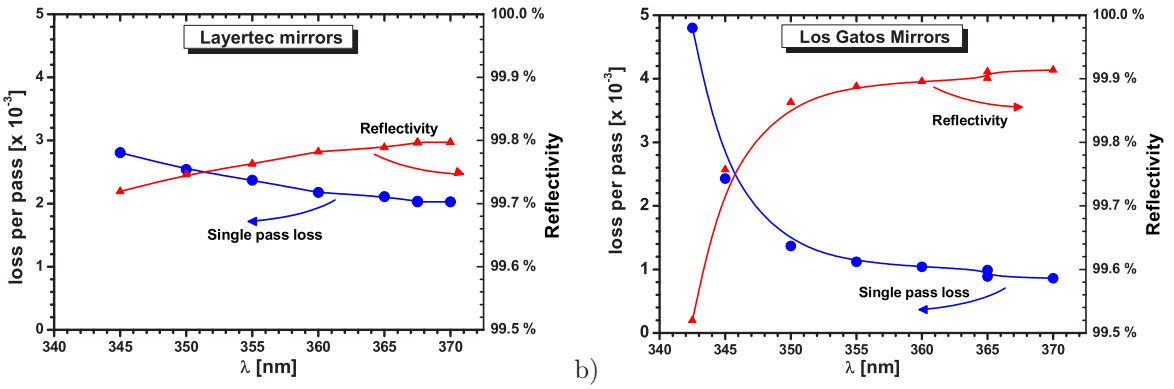


Figure 2.40: Comparison of mirror losses/reflectivities for the two sets of mirrors used: (a) Layertec and (b) Los Gatos.

Other problems in the CRDS experiments were encountered due to thermal drift effects. This is clear from the data plotted in figure 2.41. In part (a), we can see that the absorption spectrum can take up to to 5 minutes to stabilise from the start-up of a "cold" reactor. In part (b) we see that the absorption spectrum takes about 3 shots or 0.3 seconds to reach a stable value. The amplitudes of the variations in the absorption spectra with time suggest strongly that this is caused by the time it takes for the baseline to stabilise with temperature. An empirical approach was taken to counter-act these drift effects. Firstly, the "cold" reactor (i.e. at the beginning of the day) was always "warmed up" or conditioned by at least 5 minutes of ON-OFF periods before the true experimental data was recorded. Secondly, the first three shots in the OFF and ON periods were removed to avoid the effects of drift after plasma switch on.

Another possible issue was discovered when the randomness of the ring-down data was examined. In an ideal scenario, the scatter of the measured ring-down times should be spread around a central value with a probability defined by a Gaussian function. The maximum of this Gaussian function should be equal to the average value of all the data points. Figure 2.42, however, shows that there a discrepancy of about 0.07% between the average value and the Gaussian maximum. For reference, 1000 data points, (100 seconds) were used in constructing this histogram. Although seemingly very small, in absolute terms this discrepency corresponds to a difference of 1.4 $\times 10^{-6}$, which is equivalent to an absolute absorption at 350 nm of a F^- density of 2 $\times 10^{10}$ cm^{-3}. The effect of this on the

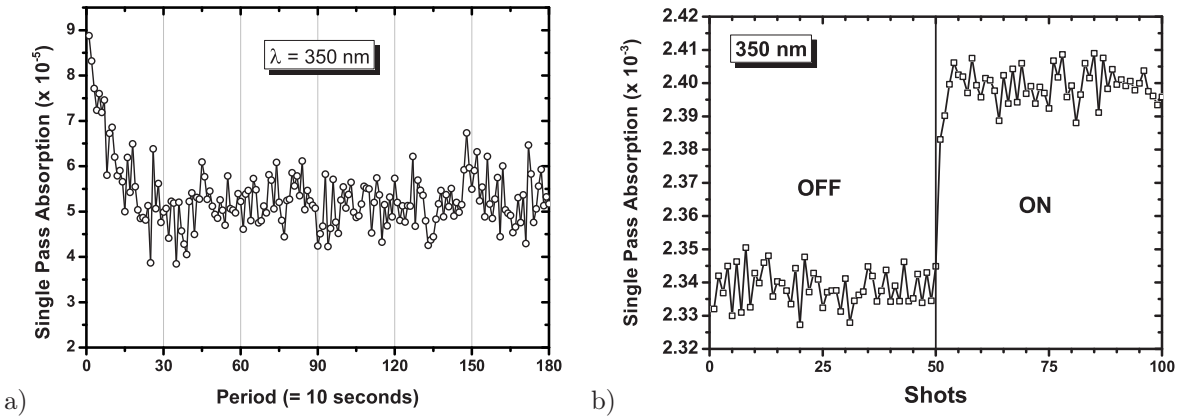


Figure 2.41: a) Absorption measured at 350 nm over time. Plasma turned on at 0, reaches stability after 30 periods (5 minutes); (b) Average of 180 OFF and ON periods on a shot by shot basis.

CRDS measurements is not known and no method for accounting for it was implemented.

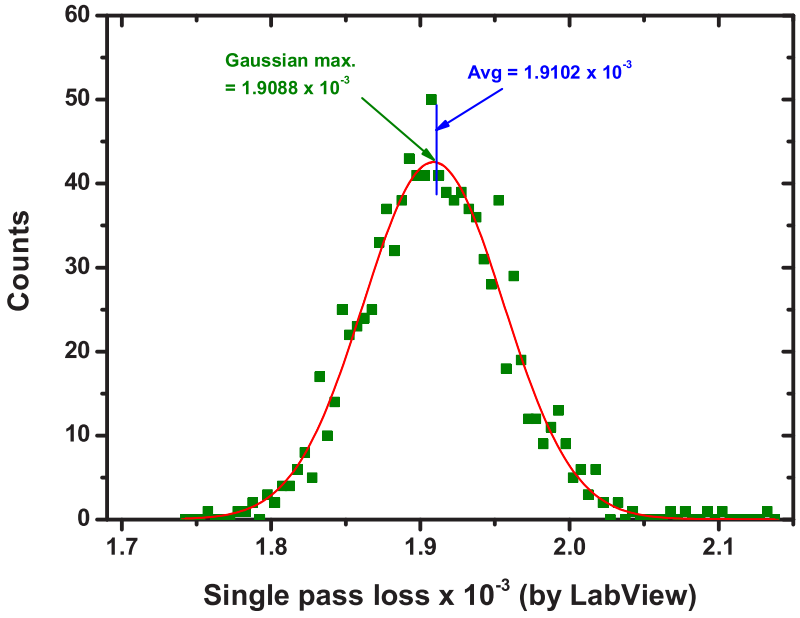


Figure 2.42: Histogram Example

Chapter 3

Results and analysis

Contents

3.1 Introduction . . . 102

3.2 Fluorine negative ion densities . . . 103

3.2.1 $Ar/O_2/c\text{-}C_4F_8$ . . . 103

3.2.2 $Ar/O_2/CF_4$ . . . 105

3.3 Determining the negative ion fraction . . . 107

3.3.1 Negative ion fractions from CRDS and the hairpin probe . . . 108

3.3.2 Two-probe technique: simple model . . . 109

3.3.3 Two-probe technique: fluid model . . . 115

3.3.4 Comparison of the various estimations of the negative ion fractions . . . 118

3.3.5 Introducing variable mobility to the fluid model . . . 120

3.4 Charged particle dynamics - Effect of gas composition . . . 126

3.4.1 $Ar/O_2/c\text{-}C_4F_8$ – varying the $c\text{-}C_4F_8$ gas flow . . . 126

3.4.2 $Ar/O_2/c\text{-}C_4F_8$ – varying the O_2 and $c\text{-}C_4F_8$ gas flows . . . 130

3.4.3 $Ar/c\text{-}C_4F_8$ – varying the $c\text{-}C_4F_8$ gas flow . . . 133

3.4.4 $Ar/O_2/CF_4$ – varying the O_2 and CF_4 gas flows . . . 135

3.4.5 $Ar/O_2/CF_4$ – varying the O_2 gas flow . . . 136

3.4.6 $Ar/O_2/SF_6$ – varying the O_2 and SF_6 gas flows . . . 138

3.4.7 CF_4 plasma – effects due to SF_6 addition . . . 139

3.5 Charged particle dynamics – Effect of pressure . . . 140

3.5.1 $Ar/O_2/c\text{-}C_4F_8$ – varying the pressure: 25 – 100 mTorr . . . 141

3.5.2 Pressure effects on the ion flux probe I–V curves . . . 141

3.6 Charged particle dynamics – Effect of applied power . . . 143

3.6.1 $Ar/O_2/c\text{-}C_4F_8$: 160/8/16 sccm . . . 144

3.6.2 $Ar/c\text{-}C_4F_8$: 160/24 sccm . . . 150

3.6.3 Ar/O_2 : 160/24 sccm . . . 151

3.1 Introduction

This chapter describes the principal experimental results and, apart from this introduction, is divided into four sections, as outlined in the table of contents above. It is not possible to explain the analysis techniques used without including references to the results and therefore the description of the analysis techniques will be interwoven with the presentation of the results.

Firstly, the fluorine negative ion density measurements by cavity ring-down spectroscopy will be presented. Due to the many difficulties that were encountered (poor mirror reflectivities and weak photodetachment cross-section of F^-), it was not possible to explore as large a parameter space compared to when using the electrostatic probes. However, the presence of negative fluorine ions was verified in several experimental conditions and we could then determine the negative ion fractions so that a comparison between the CRDS results and electrical probe results could be made.

Secondly, we will examine the various methods which can be used in determining the negative ion fraction, with particular emphasis on understanding the relationship between the electrostatic probe results and the plasma electronegativity. The negative ion fractions will first be calculated using the F^- densities measured by CRDS and the corresponding electron densities as measured by the hairpin probe. The process of using probe only results for calculating the negative ion fraction will then be introduced using first a simple modelling approach and then by using the results from the fluid model presented in section 1.5.2. The electronegativities calculated from the combined CRDS and hairpin results will be used as a benchmark for the models. The large discrepencies between the theory and the experimental results will lead us to modify the existing theory.

Next, the influence of the gas composition (gas species and gas flows used) on the plasma properties (n_e, Γ_i, α, T_e) will be looked at for various single and dual frequency plasma conditions. The RF currents and voltages will also be examined where they are available. The gases used are argon (Ar), oxygen (O_2), octafluorcyclobutane (c-C_4F_8), cabontetrafluoride (CF_4) and in some cases sulphur hexafluoride (SF_6). The RF powers used were usually 250 W for each of the generators (2 MHz & 27.12 MHz), and so the total power was 500 W during dual frequency operation.

Finally, the effect of changing the applied RF power will be studied for various gas mixtures. These mixtures have been chosen to reflect those that are commonly used in an industrial context, but also to tie in with the mixtures used elsewhere in this thesis. As in the preceding section, the effects will be observed through changes in the plasma properties.

The ion flux probe measurements were carried out for the most part with the guard ring in operation. There were some situations where connecting the guard ring caused

RF to perturb the mass flow controllers and so the guard ring was not used. However, the slope parameter in the fitting algorithm proved to be very robust in eliminating the edge sheath effects and so the errors due to non-use of the guard ring are considered negligible. The hairpin probe results were corrected for sheath effects (see section 2.2.2). We initially believed that the sheath effects were negligible, which was the case in many of our experimental conditions. However, the results were often very interesting in situations where the electron density declines, which are precisely the situations where sheath effects on the hairpin become important. This is particularly obvious when calculating the ion flux to electron density ratio, as was shown previously (see figure 2.24 on page 79).

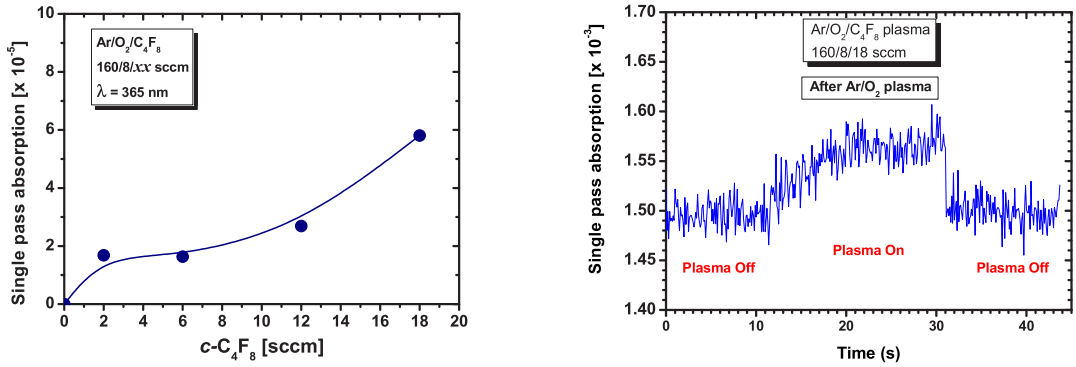
3.2 Fluorine negative ion densities

The presence of a significant unidentified background continuum in the measurements, coupled with the unstable nature of that baseline, made taking CRDS measurements of F^- very difficult and very time consuming. As such, it was not possible to measure negative fluorine ion densities over a large parameter range. The parameter combinations chosen were those which would prove valuable in making comparisons with the electrostatic probe measurements, i.e. varying oxygen and fluorocarbon gas flow rates. An aim was also to test the numerical results of Georgieva.

3.2.1 $Ar/O_2/c\text{-}C_4F_8$

This is the main gas chemistry studied in this thesis and was expected to produce high negative ion densities. An unidentified background continuum caused numerous difficulties in the measurements. The evolution of this continuum with increasing c-C_4F_8 flow in an Ar/O_2 plasma is shown in figure 3.1 (a). The solid line is a simple B-spline curve to help guide the eye. The measurements were taken at 365 nm where no photodetachment due to the presence of F^- occurs. Note that the continuum is absent from an Ar/O_2 plasma and then increases as the c-C_4F_8 flow is increased. This suggests that the continuum is related to some form of fluorocarbon species in the plasma or that O_2 destroys the species that is causing the continuum absorption (some unsaturated C_xF_y molecule maybe). There is a possibility that it could be due to another negative ion species such as CF_3^-, but the negative ion densities required to produce such an offset seem unrealistically high ($> 10^{12}$ cm^{-3}). Figure 3.1 (b) shows the interesting case where the evolution of the continuum is followed over time at the beginning of an $Ar/O_2/c$-C_4F_8 plasma in the case where the reactor has being previously "cleaned" or conditioned using an Ar/O_2 plasma. This data suggests a different story in that the continuum may be related to surface chemistry effects, possibly the creation of Si_xF_y species.

Figure 3.2 shows a typical absorption spectrum in an $Ar/O_2/c$-C_4F_8 mixture for both



a) b)

Figure 3.1: (a)Baseline amplitude at 365 nm (no F^- photodetachment) in an $Ar/O_2/c\text{-}C_4F_8$ plasma for various $c\text{-}C_4F_8$ gas flow rates (0 – 18 sccm). (b) The increase in the baseline at 365 nm at the start of an $Ar/O_2/c\text{-}C_4F_8$ plasma after the reactor has being exposed to an Ar/O_2 plasma.

single (27 MHz = 250 W) and dual (27 MHz = 250 W, 2 MHz = 250 W) frequency plasmas. The data is fitted by using the cross-sections of Vacquié et al. (solid lines). The error bars on the data points correspond to the standard deviation of the mean, whereas no error bars are shown on the fit curves (from uncertainties in the cross-sections) for aesthetic reasons, but are expected to be no more than 24 % [Vacquie 87]. The F^- densities estimated during this particular experiment were 1.7×10^{11} cm^{-3} and 2.0×10^{11} cm^{-3} for the single and dual frequency cases respectively.

In figure 3.3 is shown the variation of the negative fluorine ion density as the $c\text{-}C_4F_8$ and O_2 gas flow rates are varied from 0–24 sccm (24–0 sccm), with the combined $c\text{-}C_4F_8$+O_2 flow rate remaining constant at 24 sccm. The pressure remained roughly constant at about 54 mTorr. The maximum F^- density obtained was, naturally, in the $Ar/c\text{-}C_4F_8$ plasma (right-hand side), with a value of 1.0×10^{11} $cm^{-3} \pm 0.5 \times 10^{11}$ cm^{-3}. No F^- was detectable (noise-limited) below a $c\text{-}C_4F_8$ flow rate of 12 sccm (below 50% $c\text{-}C_4F_8$ flow with respect to O_2 flow). The error bars are indicative only and reflect the uncertainty resulting from the standard deviation in the mean (raw CRDS result), the uncertainty in the density fit curves (cross-section errors and deviations from the fit line) and the uncertainty arising from the baseline.

The negative fluorine ion density did not appear to vary from single frequency operation to dual frequency operation. This also suggests a lack of density dependence on the total power, which increased from 250 W to 500 W in each case respectively. Variations may of course occur within the limits of the error bars. The conclusion is that, under our experimental conditions, the presence of the 2 MHz power source does not result in a decrease in the negative fluorine ion density, as was suggested by Georgieva and coworkers [Georgieva 06a]. That study examined numrically an $Ar/CF_4/N_2$ dual frequency (27+2 MHz) reactor with applied high frequency (HF) and low frequency (LF) voltages

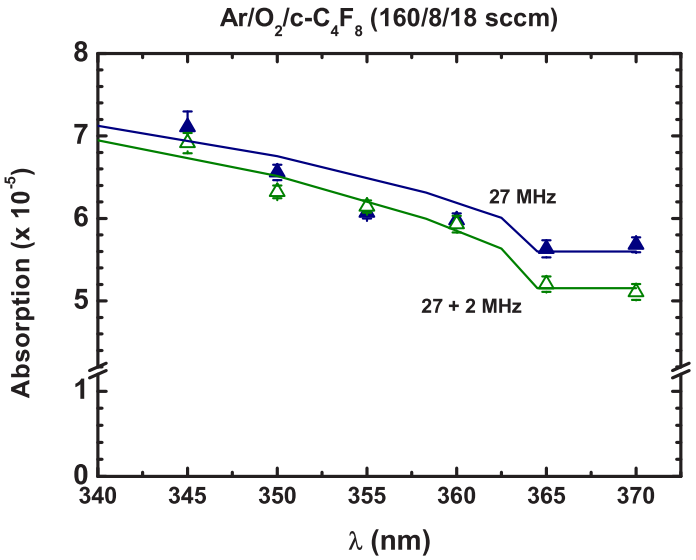


Figure 3.2: The absorption as a function of laser wavelength for $Ar/O_2/c\text{-}C_4F_8$ (160/8/18 SCCM) single (HF=250 W) and dual frequency (HF=250 W, LF=250 W) discharges at 50 mTorr. The estimated F^- densities are 1.7×10^{11} cm^{-3} and 2.0×10^{11} cm^{-3} for the single and dual frequency cases respectively.

of 200 V and 400 V respectively. A pressure of 30 mTorr and an inter-electrode distance of 2 cm were used. For comparison, the HF and LF voltages in our conditions were of the order of 100 V and 700 V respectively in conditions of high $c\text{-}C_4F_8$ flow rates. Although these are not exactly the same conditions, that paper proposed that the decrease in F^- was due to their acceleration across the sheaths and loss to the walls by the high voltage low frequency source. The detection of F^- in the presence of a 2 MHz RF source at 700 V shows that the application of a high voltage low frequency source alone is not sufficient to remove the negative fluorine ions.

Although not presented here, when an Ar/O_2 plasma was run after a F^- rich $Ar/O_2/c\text{-}C_4F_8$ plasma, it was still possible to detect F^- for several minutes, suggesting that fluorine from the chamber surfaces contributed to the creation of F^-.

3.2.2 $Ar/O_2/CF_4$

In this gas mixture the background continuum was less pronounced over the parameter space studied. Examples of negative fluorine ion absorption spectra in Ar/CF_4 and $Ar/O_2/CF_4$ plasmas are shown in figure 3.4 for both single and dual frequency cases. The experimental conditions are similar to those used in the $c\text{-}C_4F_8$ experiments. A CF_4 gas flow rate of 36 sccm was chosen as this is twice the $c\text{-}C_4F_8$ flow rate (18 sccm) presented earlier. This means that the same number of fluorine atoms are introduced into the system in both experiments, allowing a possible comparison of both. Figure 3.5 shows the variation of the negative fluorine ion density as the CF_4 and O_2 gas flow rates are varied from 0–36 sccm, with the combined CF_4 + O_2 flow rate remaining constant at 36 sccm.

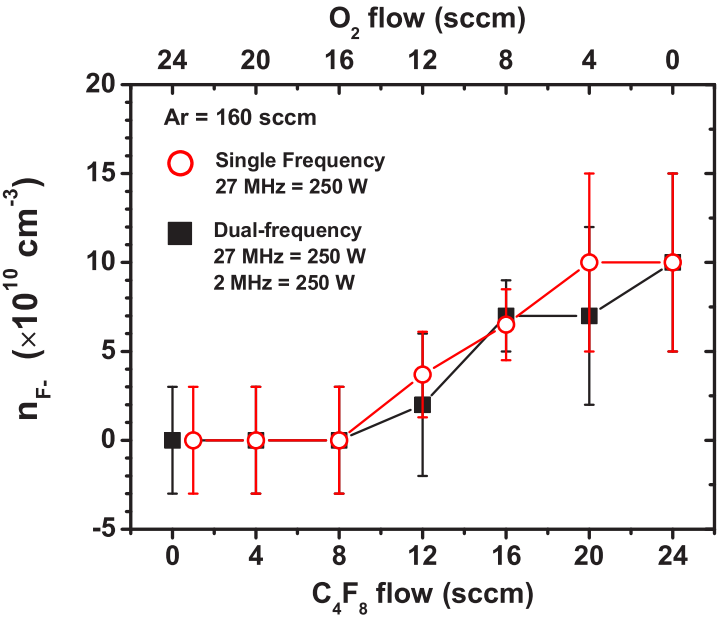


Figure 3.3: F- density for various c-C_4F_8 and O_2 mixtures in Argon

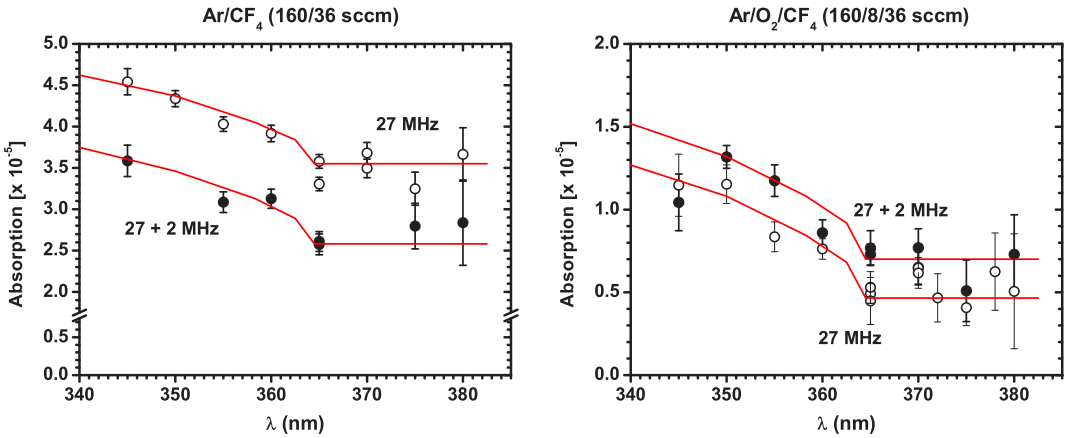


Figure 3.4: The absorption as a function of laser wavelength for Ar/CF_4 (160/36 SCCM) and $Ar/CF_4/O_2$ (160/36/8 SCCM) single (HF=250 W) and dual frequency (HF=250 W, LF=250 W) discharges at 48 mTorr. The estimated F^- densities are 1.2×10^{11} cm^{-3} (Ar/CF4) and 0.9×10^{11} cm^{-3} (Ar/CF4/O2), irrespective of the presence of 2 MHz power.

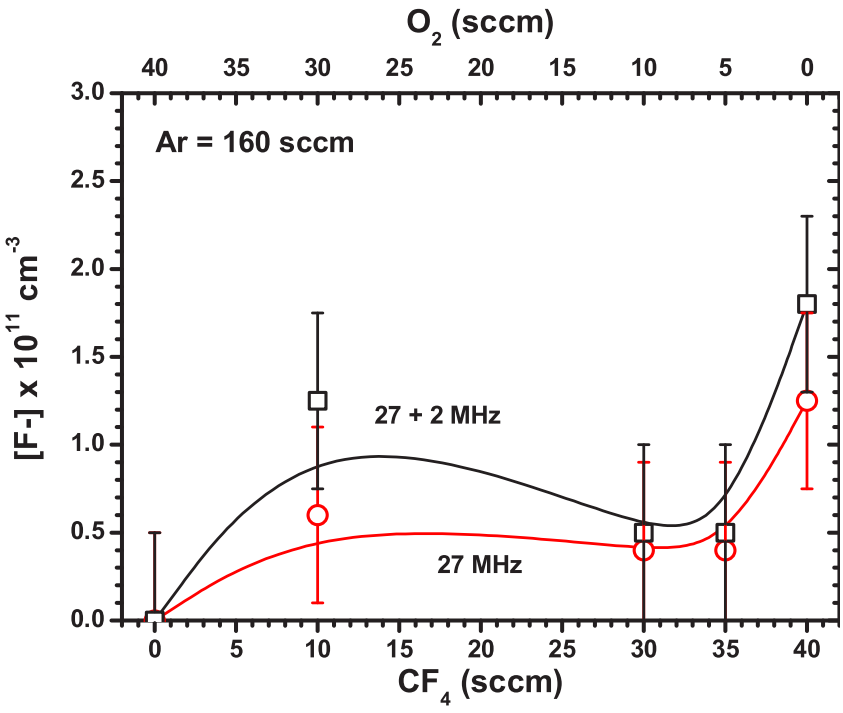


Figure 3.5: Fluorine negative ion densities for various CF_4 and O_2 mixtures in argon (160 sccm). Single frequency (27 MHz) power was 250 W. Dual frequency power (27+2 MHz) was 250+250 W. Pressure was approximately 54 mTorr.

3.3 Determining the negative ion fraction

This section aims to compare and contrast the different approaches used in this study for estimating the negative ion fraction in the centre of the discharge, α_0. Some of this material has already being discussed in section 1.5, but here it will be examined in more detail and with practical examples. Firstly, estimates of α using the combined measurements of F^- by CRDS and n_e by the hairpin probe will be presented. Then, the sole use of electrostatic probes, i.e. the ion flux probe and the hairpin probe, in determining the negative ion fraction will be discussed.

The electron density at the plasma centre, n_{e0}, is measured by the hairpin probe, while the ion flux to the upper electrode surface, Γ_{is}, is measured by the planar RF ion flux probe. The evolution of these two parameters relative to one another, at fixed pressures, should indicate trends in the plasma electronegativity. Two models for determining the negative ion fraction are discussed.

A comparison of the probe only approach and the CRDS & hairpin probe approach will then be examined, allowing validation to a certain extent of the theoretical models and to estimate the values of $\gamma = T_e/T_n$ that we should assume in those models. It will become apparent that the electronegativities obtained by application of the fluid model developed by Sheridan et al. are not easily correlated with those obtained using the CRDS

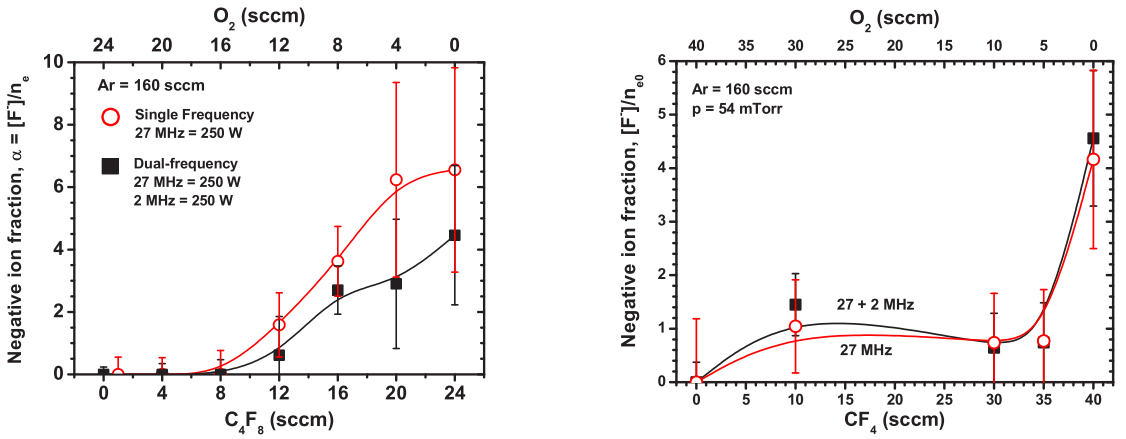
& hairpin probe. This leads us to examine the assumptions made within the model, and eventually the modification of the model and a reanalysis of the results.

3.3.1 Negative ion fractions from CRDS and the hairpin probe

We now look at the calculations of α_0 by combining measurements of the fluorine negative ion determined by CRDS and the electron density using the hairpin probe. Based on the same experimental conditions as for the electrostatic probe measurements only, the F^- densities and electron densities are measured for various flow rates of O_2 and c-C_4F_8 and for various flow rates of O_2 and CF_4 for both single and dual frequency powered plasmas. We then calculate the negative ion fraction using:

$$\alpha_0 = [F^-]/n_{e0} \tag{3.1}$$

where $[F^-]$ is the line averaged density over the 20 cm diameter plasma and n_{e0} is the electron density measured roughly half-way between the two electrodes and about 5 cm off-axis. The assumption is made that α is dominated by the negative fluorine ions (see earlier discussion in section 1.5.1). Figures 3.6 (a) and (b) show the negative ion fractions calculated using this method for both $Ar/O_2/c$-C_4F_8 and $Ar/O_2/CF_4$ plasmas respectively. The error bars on the α curves are calculated from the uncertainties that arise from the CRDS measurements. The errors in the electron density were considered to be either small or accounted for (e.g. sheath corrections). Some of the principal remarks



a) b)

Figure 3.6: Negative ion fractions calculated from measurements of F^- and n_e using CRDS and the hairpin probe respectively a) $Ar+O_2+c$-C_4F_8 plasma at 50 mTorr; b) $Ar+O_2+CF_4$ plasma at 50 mTorr.

from these results are outlined below:

- Negative fluorine ions may be present in the region $0 < c$-$C_4F_8 \leq 8$ but would not be detectable due to the poor signal-to-noise when $F^- < 5 \times 10^{10}$ cm^{-3} .

- The Ar/O_2 mixture (left-hand side of graphs) has $\alpha = 0$. If oxygen negative ions are present then this may not be the case.
- In $Ar/O_2/c\text{-}C_4F_8$ the F^- density was shown to be similar in both the single and dual frequency cases. However the same cannot be said for the values of α where the single frequency plasma has a higher negative ion fraction than in the dual frequency plasma. In other words, the dual frequency plasma has a higher electron density than the single frequency plasma but has the same negative ion density.
- In $Ar/O_2/CF_4$, the electronegativities are practically identical in both the single frequency and dual frequency cases. The raw CRDS results showed $[F^-]$ to be slightly higher in the dual-frequency case, but the higher n_e in the dual frequency case results in an equivalent α.

Overall, the $c\text{-}C_4F_8$ plasma is the more electronegative, with values of α_0 of up to 6.5 ± 3 compared to a maximum of 4.5 ± 1 when using CF_4. However, the actual negative fluorine ion densities are higher in the CF_4 plasma, although when the error bars are taken into account the densities are more or less the same. The lower α in CF_4 is therefore the result of a higher electron density.

3.3.2 Two-probe technique: simple model

The ion flux at the planar probe surface is equal to the ion flux at the plasma-sheath edge in front of the upper electrode. When $n_i = n_e$, the relationship between the ion current (flux) measured by the ion flux probe and the electron density measured by the hairpin probe is:

$$\Gamma_{is} = h_l n_{e0} u_s \tag{3.2}$$

where u_s is the ion drift velocity at the entrance to the sheath. When $n_i = n_e + n_n$ we have:

$$\Gamma_{is} = h_l (n_{e0} + n_{n0}) u_s \tag{3.3}$$

We initially assume that u_s is the same as for the electropositive case, i.e. $u_s = u_B$ and that the h_l-factor is constant (at fixed pressure) and is also equivalent to its electropositive value. Equation 3.3 can then be re-written as follows:

$$\frac{1}{h_l u_B} \frac{\Gamma_{is}}{n_{e0}} = 1 + \alpha_0 \tag{3.4}$$

so that measurements of the ion flux and the electron density, together with estimates of h_l and u_B, allow us to estimate the negative ion fraction. The ratio of the positive ion flux to the electron density will be used frequently throughout this thesis, so we will define it here as:

$$R_{ie} = \Gamma_{is}/n_{e0} \tag{3.5}$$

where the subscript ie is a simple reminder – $i$on flux and $e$lectron density – and hopefully aids in clarity. When $\alpha_0 = 0$ then $R_{ie} = R_{ie}|_{pos} = h_l u_B$.

Rearranging equation 3.4 we can express the negative ion fraction solely in terms of this ratio:

$$\alpha_0 = \frac{R_{ie}|_{meas}}{R_{ie}|_{pos}} - 1 \tag{3.6}$$

where $R_{ie}|_{meas}$ is the ratio deduced from the probe measurements. Again, the assumptions made are:

- u_B remains constant, i.e. its electropositive value. Due to the stratified nature of electronegative plasmas, this assumption is only valid for low electronegativities, usually $\alpha \leq 3$.
- h_l is unaffected by the variations in the plasma's electronegativity.

The procedure then for determining the charged particle densities using this simple approach combined with ion flux and electron density measurements is as follows:

1. Simultaneous hairpin and ion flux probe measurements $\rightarrow n_{e0}, \Gamma_{is}$.
2. Calculate $R_{ie}|_{meas}$ from measured data.
3. Calculate $R_{ie}|_{pos}$ from theoretical estimations of h_l and u_B.
4. Use equation 3.6 to estimate α_0.
5. Calculate n_{n0} from $\alpha_0 n_{e0}$.
6. Calculate n_{i0} from $n_{e0} + n_{n0}$.

The principal flaw in this method is the assumption that $u_s = u_B$, as this assumption is only true for small electronegativities ($\alpha_0 < 3$). Once the negative ion fraction becomes significant at the sheath edge ($\alpha_s > 0$) then u_s will quickly be modified from its electropositive value, as shown in equation 1.47. Moreover, and as illustrated in figure 1.17, for values of α_s greater than 1, the modification of u_s reaches an asymptotic value determined by the temperature ratio of the two negatively charged species:

$$u_s|_{\alpha_s > 1} \rightarrow u_B \sqrt{\frac{1}{\gamma}} \tag{3.7}$$

It would, therefore, be more correct to include this modified form of u_s when calculating the negative ion fraction, particularly for high centre electronegativities. Both the modified and unmodified forms of u_s will therefore be used in the initial analysis, and their respective results compared.

Estimating the h_l-factor

The positive ions are accelerated through the pre-sheath, such that in a low-pressure plasma the edge-to-centre density ratio, $h_l = n_{is}/n_{i0}$, is about 0.5. When collisions

become significant this ratio is reduced further. It is possible to construct a heuristic solution that closely approximates the low-pressure, variable mobility regime (i.e. $\lambda_i \leq l$), but has a transition to the approximate collisionless solution as $\lambda_i/l \rightarrow \infty$ [Godyak 86]:

$$h_l \approx 0.86 \left(3 + \frac{l}{2\lambda_i}\right)^{-1/2} \tag{3.8}$$

where l is the plasma bulk length and $\lambda_i = 1/n_g\sigma_{ig}$ is the positive ion mean free path. This heurisitic solution joins the variable mobility diffusion model to the collisionless flow (Langmuir) model. We can only roughly estimate h_l for our conditions as we must make a number of assumptions. First, with an inter-electrode distance, d, of 2.5 cm we assume a bulk plasma length, l, of 2 cm i.e. 2.5 mm sheaths). This value is justified by both visually looking at the plasma as well as by considering certain theoretical results on DF-CCP sheath widths, such as those by Boyle and Robiche [Boyle 04b, Robiche 03]. However, it is accepted that the sheaths may be larger than 2.5 mm, particularly in the presence of 2 MHz RF power. Estimating λ_i requires knowing the collision cross-section of the majority positive ion in the background gas. As approximately 85% of the gas mixture is argon, we take this as the background gas. At a pressure of 50 mTorr and a gas temperature of $\sim$ 500 K we get a neutral argon gas density, n_g, of 1×10^{21} m^{-3}.

We do not, however, know the collisional cross-sections of the majority ions (possibly $C_2F_4^+$, $C_3F_5^+$ and CF_3^+) with argon. We can only assume, therefore, that the average cross-section for all positive ion species is of the same order of magnitude as that of argon positive ions. The Ar^+–Ar cross sections can be found in figure 1.4 (data from [Phelps 94]). The positive ions are accelerated across through the plasma, reaching a maximum energy of about $T_e/2$, which is roughly 1.5–2 eV in absolute terms. The cross-section, σ_{ig}, is relatively constant in the region between 1–2 eV with a value of approximately 0.7×10^{-18} m^2.

Once all these assumptions are made, we find an estimated h_l-factor in our experimental conditions of approximately 0.275. It is important to note that the gas temperature and plasma bulk length (n_g and l) play a large role in determining this value. If we had assumed a gas temperature of 300 K and a plasma length equal to that of the inter-electrode distance (2.5 cm) we would have found a value of 0.208 for the h_l-factor. Likewise, if we had assumed a gas temperature of 600 K and larger sheaths, say 5 mm (and so a plasma length of 15 mm), we would have found a value of 0.32 for the h_l-factor.

Estimating u_B

The calculation of u_B requires knowing T_e and m_i. The ion flux probe sweeps through the tail of the EEDF and so the tail electron temperature can be measured. If the EEDF was perfectly Maxwellian, then this tail temperature would also reflect the bulk temperature.

However, this is not always the case and large fluctuations in the tail temperature, from 3 eV to 12 eV, are testament to non-reliability of associating it with the bulk T_e. In situations where the ion flux probe current appears to follow a perfect Maxwellian, it is usually found that T_e is equal to 3 eV and 5 eV in single (27 MHz only) and dual (2+27 MHz) frequency plasmas respectively. A self-consistent global model approach to solving T_e in our conditions found a value of 5 eV [Braithwaite 05]. For the purpose of this study we will often assume that $T_e = 5$ eV, unless otherwise stated.

Choosing a value for m_i is somewhat more tricky. Going on the discussion in section 1.4.1, we will assume an average value of $m_i = 100$ amu in c-C_4F_8 containing plasmas, and an average value of $m_i = 50$ amu in CF_4 containing plasmas.

The theoretical estimations for u_B are then 2192 m.s^{-1} and 3100 m.s^{-1} for c-C_4F_8 and CF_4 containing plasmas respectively.

Practical example of the simple model

Let us take a look at a practical application of this technique. Figure 3.7 shows the electron density and ion current density ($J_i = I_i/A = e\Gamma_{is}$) in the case of both single frequency (27 MHz = 250 W) and dual frequency (27 MHz = 250 W; 2 MHz = 250 W) $Ar/O_2/c$-C_4F_8 plasma mixtures. The O_2 and c-C_4F_8 flow rates are varied between 0 and 24 sccm such that the total flow rate is always 24 sccm. In this way, the pressure remained fairly constant at about 50 mTorr.

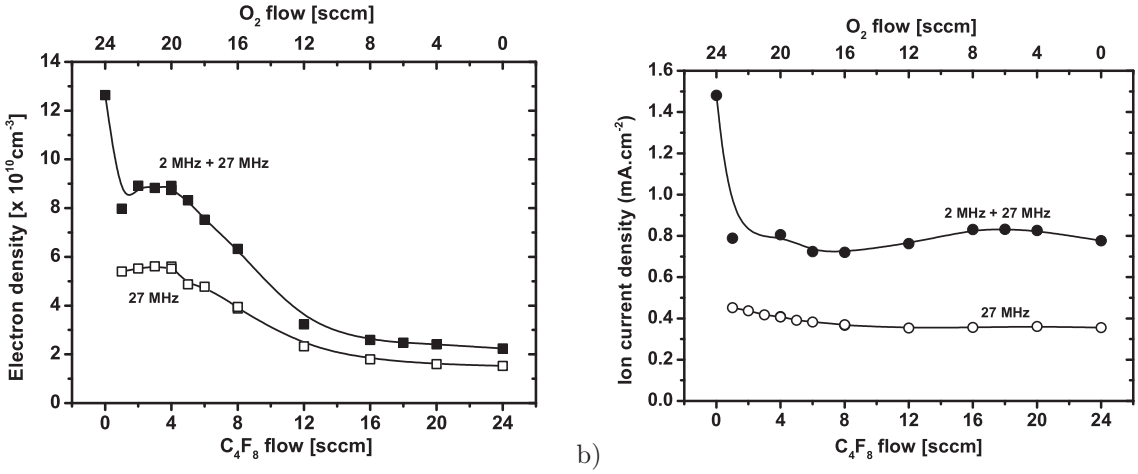


Figure 3.7: $Ar/O_2/C_4F_8$ dual-frequency plasma with varying C_4F_8 and O_2 flow rates. a) Electron density b) Ion current

The ratios of the ion flux to the electron density from these data sets are shown in figure 3.8 (a). Our theoretical electropositive value of this ratio, $R_{ie}|_{pos}$, is equal $0.275 \times 2192 = 602.8$ m.s^{-1}. We then proceed to convert these ratio values to negative ion fractions using equation 3.6. Figure 3.8 (b) shows the negative ion fractions obtained using this model. The values of α range from 0–3.5, with the dual frequency case slightly

more electronegative than the single frequency case. The c-C_4F_8 rich plasma exhibits the strongest electronegativity with the O_2 rich plasma showing only a slight increase in α. The region around 4 sccm of c-C_4F_8 and 20 sccm of O_2 is apparently electropositive. Note, however, that in the single frequency case we have physically meaningless negative values for α. It is difficult to put error bars on these graphs as many assumptions are made in the model, particularly with the calculation of $h_l * u_B$. In the estimation of u_B, T_e was assumed to be 5 eV for both single and dual frequency cases. Ion flux probe measurements, however, suggest that the single-frequency (27 MHz) temperature may be lower and closer to 3 eV. If this difference in T_e is taken into account, then no negative values occur and both cases have $\alpha = 0$ at c-$C_4F_8/O_2 = 4/20$ sccm.

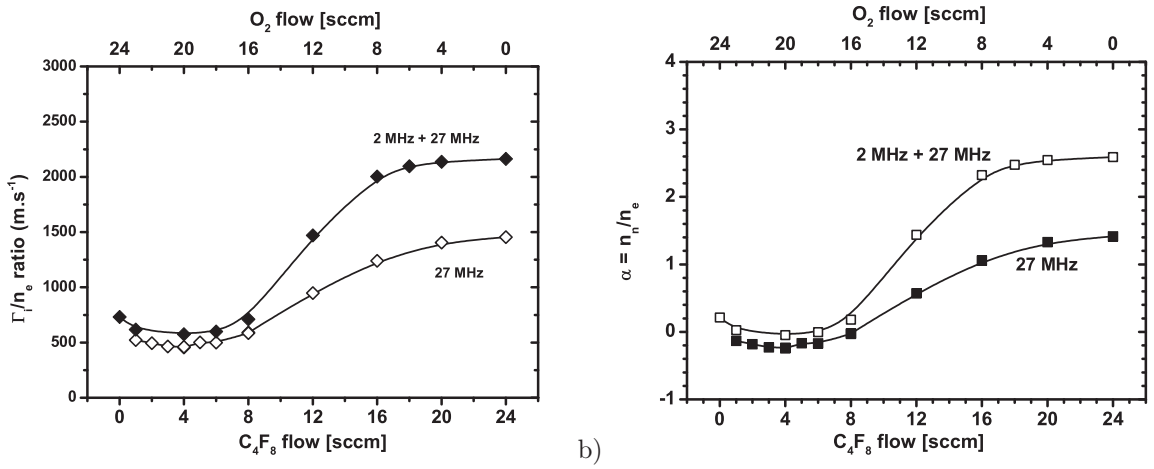


Figure 3.8: $Ar/O_2/C_4F_8$ dual-frequency plasma with varying C_4F_8 and O_2 flow rates. a) Γ_i/n_e ratios; b) negative ion fractions calculated using the simple model. T_e is taken as 5 eV and m_i is assumed to be ~ 100 amu.

We now apply this simple model to $Ar/O_2/CF_4$ plasma mixtures. Figure 3.9 shows the electron density and ion current density in the case of both single frequency (27 MHz = 250 W) and dual frequency (27 MHz = 250 W; 2 MHz = 250 W) $Ar/O_2/CF_4$ plasma mixtures. The O_2 and CF_4 flow rates are varied between 0 and 40 sccm such that the total flow rate is always 40 sccm. In this way, the pressure remained fairly constant at about 50 mTorr. Both the single and dual frequency data follow the same trends for $CF_4 > 5$ sccm. The drop in electron density and ion flux in the single frequency Ar/O_2 mixture was caused primarily with RF matching problems in this region. The delivered 27 MHz power was somewhere in the region of 150–200 W instead of the nominally applied 250 W. The ratios of the ion flux to the electron density from these data sets are shown in figure 3.10 (a). Our theoretical electropositive value of this ratio, $R_{ie}|_{pos}$, is equal $0.275 \times 3100 = 852.7$ m.s^{-1}. We then proceed to convert these ratio values to negative ion fractions using equation 3.6. Figure 3.10 (b) shows the negative ion fractions thus obtained. The negative values again indicate the fundamental problems with our assumptions, and demonstrate the limits of this technique. The rise in both the Γ_i/n_e

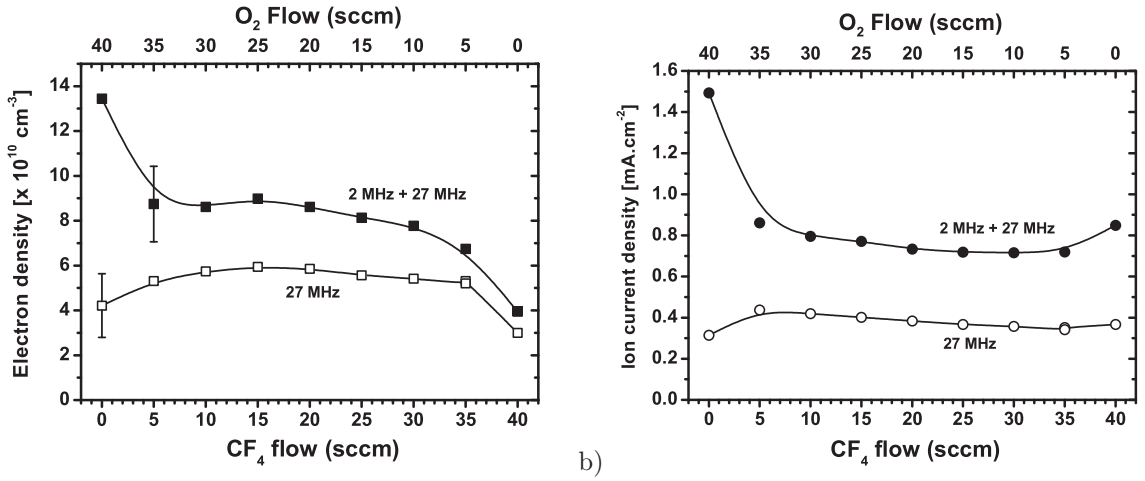


Figure 3.9: $Ar/O_2/CF_4$ dual-frequency plasma with varying CF_4 and O_2 flow rates. a) Electron density b) Ion current

ratio and the α curves when $CF_4 = 40$ sccm and $O_2 = 0$ sccm, point to the possible evidence of negative ions in this region.

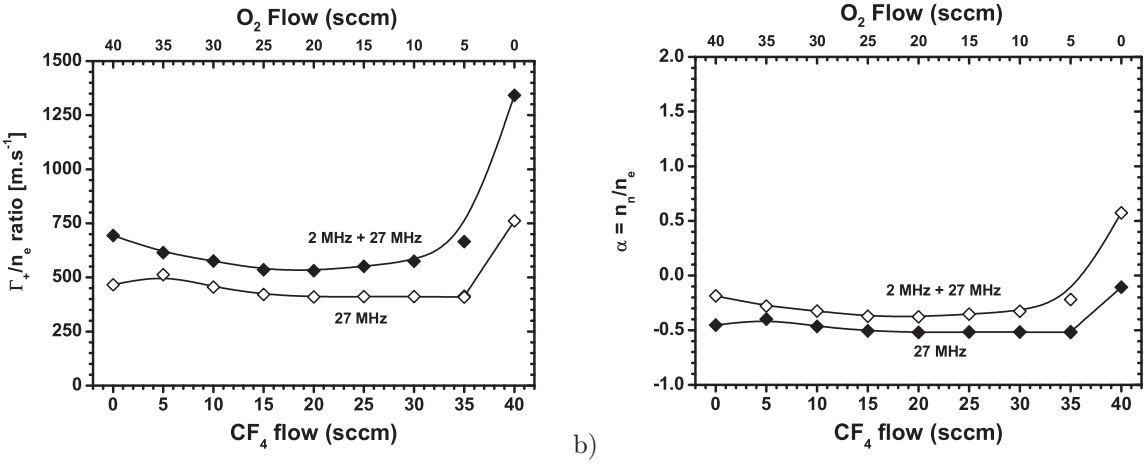


Figure 3.10: $Ar/O_2/CF_4$ dual-frequency plasma with varying CF_4 and O_2 flow rates. a) Γ_i/n_e ratios; b) negative ion fractions calculated using the simple model. T_e is taken as 5 eV and m_i is assumed to be ~ 50 amu.

The next step is to see the effect of including the modified Bohm velocity using the factor $\sqrt{1/\gamma}$ (see equation 3.7 on page 110). As we do not know the value of γ, we make several estimations of its value, thereby giving us a range of possible negative ion fraction curves. A more in-depth look into the final value of γ to be used will be discussed later on. For the moment, the values to be used will be $\gamma = 5$, 10 and 20. The following table outlines the influence of using the modification factor in our calculation of $R_{ie}|_{pos}$.

The negative ion fractions found using the modified Bohm velocity are presented in figures 3.11 ($Ar/O_2/C_4F_8$) and 3.12 ($Ar/O_2/CF_4$). The most obvious effect is that there are no longer negative values for α. This is an intrinsic result of using the correction factor,

			$h_l \times u_B \times \sqrt{1/\gamma}$		
	u_B	$h_l \times u_B$	$\gamma = 5$	$\gamma = 10$	$\gamma = 20$
c-C_4F_8($m_i = 100$ amu)	2192	603	270	191	135
CF_4 ($m_i = 50$ amu)	3100	853	381	270	191

Table 3.1: Effect of using the Bohm velocity modification factor, $\sqrt{1/\gamma}$, in calculating the electropositive ratio value. $h_l = 0.275$, $T_e = 5$ eV.

which is not suited for regions of low electronegativity where it artificially increases the apparent value of α. The use of the modified Bohm velocity is much more apt for regions of high electronegativity ($\alpha > 3$).

The principal weakness of the simple theory method in estimating negative ion fractions, therefore, is accounting for the transitions from an electropositive regime to an electronegative regime, and also the subset transition of a stratified electronegative plasma to a non-stratified electronegative plasma.

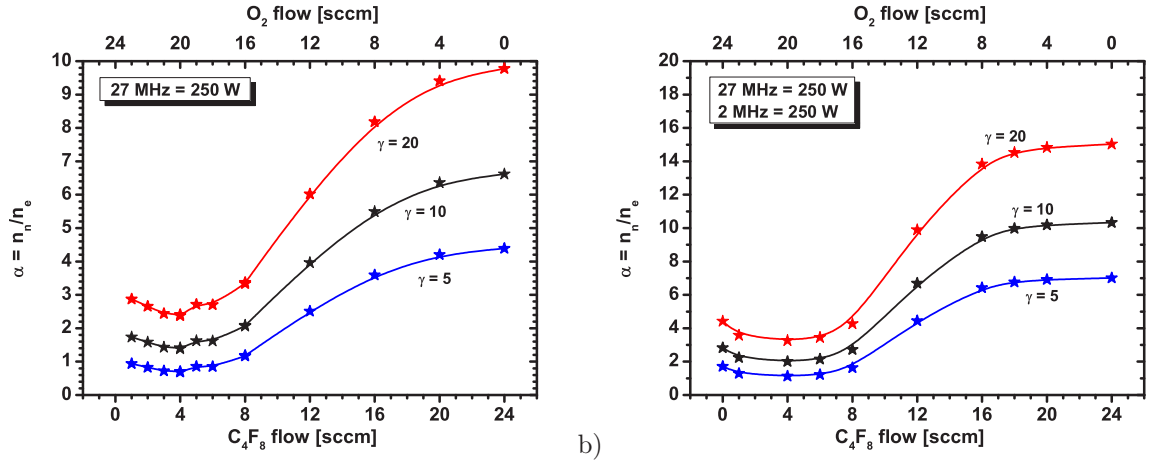


Figure 3.11: $Ar/O_2/C_4F_8$ plasma mixtures with varying C_4F_8 and O_2 flow rates. Negative ion fractions calculated using the simple model, but using the modified Bohm velocity for various values of γ (5,10 and 20) in a) single frequency and b) dual frequency. T_e is taken as 5 eV and m_i is assumed to be ~ 100 amu.

3.3.3 Two-probe technique: fluid model

This method involves using the fluid models of Sheridan et al [Sheridan 99b, Sheridan 99a] to interpret the probe data in an electronegative plasma, as was first applied in this way by Chabert et al. [Chabert 99b, Chabert 99a] using the low-pressure model. This thesis presents the application of the intermediate pressure (modestly collisional) fluid model to the probe results. The basic details of the model have already being outlined in section 1.5.2. To use the model results in determing α_0, the technique first involves normalising R_{ie} by dividing it by the electropositive ion sound speed, u_B (c_s in Sheridan's papers). Figure 3.13 shows this *normalised ion flux* using the same data as in the previous section for the simple method. However, whereas the electron temperature remains at 5 eV for

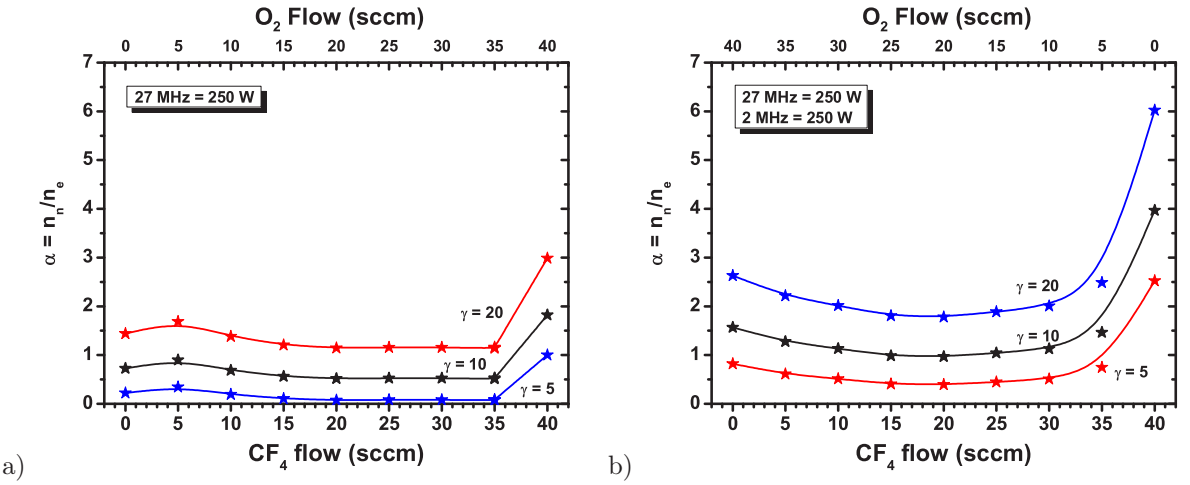


Figure 3.12: $Ar/O_2/CF_4$ plasma mixtures with varying CF_4 and O_2 flow rates. Negative ion fractions calculated using the simple model, but using the modified Bohm velocity for various values of γ (5,10 and 20) in a) single frequency and b) dual frequency. T_e is taken as 5 eV and m_i is assumed to be ~ 50 amu.

the dual frequency data, a value of 3 eV has been chosen for the single frequency data, better reflecting the value of T_e measured by the ion flux probe.

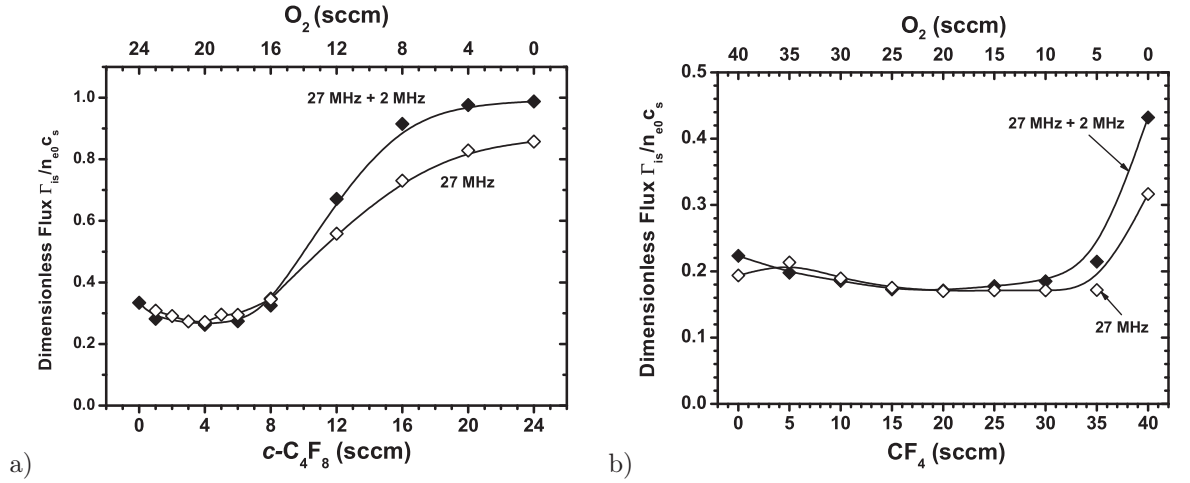


Figure 3.13: The normalised ratio in a) $Ar/O_2/c\text{-}C_4F_8$ and b) $Ar/CF_4/O_2$ plasma mixtures for both single and dual frequency RF power modes. The c_s used for normalising used a T_e of 3 eV in the single frequency data and 5 eV in the dual frequency data. Positive ion masses of 100 amu and 50 amu for the $c\text{-}C_4F_8$ and CF_4 containing plasmas respectively.

These normalised ion fluxes are then compared to the normalised values found using the Sheridan model under similar conditions. However, it can be challenging to find the appropriate parameters in the fluid model which can be used in the analysis of the experimental data. The fluid model requires knowledge of the electron temperature to negative ion temperature ratio, $\gamma = T_e/T_n$, and also requires a value for the ion collisionality factor, β_{cm}, which contains information on the gas pressure and the ionisation rate. The β_{cm}-factor can be estimated using a graphical technique which involves using figure 1.18

(b) (see page 37). In that figure, $\alpha = 0$ and so the normalised ion flux is equivalent to the h_l-factor. We calculated its value to be about 0.275 earlier on in this chapter and this would correspond to $\beta_{cm} \simeq 10$. One will notice, however, that the normalised ion flux in figure 3.13 (b) (CF_4) dips below 0.275 and has a value as low as 0.17, which would correspond to $\beta_{cm} = 30$. The reasons for this are not well understood. It could be as a result of the normalisation (m_i is possibly much larger than 50 amu) or it could be that such a plasma is physically more collisional (Ar^+–Ar collision cross-sections used here possibly underestimate the true ion-neutral collision cross-section). For the purpose of having as physically realistic negative ion fractions as possible, i.e. $\alpha > 0$, we will use the lowest value of the normalised ion flux for calculating β_{cm} in the case of the $Ar/O_2/CF_4$ plasma. This gives us, for the c-C_4F_8 and CF_4 mixtures, values for β_{cm} of 10 and 30 respectively. From figures 1.20 (a) and (b) we can therefore obtain the negative ion fraction associated with a particular normalised flux. To automate the process, we fit those curves using polynomial expressions which are then used in a spreadsheet to calculate α.

$\beta_{cm} = 10$	
$\gamma = 5$	α_0 = -3.3672 + 6.03814 Γ_{is} + 27.82757 Γ_{is}^2
$\gamma = 10$	α_0 = -8.94591 + 23.5165 Γ_{is} + 40.3344 Γ_{is}^2
$\gamma = 20$	α_0 = -13.62425 + 23.15997 Γ_{is} + 111.22287 Γ_{is}^2
$\gamma = 50$	α_0 = -30.9304 + 41.9767 Γ_{is} + 294.7645 Γ_{is}^2
$\beta_{cm} = 20$	
$\gamma = 5$	α_0 = -3.6705 + 7.23012 Γ_{is} + 55.59168 Γ_{is}^2
$\gamma = 10$	α_0 = -6.51363 + 10.04548 Γ_{is} + 112.24944 Γ_{is}^2
$\gamma = 20$	α_0 = -11.83955 + 13.81673 Γ_{is} + 227.04042 Γ_{is}^2
$\gamma = 50$	α_0 = -28.08739 + 26.19631 Γ_{is} + 571.63779 Γ_{is}^2
$\beta_{cm} = 30$	
$\gamma = 5$	α_0 = -3.49024 + 6.12354 Γ_{is} + 86.30429 Γ_{is}^2
$\gamma = 10$	α_0 = -6.43199 + 9.95009 Γ_{is} + 165.8008 Γ_{is}^2
$\gamma = 20$	α_0 = -11.52572 + 12.11002 Γ_{is} + 333.062 Γ_{is}^2
$\gamma = 50$	α_0 = -27.53857 + 23.78933 Γ_{is} + 826.66359 Γ_{is}^2
$\beta_{cm} = 40$	
$\gamma = 5$	α_0 = -3.44129 + 5.76084 Γ_{is} + 116.25543 Γ_{is}^2
$\gamma = 10$	α_0 = -6.03813 + 7.01846 Γ_{is} + 225.22653 Γ_{is}^2
$\gamma = 20$	α_0 = -11.26315 + 10.19461 Γ_{is} + 440.50918 Γ_{is}^2

Table 3.2: Polynomial fit functions for obtaining α_0 values from normalised ion flux data, for β_{cm} = 10, 20, 30 and 40.

The temperature ratio, γ, however, is almost completely unknown due to the fact that very little experimental data on T_n is available. However, we do know that:

- a) as negative ions are created by dissociative attachment, they begin life with an excess of kinetic energy from the dissociation process. This should lead to them having high temperatures.
- b) the negative ions are likely to be relatively hot ($T_e/T_n \ll T_e/T_i \approx 100$) because they are trapped within the plasma bulk by the potential well imposed by the

sheaths.

- c) although very few experimental T_n measurements exist, those that do (see [Bacal 00]) have found T_n to be no less than 0.1 eV.

Table 3.3 outlines what the absolute values of T_n would be for various values of T_e and γ. As we cannot chose one single value for γ without further information, it is necessary to try out several values, in this case 5, 10, 20 and 50. During the analysis that follows and when a comparison with the CRDS results is made, we will get a better idea of what value of γ is the more appropriate.

Negative ion temperature			
γ	Te = 3 eV	Te = 4 eV	Te = 5 eV
5	0.6 eV	0.8 eV	1.0 eV
10	0.3 eV	0.4 eV	0.5 eV
20	0.15 eV	0.2 eV	0.25 eV
50	0.06 eV	0.08 eV	0.1 eV

Table 3.3: Negative ion temperatures

Figure 3.14 shows the negative ion fractions in single and dual frequency $Ar/O_2/c$-C_4F_8 plasmas for various γ values and for $\beta_{cm} = 10$. Figure 3.15 shows the negative ion fractions in single and dual frequency $Ar/O_2/CF_4$ plasmas for various γ values and for $\beta_{cm} = 30$. The values for α are much larger than those found using the simple theory method. Moreover, if we remember that the measured electron densities (c.f. fig. 3.7) are of the order of 10^{10} cm^{-3} and that it would be difficult to imagine negative ion densities greater than 5×10^{11} cm^{-3} when taking results from the literature into account, then it is very unlikely that we have $\alpha > 50$. This leads us to conclude that the temperature ratio, γ, is ≤ 10 in the single frequency experiments and is ≤ 5 in the dual frequency experiments. In absolute terms this equates to very hot negative ions, in the region $0.3 \text{ eV} \leq T_e \leq 1.0 \text{ eV}$.

3.3.4 Comparison of the various estimations of the negative ion fractions

The negative ion fractions estimated thus far using the various methods are summarised in table 3.4. The results vary quite significantly from one another. When using the probe only methods, the electronegativity is always greater in the dual frequency case than in the single frequency, whereas the combined CRDS and hairpin method shows the opposite. However, in the latter method, the error bars for both the single and dual frequency case overlap one another (see figure 3.6). The simple model (no modified Bohm flux) produces results that are considerably lower than the CRDS and hairpin results. The simple model does, however, allow for $\alpha = 0$ in regions of low fluorocarbon gas flow. The modified simple model gives negative ion fractions in the same order of magnitude as the CRDS & hairpin, particularly for $\gamma = 10$. However, it does not allow for $\alpha = 0$ in

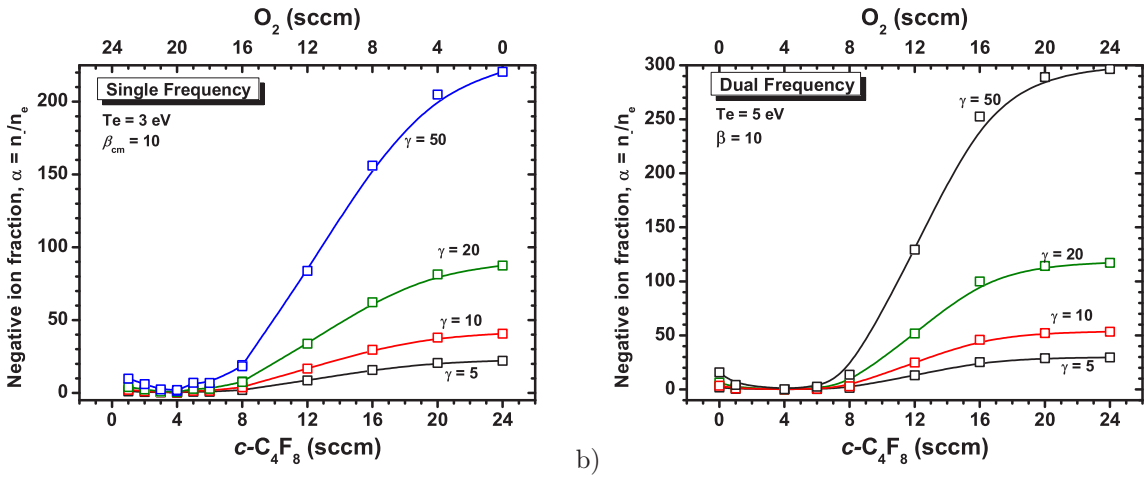


Figure 3.14: $Ar/O_2/c\text{-}C_4F_8$ Negative ion fractions calculated using the electronegative fluid model and using the dimensionless flux data in figure 3.13 for various estimates of γ. $\beta_{cm} = 10$. (a) Single frequency (27 MHz = 250 W) and (b) dual frequency (27 MHz = 250 W, 2 MHz = 250 W)

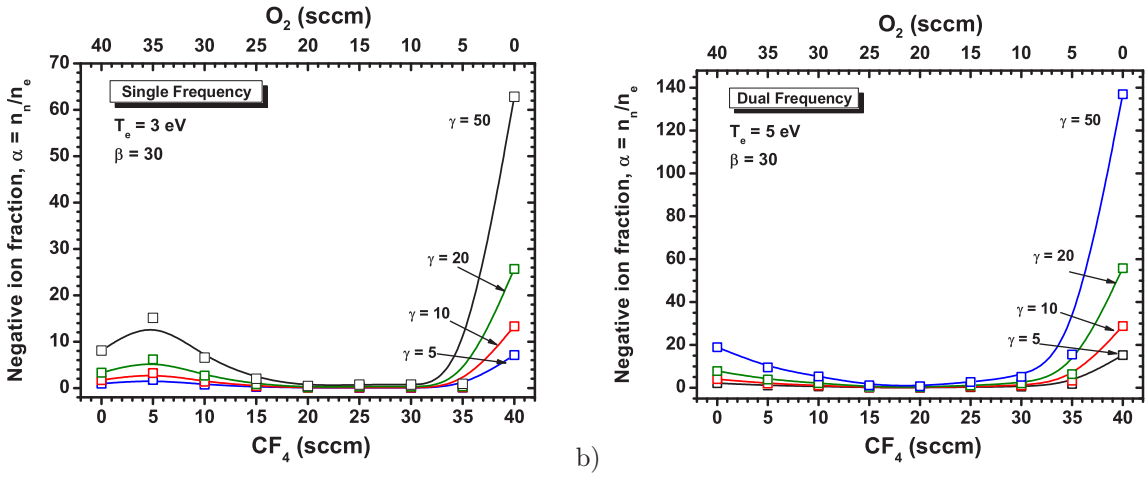


Figure 3.15: $Ar/O_2/CF_4$: Negative ion fractions calculated using the electronegative fluid model and using the dimensionless flux data in figure 3.13 for various estimates of γ. $\beta_{cm} = 30$. (a) Single frequency (27 MHz = 250 W) and (b) dual frequency (27 MHz = 250 W, 2 MHz = 250 W)

regions of low fluorocarbon gas flow. This indicates, as expected, that it is valid only for large electronegativities ($\alpha_0 > 3$) such that the negative ion fraction at the plasma edge is non negligible.

The fluid model estimates values of α much greater than both the CRDS & hairpin results and the simple models, with the possible exception of the negative ion fractions found in the $Ar/O_2/CF_4$ plasma when $\gamma = 5$. There are two conclusions that can be drawn from this result. The first is to assume that the model correctly describes the electronegative discharge, meaning that the negative ion temperature must be very high, i.e. $\gamma < 5$ in the case of c-C_4F_8 and $\gamma \simeq 5$ in the case of CF_4. The second is to assume that the other methods give a better indication of the plasma electronegativity, meaning that the fluid model is incomplete. On further inspection of the fluid model proposed by Sheridan, it was indeed found to be incomplete, or to be more precise, to be unsuitable for the pressure regime under study in this thesis: the intermediate pressure or variable mobility regime. The next section describes the modifications that were required to address this issue.

	c-C_4F_8		CF_4	
Model	Single Frequency	Dual frequency	Single Frequency	Dual frequency
CRDS & hairpin probe	9	6	4.6	4.2
Probes - simple model	1.4	2.6	0	0.6
Probes - simple modified	4.5 ($\gamma = 5$) 6.5 ($\gamma = 10$) 10 ($\gamma = 20$)	7 ($\gamma = 5$) 10 ($\gamma = 10$) 15 ($\gamma = 20$)	1 ($\gamma = 5$) 2 ($\gamma = 10$) 3 ($\gamma = 20$)	2.5 ($\gamma = 5$) 4 ($\gamma = 10$) 6 ($\gamma = 20$)
Probes - fluid model (constant mobility)	22 ($\gamma = 5$) 40 ($\gamma = 10$) 85 ($\gamma = 20$)	30 ($\gamma = 5$) 53 ($\gamma = 10$) 115 ($\gamma = 20$	7 ($\gamma = 5$) 13 ($\gamma = 10$) 25 ($\gamma = 20$)	15 ($\gamma = 5$) 28 ($\gamma = 10$) 55 ($\gamma = 20$)

Table 3.4: Negative ion fractions

3.3.5 Introducing variable mobility to the fluid model

Let us return to the initial equations in the fluid model (see page 35). The equation of motion for the cold, positive ion fluid is:

$$m_i n_i v_i \frac{dv_i}{dx} + m_i v_i \nu_{iz} n_{e0} \exp\left(\frac{e\phi}{kT_e}\right) = n_i eE - n_i F_c \tag{3.9}$$

where v_i is the ion drift velocity, ν_{iz} is the net ionisation frequency and F_c is the collisional drag force. In the original model, this drag force was assumed to have the form $F_c = m_i v_i \nu_p$, where ν_p is a constant ion collision frequency for momentum transfer, i.e. constant mean-free-time collisions or *constant mobility*. This relied on the condition that ν_p is independent of v_i, which is applicable only to quite high pressures where $\lambda_i \ll l$. In such

conditions, $v_i \ll v_{th}$, where v_{th} is the average ion thermal velocity and is given by:

$$v_{th} = \sqrt{\frac{8kT_i}{\pi m_i}}$$

and is considered constant throughout the plasma bulk. In high pressure conditions, this ion thermal velocity is considered the effective velocity for collisions of ions with neutrals and so the ion collision frequency for momentum transfer is given by:

$$\nu_p = \frac{v_{th}}{\lambda_i} \quad \text{(constant mobility)} \tag{3.10}$$

and is therefore considered constant over the entire plasma bulk region. When the drag force term is set to zero, the model becomes a low-pressure, collisionless (for momentum transfer) model, also referred to as the *Langmuir solution*. In this way, Sheridan believed that the model correctly encompassed the transition from the high-pressure to low-pressure regimes (and vice-versa) by the modification of this drag force term, or more specifically, by modifying the normalised β_{cm} parameter (referred to simply as β in Sheridan's papers).

There exists, however, an intermediate pressure regime where $\lambda_i \lesssim l$, such that the ion drift velocity can attain a magnitude greater than the ion thermal velocity. In this regime the effective ion velocity for collision of ions with neutrals is the ion drift velocity rather than the ion thermal velocity. In other words, $v_i \gg v_{th}$ over most of the discharge region. When this is the case, the ion-neutral collision rate then becomes:

$$\nu_p = \frac{\pi}{2}\frac{v_i}{\lambda_i} \quad \text{(variable mobility)} \tag{3.11}$$

where the factor of $\pi/2$ arises from a redefinition of the ion mobility due to its dependence on v_i[Lieberman 05]. The ion mean-free-path is still considered to be independent of v_i, which is a reasonable assumption over the usual velocity ranges (see figure 1.4). The variable mobility drag force term is now described by:

$$F_c = m_i \frac{\pi}{2}\frac{v_i^2}{\lambda_i} \tag{3.12}$$

The normalised fluid equations are identical to those used by Sheridan. However, the normalised ion collision parameter is redefined as a result of including variable mobility (see the Appendix, equations C -12 and C -13). The subscript vm is now used to differentiate from the constant mobility model:

$$\beta_{vm} = \frac{\pi}{2}\frac{\Lambda}{\lambda_i} \tag{3.13}$$

where Λ is still defined as c_s/ν_{iz}. The variable mobility collision parameter is related to

the constant mobility collision parameter by:

$$\beta_{vm} = \beta_{cm}\sqrt{\frac{\pi^3}{24}}\sqrt{\frac{T_e}{T_i}} \tag{3.14}$$

$$\beta_{vm} \simeq \beta_{cm}\sqrt{\frac{T_e}{T_i}} \tag{3.15}$$

Application of the variable mobility model

The procedure is the same as that which we used with the original model. First, we must determine the value to be used for the ion collisional parameter. We do this, as before, by finding the value of β_{vm} that corresponds to the electropositive h_l-factor of our experimental conditions. Figure 3.16 shows the normalised ion flux, or h_l-factor, as a function of the variable mobility ion collision parameter in an electropositive plasma. We will use the same h_l-factors as before, namely 0.275 for the $Ar/O_2/c\text{-}C_4F_8$ plasma and 0.17 for the $Ar/O_2/CF_4$ plasma. This gives us values for β_{vm} of 33 and 180 respectively, but for the sake of having round figures we will use 35 and 200 without incurring much error.

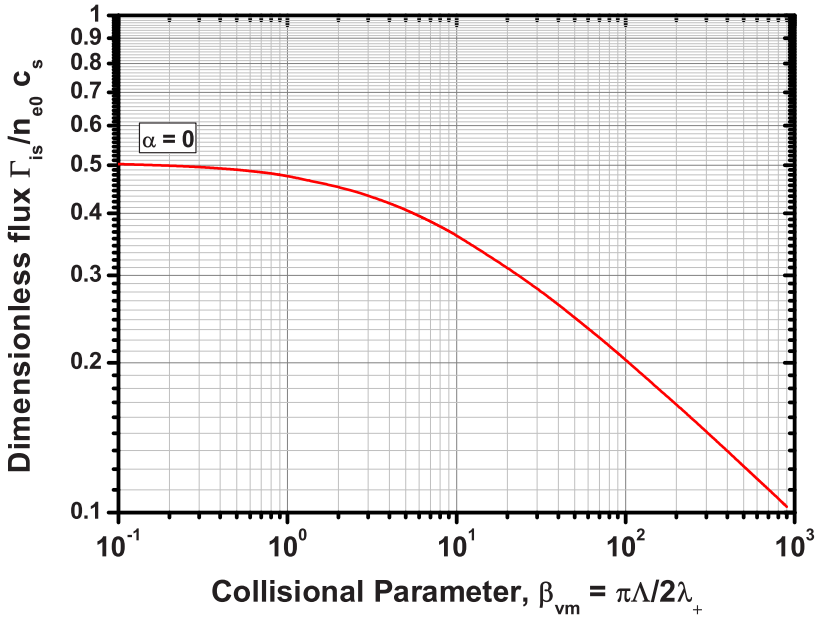


Figure 3.16: The normalised ion flux as a function of the variable mobility ion collision parameter in an electropositive plasma.

The normalised ion flux is then calculated as a function of the negative ion fraction for these values of β_{vm} and for various values of γ (5, 10, 20). The results are graphed in figure 3.17.

From these results the negative ion fraction is plotted as a function of the normalised ion flux (not shown) for each value of β_{vm} and γ. Polynomial functions are then used

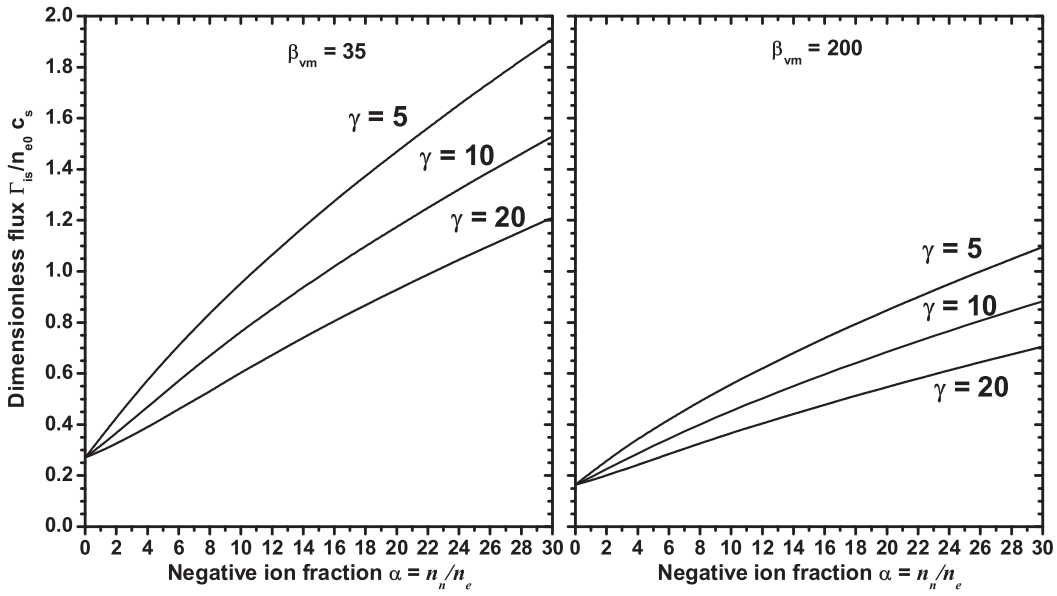


Figure 3.17: The normalised ion flux as a function of α for $\beta_{vm} = 35$ and 200, corresponding to electropositive h_l-factors of 0.275 and 0.17 respectively.

to fit these curves so that we can easily determine α_0 for every measured Γ_{is}/n_{e0} ratio. These fit functions are shown in table 3.5. 2^{nd}-order (parabolic) fit functions were found to suffice. $\gamma = 50$ is no longer used as we have excluded it earlier.

$\beta_{vm} = 35$	
$\gamma = 5$	α_0 = -3.01459 + 10.0686 Γ_{is} + 3.79109 Γ_{is}^2
$\gamma = 10$	α_0 = -4.09708 + 14.69058 Γ_{is} + 4.9755 Γ_{is}^2
$\gamma = 20$	α_0 = -6.22278 + 23.72277 Γ_{is} + 5.01013 Γ_{is}^2
$\beta_{vm} = 200$	
$\gamma = 5$	α_0 = -3.17532 + 16.80419 Γ_{is} + 12.38664 Γ_{is}^2
$\gamma = 10$	α_0 = -4.28984 + 23.95269 Γ_{is} + 16.89050 Γ_{is}^2
$\gamma = 20$	α_0 = -6.32091 + 37.17099 Γ_{is} + 20.19266 Γ_{is}^2

Table 3.5: Polynomial fit functions for obtaining α_0 values from normalised ion flux data, for $\beta_{vm} = 35$ and $\beta_{vm} = 200$.

As with the analysis using the original model, the normalised ion fluxes are then converted to their respective α values. The same data that has been used throughout this section is treated in this way, namely the $Ar/O_2/c$-C_4F_8 and $Ar/O_2/CF_4$ plasma mixtures. The results can be seen in figures 3.18 and 3.19 for both mixtures respectively. It is apparent that the electronegativities are significantly lower than those found using the constant mobility model. For all values of γ, the negative ion fraction remains below 20. The effect of using variable mobility in the model can be seen more clearly in table 3.6, which summarises the results of all the models.

If we take the CRDS & hairpin experimental α values as our benchmark, then the VM fluid model shows good agreement when $\gamma = 5$ for both the single and dual frequency

$Ar/O_2/c\text{-}C_4F_8$ plasma and for the dual frequency $Ar/O_2/CF_4$ plasma. In the case of the single frequency $Ar/O_2/CF_4$ plasma, $\gamma = 10$ has a better agreement. In any case, the results continue to suggest that the negative ion temperature must be considered to be quite high for some form of agreement to occur. In the dual frequency case ($T_e = 5$ eV) this would mean an absolute value of $T_n \sim 1$ eV. In the single frequency case ($T_e = 3$ eV) this would mean an absolute value of $T_n \sim 0.6$ eV for the $c\text{-}C_4F_8$ mixture and $T_n \sim 0.3$ eV for the CF_4 mixture.

It is possible, however, that due to the low S/N in the CRDS measurements the negative ion density may have been underestimated. In particular, should the background continuum in the CRDS absorption profiles be a result of another negative ion species, then this too could result in an underestimation of n_n. The value of γ would therefore be slightly higher, possibly closer to 10 or 15. We must, however, use the evidence before us which suggests that $\gamma \sim 5$. Looking at the values of α obtained with $\gamma = 10$ and 20, we note that the difference from the $\gamma = 5$ curve is about a factor of two. Such a low value of γ points to the high temperatures (0.6 – 1.0 eV) that the negative ions can obtain. This is likely due to the capability of the light F^- ions to gain energy from the RF field, especially in the dual frequency case, i.e. in the presence of 2 MHz. This had been predicted numerically by Georgieva et al. [Georgieva 06b].

To conclude this analysis, the variable mobility fluid model is retained as the model to be used in determining the negative ion fraction from the ion flux probe and hairpin probe measurements. It will also be assumed that $\gamma = 5$ for the remainder of the analysis. Although this may be an overestimation of the negative ion temperature, the results obtained will be useful in determining the overall trends in plasma electronegativity with a large degree of confidence that the values of α_0 obtained are within a factor of 2 of their actual values.

	$c\text{-}C_4F_8$		CF_4	
Model	Single Frequency	Dual frequency	Single Frequency	Dual frequency
CRDS & hairpin probe	9	6	4.6	4.2
Probes - simple model	1.4	2.6	0	0.6
Probes - simple modified	4.5 ($\gamma = 5$) 6.5 ($\gamma = 10$) 10 ($\gamma = 20$)	7 ($\gamma = 5$) 10 ($\gamma = 10$) 15 ($\gamma = 20$)	1 ($\gamma = 5$) 2 ($\gamma = 10$) 3 ($\gamma = 20$)	2.5 ($\gamma = 5$) 4 ($\gamma = 10$) 6 ($\gamma = 20$)
Probes - fluid model (constant mobility)	22 ($\gamma = 5$) 40 ($\gamma = 10$) 85 ($\gamma = 20$)	30 ($\gamma = 5$) 53 ($\gamma = 10$) 115 ($\gamma = 20$	7 ($\gamma = 5$) 13 ($\gamma = 10$) 25 ($\gamma = 20$)	15 ($\gamma = 5$) 28 ($\gamma = 10$) 55 ($\gamma = 20$)
Probes - fluid model (variable mobility)	8.4 ($\gamma = 5$) 12 ($\gamma = 10$) 18 ($\gamma = 20$)	10 ($\gamma = 5$) 15 ($\gamma = 10$) 22 ($\gamma = 20$	3.4 ($\gamma = 5$) 5 ($\gamma = 10$) 7.5 ($\gamma = 20$)	6.4 ($\gamma = 5$) 9.2 ($\gamma = 10$) 13.5 ($\gamma = 20$)

Table 3.6: Negative ion fractions

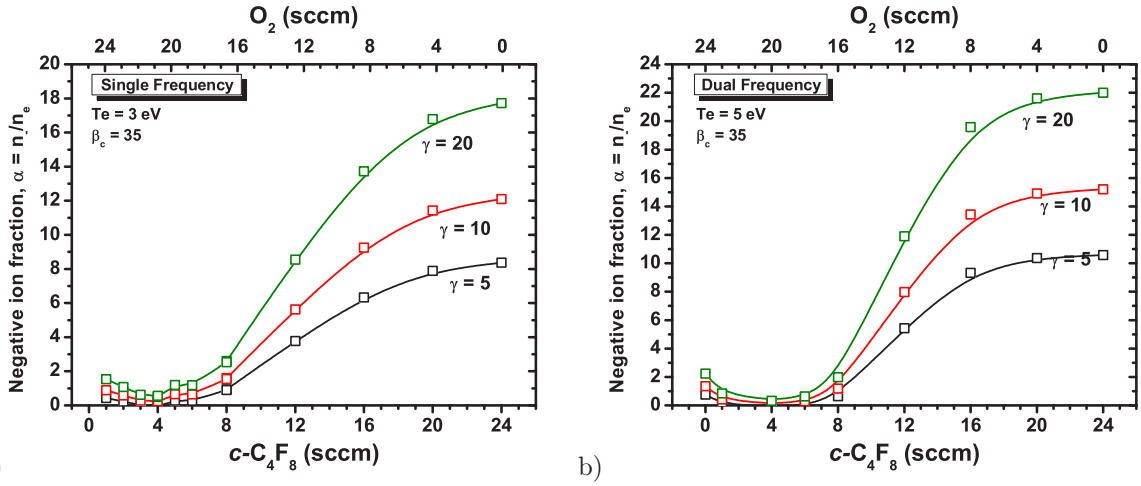


Figure 3.18: $Ar/O_2/c\text{-}C_4F_8$: Negative ion fractions calculated using the electronegative fluid model and using the dimensionless flux data in figure 3.13 for various estimates of γ. $\beta_{vm} = 35$. (a) Single frequency (27 MHz = 250 W) and (b) dual frequency (27 MHz = 250 W, 2 MHz = 250 W)

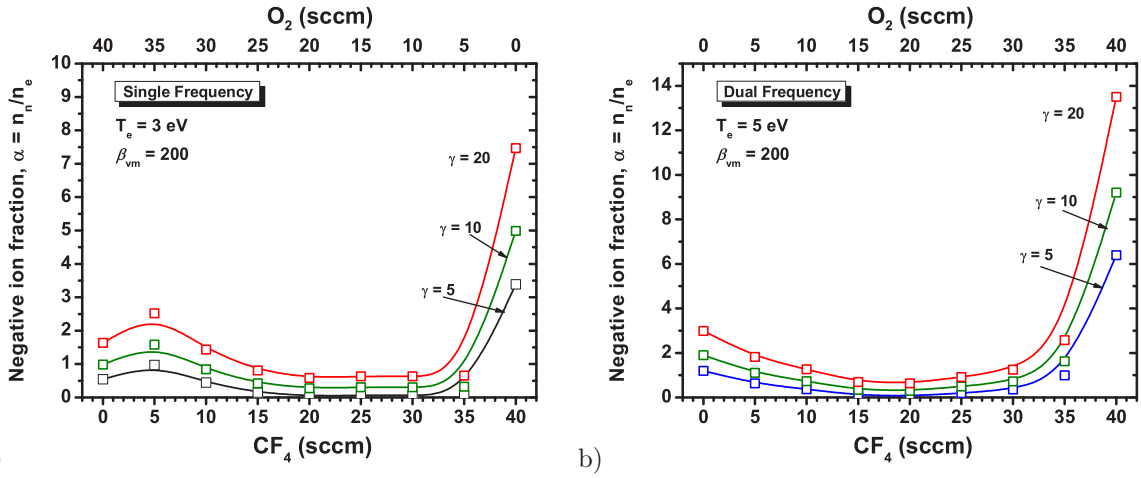


Figure 3.19: $Ar/O_2/CF_4$: Negative ion fractions calculated using the electronegative fluid model and using the dimensionless flux data in figure 3.13 for various estimates of γ. $\beta_{vm} = 200$. (a) Single frequency (27 MHz = 250 W) and (b) dual frequency (27 MHz = 250 W, 2 MHz = 250 W)

3.4 Charged particle dynamics - Effect of gas composition

The charged particle densities and fluxes will vary for different gas mixtures for several reasons, including changes in ionisation thresholds, the modification of wall conditions, the variation of the plasma electronegativity, the increase (or decrease) in pressure due to an increase (or decrease) of the presence of large molecular gases.

The following results attempt to isolate those changes that are a direct result of the change in plasma electronegativity. A major reason for the dependence on chemistry is that the density of precursors for dissociative attachment is modified. Also, the negative ions can be destroyed by associative detachment (e.g. $F^- + CF \rightarrow CF_2 + e$). The negative ion fractions presented here are intended to give a general idea of the true plasma electronegativity, i.e. what the orders of magnitude are likely to be. Several gases were used in the study, namely argon (Ar), oxygen (O_2), octafluorocyclobutane (c-C_4F_8), carbon tetrafluoride (CF_4) and sulphur hexafluoride (SF_6). The principal combinations of gas mixtures used were often chosen for their relevance to the dielectric etch industry. For example, a typical fluorocarbon based etch recipe contains 160 sccm of Ar, 8 sccm of O_2 and 18 sccm of c-C_4F_8 at a pressure of about 50 mTorr. Variations of these mixtures were then chosen for their usefulness in determining the charged particle dynamics, and in particular the plasma electronegativity. SF_6 was used because of a desire by Lam Research to understand the effects of the addition of SF_6 to a CF_4 plasma. It is also an interesting case in its own right because it is known for its strong electronegativity. However, it's usefulness was limited due to the fact that negative fluorine ions cannot be detected in SF_6 plasma mixtures using broadband or CRDS absorption spectroscopy (see figure 2.34).

Some of the results in $Ar/O_2/c$-C_4F_8 and $Ar/O_2/CF_4$ plasmas have already been presented in the previous section. As such, references will be made to the data already presented so as to avoid repetition.

3.4.1 $Ar/O_2/c$-C_4F_8 – varying the c-C_4F_8 gas flow

Figure 3.20 shows the electron density and ion flux in a dual-frequency (27.12 MHz = 250 W; 2 MHz = 250 W) argon and oxygen plasma as c-C_4F_8 is gradually introduced. The Ar/O_2 composition, 160/8 sccm, is chosen as we commonly use $Ar/O_2/c$-C_4F_8 in a composition of 160/8/18 sccm for this is close to a standard industrial etch mixture. The c-C_4F_8 was varied from 0–22 sccm as the mass flow controller was limited to 27 sccm. The figure shows clearly the important variations that occur in the densities and fluxes, particularly in the 0 - 12 sccm region of c-C_4F_8 flow. The interesting thing to note is the completely different rates of change for both n_e and Γ_i in this region. The ion flux drops dramatically (-50 %) as soon as a small amount (2 – 4 sccm, or 1 – 2 % of total gas

flow) of c-C_4F_8 is added. It then levels out before beginning to rise slightly again. The electron density, on the other hand, stays constant up to 4 sccm before droping to less than a third of its value over the 4 - 12 sccm range. It then continues to decline in value at a slow rate.

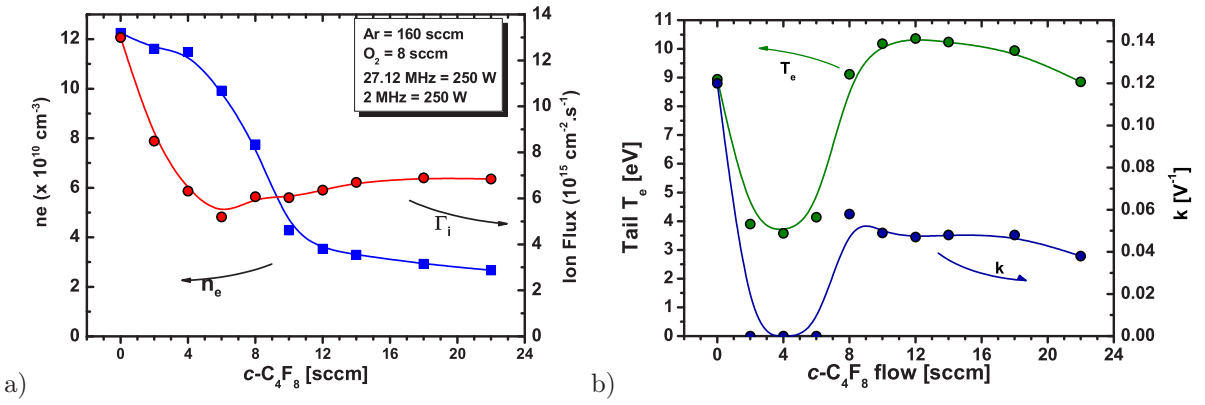


Figure 3.20: (a) Electron densities and ion flux in an Ar/O_2 dual-frequency plasma with varying c-C_4F_8 flow. (b) Tail electron temperature and "Druyvesteyn" factor for the same conditions.

The tail electron temperature and the corresponding *k-factor* or*Druvesteyn-factor* (see section 2.2.1, equation 2.17) is shown in part (b) of figure 3.20. Spline curves are again used to guide the eye. The I–V curve fit function follows an ideal Maxwellian for c-C_4F_8 gas flow rates of 2 – 6 sccm, with a measured T_e of 4 eV. All other values of the c-C_4F_8 gas flow rate require the use of the k-factor and have tail electron temperatures of around 9–10 eV. These high electron temperatures may indicate electronegativity. To gain an

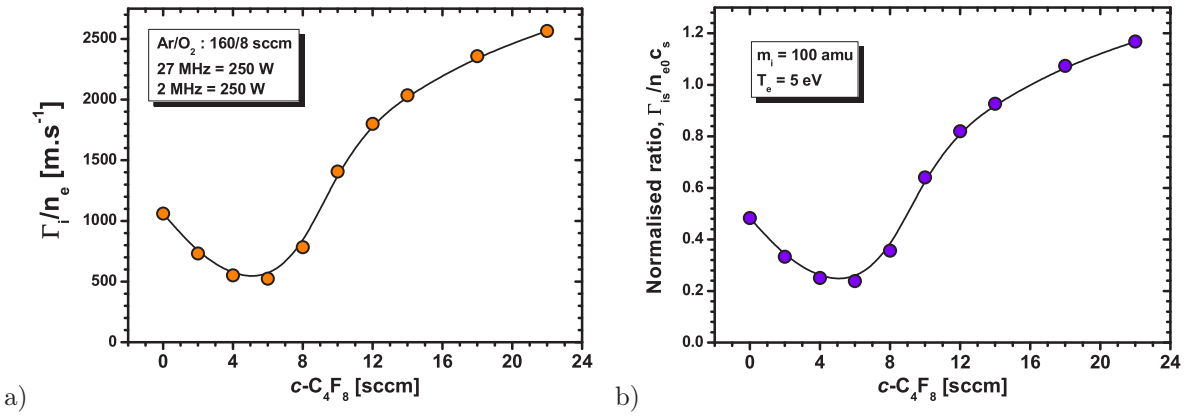


Figure 3.21: (a) Ion flux to electron density ratio, R_{ie} and (b) the normalised ratio in an Ar/O_2 dual-frequency plasma with varying c-C_4F_8 flow. For normalising, values of 5 eV and 100 amu were chosen for T_e and m_i respectively.

insight into the trends in electronegativity, the ion flux to electron density ratio, R_{ie}, is calculated. The non-normalised and normalised ratios are shown in parts (a) and (b) of figure 3.21 respectively. For the normalisation, values of 5 eV and 100 amu were chosen

for T_e and m_i respectively. The measured tail electron temperatures were not used as they almost certainly do not reflect the bulk T_e. In the region where the I–V curves seemed Maxwellian (2–4 sccm c-C_4F_8) it is possible that the bulk T_e maybe equivalent to the tail temperature, i.e. 4 eV. However, as (i) this cannot be verified, (ii) self-consistent models indicate $T_e = 5$ eV, (iii) the normalisation depends only on $\sqrt{T_e}$ and (iv) for reasons of consistency throughout this thesis, the choice of 5 eV was chosen. The choice of 100 amu for m_i, however, is not strictly true throughout the entire range of c-C_4F_8 flow rates. When c-$C_4F_8 = 0$ sccm, the predominant positive ions will be a mixture of Ar^+ (40 amu) and O_2^+ (32 amu) [Seo 04], and so the value of m_i will be closer to 40 amu. If the change in ion mass was taken into account, then the rise on the left-hand side in the normalised ion flux would not be as pronounced, but it would still exist.

One thing I have always noticed about the R_{ie} curve is that it is relatively smooth and continuous in nature. When one looks at the original ion flux and electron density data in figure 3.20 one can easily see by eye that the individual data points to not all follow a smooth trend. The spline curve that is used to link the data points emphasises this by not passing through the centre of all the data points. However, when the ratio is traced, each point appears to place itself so as to form a *smooth* curve. The spline curve now passes through the centre of each point. Even in situations where RF matching was not ideal (and producing lower electron and ion densities) and created noisy density and flux curves, the ratio curve almost always remained smooth. It is believed that this smoothness in the ratio curves is a result of the strong dependence of the plasma electronegativity on the gas mixture, but also a very weak dependence of α on the power, pressure and temperature parameters. In other words:

> *For a given gas composition small changes in the power, pressure and temperature, will not affect the electronegativity of the plasma: α is a smooth continuous function of the gas composition.*

The fact that the trends in the ratio are smoother than the original n_e and Γ_i trends is testament to the ability of both the hairpin probe and the ion flux probe to follow, with high repeatability, small changes to the plasma condition. This important quality of both these probes is evidence of the usefulness they should have as plasma control diagnostics in industrial processing.

Using the normalised ion flux, the negative ion fraction in the centre of the discharge, α_0, is then calculated using the results of the variable mobility fluid model (see figure 3.22). A value of $\gamma = 5$ was chosen for the electron to negative ion temperature ratio. What we see are three distinct regions – an electropositive region for c-C_4F_8 flows of 4–6 sccm, bordered on the left with a slightly electronegative region of Ar/O_2 plasma (possibly due to the presence of O^- ions) and on the right with a strongly electronegative region in the c-C_4F_8 rich plasma, very likely due to the presence of F^- ions and possibly

larger anion species such as CF_3^- or SiF_5^-. The electronegativity of the Ar/O_2 plasma is almost certainly overestimated due to the assumption that $m_i = 100$ amu, although some electronegativity is to be expected. The electropositive region corresponds roughly to a

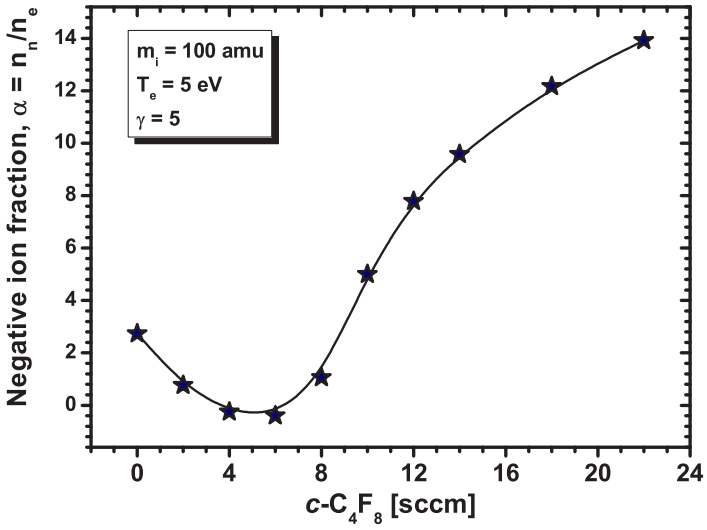


Figure 3.22: The negative ion fraction in an Ar/O_2 dual-frequency plasma with varying c-C_4F_8 flow. A value of 5 was chosen for the electron to negative ion temperature ratio, γ, and a value of 35 was chosen for the ion collision parameter, β_{vm}.

regime where there is an equal flow of carbon and atomic oxygen atoms. This is exactly true when the c-C_4F_8 flow is 4 sccm:

$$4(c\text{-}C_4F_8) + 8(O_2) \rightarrow 16C + 16O + 32F$$

Therefore, at low c-C_4F_8 flow rates (< 4 sccm) the plasma is electronegative, possibly due to the presence of O^-. When the c-C_4F_8 flow rate is 5 ± 1 sccm, the precursors to both O^- and F^- formation are destroyed. For example, F^- can be created through dissociative detachment:

$$CF_2 + e \rightarrow CF + F^-$$

but in the presence of oxygen, the CF_2 precursor can be removed:

$$O + CF_2 \rightarrow COF + F$$

$$COF + O \rightarrow CO_2 + F$$

The removal of CF and CF_2 through the addition of O_2 was observed in a Ar/CF_4 plasma under similar conditions. The CF and CF_2 densities were measured by UV broadband absorption spectroscopy and the results are shown in figure 3.28. When the c-C_4F_8 flow increases beyond 6 sccm, the plasma then becomes electronegative due to the formation of F^-. This is backed up by the CRDS measurements shown in section 3.2, figure 3.3.

The most important observation from this data (and the data which follows) is the highly decoupled nature of the electron density from the ion flux. This data shows clearly that, in a complex, electronegative industrial plasma, one cannot easily relate n_e and Γ_i:

$$\Gamma_i \not\propto n_e \tag{3.16}$$

or in other words, the ion flux is not a function of the electron density, $\Gamma_i \neq \Gamma_i(n_e)$, but rather is a complex function of both the electron density and the negative ion density:

$$\Gamma_i = \Gamma_i(n_e, n_n) \equiv \Gamma_i(\alpha) \tag{3.17}$$

3.4.2 $Ar/O_2/c\text{-}C_4F_8$ – varying the O_2 and $c\text{-}C_4F_8$ gas flows

We now return to the data already presented in the section on determining the negative ion fraction (section 3.3), namely the effect of varying both the fluorocarbon gas flow and the oxygen gas flow. First, we look at the effect of varying the O_2 and c-C_4F_8 gas flows. Both gases are introduced at flow rates such that the total flow rate of both is 24 sccm. Figure 3.7 on page 112 showed the variation of the electron density and the ion current density ($J_i = eA\Gamma_i$) for both single and dual frequency cases. The tendencies are slightly different from those which were observed when only c-C_4F_8 was varied. Due to the difficulties in matching and confining an Ar/O_2 plasma at 50 mTorr, there is only data for the dual-frequency case when c-C_4F_8/O_2 = 0/24 sccm. When this is the case, both the electron density and ion current are very large in comparison to the densities which follow. Once a small amount of c-C_4F_8 is added (just 1 sccm!) the electron density drops by 30 % and the ion current drops by almost 50 %. In both the single and dual frequency plasmas the electron density and ion current then follow the same trends. The electron density stays constant up until c-C_4F_8/O_2 = 4/20 sccm and then decreases slowly up to c-C_4F_8/O_2 = 16/8 sccm. It then remains at a fairly constant density up until c-C_4F_8/O_2 = 24/0 sccm. The ion current remains relatively constant over the entire range of c-C_4F_8 = 1–24 sccm (O_2 = 23–0 sccm). It does, however, decrease slightly from c-C_4F_8/O_2 = 1/23 sccm up until c-C_4F_8/O_2 = 8/16 sccm before recovering with a small maximum at c-C_4F_8/O_2 = 17/7 sccm. This small rise is also present in the single frequency case but is not as obvious due to the large scale. Whereas the single and dual frequency ion currents reflect the difference in applied power (double the power, double the current), the dual frequency electron density decreases at a faster rate than the single frequency density. This decoupled nature suggests in itself a greater presence of negative ions in the dual frequency case. This is made clearer when the ratio R_{ie} is plotted (see figure 3.8). Somewhat surprisingly, the trends in R_{ie} are very similar to those in figure 3.21. When this ratio is normalised and converted to α_0 (figure 3.23 (b)) we again get the three distinct regions: (i) weakly electronegative Ar/O_2 plasma, (ii) electropositive $Ar/O_2/c$-

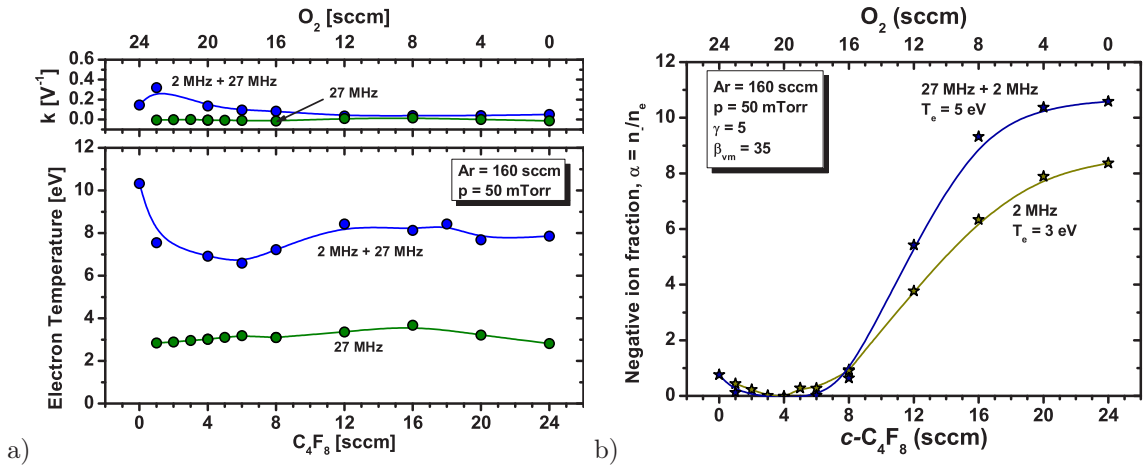


Figure 3.23: $Ar/O_2/c\text{-}C_4F_8$ single (27 MHz = 250 W) and dual-frequency (27 MHz = 250 W; 2 MHz = 250 W) plasmas with varying $c\text{-}C_4F_8$ and O_2 flow rates. a) tail electron temperature and k-factor; b) Negative ion fraction.

C_4F_8 mixture and (iii) strongly electronegative $Ar/c\text{-}C_4F_8$ plasma. The tail electron temperature and k-factor are also shown in part (a) of figure 3.23. The single frequency plasma remains mostly Maxwellian ($k \simeq 0$) throughout the studied parameter range and has a T_e of 3 eV. The dual frequency I–V curves mostly deviate from Maxwellian and have tail temperatures of 7–10 eV. For the calculation of α_0, the values of the various parameters are the same as were used for figure 3.22: $\beta = 35$, $\gamma = 5$, $m_i = 100$ amu, $T_e = 3$ eV (single frequency) or 5 eV (dual frequency).

Again, the electronegativity of the Ar/O_2 plasma may be overestimated because of the assumption that $m_i = 100$ amu. The reason why the $Ar/O_2 = 160/8$ sccm plasma (see figure 3.22) appears more electronegative than the $Ar/O_2 = 160/24$ sccm plasma is not fully understood, when one would have expected to find the latter more electronegative because of the increased O_2 content. There is also the possibility that α is being overestimated because of an increase in the measured ion current due to secondary electron emission. The presence of O_2 will result in the oxidation of the Si surfaces to SiO_2. These surfaces have much higher secondary electron emission coeffiecients, thereby creating a higher density plasma by a *gamma* mechanism. As soon as fluorocarbon is added this SiO_2 layer will be etched off. The higher tail T_e in the Ar/O_2 plasma is consistent with this theory, at least in the dual frequency case where data is available.

The electropositive region occurs around the $O_2/c\text{-}C_4F_8 = 20/4$ sccm flow regime. This cannot be explained using the same reasoning as before, where we may have expected the electropositive region to have been centred around the $O_2/c\text{-}C_4F_8 = 16/8$ sccm flow regime such that the atomic oxygen and carbon quantities were equal. What the results do suggest is that the electronegativity is highly dependent on the $c\text{-}C_4F_8$ flow rate and only very weakly dependent on the O_2 flow rate, and that the 2–6 sccm region of $c\text{-}C_4F_8$

flow is consistently electropositive.

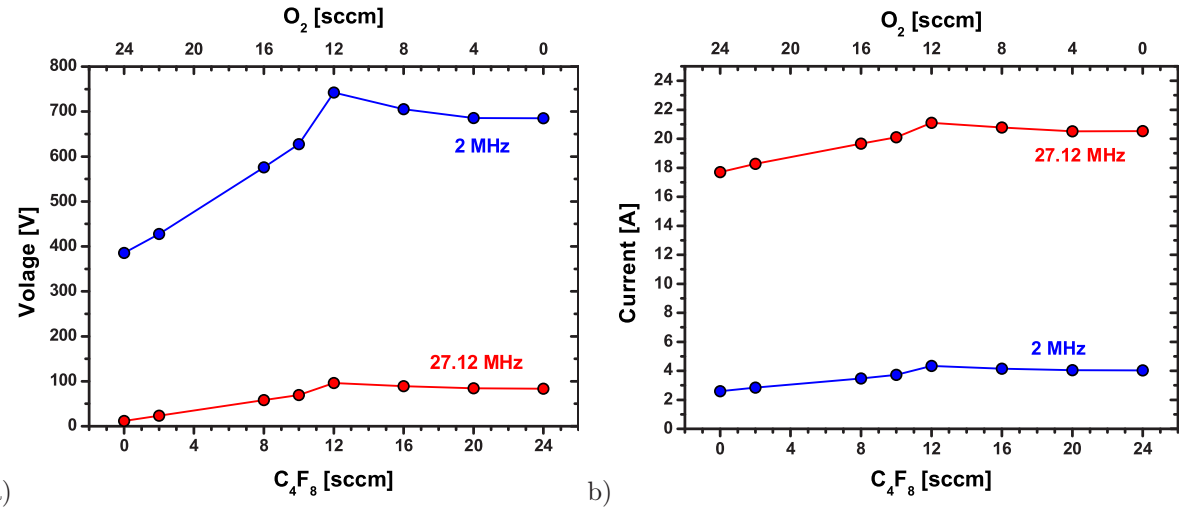


Figure 3.24: (a) Voltage and (b) current data obtained from the Onebox VI probe in a dual frequency $Ar/O_2/c\text{-}C_4F_8$ dual frequency plasma

Figures 3.24 (a) and (b) show the voltage and current for both the 2 MHz generator and the 27.12 MHz RF generators in the dual frequency $Ar/O_2/c\text{-}C_4F_8$ plasma as a function of O_2 and $c\text{-}C_4F_8$ flows. The data was obtained using the Onebox^{TM} integrated VI probe. The trends in the voltage and current are summarised below:

- The **27.12 MHz voltage** increases from 11.6 V in the Ar/O_2 plasma to 96.1 V when $O_2/c\text{-}C_4F_8 = 12/12$ sccm, an 8-fold increase. It then stays relatively constant, dropping to 83.5 V when $O_2/c\text{-}C_4F_8 = 0/24$ sccm.
- The **2 MHz voltage** increases from 385.5 V in the Ar/O_2 plasma to 742.5 V when $O_2/c\text{-}C_4F_8 = 12/12$ sccm, a 2-fold increase. It then also remains relatively constant, dropping to 685.3 V when $O_2/c\text{-}C_4F_8 = 0/24$ sccm.
- The **27.12 MHz current** increases from 17.7 A in the Ar/O_2 plasma to 21.1 A when $O_2/c\text{-}C_4F_8 = 12/12$ sccm, a 20% increase. It then stays relatively constant, dropping to 20.53 A when $O_2/c\text{-}C_4F_8 = 0/24$ sccm.
- The **2 MHz current** increases from 2.6 A in the Ar/O_2 plasma to 4.34 A when $O_2/c\text{-}C_4F_8 = 12/12$ sccm, a 60% increase. It then also remains relatively constant, dropping to 4.03 A when $O_2/c\text{-}C_4F_8 = 0/24$ sccm.

The curves are slightly correlated with the change in plasma electronegativity. The basic conclusion is that as $c\text{-}C_4F_8$ is added and O_2 is removed (or as the plasma electronegativity increases) the RF voltage and current both increase until the $O_2/c\text{-}C_4F_8$mixture is 12/12 sccm. The voltage and current then remain constant regardless of the further addition of $c\text{-}C_4F_8$ or the further removal of O_2. As the delivered power remains at 250 W for both the 2 MHz and 27.12 MHz RF power supplies, the significant changes in V_{RF} and

I_{RF} implies that there are significant changes in the phase difference between the two. In other words, the load becomes more reactive as evidenced by the more out-of-phase current.

3.4.3 Ar/c-C_4F_8 – varying the c-C_4F_8 gas flow

To better understand the individual effect of c-C_4F_8 the case of an Ar/c-C_4F_8 plasma mixture with varying c-C_4F_8 gas flow was studied. When compared to the previous results, this will also give us insight into the individual effects of oxygen addition. Figure 3.25 shows the trends in the charged particles' densities and fluxes as a function of c-C_4F_8 addition to argon. Three RF power combinations were used:

- single frequency: 27 MHz = 250 W
- single frequency: 27 MHz = 500 W
- dual frequency: 27 MHz = 250 W; 2 MHz = 250 W (Total = 500 W)

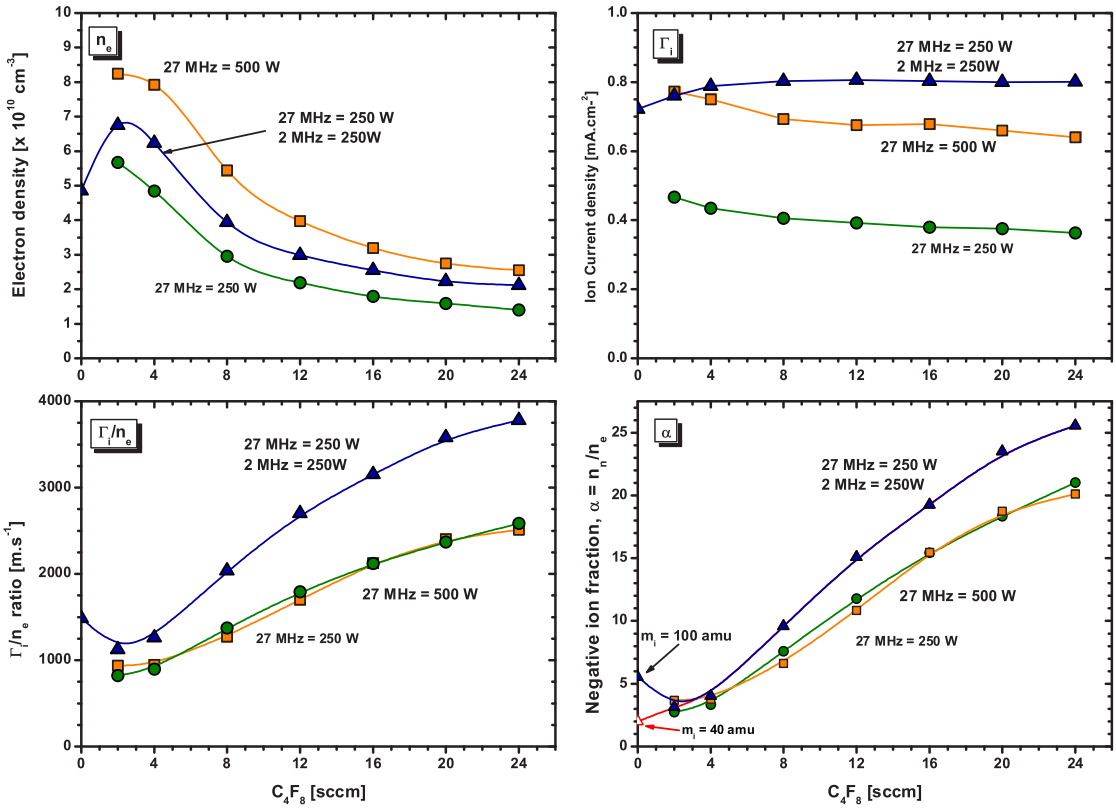


Figure 3.25: Data from the addition of c-C_4F_8 to an argon (170 sccm) plasma. Pressure was not constant but varied from 56 – 60 mTorr with the addition of c-C_4F_8

It was only possible to strike a pure argon plasma in the dual frequency case. In the single frequency case the plasma quickly deconfined, i.e. struck outside the confinement rings. The striking of a DF argon plasma was only practical for short periods of time

that were insufficient for the plasma to reach thermal stability (required for repeatable results). The pressure was not kept constant but instead was allowed to vary from 56 – 60 mTorr with the addition of c-C_4F_8. For the calculation of α, the usual parameters were used ($\gamma = 5$, $\beta_{vm} = 35$, $T_e = 3$ eV for single frequency and 5 eV for dual frequency, $m_i = 100$ amu).

There are quite a number of important observations and results which can be gleaned from figure 3.25. To begin with, it is clear that the addition of c-C_4F_8 significantly affects n_e regardless of what and how power is applied. This is a good example of how sensitive n_e is to the plasma chemistry. The electron density is, however, more sensitive to the 27 MHz power source as can be seen in the differences between the single frequency 500 W case and the dual frequency 500 W case (2 x 250 W). The opposite is true for the ion current, which is higher in the dual frequency case than in the single frequency case, although strictly speaking this is only when c-$C_4F_8$is present. The electron density is lower in an Ar only plasma (dual-frequency) than an Ar/ c-C_4F_8 plasma with 1–5 sccm of c-C_4F_8. It appears that a similar scenario may also occur in the single frequency cases, when their respective trends are taken into account. The addition of c-C_4F_8 therefore favours ionisation due to the lower dissociative ionisation thresholds. This is again proof that the fluorocarbon ions rapidly become the dominant positive ion species.

Turning to the R_{ie} ratios, the single frequency 250 W and 500 W ratios are identical, meaning that their respective negative ion fractions are identical as the same electron temperature ($T_e = 3$ eV) is used the normalisation process in both. The dual frequency 250 W plasma has a slightly higher ratio/negative ion fraction than the single frequency plasmas. The rise in the ratio/negative ion fraction in the argon plasma can be easily explained by a change in the dominant positive ion mass from the heavy fluorocarbon ions to the lighter argon ions. This is indicated on the graph of negative ion fractions by the red line, where an ion mass of 40 amu is considered when the c-C_4F_8 flow is 0 sccm. However, an electronegativity of $\alpha = 4$ is still present, which could be a result of either errors in the experimental measurements or errors in the assumptions used in the model, in particular the ion collision parameter, β_{vm}. The possibility that secondary electron emission is playing a role has also being proposed earlier.

From this data, it is also apparent that the plasma would likely become more electronegative with c-$C_4F_8 > 24$ sccm, probably reaching $\alpha_0 = 35$, were we not limited by the MFC (max 27 sccm). Finally, when we compare this data with that of the $Ar/O_2/c$-C_4F_8 data, we see that in our experimental conditions an Ar/O_2 plasma produces higher electron densities and ion currents than a pure argon plasma. This is contrary to experimental and numerical results in the literature (see references [Seo 04, Lee 95]) and is also contrary to intuition. This can only be explained, therefore, by issues with power coupling to the argon plasma in our reactor, although very little, if any, difference is

observed in the OneBox current and voltage data (not shown).

3.4.4 $Ar/O_2/CF_4$ – varying the O_2 and CF_4 gas flows

We again return to the data already presented in the section on determining the negative ion fraction (section 3.3),but now we look at the effect of varying the O_2 and CF_4 gas flows. Both gases are introduced at flow rates such that the total flow rate of both is 40 sccm. Figure 3.9 on page 114 showed the variation of the electron density and the ion current density ($J_i = e\Gamma_i$) for both the single and dual frequency cases. Due to the difficulties in the matching and confining of a single-frequency Ar/O_2 plasma at 50 mTorr, the values of n_e and J_i when O_2 = 40 sccm are likely lower than would be expected. For the rest of the gas flow rates, however, the electron density and ion current follow the same trends for both the single and dual frequency plasmas. The electron density remains relatively constant from CF_4/O_2 flow rates of 5/35 sccm to 35/5 sccm, before incurring a significant drop when CF_4/O_2 = 40/0 sccm. The ion current also remains relatively constant from CF_4/O_2 flow rates of 5/35 sccm to 35/5 sccm, before rising slightly CF_4/O_2 = 40/0 sccm. In the dual frequency Ar/O_2 plasma, n_e and J_i are significantly higher than when CF_4 is present, and as expected, have values close to that which was found in the c-C_4F_8/O_2 experiments.

Plots of the Γ_i/n_e ratio are shown in figure 3.10 (a) on page 114. The first thing we notice is that the trends are identical in both the SF and DF plasmas, despite the matching problems in the SF Ar/O_2 plasma. This again is evidence that the ratio (and therefore α) is primarily dependent on the gas mixture and not the absolute plasma characteristics. The negative ion fraction is plotted in figure 3.26 (b), showing that when normalisation is performed both the SF and DF plasmas have almost identical values of α, except when $CF_4 \geq 35$ sccm. Here it is reminded (see page 122) that an ion collision parameter, β_{vm}, of 200 is used to avoid negative values of α. The measured tail electron temperatures in figure 3.26 (a) are similar to those in the c-C_4F_8 experiments and again help justify our choice of T_e for the normalisation process. The SF plasma always exhibits Maxwellian tail temperatures, whereas the DF plasma always requires the Druyvesteyn k-factor for satisfactory I–V curve fitting.

Again we see evidence of electronegativity in the Ar/O_2 plasma, but again most of this is likely due to the change in positive ion mass. Unlike the O_2/c-C_4F_8 experiments, the rise in α towards low CF_4 flows is gradual, possibly reflecting the fact that the shift in dominant ion mass is more gradual as CF_3^+ has an ion mass of 69 amu and Ar^+ has an ion mass of 40 amu. In c-C_4F_8 the change was from an ion mass > 100 amu. Also unlike the O_2/c-C_4F_8 experiments, the rise in α with the addition of CF_4 only occurs when the O_2 flow rate approaches zero. Whereas c-C_4F_8 dominated the change in electronegativity over most of the flow rates under study, CF_4 only has an effect one the O_2 flow is close

to or equal to 0 sccm. O_2 is therefore plays a role of "quenching" the electronegativity created by CF_4. This will be examined in more detail in the next section.

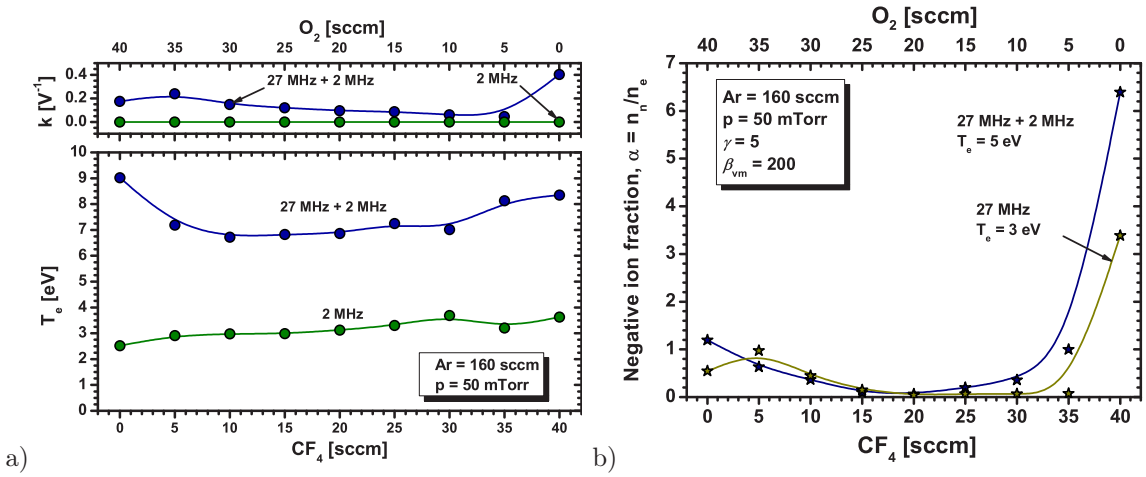


Figure 3.26: $Ar/O_2/CF_4$ single (27 MHz = 250 W) and dual-frequency (27 MHz = 250 W; 2 MHz = 250 W) plasmas with varying CF_4 and O_2 flow rates. a) tail electron temperature and k-factor; b) Negative ion fraction.

3.4.5 $Ar/O_2/CF_4$ – varying the O_2 gas flow

We examine here the addition of small amounts of oxygen to an Ar/CF_4 plasma. This is to gain insight into what occurs in the transition from an $Ar/O_2/CF_4$ plasma to an Ar/CF_4 plasma, which in the previous section was shown to be an important region in terms of the variations in plasma electronegativity.

The base mixture used was an Ar/CF_4 mixture of 180/36 sccm. O_2 was then added in amounts varying from 2–10 sccm in steps of 2 sccm. Both a SF (27 MHz = 250 W) and a DF (27 MHz = 250 W; 27 MHz = 250 W) powered plasmas are studied. The pressure was not constant but varied from 52 – 56 mTorr with the addition of O_2. The results (n_e, J_i, R_{ie} and α_0) are shown in figure 3.27. References to the experimental results in figure 3.9 are used in the analysis of this data. The right most part of the data in the graphs in figure 3.9 (Ar/CF_4 = 160/40 sccm) corresponds roughly to the left most part of the data in the graphs in figure 3.27 (Ar/CF_4 = 180/36 sccm)

The small differences in the gas mixtures are the cause of some discrepancies in absolute values. Notwithstanding these discrepancies, the trends should give us the insight we are looking for. The ion current is hardly affected by the addition of oxygen, with no change in the SF ion current and only a 15% drop in the DF ion current. The electron density, however, is strongly affected by the addition of O_2, particularly in the DF case where the density doubles between 4 and 8 sccm. The SF case sees a gradual 50% increase over the 0–6 sccm range of O_2 flow. In both cases, the majority of the density variations have occured by 10 sccm of O_2 addition. This is also seen in the ratio and α graphs, where

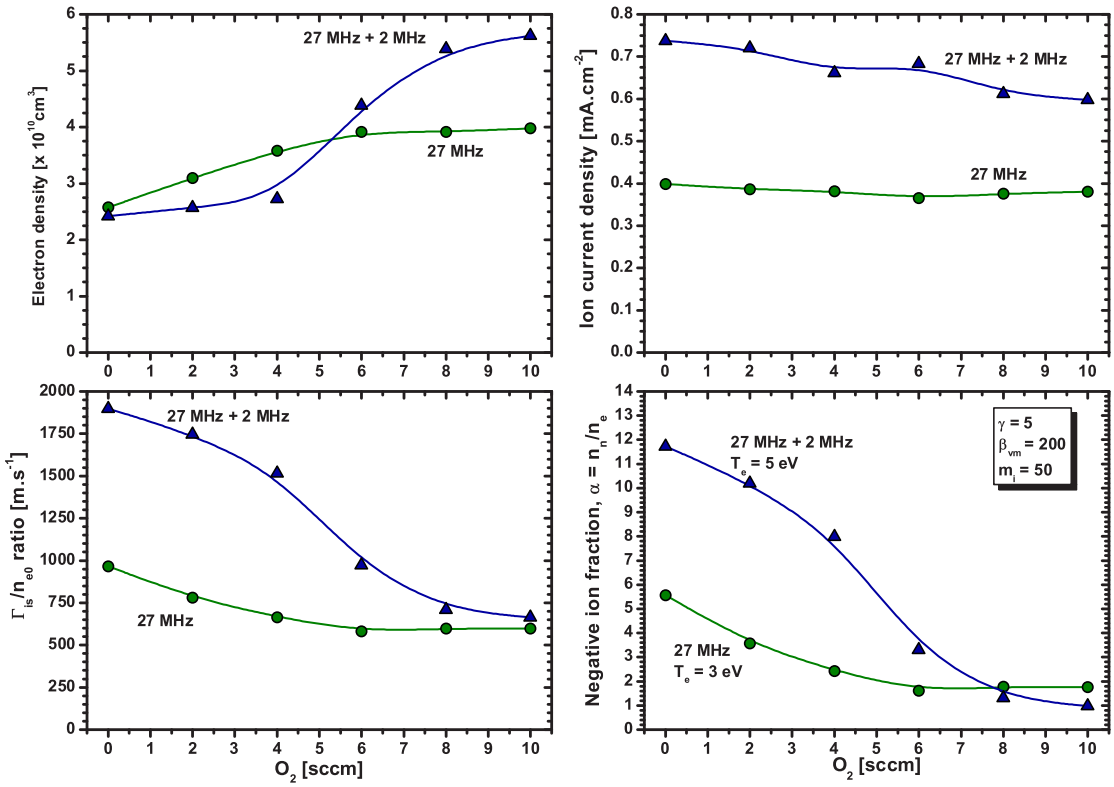


Figure 3.27: Data from the addition of O_2 to an Ar/CF_4 (180/36 sccm) plasma. Pressure was not constant but varied from 52 – 56 mTorr with the addition of O_2.

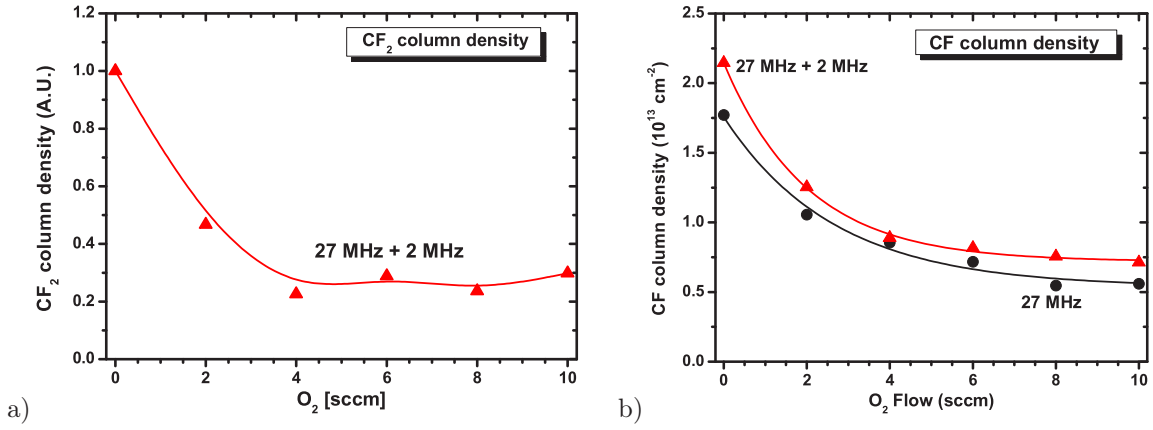


Figure 3.28: (a) CF_2 and (b) CF column densities in $Ar/CF_4/O_2$ (180/36/xx sccm) plasma as a function of O_2 flow. RF power was 250 W for both the 27 MHz and 2 MHz generators. Measurements were performed using UV-BBAS and data analysis was carried out with the help of Nicolas Bulcourt.

the plasma changes from a strongly electronegative to weakly electronegative plasma. Going on previous results, the weak electronegativity at 10 sccm of O_2 addition is likely to be an artefact of the choice of fluid model parameters and the plasma is possibly electropositive in this region. This means that when the atomic oxygen, O, count reaches half the carbon, C, count in an $Ar/O_2/CF_4$ plasma then a shift from an electronegative to an electropositve plasma will occur. The availability of carbon to form fluorocarbon molecules is therefore a prerequisite to the formation of negative ions.

At the time these experiments were taken, we had the possibility to measure the CF and CF_2 densities, under the same conditions, using broadband UV absorption spectroscopy (UV-BBAS), with the help of Nicolas Bulcourt. The results are shown in figure 3.28. The effect of adding O_2 is roughly a four-fold reduction in the densities of both these radicals. Most of this reduction occurs in the first 4–6 sccm of O_2 addition. As CF and CF_2 are both presumed to be precursors to the formation of F^- through dissociative attachment, we would expect some correlation between their densities and the trends in plasma electronegativity. This appears to be somewhat the case, although their trends are not exactly correlated. We do get, however, a better overall picture of how small changes in the gas mixture can significantly modify the plasma chemistry, and so significant changes in the ion flux and electron density are to be expected.

3.4.6 $Ar/O_2/SF_6$ – varying the O_2 and SF_6 gas flows

The availability of SF_6 in the laboratory presented an opportunity to apply the probe measurements and the fluid model to this well known electronegative gas. As with the c-C_4F_8 and CF_4 experiments, the electronegativity of SF_6 was studied in the context of an argon plasma with varying O_2 and SF_6 flow rates. This allowed us to compare the results using SF_6 with those using the fluorocarbon gases, but it was also to keep the study within the context of this thesis, where data on complex $Ar/O_2/SF_6$ gas mixtures is more interesting from an industrial viewpoint than "simple" Ar/SF_6 mixtures or pure SF_6 plasmas.

The O_2 and SF_6 flows were varied from 0–40 sccm in such a way that the total flow rate of both was 40 sccm. The argon flow rate was 150 sccm and the pressure remained constant at 60 mTorr. This is 10 mTorr higher than what is usually used in this thesis. This is because these experiments were taken at a late stage, when the confinement ring configuration had been modified to allow for higher pressures. The study was undertaken in a single frequency RF plasma at fixed power (27 MHz = 250 W).

The electron density and the ion current density are plotted in figure 3.29 (a) and the estimated negative ion fraction is plotted in figure 3.29 (b). The trends are closer in resemblance to those obtained using c-C_4F_8 than those using CF_4 in that the major variations in densities and fluxes occur with the initial addition of SF_6. Only a small

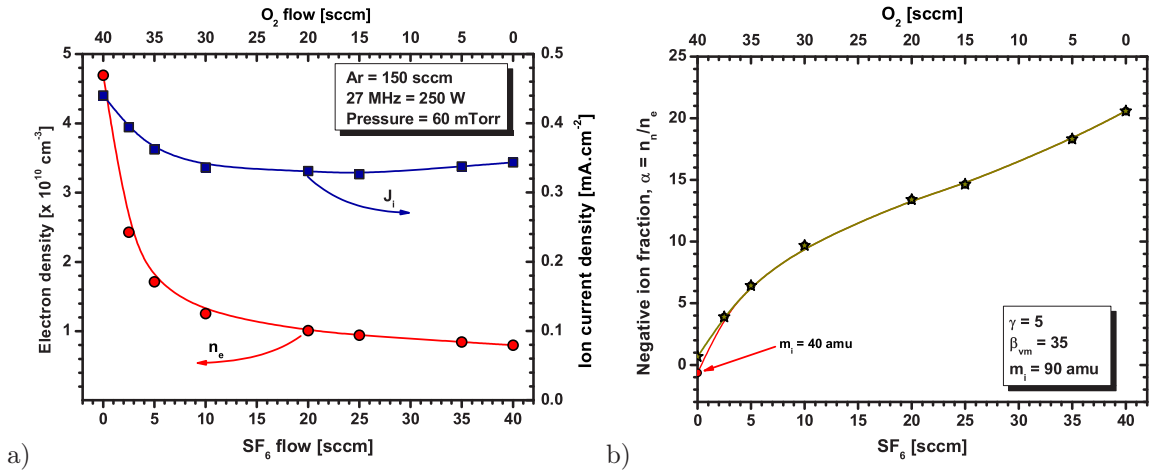


Figure 3.29: (a) Electron density and ion current and (b) negative ion fraction in a single frequency $Ar/O_2/SF_6$ plasma with varying of O_2/SF_6 flows.

amount of SF_6 (2.5 sccm) is required to reduce by half the electron density in an Ar/O_2 plasma. The ion current is not affected as much, and these decoupled trends in n_e and Γ_i are evidence of changing electronegativity. This is illustrated in part (b) of this figure where the negative ion fraction at the plasma centre, α_0, is calculated from the normalised ion flux. The normalisation assumes $T_e = 5$ eV and $m_i = 90$ amu. The ion mass is assumed to be close to that of SF_3^+ (89 amu) [Sasaki 97]. It may be large with increasing SF_6 flow due to the presence of SF_5^+ (127 amu), but it will certainly be smaller in the Ar/O_2 plasma, around the order of 40 amu. The negative ion fraction in the Ar/O_2 for this value of m_i is also plotted for reference. The ion collision parameter used was $\beta_{vm} = 35$ as in the case of c-C_4F_8.

The negative ion fraction is a continuously increasing function of the $SF_6/(SF_6 + O_2)$ ratio. It increases rapidly and non-linearly from a weakly electronegative plasma (possibly electropositive) between O_2/SF_6 flows of 40/0 sccm and 30/10 sccm before contining to increase at a reduced linear rate up to a maximum of $\alpha_0 \sim 20$ at O_2/SF_6 flows of 0/40 sccm. It would likely keep increasing with further addition of SF_6.

In comparison to the c-C_4F_8 experiments, the most obvious difference is that there is no dip in electronegativity – the presence of O_2 appears to have little effect on the capacity of SF_6 to produce negative ions. In other words, the O atoms do not destroy SF_x precursors to the negative ions (e.g. F^- or SF_5^-), in contrast to their ability to destroy the C_xF_y precursors.

3.4.7 CF_4 plasma – effects due to SF_6 addition

It was requested by our industrial partners that the study of SF_6 addition to a CF_4 plasma be undertaken to observe whether or not the addition of SF_6 can make such a plasma more electronegative. This maybe important to industrial processes as an increase

in electronegativity would mean less control over the electron-driven dissociation of CF_4 and therefore less control over the densities of radicals such as F, CF, CF_2, etc. which are important in various process recipes. The conditions to be studied were a single frequency RF powered plasma (27 MHz) at 400 W in 100 mTorr of CF_4. The SF_6 flow was to be varied from 0–50 sccm. The mass flow controllers at our disposal, however, limited our conditions to about 80 mTorr and 0–30 sccm of SF_6.

The results of this study are shown in figure 3.30. The ion current is not affected by the addition of SF_6 whereas the electron density decreases almost linearly and at a relatively high rate. The only possible source of this decline is an increase in the plasma electronegativity, which is plotted in the second graph. Here, an ion collision parameter of 200 was used to give a rough estimate of α (fluid model results for this value of β_{vm} were readily available). The negative ion fraction is estimated to at least double with the addition of 30 sccm of SF_6.

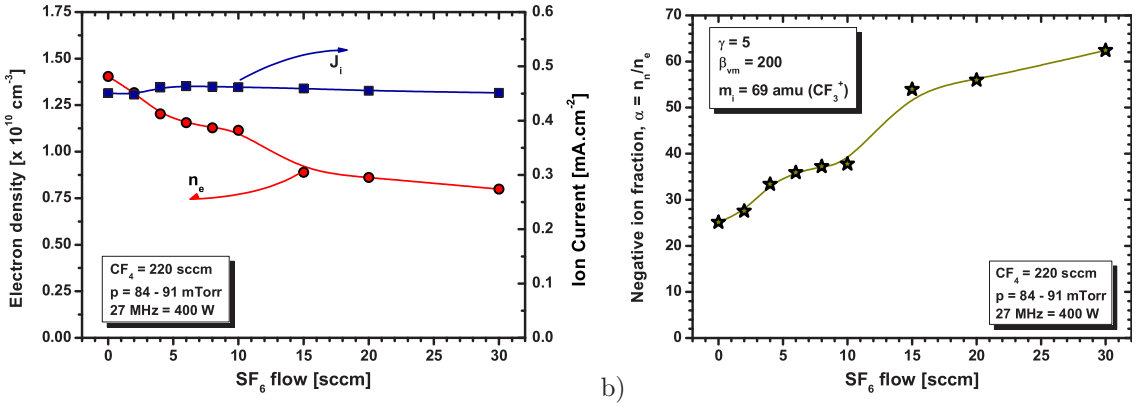


Figure 3.30: (a) Electron density and ion current and (b) negative ion fraction in a single frequency CF_4 plasma with addition of SF_6.

3.5 Charged particle dynamics – Effect of pressure

The effect of pressure on the plasma characteristics was not a focus of this thesis. However several experiments were undertaken at various pressures as a form of control, i.e. to verify that variations in pressure did not influence significantly the final result. This was found to be the case, as will be shown in the example of an $Ar/O_2/c\text{-}C_4F_8$ plasma in the first part of this section. Of greater interest, but beyond the scope of this thesis in terms of being fully investigated, were the distortions which occurred in the I–V curves of the ion flux probe at higher pressures ($\geq$ 100 mTorr). These are briefly presented in the second part of this section.

3.5.1 $Ar/O_2/c\text{-}C_4F_8$ – varying the pressure: 25 – 100 mTorr

The pressure was varied in a single frequency (27 MHz) plasma containing an $Ar/O_2/c\text{-}C_4F_8$ gas mixture supplied in various flow rates, each with a contention ratio of 24:1:2. This ratio was chosen so as to be as close as possible to the ratio used in the industrial $Ar/O_2/c\text{-}C_4F_8$ etch recipes, while at the same time facilitating the control of the MFC's that were used. Seven flow sets were used, corresponding to seven different plasma pressures. These are outlined in table 3.7. The gas flow rates can also be expressed as a fraction of the total gas flow rate: 88.9% / 3.7% / 7.4%. In the preceding $Ar/O_2/c\text{-}C_4F_8$ experimental results, this ratio would roughly correspond to the 160/8/16 sccm flow regime. The RF applied power was set to 250 W.

Ar (sccm)	O_2 (sccm)	$c\text{-}C_4F_8$ (sccm)	Pressure (mTorr)
60	2.5	5	24.8
90	3.8	7.5	35.8
120	5	10	46.0
180	7.5	15	65.0
240	10	20	82.6
300	12.5	25	99.2

Table 3.7: Various flow rates used and their corresponding wafer area pressures.

The response of the plasma characteristics to varying pressure is shown in figure 3.31. Both the electron density and the ion current decrease with increasing pressure, though at reasonably slow rates. Strictly speaking, both stay relatively constant over the 20–40 mTorr pressure range before beginning to decrease. The electron density decreases at a faster rate than the ion current. This is reflected as an increase in the negative ion fraction, as plotted in part (b). Here again we see that there is little change over the 20–40 mTorr pressure range, with $\alpha_0 \simeq 4.5$ It then rises to a value of approximately 6 when $p = 100$ mTorr. Although not shown here, the tail electron temperature decreases from 3.5 eV to 2.2 eV over this range.

The plasma electronegativity is therefore only weakly dependent on changes in pressure, and this being only the case over an order of magnitude change in pressure. It is the ratio of the different gases to one another (particularly between O_2 and $c\text{-}C_4F_8$) that determine α. Over the small variations of pressure often encountered in this thesis (e.g. 52 $\pm$2 mTorr) it can be assumed that there are no effects due to pressure.

3.5.2 Pressure effects on the ion flux probe I–V curves

Distortions in the characteristic I–V curves obtained using the ion flux probe were observed at higher pressures ($\geq$ 100 mTorr). This was first brought to our attention through discussions with our industrial partner who were also using a similar probe set-up. It was

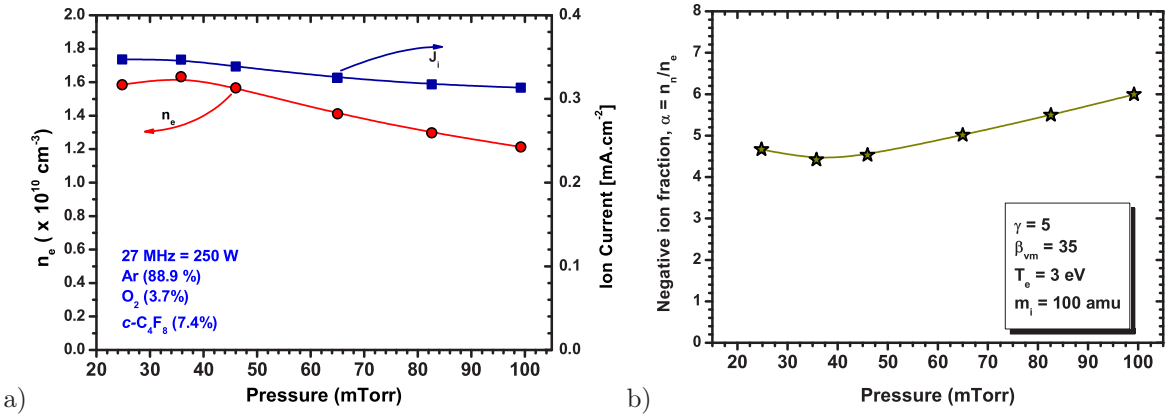


Figure 3.31: (a) Electron density and ion current and (b) negative ion fraction in a 27 MHz (250 W) $Ar/O_2/c\text{-}C_4F_8$ plasma as a function of the wafer area pressure.

subsequently demonstrated in our experimental reactor during experiments designed to examine the effects of pressure (see previous section). The evolution of the I–V curves as the pressure is increased is shown in figure 3.32. Seven pressure regimes are presented, starting at 46.6 mTorr and finishing at 466.6 mTorr.

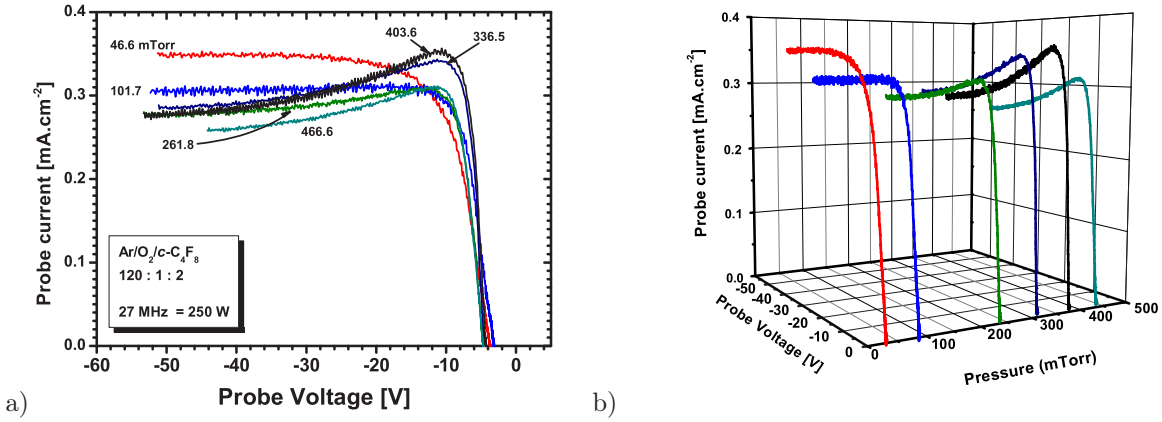


Figure 3.32: Ion flux probe I–V curves obtained at various pressures. (a) and (b) present the same data (same colour scheme) but presented in 2-D and 3-D resepectively.

The I–V curve at 46.6 mTorr is not distorted - it has a Maxwellian profile with a flat ion saturation region followed by a smooth roll-off towards zero current as it approaches the floating potential, V_f, where the electron current, determined by T_e in the tail of the EEDF, increases. Fitting this curve produces a tail T_e of 4.7 eV. When the pressure is increased to 101.7 mTorr, the ion saturation current decreases and the roll-off becomes very steep. This is characteristic of a very low electron temperature. When this curve is fitted a tail T_e of 3 eV is found. However, the fit function does not perfectly fit the I–V curve, particularly at the beginning of the steep roll-off. In previous experiments, this was characteristic of a shift to a more Druyvesteyn EEDF. Whether the two are in fact

related is not fully clear, but what follows as the pressure is further increased suggests that this difficulty in fitting the roll-off is a separate issue.

As the pressure rises, the roll-off now becomes a roll-up or a "bump". If we were to assume that the probe is correctly depicting the sum of the ion and electron currents, then this bump would mean that there is more ion current in a region of low probe bias than at large probe bias. This is not a physically possible solution under normal plasma conditions. Another approach would be to examine the evolution of the I–V curve from the floating potential to the large negative bias. As the bias increases, the electron current decreases resulting in a net positive (ion) current. Beyond a certain bias voltage (here, $V - V_f \simeq -6$ V) the ion current begins to decrease, suggesting that the probe sheath is expanding in to a positive ion depleted region. It then, for some reason, reaches an asymptotic value. Such I–V curves are, of course, impossible to fit using standard plasma and sheath theory. Measurements of ion currents are therefore limited to ≤ 100 mTorr in these experimental conditions.

The ion flux probe data in figure 3.32 was taken using a guard-ring to remove edge effects due to non-linear sheath expansion. Data taken without a guard-ring to examine the effects of the probe surface area on the I–V curves is shown in figure 3.33. The effect of removing the guard-ring, and therefore reducing the total ion current collection area by a factor of 8, is a reduction in the prominence of the "bump feature" at high pressures. The ion current in the ion saturation region continues to increase as a result of the expanding sheath at the probe edges. Where no bump is apparent (e.g. 262 mTorr) the roll-off region still appears very steep. What is surprising is the almost identical I–V curves and ion currents regardless of the change in pressure. Indeed, the ion current even appears to rise slightly with increasing pressure, which is the opposite of what is expected to happen.

The source of these distortions in the I–V curves is still open for debate. The possibility that they could be due to some form of electrical distortion has been tested and has been eliminated.

3.6 Charged particle dynamics – Effect of applied power

In this section the effect of the applied RF power (27.12 MHz and 2 MHz) on the plasma is examined. The power parameters were varied for three different gas compositions, as outline in table 3.8. These three gas mixtures were also used in the $Ar/O_2/c\text{-}C_4F_8$ experiments in the preceding sections (see figure 3.7). The plasma parameters studied are the electron density, the ion current (flux), the electron temperature, the k-factor and in some instances the negative ion fraction. The RF powers used were in the 0 W – 850 W range for each of the RF generators, but not all combinations of 2 MHz and 27.12 MHz

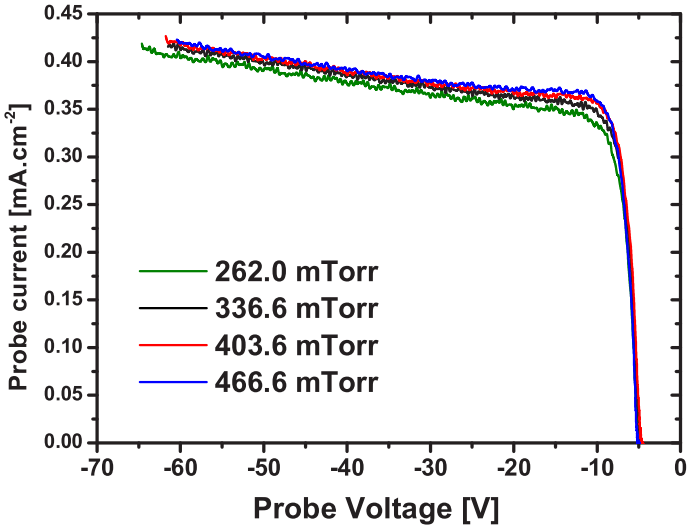


Figure 3.33: Ion flux probe I–V curves obtained at various pressures without the use of a guard-ring.

Ar (sccm)	O_2 (sccm)	c-C_4F_8 (sccm)
160	8	16
160	0	24
160	24	0

Table 3.8: Gas mixtures used in section 3.6

RF powers in this range were possible due to difficulties in keeping the plasma confined, particularly at high powers.

3.6.1 $Ar/O_2/c$-C_4F_8 : 160/8/16 sccm

This gas composition was chosen for its close proximity to common industrial etch recipes. The pressure was in the 51–54 mTorr range, the lower pressures corresponding to the lower powers and vice versa. The evolution of the ion currents as a function of (a) 2 MHz power for various set 27.12 MHz powers and (b) 27.12 MHz power for various set 2 MHz powers is shown in figure 3.34. The corresponding electron densities are shown in figure 3.35.

The ion current increases as a function of applied power for both the low frequency 2 MHz and the high frequency 27.12 MHz RF sources. It was not possible to obtain data using 27.12 MHz RF powers of 700 W and 850 W due to the plasma deconfining (i.e. striking outside the quartz confinement rings). At high 2 MHz powers ($>$ 400 W) the ion current appears to be starting to saturate. At the highest 27.12 MHz powers the ion current is still increasing linearly.The control of the ion flux ($\propto n_i$) is not independently controlled by the high frequency in these experimental condtions. Moreover, the single frequency 2 MHz ion current is higher than the single frequency 27.12 MHz ion current at low powers. This is more clearly shown in figure 3.36 (a). The 27 MHz ion current is

greater than the 2 MHz ion current beyond 700 W.

The electron density does, however, show evidence of being controlled primarily by the high frequency. This is particularly true at low powers (both LF and HF). As the power increases, the influence of the low frequency becomes more and more significant. There is a considerable difference in the electron densities produced by the 27 MHz only and the 2 MHz only plasmas, as illustrated more clearly in figure 3.36 (b). In fact, the electron density was barely measureable in a 2 MHz plasma and the small values of electron density shown are simply indicative that the density was not zero. At first, one might wonder whether this was due to some form of experimental error, large RF sheaths on the hairpin probe for example. That may be a factor, but there are several reasons to suggest the electron density is indeed extremely low. Firstly we observe the trends in the electron density as a function of 27 MHz power. Regardless of the 2 MHz power used, all the density curves are almost linear with their origin close to the zero density mark. Of course, this does not completely eliminate the possibility of sheath effects on the hairpin as they may be the reason that those curves *appear* to have their origin close to zero. The second reason is to note that when the plasma is run in dual frequency mode, it is possible to measure notable electron densities. If the 2 MHz power was the source of sheath effects, then this should have repercussions in the dual frequency mode, particularly at high low frequency powers, but this is not the case. Karkari et al. also carried out some similar measurements in an $Ar/O_2/c\text{-}C_4F_8$dual frequency plasma and found similar results (see figure 3.37). Finally, the remark is made that the light intensity of a 2 MHz plasma is substantially less than that of a 27 MHz plasma.

The question is, then, how is it possible that the ion flux in a 2 MHz plasma is greater than or equivalent to that of a 27 MHz plasma when the electron density is significantly less in the 2 MHz plasma? A plausible reason maybe that this is due to the presence of negative ions. Another possibility is that the large RF sheaths in a 2 MHz plasma result in a very narrow plasma bulk region and so there may be little or no density gradient between the centre of the discharge and the plasma-sheath boundary. This would mean that the h_l-factor could in fact be closer to 1 rather than some value less than the 0.5. This could account for the very high ion current and the low electron density.

Before we examine the electronegativity, let us first take a look at the tail electron temperature and the associated k-factor or Druyvesteyn factor. These are shown, for the same conditions, in figures 3.38 and 3.38 respectively. We note that, as expected from previous data analysis, the tail T_e exhibits distinguishably lower values in the single frequency plasmas than in the dual frequency plasmas. The temperature does increase at high powers in the single frequency 27 MHz plasma, but we will continue to assume a bulk T_e of 3 eV for normalisation purposes. The k-factor is also notably less in the majority of the single frequency cases, but again there is a departure from trend at high

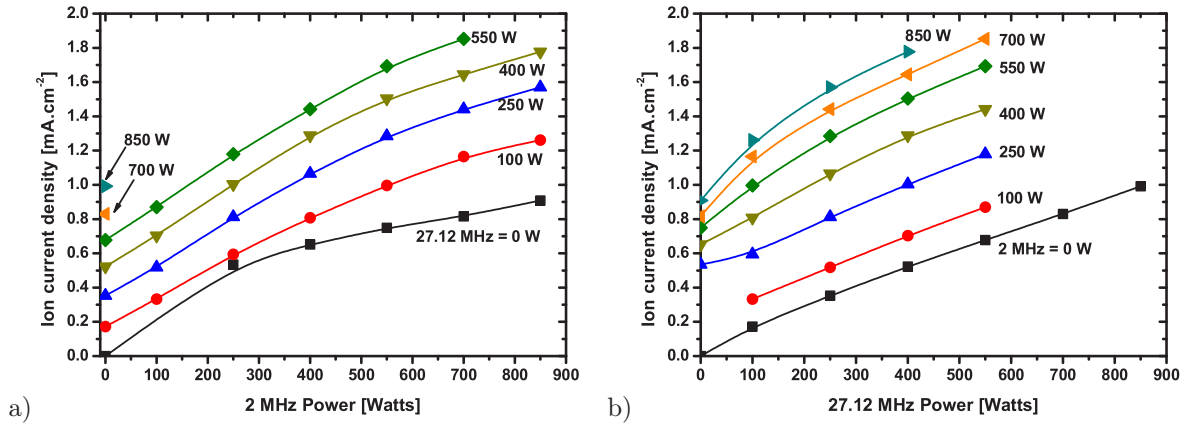


Figure 3.34: Ion current measurements in a dual frequency (27.12 MHz + 2 MHz) $Ar/O_2/c\text{-}C_4F_8$ plasma as a function of (a) 2 MHz power for various set 27.12 MHz powers and (b) 27.12 MHz power for various set 2 MHz powers.

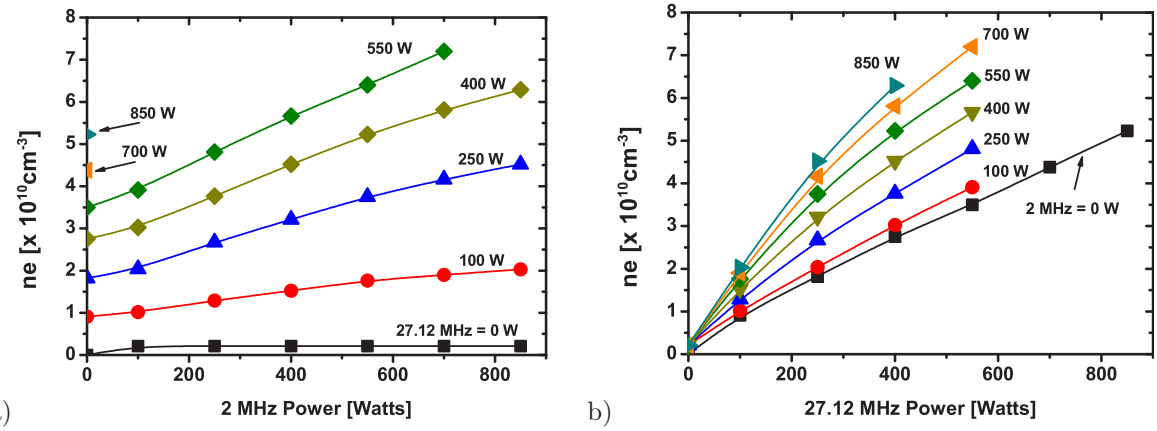


Figure 3.35: Electron density measurements in a dual frequency (27.12 MHz + 2 MHz) $Ar/O_2/c\text{-}C_4F_8$ plasma as a function of (a) 2 MHz power for various set 27.12 MHz powers and (b) 27.12 MHz power for various set 2 MHz powers.

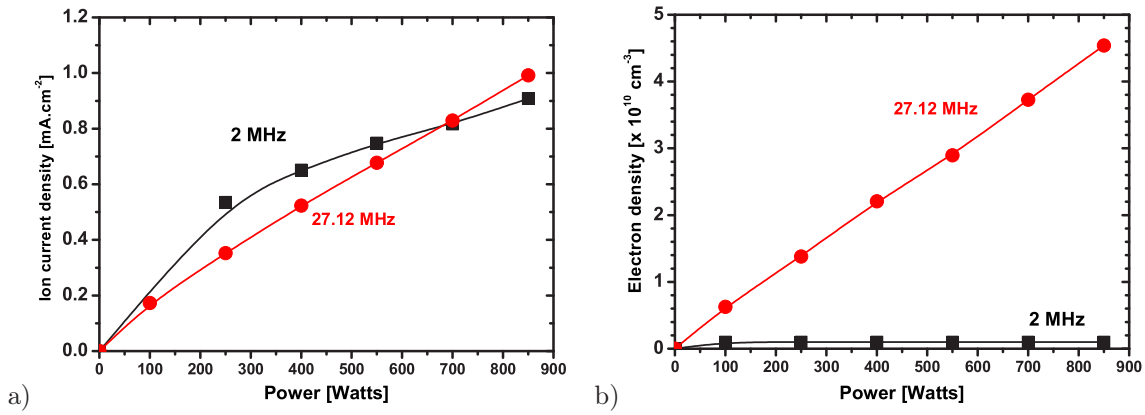


Figure 3.36: (a) Ion current and (b) electron density variations in single frequency (27 MHz or 2 MHz) $Ar/O_2/c\text{-}C_4F_8$ (160/8/16 sccm) plasmas as a function of applied RF power.

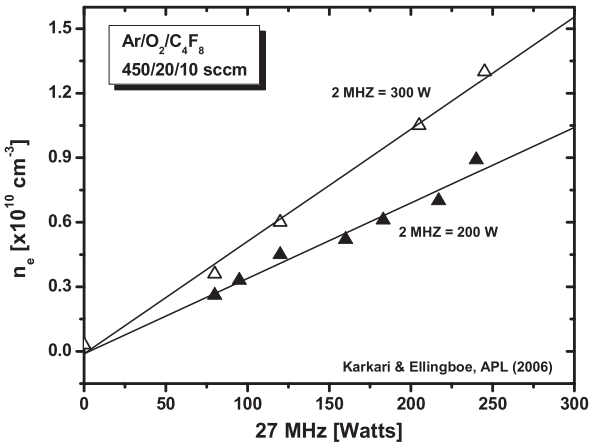


Figure 3.37: Electron density n_e with increase in 27 MHz discharge power for two sets of constant 2 MHz power, as measured by Karkari et al. in a DF-CCP [Karkari 06]. Pressure was 133 mTorr.

powers.

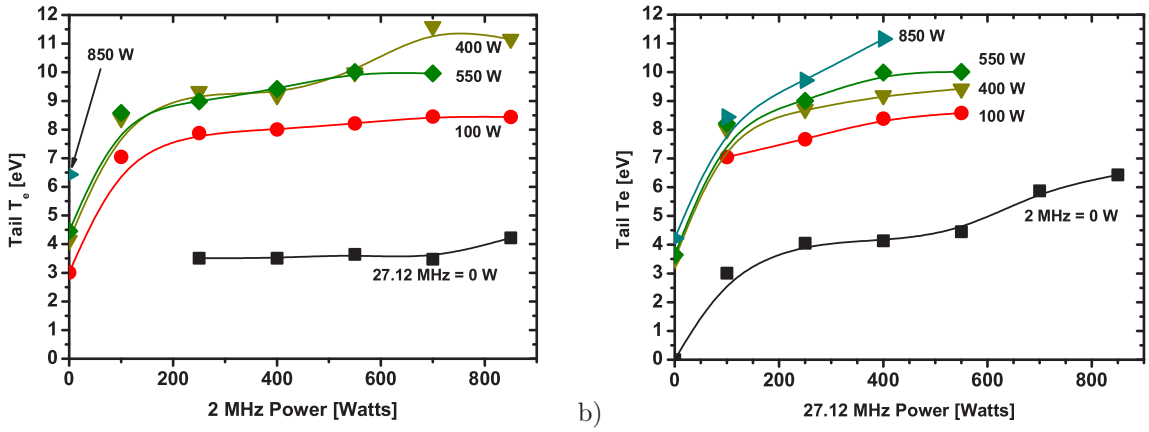


Figure 3.38: Tail electron temperature measurements in a dual frequency (27.12 MHz + 2 MHz) $Ar/O_2/c$-C_4F_8 plasma as a function of (a) 2 MHz power for various set 27.12 MHz powers and (b) 27.12 MHz power for various set 2 MHz powers.

The decoupled nature of the ion current and electron density trends as a function of power is more obvious when the ratio of one to the other is plotted, as shown in the R_{ie} ratio graphs in figure 3.40. Due to the extremely low electron densities measured in the 2 MHz only plasma, the ratio was extremely large and is not included in part (a) of this figure. These ratios are then normalised, according to the usual practice in preceding sections, and converted to their respective α_0 estimations using the variable mobility fluid model (figure 3.41). The trends are quite obvious:

- The negative ion fraction increases non-linearly with increasing, low (0–500 W) 2 MHz power. This is especially true for low 27.12 MHz powers. It then remains relatively constant with increasing, high-power ($>$ 500 W) 2 MHz power.

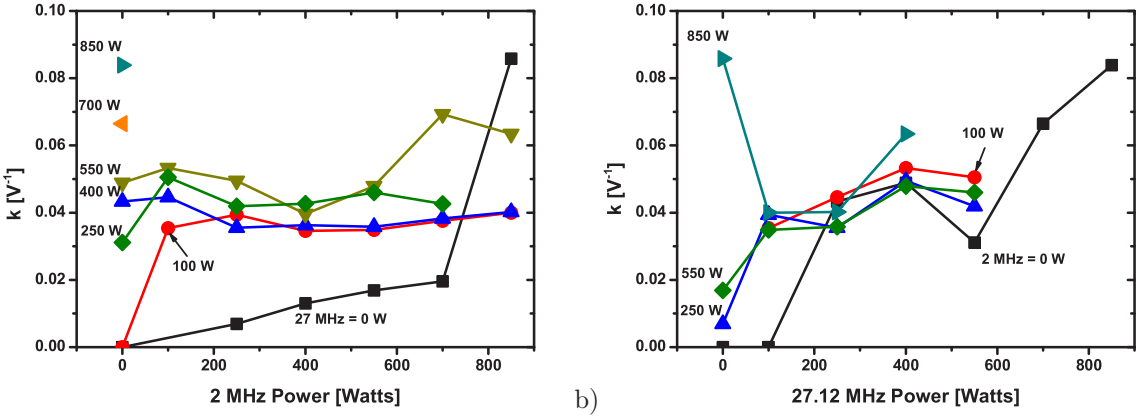


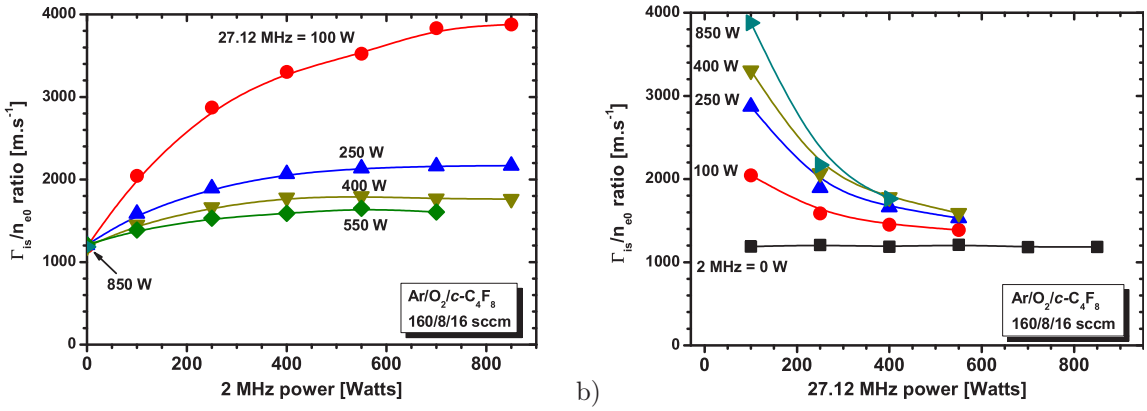
Figure 3.39: k-factor measurements in a dual frequency (27.12 MHz + 2 MHz) $Ar/O_2/c\text{-}C_4F_8$ plasma as a function of (a) 2 MHz power for various set 27.12 MHz powers and (b) 27.12 MHz power for various set 2 MHz powers.

- The negative ion fraction decreases non-linearly with increasing, low (0–500 W) 27.12 MHz power. This is especially true for high 2 MHz powers. It then remains relatively constant with increasing, high-power (> 500 W) 27.12 MHz power.

- The negative ion fraction is greater in dual frequency mode than in single frequency 27 MHz mode. This has already been observed in previous sections.

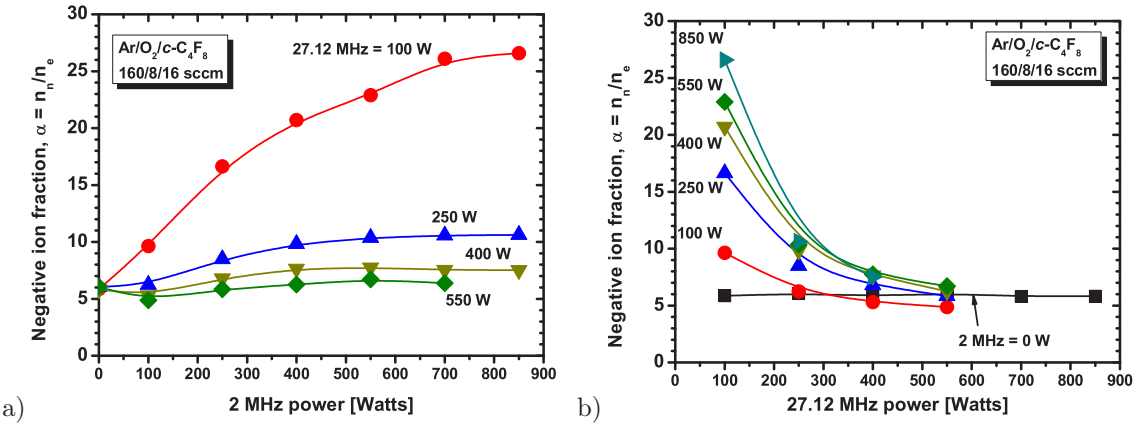
  The reason why the electronegativity appears to increase with additional LF power is fully understood. Georgieva and co-workers suggested that the opposite would be more likely, but our experimental results do not back this up. An increase in 2 MHz power is normally synonymous with an increase in sheath thickness and therefore a smaller plasma bulk. This effect could actually be dominating the ion current characteristics by significantly modifying the h_l-factor. As was mentioned earlier, we may have a case where h_l is increasing, possibly to values greater than 0.5, in situations where the plasma bulk becomes very small compared with the sheaths. However, this remains speculation. An increase in the sheath thickness on the hairpin probes may also occur, but this has already been discussed and has been ruled out. Also, as we will see later, the notion of increasing hairpin sheaths does not hold when the results in the Ar/O_2 plasma are considered.

A final remark in this mixture is to note that the negative ion fraction has no dependence on single frequency 27 MHz power, and only a small dependence on power variations in dual frequency 2 × 250 W plasmas. This will also approximately be the case in the following two gas mixtures and it explains why the R_{ie} curves are so reproducible during the experiments on gas mixture variations, even when difficulties in RF matching were encountered.



a) b)

Figure 3.40: Ion flux to electron density ratios in a dual frequency (27.12 MHz + 2 MHz) $Ar/O_2/c\text{-}C_4F_8$ plasma as a function of (a) 2 MHz power for various set 27.12 MHz powers and (b) 27.12 MHz power for various set 2 MHz powers.



a) b)

Figure 3.41: Negative ion fractions in a dual frequency (27.12 MHz + 2 MHz) $Ar/O_2/c\text{-}C_4F_8$ plasma as a function of (a) 2 MHz power for various set 27.12 MHz powers and (b) 27.12 MHz power for various set 2 MHz powers.

3.6.2 $Ar/c\text{-}C_4F_8$: 160/24 sccm

This gas composition was chosen as it corresponds to the $Ar/c\text{-}C_4F_8$ composition used in the $Ar/O_2/c\text{-}C_4F_8$ experiments earlier when the $O_2/c\text{-}C_4F_8$ flow rates were set to 0/24 sccm. That is, it corresponds to the right-most data points in those graphs (see for example figure 3.23 (b) on page 131). We learned earlier during those experiments that there was little variation in n_e, Γ_i and α_0 in the range of $O_2/c\text{-}C_4F_8$ flow rates between 8/16 sccm and 0/24 sccm. As such, it would not be surprising to find that the results in this section's gas mixture closely match those of the previous section, and this indeed proves to be the case.

The ion currents and electron densities for the various power configurations in the $Ar/c\text{-}C_4F_8$ (160/24 sccm) plasma are shown in figures 3.42 and 3.43 respectively. We find that the trends are quasi-identical to those in the $Ar/O_2/c\text{-}C_4F_8$ (160/8/16 scmm) case. The only notable difference is the reduction in the absolute values of J_i and n_e, which was to be expected as previous data showed that this is a direct result of the increased $c\text{-}C_4F_8$ flow. We still have the situation whereby the 2 MHz plasma produces similar ion currents to that of the 27 MHz plasma, while at the same time it has unmeasurable electron densities. There is still no evidence to suggest that the ion flux can be independently controlled by the high frequency, while there is some degree of independent control of the electron density. The electron temperature, k-factor and negative ion fraction are all

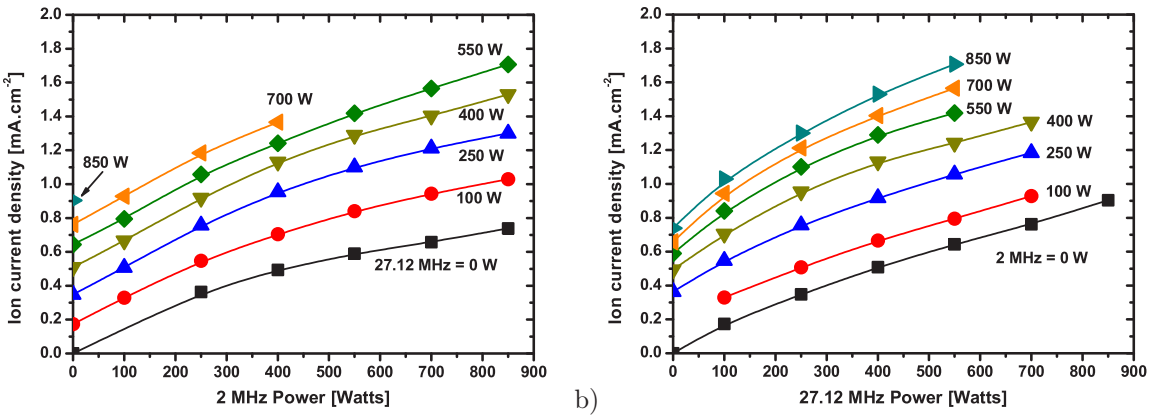


Figure 3.42: Ion current measurements in a dual frequency (27.12 MHz + 2 MHz) $Ar/c\text{-}C_4F_8$ plasma as a function of (a) 2 MHz power for various set 27.12 MHz powers and (b) 27.12 MHz power for various set 2 MHz powers.

similar in nature to the $Ar/O_2/c\text{-}C_4F_8$ (160/8/16 scmm) case and are not shown as the same conclusions can be made.

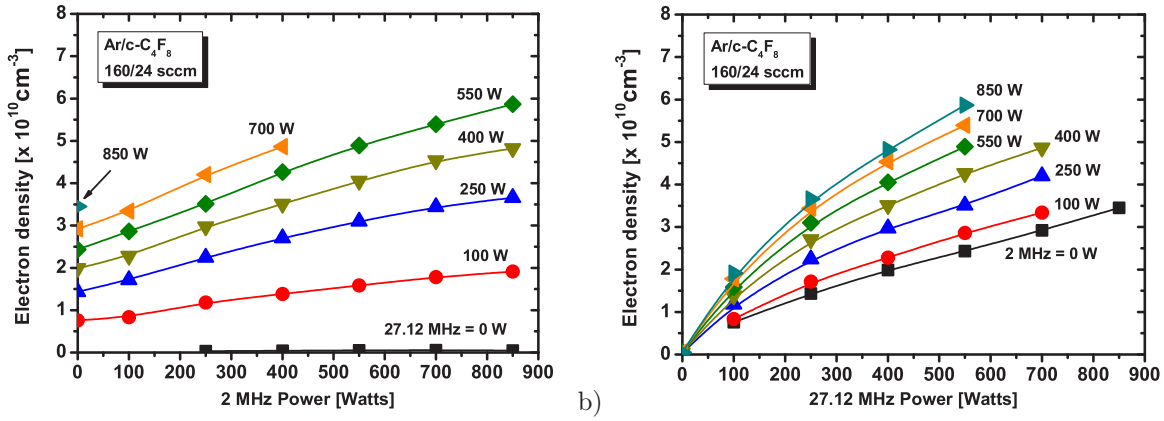


Figure 3.43: Electron density measurements in a dual frequency (27.12 MHz + 2 MHz) Ar/c-C_4F_8 plasma as a function of (a) 2 MHz power for various set 27.12 MHz powers and (b) 27.12 MHz power for various set 2 MHz powers.

3.6.3 Ar/O_2 : 160/24 sccm

Ar/O_2 plasmas have been widely studied because of their importance in integrated circuit manufacturing [Seo 04, Li 03, Lee 95, Margetić 98, Rauf 97]. They are used in their own right for conditioning and cleaning plasma chambers, as well as being present in various etch recipes in tandem with chemically reactive etching gases such as fluorocarbons, Cl_2, SF_6, $SiCl_4$, etc. Earlier in this chapter, we saw how different the plasma characteristics (n_e, Γ_i, α, T_e) were in the Ar/O_2 only mixtures compared to when small amounts of fluorocarbon gases were added. The electron densities and ion currents were up to 100% higher and the electronegativity was almost always negligeable. This is not to say that negative ions are not present in such mixtures, for example in the form of O^-, but their role was not critical to the plasma dynamics.

Here we examine the effect of various power configurations on an Ar/O_2 plasma mixture. The flow rates (160/24 sccm) are chosen so that the results may be taken in the context of previous results in this chapter. Compared to the c-C_4F_8 containing plasmas, the Ar/O_2 mixture is characterised by high densities and currents. This is very clearly illustrated in figures 3.44 (ion current) and 3.45 (electron density). J_i is greater than 1 mA.cm^{-2} in the majority of configurations and n_e is greater than 1 $\times 10^{11}$ cm^{-3} in the majority of configurations. Unfortunately, it was not possible to confine an Ar/O_2 single frequency (27 MHz or 2 MHz) plasma long enough to take measurements.

As with the $Ar/O_2/c$-C_4F_8plasma, no independent control of ion flux is obtained by use of the high frequency source. The low frequency still contributes substantially to the production of the ion flux, and is even more efficient at doing so at the lower powers. We do not see evidence of saturation at high LF powers, as was the case in the c-C_4F_8 plasmas. As the power increases, however, the high frequency begins to become more efficient in terms of ion flux production.

In a departure from the $Ar/O_2/c\text{-}C_4F_8$ and $Ar/c\text{-}C_4F_8$ cases, the electron densities follow practically the same trends as the ion current. Furthermore, the curve trends in the graph of n_e Vs 27 MHz power suggest that the electron density will be far from zero when 27.12 MHz = 0 W. This would mean that high electron densities would exist in the single frequency 2 MHz plasma, unlike when $c\text{-}C_4F_8$ was present. This further supports the theory that negative ions were the cause of electron depletion in those $c\text{-}C_4F_8$ mixtures.

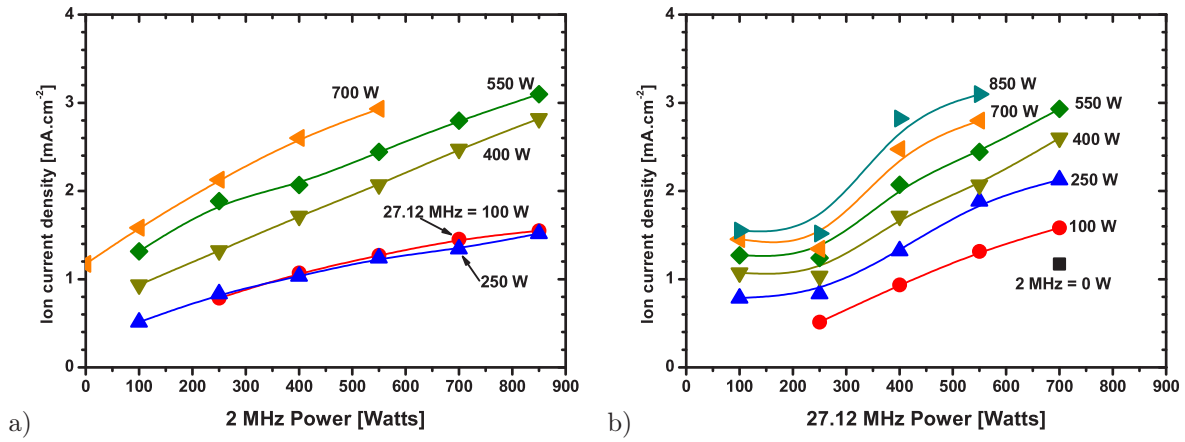


Figure 3.44: Ion current measurements in a dual frequency (27.12 MHz + 2 MHz) Ar/O_2 plasma as a function of (a) 2 MHz power for various set 27.12 MHz powers and (b) 27.12 MHz power for various set 2 MHz powers.

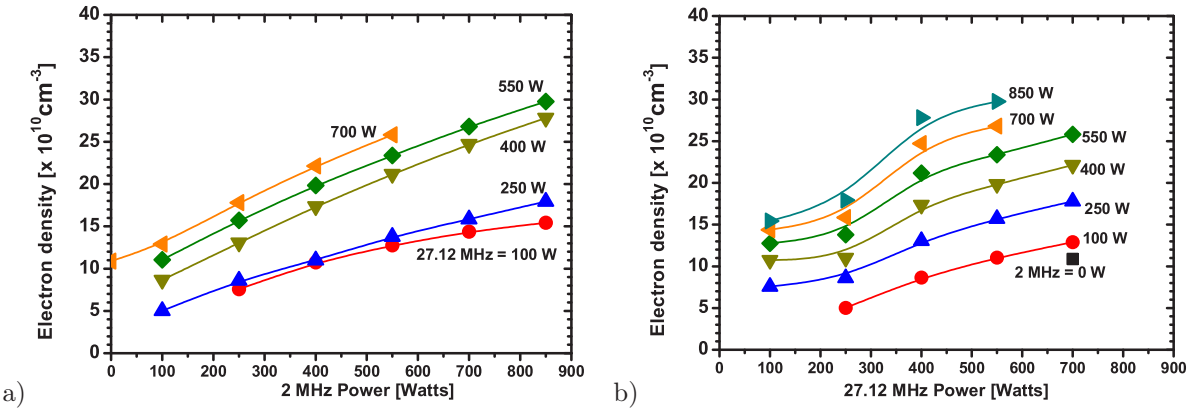


Figure 3.45: Electron density measurements in a dual frequency (27.12 MHz + 2 MHz) Ar/O_2 plasma as a function of (a) 2 MHz power for various set 27.12 MHz powers and (b) 27.12 MHz power for various set 2 MHz powers.

A quick look at the tail electron temperatures figure (3.46) show that they are of similar magnitude to those in $Ar/O_2/c\text{-}C_4F_8$ and $Ar/c\text{-}C_4F_8$, that is, 8 ± 2 eV, roughly speaking.

When the Γ_{is}/n_{e0} ratios are plotted (figure 3.47) the proposal that negative ions play no role in these Ar/O_2 plasmas is almost certainly justified. Little or no evolution of any

great significance occurs over the range of powers studied. Moreover, the amplitude of the ratios (600 ± 100 m.s^{-1}) are equivalent to what one would find in an electropositive plasma. For this reason, and the fact that evolution in the ratios occurs, the negative ion fractions are not plotted and are assumed to be approximately zero for all power configurations.

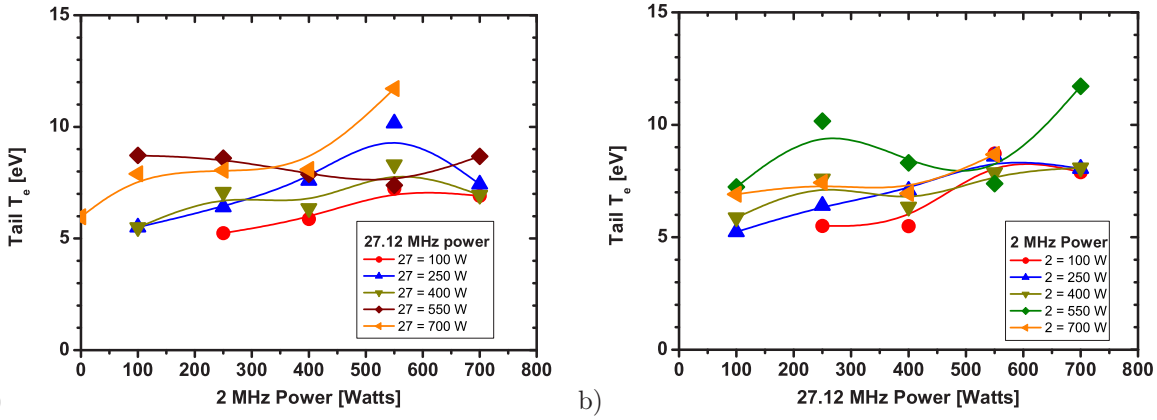


Figure 3.46: Electron temperature measurements in a dual frequency (27.12 MHz + 2 MHz) Ar/O_2 plasma as a function of (a) 2 MHz power for various set 27.12 MHz powers and (b) 27.12 MHz power for various set 2 MHz powers.

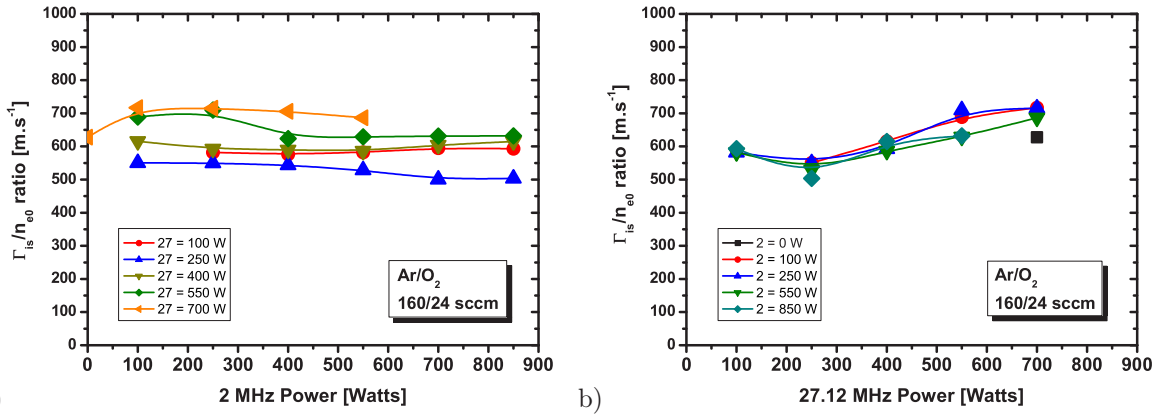


Figure 3.47: Ion flux to electron density ratio in a dual frequency (27.12 MHz + 2 MHz) Ar/O_2 plasma as a function of (a) 2 MHz power for various set 27.12 MHz powers and (b) 27.12 MHz power for various set 2 MHz powers.

Chapter 4

Conclusions and perspectives

The work in this thesis is directly related to the domain of dielectric etching in the manufacturing of integrated circuits and devices. This is seen through the use of a dual frequency capacitively-coupled plasma (DF-CCP) chamber along with complex fluorocarbon gas mixtures which are typically used in such manufacturing. The motivation for this thesis was to study the physical properties of the DF-CCP in an industrial context and was challenged with developing measurement techniques capable of being used in such reactors. The emphasis was placed on studying the dynamics of the electron density, n_e, the ion flux, Γ_i, and the plasma electronegativity, α. It is hoped, however, that the techniques developed and the knowledge acquired during this thesis will be of use to the wider plasma community.

The practical use of a modern industrial etch chamber necessitated important modifications for use in academic research. Many of the automated components (e.g. wafer handling mechanisms, pressure control system) were not employed mainly to reduce maintenance. Large windows (visible and UV light transparent) and a plasma confinement structure consisting of stacked quartz rings were installed, allowing for much improved optical access. An ion flux probe was installed co-planar with the upper electrode. During the cavity ring-down spectroscopy (CRDS) experiments, 60 cm long tubes were attached to opposite flanges to create the optical cavity.

4.1 Diagnostics in DF-CCP industrial chambers

4.1.1 Ion flux probe

The ion flux probe proved to be well adapted to the experimental conditions, with good RF biasing being obtained even in conditions where thin layer deposition was believed to be occurring on the probe surface. The use of a guard ring clearly removed edge effects and so resulted in a clear ion current saturation region. In the absence of a guard ring, the slope parameter in the fitting function did a very good job in compensating for the edge

effects, returning ion fluxes within 2–3% of those obtained when using the guard ring. The introduction of the k-parameter in the fitting function was a result of issues with non-Maxwellian I–V curves. The k-parameter, we believe, characterises the Druyvesteyn nature of the I–V curve. It was particularly important for ensuring that the ion flux at the floating potential was properly estimated, as a Maxwellian fit would normally have resulted in an over-estimation of the ion flux.

4.1.2 Hairpin probe

The microwave resonator probe, known as the hairpin probe, was effectively used in the demanding environment of a dielectric etch chamber for measuring the electron density. A floating hairpin was used to avoid sheath effects resulting from RF biasing and a sheath correction method was implemented to account for DC sheaths. The measurement of the dielectric constant of heptane showed that the hairpin probe results are reliable and also showed that the resonance shift is weighted towards the medium properties at the hairpin tip. Several probe designs were implemented with little difference in the respective densities measured. This is attributed to the self-calibrating nature of the hairpin probe, which also allowed for repeatable measurements over long time intervals.

4.1.3 Cavity ring-down spectroscopy

The CRDS experiments were the first proof of principle measurements of the negative fluorine ion photodetachment absorption spectrum. Negative fluorine ions were detected in both single (27 MHZ) and dual (27+2 MHZ) frequency plasma environments, contradicting recent simulations that suggested F^- would be lost to the walls in large quantities in the presence of the lower frequency. Due to both the very weak photodetachment cross section of F^- ($< 5 \times 10^{-18}$ cm^2) and the difficulties in working with UV optics, the CRDS experiment was difficult to implement in a systematic fashion. Problems were further exasperated due to the presence of a fluctuating baseline of unknown origin.

4.2 Validity of the two-probe technique for measuring α

Estimating the negative ion fraction, α, from the electrostatic probe results necessitated the use of an electronegative discharge model. Various approaches were examined and it was found that the introduction of variable ion mobility to an existing model by Sheridan was the most appropriate. This was confirmed by comparing α estimated from using the model in conjuction with probe results with α calculated from experimental measurements of F^- by CRDS and n_e by the hairpin probe.

The adaptation to variable mobility made sense for our experimental conditions as the ion mean free path, λ_i, was of the order of or less than the plasma length, l. The

introduction of variable mobility will allow for a more consistent transition from the low-pressure ($\lambda_i \gg l$) to the high pressure ($\lambda_i \ll l$) models previously developed by Sheridan. However, it still remains a challenge to reliably use these models in a practical way as various plasma parameters, such as γ, m_i, σ_i, β_{vm}, can be difficult to estimate. In particular, $\gamma = T_n/T_e$ is still a fairly elusive quantity, and the assumption that T_n is in Boltzmann equilibrium still remains a hypothesis.

One of the key findings in this study is that γ is very small, about 5. The negative ions are therefore very hot, possibly from picking up energy from the RF field and/or by being created with a lot of kinetic energy during the dissociative attachment process.

4.3 The relationship between n_e and Γ_i

It is common practice in the plasma community (academic and industrial) to favour the use of the ion saturation current over the electron saturation current for determining the plasma density. This is because of the uncertainties in precisely determining the plasma potential as well as the desire to avoid complicated electron motion theory such as orbital motion. This practice is therefore reliant on the assumption that the trends in ion current are correlated with those in the plasma density (n_e).

The ion currents and electron densities measured in this study showed that this is not the case in a complex industrial gas mixture and serve as a reminder that the assumption that $\Gamma_i \propto n_e$ should not be taken for granted. In c-C_4F_8 CF_4 and SF_6 containing plasmas, this non-correlation was attributed to variations in the plasmas' electronegativity, caused primarily by the significant changes occurring in the plasma chemistry leading to variations in the precursors to negative ion formation. As an example, in fluorocarbon plasmas, the addition of O_2 destroys CF_2, a possible precursor to the creation of F^-, causing the electronegativity to fall to zero. However, even in an electropositive plasma, the absolute relationship maybe uncorrelated due to variations in T_e, m_i, plasma bulk length and σ_i (and therefore h_l).

This important result can be formulated in the following statement:

> *Variations and trends in the electron density can be independent of variations and trends in the positive ion flux at a boundary, and vice-versa.*

or in a more pragmatic way:

> *For any given complex gas mixture, one cannot always justify an estimation of the electron density and trends in that density from measurements of the positive ion flux.*

4.4 The role of dual frequency RF power coupling

The interest in DF-CCP sources is inspired by the desire to control the ion flux (ion density) and the ion energy (sheath voltage) independently from one another by using a high frequency (HF) source to control the former and a low frequency (LF) source to control the latter. In this thesis the influence of both the HF and LF sources on the ion flux was studied in a real life industrial context. The results were conclusive in all plasma conditions studied: no obvious independent control of ion flux was observed in dual frequency mode. The electron density, however, did exhibit some form of independent control, but only in the strongly electronegative cases.

The idea, therefore, of a DF-CCP as a plasma responding independently to each RF source is evidently untrue. This had already been proposed in the recent theoretical models of Turner & Chabert [Turner 06a, Turner 07], as well as those by Kawamura et al. [Kawamura 06]. Pierre Levif, a former Ph. D. student at the LPTP, demonstrated nicely in his thesis the coupling that exists between two RF sources in a DF-CCP [Levif 07]. A graph from that thesis is reproduced in figure 4.1. We note first that in the case of a single frequency excitation and for a fixed high frequency current to low frequency current ratio, J_{HF}/J_{LF}, the ion energy is directly proportional to the ion current (and vice-versa of course). The dotted orange line marks the ion energy for a low frequency current of 4 mA.cm^{-2} in single frequency mode ($J_{HF}/J_{LF} = 0$). In an ideally decoupled system and as the HF current is increased, the ion energy should remain at a fixed value for a fixed LF current, i.e. at 700 eV along the dotted line. However, this figure demonstrates that the ion energy follows another non-linear locus, shown here as the solid orange line. Therefore, at a HF current of 8 mA.cm^{-2} and 16 mA.cm^{-2} ($J_{HF}/J_{LF} = 2$ and 4), the ion energy drops to about 500 eV and 400 eV respectively. The ion energy therefore has a dependence on the high frequency RF current. Similarly, the ion current can be demonstrated to have a dependence on the low frequency RF current. However, this graph also shows that DF-CCP's have an important role to play in terms of ion flux and energy. By correctly choosing the input parameters, one can explore the E_i–J_i space bounded by the single frequency 13.56 MHz and 95.92 MHz curves, something which is impossible to achieve in the single frequency case alone. The role of DF-CCP's is therefore not to explicitly allow for independent control of the ion flux and ion energy, but to open up a much larger parameter space thanks to the significant increase in E_i–J_i possibilities.

4.5 Processing plasmas and the role of electronegativity

One of the main areas of study that this thesis focused on was electronegativity in processing plasmas. What conclusions can be made which will be of direct importance to the plasma processing industry? Firstly, as mentioned earlier, the electronegativity is

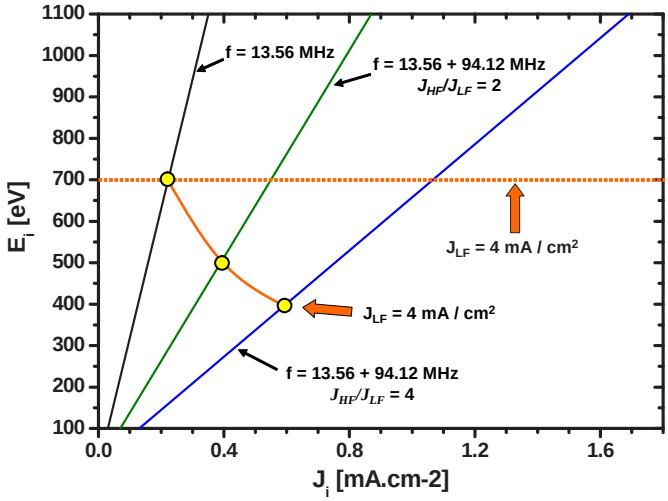


Figure 4.1: The energy gained by the ions as they traverse the sheath as a function of the ion flux in both single (13.56 MHz) and dual (13.56 + 92.92 MHz) frequency plasmas. Two high frequency current to low frequency current ratios are shown for the dual frequency case [Levif 07].

responsible for the decoupling of the ion flux and the electron density trends. If simple plasma diagnostics are performed (e.g. Langmuir probe) and no means of determining the electronegativity is available, then the assumptions made maybe subject to large errors. Secondly, small values of α are sufficient for a significant decrease in Γ_i and n_e to occur. The variations due to changing electronegativity can take place over very small changes in the plasma mixture, depending on the gas and the overall stoichiometric mix, with only a small percentage change required to shift the plasma from behaving electropositively to behaving electronegatively. The change in Γ_i has an obvious direct impact on the etching characteristics. The decrease in n_e has a more indirect impact on etching, as it may lead to reduced production of radicals required in the etching and/or passivating process.

4.6 Perspectives

The measurements undertaken in this thesis have permitted a better understanding of the charged particle dynamics in an industrial DF-CCP etch reactor. Several measurements could prove useful in furthering this understanding. Some examples of, but not limited to, such measurements are listed here:

- Positive ion energy (IEDF) measurements at the electrode surface.
- Positive ion mass measurements at the electrode surface.
- Spatial measurements of the electron density.

- Spatial measurements of the negative ion density, using either CRDS or photodetachment (with a hairpin probe).

Many of these measurements may be difficult to implement but their results would allow for a greater validation of the conclusions made in this thesis, as well as removing many of the assumptions used in the combined fluid model and probe estimations of the negative ion fraction.

The detection of negative ions by absorption may prove more straightforward in future experiments thanks to better light sources (UV LED's for example) and better UV-mirrors. Developments in these areas will also be useful for detecting various radicals (e.g. CF and CF_2) in a more simple manner.

There is an obvious need for further work to resolve the ion flux probe "bump" issue at high pressures. A larger parametric study in more suitable plasma conditions (an argon plasma study for example) as well as analytical and PIC modelling would be amongst the tools necessary to attack this problem.

Hairpin probe measurements still need some form of independent verification under certain conditions, for example, in the single frequency 2 MHz c-C_4F_8 containing plasmas where n_e was practically zero. In fact, the development of a microwave resonator probe capable of measuring low densities ($< 10^9$ cm^{-3}) would indeed be very welcome.

The question of the nature and the value of the negative ion temperature is still largely speculative, and as seems to be the tradition in papers and thesis on electronegative plasmas, it is suggested that further theoretical and experimental work needs to be carried out in this area. It is clear, however, that the results in this thesis strongly indicate that they are very hot.

There is a need for more understanding of the plasma chemistry and the negative ion creation and destruction mechanisms, especially in the context of plasma kinetic models.

Finally, there appears to be a distinct lack of modelling of complex industrial gas mixtures in DF-CCP's in the literature, and where they do exist their results have not yet been verified experimentally. Indeed, this thesis showed how the results in such a model were not backed up by experiments. Unfortunately, models and experiments are often carried out in unrelated laboratories, with each working in a specific unrelated parameter space. A ground-up approach of developing both an experiment and a model in tandem with one another is required, in essence building an experiment to suit the model and vice versa. This appears to be the only way for theory and experiments to be compared.

Appendix A - Hairpin Sheath Correction

Equating equations 2.34 and 2.40:

$$\frac{\epsilon_p}{\ln(\frac{2h}{b}) + \epsilon_p \ln(\frac{b}{a})} = \frac{\epsilon_{eff}}{\ln(\frac{2h}{a})} \tag{A-1}$$

$$\epsilon_p = \frac{\epsilon_{eff} \ln(\frac{2h}{b})}{\ln(\frac{2h}{a})} + \frac{\epsilon_p \epsilon_{eff} \ln(\frac{b}{a})}{\ln(\frac{2h}{a})} \tag{A-2}$$

$$\epsilon_p \left[1 - \frac{\epsilon_{eff} \ln(\frac{b}{a})}{\ln(\frac{2h}{a})}\right] = \frac{\epsilon_{eff} \ln(\frac{2h}{b})}{\ln(\frac{2h}{a})} \tag{A-3}$$

$$\epsilon_p = \frac{\epsilon_{eff} \ln(\frac{2h}{b})}{\ln(\frac{2h}{a})} \times \frac{\ln(\frac{2h}{a})}{\ln(\frac{2h}{a}) - \epsilon_{eff} \ln(\frac{b}{a})} \tag{A-4}$$

$$\epsilon_p = \frac{\epsilon_{eff} \ln(\frac{2h}{b})}{\ln(\frac{2h}{a})} \times \frac{1}{1 - \epsilon_{eff} \frac{\ln(\frac{b}{a})}{\ln(\frac{2h}{a})}} \tag{A-5}$$

Replacing for ϵ_p, ϵ_{eff} and defining $\Lambda = \frac{\ln(\frac{b}{a})}{\ln(\frac{2h}{a})}$ we have:

$$1 - \frac{f_p^2}{f_r^2} = \frac{f_0^2}{f_r^2}\frac{\ln(\frac{2h}{b})}{\ln(\frac{2h}{a})} \times \frac{1}{1 - \frac{f_0^2}{f_r^2} \cdot \Lambda} \tag{A-6}$$

$$f_r^2 - f_p^2 = f_0^2\frac{\ln(\frac{2h}{b})}{\ln(\frac{2h}{a})} \times \frac{1}{1 - \frac{f_0^2}{f_r^2} \cdot \Lambda} \tag{A-7}$$

$$f_p^2 = f_r^2 - f_0^2\frac{\ln(\frac{2h}{b})}{\ln(\frac{2h}{a})} \times \frac{1}{1 - \frac{f_0^2}{f_r^2} \cdot \Lambda} \tag{A-8}$$

$$f_p^2 = \frac{f_r^2 - f_0^2 \cdot \Lambda - f_0^2\frac{\ln(\frac{2h}{b})}{\ln(\frac{2h}{a})}}{1 - \frac{f_0^2}{f_r^2} \cdot \Lambda} \tag{A-9}$$

$$f_p^2 = \frac{f_r^2 - f_0^2\left[\frac{\ln(\frac{b}{a}) + \ln(\frac{2h}{b})}{\ln(\frac{2h}{a})}\right]}{1 - \frac{f_0^2}{f_r^2} \cdot \Lambda} \tag{A-10}$$

$$f_p^2 = \frac{f_r^2 - f_0^2\frac{\ln(\frac{2h}{a})}{\ln(\frac{2h}{a})}}{1 - \frac{f_0^2}{f_r^2} \cdot \Lambda} \tag{A-11}$$

$$f_p^2 = \frac{f_r^2 - f_0^2}{1 - \frac{f_0^2}{f_r^2} \cdot \Lambda} \tag{A-12}$$

Appendix B - Comparison of Stenzel's hairpin with Kim's hairpin

This appendix refers to the microwave resonator probes proposed by R. L. Stenzel (see ref [Stenzel 76]) and by J. Kim in the following article:

> Jongdae Kim & K. C. Jungling. *Measurement of Plasma Density Generated by a Semiconductor Bridge: Related Input Energy and Electrode Material.* ETRI Journal, vol. 17, no. 2, pages 11–19, 1995.

This is included as an Appendix as I feel that it maybe debated that Kim puts a false claim on the invention of the hairpin probe as no references are made towards Stenzel's article. It maybe possible that Kim was unaware of Stenzel's work and independently invented the hairpin probe, and this Appendix allows readers the chance to decide for themselves.

As Kim's article was destined for a small industry focused readership, it went almost unnoticed amongst the academic plasma community. It was not until after much bibliographic research that I stumbled across the article. Nevertheless, the claim made by the authors is surprising considering that their hairpin probe appears as if it is a carbon copy of the one proposed by Stenzel, and yet not a single reference to Stenzel's work is made. I have included a comparison of J. Kim's and Stenzel's microwave resonators in figure 2

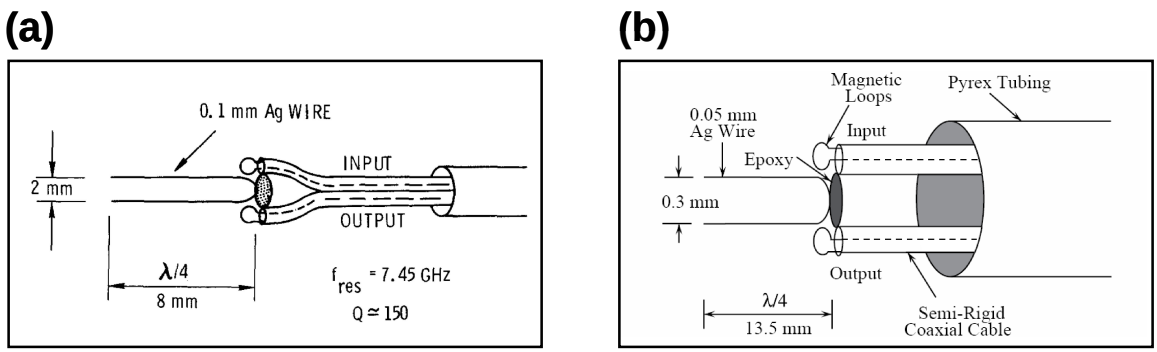


Figure 2: A comparison between the microwave resonator probe (a) invented by Stenzel in 1976 and (b) invented (?) by J. Kim et al. in 1995.

Appendix C - Normalisation of ion fluid equations - variable mobility

Constants

$$c_s = \sqrt{\frac{kT_e}{M_i}}$$

$$\lambda_{e0} = \sqrt{\frac{\epsilon_0 kT_e}{n_{e0}e^2}}$$

Non-normalised equations

Equations of continuity and motion:

$$\frac{d(n_i v_i)}{dx} = \nu_{iz} n_{e0} \exp\left(\frac{e\phi}{kT_e}\right) \tag{C -1}$$

$$M_i n_i v_i \frac{dv_i}{dx} + M_i v_i \nu_{iz} n_{e0} \exp\left(\frac{e\phi}{kT_e}\right) = n_i eE - n_i F_c \tag{C -2a}$$

$$F_c = M_i v_i \nu_p \tag{C -2b}$$

Poisson's equation:

$$\epsilon_0 \frac{dE}{dx} = e\left[n_i - n_{-0} \exp\left(\frac{e\phi}{kT_-}\right) - n_{e0} \exp\left(\frac{e\phi}{kT_e}\right)\right] \tag{C -3a}$$

$$E = -\frac{d\phi}{dx} \tag{C -3b}$$

Normalisation

$$\begin{aligned} \tilde{n} &= n_i/n_{e0} \\ \rightarrow n_i &= \tilde{n} n_{e0} \end{aligned} \tag{C -4}$$

$$\begin{aligned} \tilde{\xi} &= x/\Lambda \\ \rightarrow x &= \tilde{\xi}\Lambda \end{aligned} \tag{C -5}$$

$$\begin{aligned} \tilde{\eta} &= -e\phi/kT_e \\ \rightarrow e\phi/kT_- &= -\tilde{\eta}\frac{T_e}{T_-} \end{aligned} \tag{C -6}$$

$$\rightarrow \phi = -\tilde{\eta}\frac{kT_e}{e} \tag{C -7}$$

$$\begin{aligned} \tilde{u} &= v_i/c_s \\ \rightarrow v_i &= \tilde{u}c_s \end{aligned} \tag{C -8}$$

$$\Lambda = c_s/\nu_{iz} \tag{C -9}$$

For equation C -3b the normalisation process is as follows:

$$\begin{aligned} E &= -\frac{d\phi}{dx} \\ \rightarrow E &= -\frac{d}{dx}\left(-\tilde{\eta}\frac{kT_e}{e}\right) \\ \rightarrow E &= \frac{1}{\Lambda}\frac{d\tilde{\eta}}{d\xi}\frac{kT_e}{e} \\ \rightarrow E &= \tilde{\eta}'\frac{kT_e}{\Lambda e} \\ \rightarrow \tilde{\eta}' &= \frac{\Lambda e E}{kT_e} = \epsilon \end{aligned} \tag{C -10}$$

For equation C -1 the normalisation process is as follows:

$$\begin{aligned} \frac{d(n_i v_i)}{dx} &= \nu_{iz} n_{e0} \exp\left(\frac{e\phi}{kT_e}\right) \\ \frac{1}{\Lambda}\frac{d}{d\tilde{\xi}}(\tilde{n} n_{e0} \tilde{u} c_s) &= \nu_{iz} n_{e0} e^{-\tilde{\eta}} \\ \frac{\nu_{iz}}{c_s} n_{e0} c_s \frac{d}{d\tilde{\xi}}(\tilde{n}\tilde{u}) &= \nu_{iz} n_{e0} e^{-\tilde{\eta}} \\ \frac{d}{d\tilde{\xi}}(\tilde{n}\tilde{u}) &= e^{-\tilde{\eta}} \\ (\tilde{n}\tilde{u})' = e^{-\tilde{\eta}} & \end{aligned} \tag{C -11}$$

For equation C -2 the normalisation process is as follows:

$$\begin{aligned}
M_i n_i v_i \frac{dv_i}{dx} + M_i v_i \nu_{iz} n_{e0} \exp\left(\frac{e\phi}{kT_e}\right) &= n_i eE - n_i M_i v_i \nu_p \\
M_i n_i v_i \frac{dv_i}{dx} + M_i v_i \frac{d(n_i v_i)}{dx} &= n_i eE - n_i M_i v_i \nu_p \\
M_i \frac{d}{dx}(n_i v_i v_i) &= n_i eE - n_i M_i \frac{v_i^2}{\lambda_i}\frac{\pi}{2} \\
M_i n_{e0} c_s^2 \frac{1}{\Lambda}\frac{d}{d\xi}(\tilde{n}\tilde{u}\tilde{u}) &= n_{e0}\tilde{n}\frac{kT_e\epsilon}{\Lambda} - M_i n_{e0} c_s^2 \tilde{n}\frac{\tilde{u}^2}{\lambda_i}\frac{\pi}{2} \\
\frac{c_s^2}{\Lambda}\frac{d}{d\xi}(\tilde{n}\tilde{u}\tilde{u}) &= \tilde{n}\epsilon\frac{c_s^2}{\Lambda} - c_s^2\tilde{n}\frac{\tilde{u}^2}{\lambda_i}\frac{\pi}{2} \\
\frac{d}{d\xi}(\tilde{n}\tilde{u}\tilde{u}) &= \tilde{n}\epsilon - \frac{\Lambda}{\lambda_i}\frac{\pi}{2}\tilde{n}\tilde{u}^2 \\
\frac{d}{d\xi}(\tilde{n}\tilde{u}\tilde{u}) &= \tilde{n}\epsilon - \beta\tilde{n}\tilde{u}^2 \\
(\tilde{n}\tilde{u}\tilde{u})' &= \tilde{n}\epsilon - \beta\tilde{n}\tilde{u}^2 \qquad \text{(C -12)}
\end{aligned}$$

$$\beta = \frac{\pi}{2}\frac{\Lambda}{\lambda_i} = \frac{\pi}{2}\frac{c_s}{\nu_{iz}\lambda_i} \qquad \text{(C -13)}$$

For equation C -3a the normalisation process is as follows:

$$\begin{aligned}
\epsilon_0\frac{dE}{dx} &= e\left[n_i - n_{-0}\exp\left(\frac{e\phi}{kT_-}\right) - n_{e0}\exp\left(\frac{e\phi}{kT_e}\right)\right] \\
\epsilon_0\frac{d}{dx}\frac{kT_e}{\Lambda e}\epsilon &= e\left[\tilde{n}n_{e0} - n_{-0}e^{-\gamma\eta} - n_{e0}e^{-\eta}\right] \\
\frac{\epsilon_0 kT_e}{\Lambda e^2 n_{e0}}\frac{1}{\Lambda}\frac{d}{d\xi}\epsilon &= \tilde{n} - \alpha e^{-\gamma\eta} - e^{-\eta} \\
\left(\frac{\epsilon_0 kT_e}{e^2 n_{e0}}\right)\frac{1}{\Lambda^2}\epsilon' &= \tilde{n} - e^{-\eta} - \alpha e^{-\gamma\eta} \\
q^2\epsilon' &= \tilde{n} - e^{-\eta} - \alpha e^{-\gamma\eta} \qquad \text{(C -14)}
\end{aligned}$$

$$q = \lambda_{e0}/\Lambda \qquad \text{(C -15)}$$

Bibliography

[Amemiya 88] Hiroshi Amemiya. *Negative Ion-Sensitive Probe.* Jpn. J. Appl. Phys., vol. 27, no. 10, pages 1966–1975, October 1988.

[Amemiya 90] H Amemiya. *Plasmas with negative ions – probe measurements and charge equilibrium.* J. Phys D: Appl. Phys., vol. 23, no. 8, pages 999–1014, August 1990.

[Bacal 91] M. Bacal, P. Berlemont, A. M. Bruneteau, R. Leroy & R. A. Stern. *Measurement of the H^- thermal energy in a volume ion source plasma.* J. App. Phys., vol. 70, no. 3, pages 1212–1219, August 1991.

[Bacal 93] M Bacal. *Plasma diagnostics in negative ion sources.* Plasma Sources Sci. Technol., vol. 2, pages 190–197, 1993.

[Bacal 00] M Bacal. *Photodetachment diagnostic techniques for measuring negative ion densities and temperatures in plasmas.* Rev. Sci. Instrum., vol. 71, no. 11, pages 3981–4006, Nov 2000.

[Bardeen 50] John Bardeen & Walter H. Brattain. *Three-electrode circuit element utilizing semiconductive materials.*, October 1950.

[Belostotsky 05] S G Belostotsky, D J Economou, D V Lopaev & T V Rakhimova. *Negative ion destruction by $O(^3P)$ atoms and $O_2(a\ ^1\Delta_g)$ molecules in an oxygen plasma.* Plasma Sources Sci. Technol., vol. 14, pages 532–542, 2005.

[Berden 00] G Berden, R Peeters & G Meijer. *Cavity ring-down spectroscopy: Experimental schemes and applications.* Int. Rev. Phys. Chem., vol. 19, no. 4, pages 565–607, October 2000.

[Bisschops 87] Theodorus Hubertus Josephus Bisschops. *Investigations on an RF-plasma related to plasma etching.* PhD thesis, Technische Universiteit Eindhoven, Department of Applied Physics, June 1987.

[Blackwell 05] David D. Blackwell, David N. Walker & William E. Amatucci. *Measurement of absolute electron density with a plasma impedance probe.* Rev. Sci. Instrum., vol. 76, page 023503, 2005.

[Blondel 01] Christophe Blondel, Christian Delsart & Fabienne Goldfarb. *Electron spectrometry at the μeV level and the electron affinities of Si and F.* J. Phys. B: At. Mol. Opt. Phys., vol. 34, no. 9, pages L281–L288, May 2001.

[Bohm 49] D. Bohm. The characteristics of electrical discharges in magnetic fields. New York: McGraw-Hill, 1949.

[Bonham 94] Russell A Bonham. *Electron Impact Cross Section Data for Carbon Tetrafluoride.* Jpn. J. Appl. Phys., vol. 33, no. Part 1, 7B, pages 4157–4164, July 1994.

[Booth 98] J-P Booth, G Cunge, F Neuilly & N Sadeghi. *Absolute radical densities in etching plasmas determined by broad-band UV absorption spectroscopy.* Plasma Sources Sci. Technol., vol. 7, no. 3, pages 423–430, August 1998.

[Booth 06] J-P Booth, C S Corr, G A Curley, J Jolly & J Guillon. *Fluorine negative ion density measurement in a dual frequency capacitive etch reactor by cavity ring-down spectroscopy.* App. Phys. Lett., vol. 88, page 151502, 2006.

[Boyle 04a] P C Boyle, A R Ellingboe & M M Turner. *Independent control of ion current and ion impact energy onto electrodes in dual frequency plasma devices.* J. Phys D: Appl. Phys., vol. 37, pages 697–701, 2004.

[Boyle 04b] P C Boyle, J Robiche & M M Turner. *Modelling of the dual frequency capacitive sheath in the intermediate pressure range.* J. Phys D: Appl. Phys., vol. 37, pages 1451–1458, 2004.

[Braithwaite 88] N St J Braithwaite & J E Allen. *Boundaries and probes in electronegative plasmas.* J. Phys D: Appl. Phys., vol. 21, no. 12, pages 1733–1737, December 1988.

[Braithwaite 96] N St J Braithwaite, J P Booth & G Cunge. *A novel electrostatic probe method for ion flux measurements.* Plasma Sources Sci. Technol., vol. 5, pages 677–684, 1996.

[Braithwaite 03] N St J Braithwaite, T E Sheridan & R W Boswell. *Transient RF self-bias in electropositive and electronegative plasmas.* J. Phys D: Appl. Phys., vol. 36, no. 22, pages 2837–2844, November 2003.

[Braithwaite 05] Nicholas St. John Braithwaite & Raul N Franklin. Private communication - self-consistent global model. This model solves the simultaneous balance of particle production/loss and that of the ion

momentum. Here, ionisation is taken to be proportional to electron density. There is no recombination and an effective ionisation rate function is used. Electrons are presumed to be in thermal equilibrium with the local potential. Quasineutrality is invoked and the boundaries of the 'plasma solution' are deduced. In effect the electron temperature is that which will sustain ionisation sufficient to balance electric field driven ion loss across the boundary. The model encompasses the low pressure, or free-fall, limit (in which denisties at the plasma boundary are half the 'central' value) and approaches the medium-high Schottky limit (in which wall densities reach zero)., January 2005.

[Bulcourt 02] N Bulcourt, J-P Booth & Jacques Jolly. *IEDF study of positive ions in an $Ar/C_4F_8/O_2$ capacitive discharge.* In 4th International Workshop on Fluorocarbon Plasmas, page 13, Col de Porte, Isère, France, March 2002.

[Bulcourt 04] N Bulcourt, J P Booth, E A Hudson, J Luque, D K W Mok, E P Lee, F T Chau & J M Dyke. *Use of the ultraviolet absorption spectrum of CF_2 to determine the spatially resolved absolute CF_2 density, rotational temperature, and vibrational distribution in a plasma etching reactor.* J. Chem. Phys., vol. 120, no. 20, pages 9499 – 9508, May 2004.

[Bulcourt 07] Nicolas Bulcourt. *Etude des radicaux CF et CF_2 dans une décharge capacitive double fréquence 27 + 2 MHz en $Ar/O_2/C_4F_8$.* Plasma physics, Université Paris XI Orsay, LPTP, Ecole Polytechnique, 91128 Palaiseau, France, 2007.

[Chabert 99a] P Chabert. *Etude d'un plasma de SF_6 créé dans un réacteur hélicon : application à la gravure du carbure de silicium.* PhD thesis, Université Paris XI Orsay, July 1999.

[Chabert 99b] P Chabert, T E Sheridan, R W Boswell & J Perrin. *Electrostatic probe measurement of the negative ion fraction in an SF_6 helicon discharge.* Plasma Sources Sci. Technol., vol. 8, pages 561–566, 1999.

[Chabert 01] P Chabert, A J Lichtenberg, M A Lieberman & A M Marakhtanov. *Instabilities in low-pressure electronegative inductive discharges.* Plasma Sources Sci. Technol., vol. 10, no. 3, pages 478–489, August 2001.

[Christophorou 01] L G Christophorou & J K Olthoff. *Electron Interactions with c-C_4F_8*. J. Phys. Chem. Ref. Data, vol. 30, no. 2, pages 449–473, March 2001.

[Coburn 79] J. W. Coburn & H. F. Winters. *Ion- and electron-assisted gas-surface chemistr – An important effect in plasma etching*. J. App. Phys., vol. 50, no. 5, pages 3189–3196, May 1979.

[Curley 04a] G A Curley, J-P Booth, S Dine & N Bulcourt. *Negative Ions in a Dual-Frequency Capacitive Plasma in $Ar/C_4F_8/O_2$*. In APS, editeur, Bulletin of the American Physical Society, volume 49, page 43. Gaseous Electronics Conference, September 2004.

[Curley 04b] Garrett Curley. Ions négatifs dans un plasma capacitif à double fréquence de Ar/c-C_4F_8/O_2. Master's thesis, Ecole Polytechnique, Palaiseau, France, June 2004.

[Curley 07] G A Curley, D Maric, J-P Booth, C S Corr, P Chabert & J Guillon. *Negative ions in single and dual frequency capacitively coupled fluorocarbon plasmas*. Plasma Sources Sci. Technol., vol. 16, pages S87–S93, 2007.

[D'Angelo 66] N. D'Angelo, S. v. Goeler & T. Ohe. *Propagation and Damping of Ion Waves in a Plasma with Negative Ions*. Physics of Fluids, vol. 9, no. 8, pages 1605–1606, August 1966.

[Dine 05] S Dine, J-P Booth, G A Curley, C S Corr, J Jolly & J Guillon. *A novel technique for plasma density measurement using surface-wave transmission spectra*. Plasma Sources Sci. Technol., vol. 14, no. 4, pages 777–786, November 2005.

[Donkó 06] Zoltán Donkó & Zoran Lj. Petrovic. *Analysis of a capacitively coupled dual-frequency CF_4 discharge*. Jpn. J. Appl. Phys., vol. 45, no. 10B, pages 8151–8156, October 2006.

[Druyvesteyn 40] M J Druyvesteyn & F M Penning. *The Mechanisms of Electrical Discharges in Gases of Low Pressure*. Rev. Mod. Phys., vol. 12, no. 2, pages 87–174, April 1940.

[Edgley 75] P D Edgley. *D. Phil. Thesis*. Physics of plasmas, University of Oxford, 1975.

[Emeleus 38] K G Emeleus & J Sayers. *Negative Ions in Discharge Tubes*. Proc. R. Irish. Acad., vol. 24A, pages 87–100, 1938.

[Emeleus 70] K G Emeleus & G A Woolsey. Discharges in electronegative gases. London: Taylor and Francis, 1970.

[Ferreira 88] C M Ferreira, G Gousset & M Touzeau. *Quasi-neutral theory of positive columns in electronegative gases.* J. Phys D: Appl. Phys., vol. 21, no. 9, pages 1403–1413, September 1988.

[Folgerø 96] Kjetil Folgerø. *Bilinear calibration of coaxial transmission/reflection cells for permittivity measurement of low-loss liquids.* Meas. Sci. Technol., vol. 7, no. 9, pages 1260–1269, September 1996.

[Font 02] G I Font, W L Morgan & G Mennenga. *Cross-section set and chemistry for the simulation of c-C_4F_8 plasma discharges.* J. App. Phys., vol. 91, no. 6, pages 3530–3538, March 2002.

[Franklin 02] R N Franklin. *Electronegative plasmas – why are they so different?* Plasma Sources Sci. Technol., vol. 11, no. 31, pages A31–A37, August 2002.

[Gans 06] T. Gans, J. Schulze, D. O'Connell, U. Czarnetzki, R. Faulkner, A. R. Ellingboe & M. M. Turner. *Frequency coupling in dual frequency capacitively coupled radio-frequency plasmas.* App. Phys. Lett., vol. 89, no. 26, page 261502, December 2006.

[Georgieva 03a] V. Georgieva, A. Bogaerts & R. Gijbels. *Numerical study of $Ar/CF_4/N_2$ discharges in single- and dual-frequency capacitively coupled plasma reactors.* J. App. Phys., vol. 94, pages 3748–3756, 2003.

[Georgieva 03b] V Georgieva, A Bogaerts & R Gijbels. *Particle-in-cell/Monte Carlo simulation of a capacitively coupled radiofrequency Ar/CF_4 discharge: Effect of gas composition.* J. App. Phys., vol. 93, pages 2369–2379, March 2003.

[Georgieva 06a] V. Georgieva & A. Bogaerts. *Negative ion behavior in single- and dual-frequency plasma etching reactors: Particle-in-cell/Monte Carlo collision study.* Phys. Rev. E., vol. 73, no. 3, page 036402, March 2006.

[Georgieva 06b] V Georgieva & A Bogaerts. *Plasma characteristics of an $Ar/CF_4/N_2$ discharge in an asymmetric dual frequency reactor: numerical investigation by a PIC/MC model.* Plasma Sources Sci. Technol., vol. 15, no. 3, pages 368–377, April 2006.

[Godyak 86] V A Godyak. Soviet radio frequency discharge research. Delphic Associates, Falls Church, VA, 1986.

[Goto 92] H H Goto, H-D Lowe & T Ohmi. *Dual excitation reactive ion etcher for low energy plasma processing.* vol. 10, no. 5, pages 3048–3054, Sept/Oct 1992.

[Gottscho 86] Richard A. Gottscho & Carl E. Gaebe. *Negative Ion Kinetics in RF Glow Discharges.* IEEE Trans. Plas. Sci., vol. 14, no. 2, pages 92–102, April 1986.

[Gozadinos 01] G Gozadinos, D Vender, M M Turner & M A Lieberman. *Collisionless electron heating by capacitive radio-frequency plasma sheaths.* Plasma Sources Sci. Technol., vol. 10, no. 2, pages 117–124, May 2001.

[Grangeon 99] F Grangeon, C Monard, J-L Dorier, A A Howling, Ch Hollenstein and D Romanini & N sadeghi. *Applications of the cavity ring-down technique to a large-area rf-plasmareactor.* Plasma Sources Sci. Technol., vol. 8, no. 3, pages 448–456, August 1999.

[Haas 05] F. A. Haas, J. Al-Kuzee & N. St. J. Braithwaite. *Electron and ion sheath effects on a microwave "hairpin" probe.* App. Phys. Lett., vol. 87, no. 20, page 201503, November 2005.

[Haverlag 91] M Haverlag, A Kono, D Passchier, G M W Kroesen & W J Goedheer. *Measurements of negative ion densities in 13.56-MHz rf plasmas of CF_4, C_2F_6, and C_3F_8 using microwave resonance and the photodetachment effect.* J. App. Phys., vol. 70, no. 7, pages 3472–3480, Oct 1991.

[Heald 65] M. A. Heald & C. B. Wharton. Plasma diagnostics with microwaves. John Wiley & Sons Inc., 1965. Out of print. Available at the LPTP library: VI.4 HEA PLA.

[Hebner 00] G. A. Hebner & P. A. Miller. *Electron and negative ion densities in C_2F_6 and CHF_3 containing inductively coupled discharges.* J. App. Phys., vol. 87, no. 11, pages 7660–7666, June 2000.

[Hebner 01] G A Hebner & I C Abraham. *Characterization of electron and negative ion densities in fluorocarbon containing inductively driven plasmas.* J. App. Phys., vol. 90, no. 10, pages 4929 – 4937, November 2001.

[Hirose 98] Yuji Hirose, Itsuo Ishikawa, Shinya Sasaki, Kazuya Nagaseki, Yukinori Saito & Shinji Suganomata. *Positive Ions in RF Discharge Plasmas of C_4F_8/Ar and C_4F_8/O_2 Mixtures.* Jpn. J. Appl. Phys., vol. 37, no. 10, pages 5730–5734, October 1998.

[Ishihara 74] Takeshi Ishihara & Theodore C. Foster. *Study of the photodetachment of C^- and F^- by many-body perturbation theory.* Phys. Rev. A, vol. 9, no. 6, pages 2350–2355, June 1974.

[Jaiprakash 94] V. C. Jaiprakash & B. E. Thompson. *Plasma impedance and microwave interferometric measurements of electron concentrations in dual-frequency powered sulfur hexafluoride plasmas.* J. Vac. Sci. Technol., vol. 12, no. 4, pages 1403–1407, July 1994.

[Jauberteau 89] J L Jauberteau, G J Meeusen, M Haverlag, G M W Kroesen & F Jde Hoog. *Photodetachment effect in a radio frequency plasma in CF_4.* App. Phys. Lett., vol. 55, no. 25, pages 2597–2599, 1989.

[Jolly 05] J. Jolly & J.-P. Booth. *Atomic hydrogen densities in capacitively coupled very high-frequency plasmas in H_2: Effect of excitation frequency.* J. App. Phys., vol. 97, no. 10, page 103305, May 2005.

[Kaga 01] Kouji Kaga, Takashi Kimura, Takao Imaeda & Kazuyuki Ohe. *Spatial Structure of Electronegative Ar/CF_4 Plasmas in Capacitive RF Discharges.* Jpn. J. Appl. Phys., vol. 40, no. 10, pages 6115–6116, October 2001.

[Karkari 06] S. K. Karkari & A. R. Ellingboe. *Effect of radio-frequency power levels on electron density in a confined two-frequency capacitively-coupled plasma processing tool.* App. Phys. Lett., vol. 88, no. 10, page 101501, March 2006.

[Kawamura 06] E. Kawamura, M. A. Lieberman & A. J. Lichtenberg. *Stochastic heating in single and dual frequency capacitive discharges.* Physics of Plasmas, vol. 13, no. 5, page 053506, May 2006.

[Kim 95] Jongdae Kim & K. C. Jungling. *Measurement of Plasma Density Generated by a Semiconductor Bridge: Related Input Energy and Electrode Material.* ETRI Journal, vol. 17, no. 2, pages 11–19, 1995.

[Kim 04a] H. C. Kim & J. K. Lee. *Mode Transition Induced by Low-Frequency Current in Dual-Frequency Capacitive Discharges.* Physical Review Letters, vol. 93, no. 8, page 085003, August 2004.

[Kim 04b] Jung-Hyung Kim, Sang-Chul Choi, Yong-Hyeon Shin & Kwang-Hwa Chung. *Wave cutoff method to measure absolute electron density in cold plasma.* Rev. Sci. Instrum., vol. 75, no. 8, pages 2706–2710, August 2004.

[Kitajima 99] T. Kitajima, Y. Takeo & T. Makabe. *Two-dimensional CT images of two-frequency capacitively coupled plasma.* J. Vac. Sci. Technol. A, vol. 17, no. 5, pages 2510–2516, Sept/Oct 1999.

[Kokura 99] Hikaru Kokura, Keiji Nakamura, Ivan P. Ghanashev & Hideo Sugai. *Plasma Absorption Probe for Measuring Electron Density in an En-*

vironment Soiled with Processing Plasmas. Jpn. J. Appl. Phys., vol. 38, no. 9A, pages 5262 – 5266, September 1999.

[Kondrat'ev 02] I. G. Kondrat'ev, A. V. Kostrov, A. I. Smirnov, A. V. Strikovskiĭ & A. V. Shashurin. *Two-Wire Microwave Resonator Probe.* Plasma Phys. Rep., vol. 28, no. 11, pages 977–983, November 2002.

[Kono 91] A Kono, M Haverlag, G M W Kroesen & F J de Hoog. *Temporal behavior of the electron and negative ion densities in a pulsed radio-frequency CF_4 discharge.* J. App. Phys., vol. 70, no. 6, pages 2939–2946, Sept 1991.

[Kono 00a] A Kono & K Kato. *Measurement of negative-ion density in high-density C_4F_8 plasma usinga laser photodetachment technique combined with a millimeter-wave open resonator.* App. Phys. Lett., vol. 77, no. 4, pages 495–497, July 2000.

[Kono 00b] A Kono & Y Ohya. *Photodetachment Study of Capacitively-Coupled RF C_4F_8 Plasma.* Jpn. J. Appl. Phys., vol. 39, no. Part 1 3A, pages 1365–1368, March 2000.

[Kono 02] A Kono, Masahito Konishi & Kenji Kato. *Behaviors of electron and negative-ion densities in low-pressure high density inductively coupled plasmas of SF_6, NF_3, CF_4 and C_4F_8 gases diluted with Ar.* Thin Solid Films, vol. 407, pages 198–203, 2002.

[LeCoat 94] Y LeCoat, J-P Ziesel & J-P Guillotin. *Negative ion resonances in CF_4 probed by dissociative electron attachment.* J. Phys. B: At. Mol. Opt. Phys., vol. 27, pages 965–979, 1994.

[Lee 95] C Lee & M A Lieberman. *Global model of Ar, O_2, Cl_2, and Ar/O_2 high-density plasma discharges.* J. Vac. Sci. Technol. A, vol. 13, no. 2, pages 368–380, March 1995.

[Lee 04] J K Lee, N Yu Babaeva, H C Kim, O V Manuilenko & J W Shon. *Simulation of Coupled Single- and Dual-Frequency RF Discharges.* IEEE Trans. Plas. Sci., vol. 32, no. 1, pages 47–53, February 2004.

[Levif 07] Pierre Levif. *Excitation multifréquence dans les décharges capacitives utilisées dans la gravure en microélectronique.* PhD thesis, Ecole Polytechnique, Route de Saclay, Palaiseau, France, November 2007.

[Li 03] Xi Li, Li Ling, Xuefeng Hua, Masanaga Fukasawa, Gottlieb S. Oehrlein, Marcos Barela & H M Anderson. *Effects of Ar and O_2 additives on SiO_2 etching in C_4F_8-based plasmas.* J. Vac. Sci. Technol. A, vol. 21, no. 1, pages 284–293, Jan/Feb 2003.

[Lieberman 05] M A Lieberman & A J Lichtenberg. Principles of plasma discharges and materials processing, volume 1. Wiley Interscience, 605 Third Ave, New York, NY, USA, 2 edition, 2005.

[Lin 93] Y. Lin & L. J. Overzet. *Negative and positive ions from CF_4 and CF_4/O_2 rf discharges in etching Si.* App. Phys. Lett., vol. 62, no. 7, pages 675– 677, February 1993.

[Mandl 71] A Mandl. *Electron Photodetachment Cross Section of the Negative Ion of Fluorine.* Phys. Rev. A, vol. 3, no. 1, pages 251–255, January 1971.

[Margetić 98] V Margetić & D Veža. *Experimental Study of Ar-O_2 low-pressure discharge.* Fisika A, vol. 7, no. 2, pages 49–63, 1998.

[Mott-Smith 26] H. M. Mott-Smith & Irving Langmuir. *The Theory of Collectors in Gaseous Discharges.* Phys. Rev., vol. 4, no. 4, pages 727–763, October 1926.

[Myers 92] F R Myers & T S Cale. *A Dual Frequency Plasma Sheath Model.* J. Electrochem. Soc., vol. 139, no. 12, pages 3587 – 3595, December 1992.

[Myers 94a] F R Myers, M Ramaswami & T S Cale. *Prediction of Ion Energy and Angular Distributions in Single and Dual Frequency Plasmas.* J. Electrochem. Soc., vol. 141, no. 5, pages 1313 – 1320, May 1994.

[Myers 94b] Frank R. Myers, Michael W. Peters, Manjula Ramaswami, & Timothy S. Cale. *Transport through multicomponent dual frequency plasma sheath.* Thin Solid Films, vol. 253, no. 1-2, pages 522–528, December 1994.

[Nagaseki 95] Kazuya Nagaseki, Itsuo Ishikawa, Eiichi Nishimura, Yukinori Saito & Shinji Suganomata. *Negative Ions in 13.56 MHz Discharge of SF_6 Gas in a Planar Diode.* Jpn. J. Appl. Phys., vol. 34, no. Part 2, 7A, pages L852–L855, July 1995.

[Nikitin 96] A G Nikitin, F El Balghiti & M Bacal. *Comparison of negative ion density measurements by probes and by photodetachment.* Plasma Sources Sci. Technol., vol. 5, no. 1, pages 37 – 42, February 1996.

[O'Keefe 88] A O'Keefe & D A G Deacon. *Cavity ring-down optical spectrometer for absorpion measurements using pulsed laser sources.* Rev. Sci. Instrum., vol. 59, no. 12, pages 2544–2551, December 1988.

[Overzet 89] L. J. Overzet, J. H. Beberman & J. T. Verdeyen. *Enhancement of the negative ion flux to surfaces from radio-frequency processing discharges.* J. App. Phys., vol. 66, no. 4, page 1622, August 1989.

[Perret 05] A. Perret, P. Chabert, J. Jolly & J.-P. Booth. *Ion energy uniformity in high-frequency capacitive discharges.* App. Phys. Lett., vol. 86, no. 2, page 021501, January 2005.

[Phelps 94] A V Phelps. *The application of scattering cross sections to ion flux models in discharge sheaths.* J. App. Phys., vol. 76, no. 2, page 747, July 1994.

[Piejak 04] R. B. Piejak, V. A. Godyak, R. Garner, B. M. Alexandrovich & N. Sternberg. *The hairpin resonator: A plasma density measuring technique revisited.* J. App. Phys., vol. 95, no. 7, pages 3785–3791, April 2004.

[Piejak 05] R B Piejak, J Al-Kuzee & N St J Braithwaite. *Hairpin resonator probe measurements in RF plasmas.* Plasma Sources Sci. Technol., vol. 14, no. 4, pages 734–743, November 2005.

[Quandt 98a] E Quandt, H F Dobele & W G Graham. *Measurements of negative ion densities by absorption spectroscopy.* App. Phys. Lett., vol. 72, no. 19, pages 2394–2396, May 1998.

[Quandt 98b] E Quandt, I Kraemer & H F Dobele. *Measurements of negative-ion densities by cavity ringdown spectroscopy.* Europhys. Lett., vol. 45, no. 1, pages 32–37, Jan 1998.

[Rauf 97] S Rauf & M J Kushner. *Argon metastable densities in radio frequency Ar, Ar/O_2 and Ar/CF_4 electrical discharges.* J. App. Phys., vol. 82, no. 6, pages 2805–2813, September 1997.

[Rauf 99] S Rauf & M J Kushner. *Nonlinear dynamics of radio frequency plasma processing reactors powered by multifrequency sources.* IEEE Trans. Plas. Sci., vol. 27, no. 5, pages 1329–1338, 0ct 1999.

[Rauf 02] Shahid Rauf & Peter L. G. Ventzek. *Charged species dynamics in an inductively coupled Ar/SF_6 plasma discharge.* J. App. Phys., vol. 92, no. 12, pages 6998–7007, December 2002.

[Robiche 03] J Robiche, P C Boyle, M M Turner & A R Ellingboe. *Analytical model of a dual frequency capacitive sheath.* J. Phys D: Appl. Phys., vol. 36, no. 15, pages 1810 – 1816, August 2003.

[Salabas 05] A Salabas & R P Brinkmann. *Numerical investigation of dual frequency capacitively coupled hydrogen plasmas.* Plasma Sources Sci. Technol., vol. 14, no. 2, pages S53–S59, May 2005.

[Sasaki 97] Shinya Sasaki, Itsuo Ishikawa, Kazuya Nagaseki, Yukinori Saito & Shinji Suganomata. *Positive and Negative Ions in RF Plasmas of*

SF_6/N_2 and SF_6/Ar Mixtures in a Planar Diode. Jpn. J. Appl. Phys., vol. 36, no. 2, pages 847–853, January 1997.

[Sasaki 99] K Sasaki & K Kadota. *Decay Processes of Electrons in the Afterglow of High-Density CF_4, c-C_4F_8 and CF_4-H_2 Plasmas.* Jpn. J. Appl. Phys., vol. 38, no. 7B, pages 4383–4388, July 1999.

[Sauers 79] I. Sauers, L. G. Christophorou & J. G. Carter. *Electron attachment to perfluorocarbon compounds. III. Fragmentation of aliphatic perfluorocarbons of interest to gaseous dielectrics.* J. Chem. Phys., vol. 71, no. 7, page 3016, October 1979.

[Seo 04] Hyungtak Seo, Jung-Hyung Kim, Yong-Hyeon Shin & Kwang-Hwa Chung. *Ion species and electron behavior in capacitively coupled Ar and O_2 plasmas.* J. App. Phys., vol. 96, no. 11, pages 6039–6044, December 2004.

[Sheridan 99a] T E Sheridan. *Double layers in a modestly collisional electronegative discharge.* J. Phys D: Appl. Phys., vol. 32, no. 15, pages 1761–1767, August 1999.

[Sheridan 99b] T E Sheridan, P Chabert & R W Boswell. *Positive ion flux from a low-pressure electronegative discharge.* Plasma Sources Sci. Technol., vol. 8, pages 457–462, 1999.

[Spencer-Smith 35a] J L Spencer-Smith. *Negative ions of Iodine - Part I Probe Measurements.* Philosophical Magazine, vol. 19, pages 806–823, 1935.

[Spencer-Smith 35b] J L Spencer-Smith. *Negative ions of Iodine - Part II Ion Beams.* Philosophical Magazine, vol. 19, pages 1016–1027, 1935.

[St-Onge 00] L St-Onge, M Chaker & J Margot. *Laser-induced photodetachment in high-density low-pressure SF_6 magnetoplasmas.* J. Vac. Sci. Technol. A, vol. 18, no. 5, pages 2363–2371, Sept/Oct 2000.

[Stenzel 76] R L Stenzel. *Microwave resonator probe for localized density measurements in weakly magnetized plasmas.* Rev. Sci. Instrum., vol. 47, no. 5, pages 603–607, May 1976.

[Stoffels 98] E Stoffels, W W Stoffels & K Tachibana. *Electron attachment mass spectrometry as a diagnostics for electronegativegases and plasmas.* Rev. Sci. Instrum., vol. 69, no. 1, pages 116–122, Jan 1998.

[Swift 70] J D Swift & M J R Schwar. Electrical probes for plasma diagnostics. Iliffe Books Ltd., London, 1 edition, 1970.

[Tonks 29] L Tonks & Irving Langmuir. *A General Theory of the Plasma of an Arc.* Physical Review Letters, vol. 34, no. 6, page 876, September 1929.

[Tsai 96] W. Tsai, G. Mueller, R. Lindquist, B. Frazier & V Vahedi. *High selectivity plasma etching of silicon dioxide with a dual-frequency 27/2 MHz capacitive radio frequency discharge.* J. Vac. Sci. Technol. B, vol. 14, no. 5, pages 3276–3282, Sept/Oct 1996.

[Turner 99] M M Turner & M A Lieberman. *Hysteresis and the E-to-H transition in radiofrequency inductive discharges.* Plasma Sources Sci. Technol., vol. 8, no. 2, pages 313–324, May 1999.

[Turner 06a] M M Turner & P Chabert. *Collisionless Heating in Capacitive Discharges Enhanced by Dual-Frequency Excitation.* Physical Review Letters, vol. 96, no. 20, page 205001, May 2006.

[Turner 06b] M M Turner & P Chabert. *Electron heating mode transitions in dual frequency capacitive discharges.* App. Phys. Lett., vol. 89, no. 23, page 231502, Dec 2006.

[Turner 07] M M Turner & P Chabert. *Electron heating mechanisms in dual-frequency capacitive discharges.* Plasma Sources Sci. Technol., vol. 16, no. 2, pages 364–371, May 2007.

[Ura 96] K Ura, K Sasaki & K Kadota. *Characteristics of Fluorine Negative Ions in Helicon-Wave Excited High-Density Carbon-Tetrafluoride Plasmas.* J. Plasm. Fus. Res., vol. 72, no. 11, pages 1204–1212, November 1996.

[Vacquie 87] S Vacquie, A Gleizes & M Sabsabi. *Measurement of the photodetachment cross section of the negative ion of fluorine.* Phys. Rev. A, vol. 35, no. 4, pages 1615–1620, Feb 1987.

[Vasenkov 04] A V Vasenkov & M J Kushner. *Modeling of magnetically enhanced capacitively coupled sources: $Ar/C_4F_8/O_2$ discharges.* J. App. Phys., vol. 95, no. 3, pages 834–845, February 2004.

[Wickens 79] L M Wickens & J E Allen. *Free expansion of a plasma with two electron temperatures.* J. Plasma Phys., vol. 22, no. 1, pages 167–185, August 1979.

[Worsley 06] M. A. Worsley, S. F. Bent, N. C. M. Fuller & T. Dalton. *Characterization of neutral species densities in dual frequency capacitively coupled photoresist ash plasmas by optical emission actinometry.* J. App. Phys., vol. 100, no. 8, page 083301, Decemeber 2006.

Garrett Anthony Curley

Publications and Presentations
(As of 19th March 2008)

Refereed Journal Publications

1. "Negative ions in single and dual frequency capacitively coupled fluorocarbon plasmas", G. A. Curley, D. Marić, J-P Booth, C. S. Corr, P. Chabert and J. Guillon, Plasma Sources Science and Technology **16** (2007) S87–S93

2. "Fluorine negative ion density measurement in a plasma etch reactor by cavity ring-down spectroscopy", J-P Booth, C. S. Corr, G. A. Curley, T. Földes, J. Jolly, J. Guillon, Applied Physics Letters **8** (2006) 151502

3. "A novel technique for plasma density measurements using surface-wave transmission spectra", S. Dine, J-P Booth, G. A. Curley, C. S. Corr, J. Jolly, J. Guillon. Plasma Sources Science and Technology **14** (2005) 777–786

Contributed Conference Oral Presentations with Abstracts Only

1. G. A. Curley, J-P. Booth, D. Marić, C. S. Corr, J, Guillon, "Negative ions in dual-frequency capacitively-coupled fluorocarbon gases", AVS 53rd International Symposium and Exhibition, San -Francisco, CA, USA. November 2006.

2. G. A. Curley, J-P. Booth, C. S. Corr, J. Guillon, "Fluorine negative ion and electron density measurements in a dual-frequency capacitive dielectric reactor", 6th International Workshop on Fluorocarbon Plasmas, Villard de Lans, France. March 2006.

3. G. A. Curley, J-P. Booth, C. S. Corr, J. Guillon, S. Dine, "Measuring the densities and fluxes of charged species in a dual-frequency capacitive plasma", 58th Gaseous Electronics Conference, San Jose, CA, USA. October 2005 (Bull. Amer. Phys. Soc. ***50*** *7* (2005)).

4. G. A. Curley, J-P. Booth, J. Guillon, "Charged species' densities and fluxes in a dual-frequency capacitive plasma in $Ar/C_4F_8/O_2$", CIP 05 – 15th International Colloquium on Plasma Processes, Autrans, France. June 2005.

5. G. A. Curley, J-P. Booth, N. Bulcourt, "Negative ions in a dual-frequency capacitive plasma in $Ar/C_4F_8/O_2$", 57th Gaseous Electronics Conference, Bunratty, Ireland. October 2004 (Bull. Amer. Phys. Soc. ***49*** *5* (2004)).

Contributed Conference Poster Presentations with Abstracts Only

1. G. A. Curley, J-P. Booth, D. Marić, P. Chabert, J. Guillon, "Negative ions in a dual-frequency capacitively coupled fluorocarbon plasma", Workshop on Radio-frequency Discharges, Dublin, Ireland. June 2007.

2. G. A. Curley, J-P. Booth, D. Marić, P. Chabert, J. Guillon, "Negative ions in a dual-frequency capacitively coupled fluorocarbon plasma", CIP 07 – 16th International Colloquium on Plasma Processes, Toulouse, France. June 2007.

3. G. A. Curley, J-P Booth, C. S. Corr, T. Földes, J. Guillon, "Densités et flux des espèces chargées dans un plasma capacitif excité à deux fréquences", 9th Congrès de la division plasmas de la société française de physique, Nancy, France. May 2006.

4. G. A. Curley, C. S. Corr, J-P Booth, T. Földes, J. Guillon, "F- density measurements by CRDS in a dual-frequency capacitive plasma in $Ar/C_4F_8/O_2$", Cavity Ring-Down User Meeting, Oxford, UK. September 2005.

5. G. A. Curley, J-P. Booth, J. Guillon, "Charged species' densities and fluxes in a dual-frequency capacitive plasma", 27th International Conference on Phenomena in Ionized Gases, Eindhoven, The Netherlands. July 2005.

6. G. A. Curley, J-P. Booth, J. Guillon, "Charged species' densities and fluxes in a dual-frequency capacitive plasma", 6th Frontiers in Low Temperature Plasma Diagnostics, Les Houches, France, April 2005.

7. G. A. Curley, J-P. Booth, N. Bulcourt, "Détection des ions négatifs dans un plasma capacitif double fréquence", 3ème journée d'échanges du Réseau Plasma Froid, Bonascre, France, 17th – 20th Oct 2004.